

*ÉCOLE DOCTORALE DES SCIENCES CHIMIQUE (222)*

Équipe Ingénierie des fonctions moléculaires, Institut de Chimie, UMR 7177

# THÈSE

présentée par :

**Adrien CERDAN**

soutenue le : 8 Février 2019

pour obtenir le grade de : **Docteur de l'Université de Strasbourg**

Discipline/ Spécialité : Chimie / Chimie théorique et informatique

**Exploration de la transmission  
synaptique et de la régulation des  
récepteurs ionotropes par simulations  
de dynamique moléculaire et  
électrophysiologie numérique**

**THÈSE dirigée par :**

**M. CECCHINI Marco**

Dr, Maitre de Conférence, CNRS - Université de Strasbourg

**RAPPORTEURS :**

**M. TAREK Mounir**

**M. SANSOM Mark**

Dr, Directeur de Recherche, CNRS - Université de Lorraine

Pr, Professor, University of Oxford

---

**AUTRES MEMBRES DU JURY :**

**M. STOTE Roland**

Dr, Directeur de Recherche, CNRS – Université de Strasbourg

EXPLORING SYNAPTIC TRANSMISSION AND  
REGULATION IN IONOTROPIC RECEPTORS BY  
MOLECULAR DYNAMICS SIMULATIONS AND  
COMPUTATIONAL ELECTROPHYSIOLOGY

ADRIEN HENRI CERDAN

Institut de Chimie de Strasbourg  
École doctorale des Sciences Chimiques - ED 222  
Université de Strasbourg

Thesis Director: Dr. Marco Cecchini  
May 27, 2019

*À mes parents  
Ginette et Jean-Marie.*

## ABSTRACT

---

In the central nervous system, signals within neurons are mostly transmitted through chemical synapses. At the level of the synapse, signal transduction arises from the binding of neurotransmitters to membrane receptors in order to open ion channels. The Glycine Receptor (GlyR) is an ionotropic receptor which is involved in several neurological disorders such as addiction, chronic pain, autism, or hyperekplexia. Because of its implication in many human diseases, it is of particular interest to design novel drugs targeting this receptor. With this goal in mind, we used Molecular Dynamics (MD) simulations and computational electrophysiology to probe the functional properties of available GlyR structures. In this thesis, we showed that none of the experimental structures display the physiological behavior of the conductive state. Using MD simulations, we captured a novel conformation of the GlyR compatible with a conductive state and demonstrated the importance of lateral portals for ionic permeation. Lastly, we proposed an original protocol, named *state-based pharmacology*, to discover modulators of allosteric proteins.

Au sein du système nerveux central, les signaux entre les neurones sont principalement transmis au travers des synapses chimiques. La transduction du signal y a lieu grâce à la liaison des neurotransmetteurs aux récepteurs membranaires, ce qui induit l'ouverture de canaux ioniques. Le Récepteur de la Glycine (RGly) est un récepteur ionotrope impliqué dans de nombreux troubles neuronaux tels que l'addiction, la douleur chronique, l'autisme, ou encore l'hyperekplexie. Du fait de son rôle dans plusieurs pathologies, il est important de développer des nouveaux traitements ciblant ce récepteur. Pour cette raison, nous avons utilisé des simulations de Dynamiques Moléculaire (DM) et d'électrophysiologie numérique afin d'évaluer les propriétés fonctionnelles des structures du RGly disponibles. Dans cette thèse, nous avons montré qu'aucune des structures obtenues expérimentalement ne satisfait les propriétés fonctionnelles de l'état actif du récepteur. Grâce aux simulations de DM, nous avons caractérisé une nouvelle conformation du RGly, qui est compatible avec l'état actif du récepteur. De plus, nous avons souligné le rôle majeur des portails latéraux pour la perméation des ions. Finalement, nous avons proposé un protocole original, nommé *pharmacologie dépendante de l'état*, pour identifier de nouvelles petites molécules modulatrices de protéines allostériques.

## RÉSUMÉ DÉTAILLÉ

---

### INTRODUCTION

Le système nerveux central, qui inclut le cerveau et la moelle épinière, a pour rôles essentiels la collecte, l'intégration, ainsi que la transmission d'informations, de part et vers l'ensemble du corps. La cellule nerveuse, ou neurone, est une des pièces maîtresses de ce système du fait de sa spécialisation pour la transmission de signaux. Le point de contact entre deux neurones se nomme la synapse. Cependant, au niveau de la synapse, il n'y a en général pas de contact physique entre les deux neurones, mais une mince (20 – 40 nm) fente synaptique. L'influx nerveux, ou potentiel d'action, qui se propage depuis le corps d'un neurone, le long de son axone, en direction de sa terminaison est de nature électrique. Plus précisément, le potentiel d'action correspond à la propagation directionnelle d'un changement rapide et transitoire du potentiel électrique de la membrane cellulaire. Cependant, le signal doit changer de nature afin de se propager à travers la fente synaptique pour atteindre le neurone suivant. Dans ce but, le signal électrique est converti en un signal chimique au niveau de la terminaison présynaptique par la libération de neurotransmetteurs dans la fente synaptique. Les neurotransmetteurs diffusant au travers de la fente synaptique seront éventuellement capturés au niveau du neurone postsynaptique par des récepteurs membranaires. La liaison des neurotransmetteurs à ces récepteurs membranaires va induire l'ouverture de canaux ioniques, soit directement dans le cas des récepteurs ionotropes (c.-à-d. les canaux ioniques contrôlés par ligand), soit indirectement pour les récepteurs métabotropes (c.-à-d. les récepteurs couplés aux protéines G). En effet, les récepteurs ionotropes combinent au sein d'une même protéine, les fonctions de liaison du neurotransmetteur et de diffusion des ions au travers de la membrane grâce à leur canal ionique. La spécificité des récepteurs ionotropes est donc leur rapidité à transduire le signal chimique (c.-à-d. la liaison du neurotransmetteur) en un signal électrique (c.-à-d. la modification sélective de la perméabilité membranaire). Il est connu que le mécanisme d'isomérisation responsable de l'ouverture (ou de la fermeture) d'un canal ionique de ce type est de l'ordre de la microseconde. Les récepteurs ionotropes jouent donc un rôle central dans le fonctionnement de la synapse chimique rapide. Il n'est donc pas étonnant de les savoir impliqué dans de nombreux troubles psychiatriques ou maladies touchant le cerveau humain.

Ces récepteurs peuvent être classifiés selon le type d'ions pour les lesquels ils sont perméables ; la perméabilité cationique étant synonyme d'activité excitatrice du neurone, alors que la perméabilité anionique promeut une inhibition du neurone. La seconde façon de classifier cette superfamille de protéine est basée sur leur organisation quaternaire. Il existe la famille des récepteurs trimériques, nommés P<sub>2</sub>X, qui lient l'adénosine triphosphate (ATP) en tant que neurotransmetteur et fera l'objet d'un chapitre au sein de cette thèse. La famille des récepteurs tetramériques qui sont activés par le Glutamate, ne sera pas discutée plus longuement. Il existe également la famille des récepteurs pentamériques qui est la plus con-

nue grâce à l'illustre récepteur nicotinique de l'acétylcholine, qui fut le premier récepteur membranaire à être identifié à la fin des années 1960 (Changeux et al. 1970a). Cette famille de protéines pentamériques représente le sujet d'étude principal de cette thèse, qui portera plus particulièrement sur le Récepteur de la Glycine (RGly).

De par leur importance physiologique et pharmacologique, il est nécessaire d'avoir des modèles à résolution atomique de ces récepteurs afin de comprendre, et possiblement traiter divers troubles mentaux. Ces modèles atomiques sont, pour la plupart, obtenus en biologie structurale grâce à la cristallographie aux rayons X et plus récemment à la Cryo-Microscopie Électronique (Cryo-ME).

Les récepteurs ionotropes peuvent peupler au moins trois états fonctionnels différents (Cecchini and Changeux 2015). Le premier est un état de repos en absence de neurotransmetteur, où le canal est fermé. Le second correspond à un état actif en présence de neurotransmetteur où le canal est ouvert et sélectivement perméable. Enfin, le dernier est un état dit désensibilisé, en cas d'exposition prolongé au neurotransmetteur, où le canal est fermé, mais de façon distincte à l'état de repos (Gielen and Corringer 2018). Le modèle allostérique de Monod-Wyman-Changeux (MWC) (Monod et al. 1965) s'applique particulièrement bien à cette superfamille, et nous apprend que ces trois états sont tous préexistant et en équilibre. Cet équilibre peut être déplacé par les neurotransmetteurs ou d'autres petites molécules.

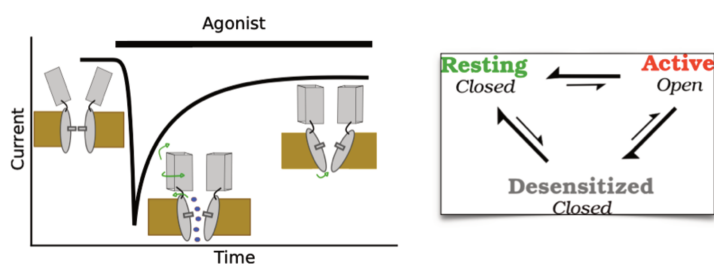


Figure 0.1 – Représentation des trois états (de repos, actif, et désensibilisé) peuplés par les récepteurs ionotropes pentamériques, selon la présence de neurotransmetteur. Ces trois états sont tous préexistant et en équilibre.

Il n'est cependant pas trivial d'assigner, a priori, un état fonctionnel (de repos, actif, ou désensibilisé) à la structure d'un canal ionique obtenue par cristallographie aux rayons X ou Cryo-ME (Trick et al. 2016), notamment à cause d'effets hydrophobes apparaissant dans les pores de taille nanométrique (Aryal et al. 2015). Les méthodologies existantes se basent principalement sur des propriétés géométriques du canal (O. S. Smart et al. 1996), ou sur le degré d'hydratation de celui-ci. Bien que ces techniques permettent d'évaluer qualitativement la perméabilité d'un canal ionique, elles ne permettent pas une comparaison de leurs résultats avec des données expérimentales. Il n'est donc pas possible de juger de la pertinence physiologique des structures étudiées. Dans le cadre de cette thèse, nous avons employés différentes méthodes de chimie informatique telles que les simulations de Dynamiques Moléculaires (DM) et d'Électrophysiologie Numérique (EN) (Gumbart et al. 2012), afin d'étudier les propriétés conductrices des structures atomiques des récepteurs RGly et P2X et de comparer

systématiquement nos résultats avec les données expérimentales disponibles. Ce qui nous permet d'assigner clairement une fonction à la structure d'un canal.

## RÉSULTATS ET DISCUSSIONS

### *Élucidation de l'état physiologiquement actif du RGly*

Le RGly est l'un des récepteurs ionotropes pentamériques les mieux caractérisés grâce à la publication en 2015 de trois structures du même canal, liés à différents ligands, et possiblement dans trois états fonctionnels distincts (Du et al. 2015). Notamment, deux de ces structures pourraient correspondre à l'état actif. Nous avons appliqué diverses méthodes de chimie numérique afin d'établir le lien entre les deux structures du récepteur RGly potentiellement représentatives de l'état actif, et leurs propriétés fonctionnelles.

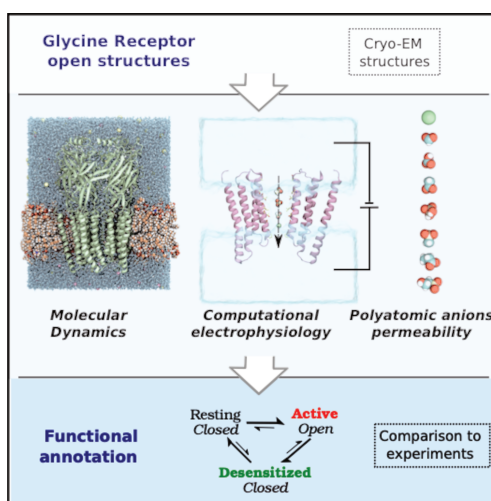


Figure 0.2 – Combinaison de simulations numériques pour une annotation fonctionnelle des structures de canaux ioniques. Adaptée de Cerdan et al. 2018.

En utilisant des simulations de DM, nous avons montré l'instabilité intrinsèque de ces deux structures du canal. De plus, l'usage de l'EN a permis de montrer qu'aucune des deux structures n'est en mesure de reproduire les propriétés expérimentales de conductance, ou de perméabilité sélective aux petits anions poly-atomiques. A contrario, une conformation nouvelle a été capturée durant nos simulations. À ce jour, cette dernière correspond au modèle le plus fidèle de l'état physiologiquement actif du RGly d'après les propriétés fonctionnelles testées (conductance, sélectivité, perméabilité d'anions poly-atomiques). Grâce à cette étude, il nous a également été possible de faire une classification fonctionnelle des structures des récepteurs ionotropes pentamériques sélectifs pour les anions.

Cette classification en trois groupes (au repos, actif, et désensibilisé) supporte le modèle selon lequel la localisation du point de constriction lors de la fermeture du canal est différente entre l'état de repos et désensibilisé (Gielen and Corringer 2018). Ces résultats ont fait l'objet d'une publication dans Structure (Cerdan et al. 2018).

### *Caractérisation des mécanismes de diffusion des anions chlorures au travers du canal du RGly*

Disposant d'une conformation du RGly stable en DM, nous avons pu l'exploiter pour identifier par EN les chemins de perméation des anions chlorures au travers de la membrane via le récepteur. Ce faisant, nous avons identifié deux routes ; la première par le haut du récepteur, qui est le chemin connu à ce jour. L'autre chemin profite de l'existence de portails latéraux à l'interface entre les cinq sous-unités au niveau du domaine extracellulaire. Nos simulations tendent à montrer que le chemin utilisant les portails latéraux est, en fait, la voie principalement utilisée par les anions chlorures. Ce résultat est supporté par la réinterprétation d'expériences de mutagenèse qui avaient permis d'identifier un acide-aminé dont la mutation diminue la conductance, et qui s'avère être positionné à l'entrée des portails latéraux. La simulation du mutant montre que le même effet est observé, soutenant notre réinterprétation mécanistique à l'échelle atomique.

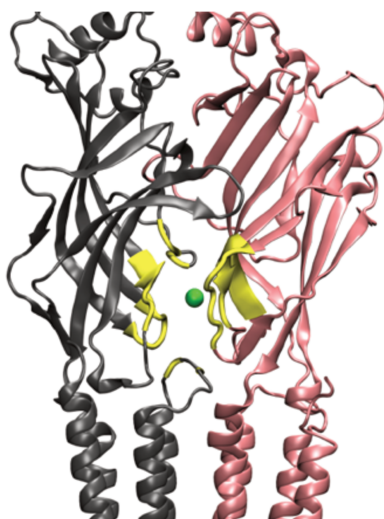


Figure 0.3 – Portails latéraux nouvellement identifiés comme étant le chemin majoritairement utilisé par les ions chlorure.

Bien que la structure du domaine intracellulaire soit méconnue pour la majorité des récepteurs ionotropes pentamériques, incluant le RGly, l'existence de portails latéraux y a été démontrée pour le récepteur de la sérotonine. Il est notamment intéressant de voir que l'effet de la mutation dans les portails du domaine extracellulaire a un effet très similaire aux mutations du domaine intracellulaire. De ce fait, il serait possible d'unifier le rôle des domaines extra- et intracellulaires vis-à-vis de la perméation des ions ; à savoir une entrée et sortie du canal par des portails latéraux, et un passage vertical au travers de la membrane. Un manuscrit décrivant ces résultats est en préparation.

## Vers une identification de petites molécules à but pharmacologique basée sur l'état fonctionnel des récepteurs

Finalement, nous avons pour but d'intégrer les conclusions précédemment obtenues concernant l'annotation fonctionnelle des structures du RGly dans un objectif de conception de médicament. Pour ce faire, nous souhaitons mettre en place une méthodologie nommée « conception de médicament basé sur l'état fonctionnel » (state-based drug design). D'après le modèle MWC de l'allostérie, il devrait être possible d'identifier un modulateur allostérique d'après son  $\Delta\Delta G_b$  de liaison pour un état fonctionnel du récepteur par rapport aux autres. Ainsi, cette méthodologie tend à dépasser la simple information sur l'énergie libre de liaison pour une structure, mais à faire la différence entre les énergies libres de liaison pour chacun des états. Cette avancée permettra notamment de prédire plus efficacement l'effet modulateur d'une petite molécule sur les transitions allostériques d'un récepteur. Dans ce but, nous avons compilé une chimiothèque de petites molécules modulatrices de la fonction du RGly. Cette chimiothèque comprend 159 petites molécules classifiées selon leur effet, leur site de liaison, et l'état fonctionnel auquel elles peuvent probablement se lier. Disposant d'un ensemble de structures pour chacun des trois états connus du RGly et d'une chimiothèque de petites molécules aux effets connus expérimentalement, nous sommes dans une position favorable pour confirmer le potentiel de cette nouvelle approche pour la conception de médicament contre des pathologies telles que les douleurs chroniques inflammatoires ou les addictions.

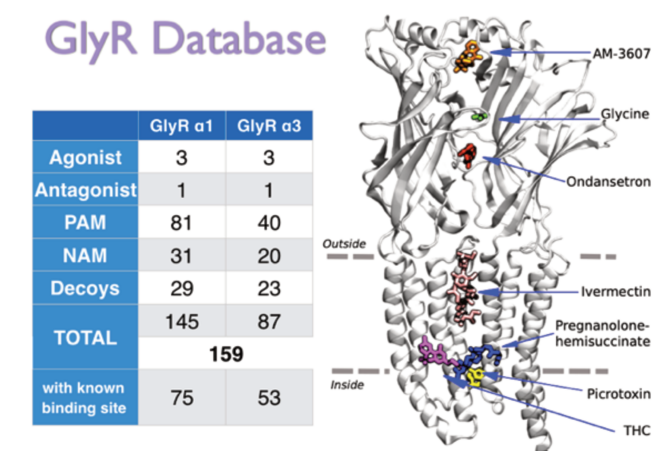


Figure 0.4 – Résumé du contenu de la chimiothèque des modulateurs du RGly. Représentation du RGly ainsi que les différents sites de liaison connus avec une des petites molécules pouvant s'y lier.

*Caractérisation des mécanismes de diffusion de larges cations poly-atomiques au travers du canal du récepteur P2X*

Ce travail fut réalisé en collaboration avec le laboratoire de biologie du Dr. Thomas Grutter à la faculté de pharmacie d'Illkirch. Nous nous sommes intéressés au passage de larges cations organiques au travers du canal du récepteur P2X4. La controverse au sujet de ce canal est de savoir si le récepteur peut être stabilisé dans une conformation dilatée, perméable aux cations organiques, a contrario de l'état actif non-dilaté. Le travail de biologie expérimentale a permis de montrer que les cinétiques de pénétration cellulaire des cations organiques sont semblables aux ions monoatomiques et qu'il n'est pas nécessaire d'invoquer l'existence de deux états actifs, dont l'un serait dilaté. Nos simulations numériques ont confirmé que l'état non-dilaté est suffisamment large pour laisser passer les cations  $\text{NMDG}^+$  et  $\text{SPD}^{3+}$ . De plus, nous avons proposé une explication atomistique concernant la très faible perméabilité du cation  $\text{NMDG}^+$  par rapport au cation  $\text{Na}^+$  basée sur l'existence d'une sélection conformationnelle et orientationnelle des cation  $\text{NMDG}^+$ , diminuant drastiquement sa perméabilité. Ces résultats ont fait l'objet d'une publication dans PNAS en collaboration avec l'équipe expérimentale (Harkat et al. 2017).

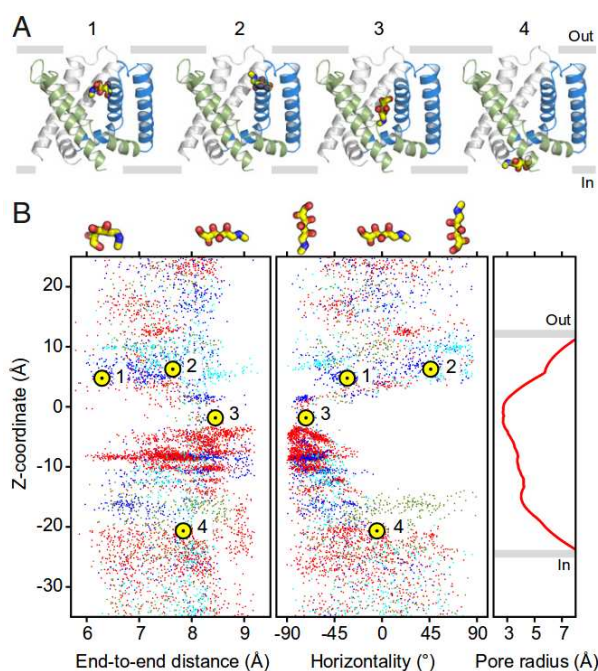


Figure 0.5 – Mécanisme de perméation du cation  $\text{NMDG}^+$  au travers du canal du récepteur P2X4. (A) Instantanés pris durant la simulation de DM. (B) De gauche à droite, la distance de bout en bout du cation, l'orientation du cation, le rayon du canal de P2X4. Adaptée de Harkat et al. 2017.

## CONCLUSION GÉNÉRALE

La combinaison de multiples techniques de simulations numériques des structures atomiques du récepteur P2X et de celui de la Glycine nous ont permis d'arriver aux conclusions suivantes : Aucune des structures du RGly obtenues par Cryo-ME ne permettent de reproduire le fonctionnement physiologique de l'état actif. Un modèle de cet état a été capturé par simulation de DM et nous a permis de reproduire qualitativement les propriétés conductrices du canal. L'obtention d'un modèle fiable de l'état actif nous a permis d'explorer les chemins empruntés par les anions pour diffuser au travers du canal et de confirmer le rôle majeur des portails latéraux récemment découvert à l'interface entre les sous-unités protéiques. En combinant le modèle MWC de l'allostérie, une chimiothèque de modulateurs connus, et l'annotation fonctionnelle des structures atomiques du RGly, nous avons proposé une méthodologie pour identifier des petites molécules, et prédire leurs potentiels effets de modulation allostérique de l'activité du récepteur. Ces travaux toujours en cours ont d'importantes implications pharmacologiques. L'application de notre méthodologie au cas du récepteur P2X a permis de démontrer que la structure correspondant à l'état actif non-dilaté est suffisamment ouverte pour permettre la diffusion des cation  $\text{NMDG}^+$  et  $\text{SPD}^{3+}$ . L'étude du mécanisme de translocation de ces cations nous a permis de rationaliser leurs cinétiques relatives de perméation.

En conclusion, nous avons développé une stratégie fondée sur des simulations moléculaires pour inférer la probable fonction des structures de récepteurs ionotropes. De plus, nous avons montré comment utiliser ces nouvelles informations pour valider les modèles de transitions allostériques précédemment proposés. L'ensemble pouvant servir dans le cadre de l'identification de petites molécules à but pharmacologique, afin de potentiellement traiter certains des troubles neurologiques et des douleurs chroniques qui affligent une part toujours croissante de l'humanité.

## PUBLICATIONS

---

Some ideas and figures have appeared previously in the following publications:

A.H. Cerdan and M. Cecchini. "New computational insights on the role of the extracellular domain for ion permeation in pentameric Ligand-Gated Ion Channels". *In preparation*.

A.H. Cerdan, N.E. Martin and M. Cecchini. "An ion permeable state of the Glycine receptor captured by Molecular Dynamics". *Structure*, 26(11), 1555–1562.e4 **2018**.

M. Harkat, L. Peverini, A.H. Cerdan, K. Dunning, J. Beudez, A. Martz, N. Calimet, A. Specht, M. Cecchini, T. Chataigneau and T. Grutter. "On the permeation of large organic cations through the pore of ATP-gated P2X receptors". *Proc. Natl. Acad. Sci*, 114(19), pp. E3786–E3795, **2017**.

## COMMUNICATIONS

---

A.H. Cerdan and M. Cecchini. "Elucidation of the physiologically active state of the glycine receptor by molecular dynamics simulations". XXème Congrès du Groupe de Graphisme et Modélisation Moléculaires (GGMM), Reims (France), Mai 2017

A.H. Cerdan and M. Cecchini. "Bridging the gap between structure and function in ligand-gated ion channels" Inaugural meeting of the CDP6 section of the Human Brain Project (HBP), Paris (France), July 2017

A.H. Cerdan and M. Cecchini. "Elucidation of the physiologically active state of the glycine receptor by molecular dynamics simulations". 5th Annual Human Brain Project Summit, Glasgow (Scotland), October 2017

A.H. Cerdan and M. Cecchini. "Modelling ion permeation in Glycine receptor channels: structure-function relationship". 2nd Annual meeting of the CDP6 : Modelling for Drug Discovery, Jülich (Germany), October 2018

## ACKNOWLEDGMENTS

---

First and foremost, I would like to thank my thesis director, Dr. Marco Cecchini, for the fantastic opportunity he gave to me three years ago to be a student in his lab. During these few years, Marco allowed me to explore my subject of research with plenty of freedom and provided to me all the resources and the appropriate pieces of advice to succeed.

I am grateful to Dr. Roland Stote, Dr. Mounir Tarek, and Pr. Mark Sansom for having accepted to be part of my thesis committee and providing such enlightening comments and discussions following my dissertation.

Part of the work presented in this thesis arises from the fruitful collaboration with Dr. Thomas Grutter and his team, to which I am definitively acknowledgeable.

I am beholden to Pr. Jean-Pierre Changeux for the chance he gave me to join the Institut Pasteur and the Human Brain Project. Jean-Pierre was also kind enough to spend plenty of time listening to my research and being such a distinguished ambassador of my research project.

I am more than thankful to Dr. Pierre-Jean Corringer and his team for hosting me in the Institut Pasteur and providing to me the precious point of view of experimentalists on computational work. A special thanks to all the members of the Channel-Receptors Unit who shared their desks with me.

I am infinitely thankful to all the member of the Laboratoire d'Ingénierie des Fonctions Moléculaires that I had the chance to meet during the years.

This thesis wouldn't have been the same without Dr. Nicolas Martin and Dr. Florian Blanc, my two fellow office-mates since day one. Nicolas was the one who gave me the idea to join the lab, and I couldn't be more thankful for that. He is also the one who did the dirty job to introduce me to ion-channel simulations and answered to all my beginner questions about them. I was lucky enough to also share my office with Florian who was a real master in a too long list of things to be enumerated here, and yet an excellent training partner during these last years of running.

I thank Dr. Simone Conti for teaching me how to deal with big robots such as Mazinger and Goldorak, Dr. Joel Montalvo Acosta for all the joy he added to the lab thanks to his talents of singer and performer, and Dr. Diego Gomez for canalizing Joel's energy far enough from my office.

I am glad to stay long enough in the lab to see the new generation replacing us, and I would like to thank Marion Sisqueles, Alison Popp and Gilberto Peirera for being so interested in learning and continuing with passion the work in pentameric ligand-gated ion channels.

This Ph.D. thesis is the beginning of a new journey, but it is also the end of my student life, which has been delightful thanks to my friends at the Faculté de Chimie de Strasbourg. A special thanks for all my mates from ALCANES who participated at making this trip unforgivable.

I have to be particularly grateful to some of my friends who were unimaginably supportive during all this year, in particular, Dr. Florian Koengen with whom I spent more time speaking accelerated Molecular Dynamics than actually rock climbing, and Morgan Remy, Lucas Holder, and Cyril Orio for being such amazing friends for so long.

I had the chance to grow up in an exceptionally supportive family, which provided me everything that is needed to succeed both as a student and as a person. For that reason, I am forever thankful to my brothers Matthieu and Harold, as well as my parents, Ginette, and Jean-Marie.

Last but not least, I could not imagine what this thesis would be without Helene Lotz, who has been entirely comprehensive during these years of hard work, even when it implied several sacrifices for our relationship. I could never be grateful enough for all the love you expressed to me.

## CONTENTS

---

Abstract	iii
Résumé détaillé	iv
Acknowledgments	xii
<b>1 INTRODUCTION</b>	<b>1</b>
1.1 Signal transmission in neurons	1
1.1.1 Neurons	1
1.1.2 An electric signal	2
1.1.3 The ionic basis for membrane potential	4
1.1.4 Generation and propagation of the action potential	5
1.2 The chemical synapses	6
1.2.1 Neurotransmitters	7
1.2.2 Release of neurotransmitter from the pre-synaptic neuron	8
1.2.3 Neurotransmitters receptors	9
1.2.4 Postsynaptic membrane potentials	9
1.3 Ligand-Gated Ion Channels for fast chemical synapses	11
1.3.1 Ligand-Gated Ion Channels Diversity	11
1.3.2 Pentameric Ligand-Gated Ion Channels diversity	12
1.4 The Glycine Receptor	14
1.4.1 Diversity and function	14
1.4.2 Pathology and Pharmacology	15
1.4.3 Structure	17
1.4.4 Ion pore properties	23
1.4.5 Gating mechanism	24
1.4.6 The functional-annotation problem	27
<b>2 THEORY</b>	<b>29</b>
2.1 Modeling ion diffusion and permeation	29
2.1.1 The Poisson-Nernst-Planck model	29
2.1.2 Brownian Dynamics	30
2.1.3 Molecular Dynamics	31
2.2 Molecular Dynamics simulations	32
2.2.1 The potential energy function	32
2.2.2 Numerical integration	34
2.3 Computational electrophysiology	35
2.3.1 Ion imbalance	36
2.3.2 Constant electric field	36
<b>3 AN ION PERMEABLE STATE OF THE GLYCINE RECEPTOR CAPTURED IN SILICO</b>	<b>39</b>
3.1 Introduction	39
3.2 Methods	42

3.3	Results and Discussion . . . . .	48
3.3.1	Structural stability of the ion channels . . . . .	48
3.3.2	Permeability to Chloride anions and conductance . . . . .	57
3.3.3	Permeability to polyatomic anions and selectivity . . . . .	60
3.3.4	A novel structural annotation of the anionic pLGICs . . . . .	61
3.4	Conclusion . . . . .	64
4	ELUCIDATION OF THE ION PERMEATION MECHANISM IN GLYCINE RECEPTOR	66
4.1	Introduction . . . . .	66
4.2	Methods . . . . .	66
4.3	Results and Discussion . . . . .	68
4.3.1	Exploration of <i>full-length</i> GlyR conductance . . . . .	68
4.3.2	Identification of a novel main permeation pathway . . . . .	72
4.3.3	A mutation that closes the portals . . . . .	75
4.4	Conclusion . . . . .	78
5	TOWARD A STATE-BASED PHARMACOLOGY FOR GLYCINE RECEPTOR	81
5.1	Introduction . . . . .	81
5.2	Methods . . . . .	82
5.3	Results and Discussion . . . . .	85
5.3.1	The Glycine Receptor Allosteric-Ligand Library . . . . .	85
5.3.2	A Drug Design protocol for Allosteric Protein . . . . .	90
5.4	Conclusion . . . . .	93
6	PERMEATION MECHANISM OF ORGANIC CATIONS IN TRIMERIC P2X RECEPTOR	95
6.1	Introduction . . . . .	95
6.2	Methods . . . . .	96
6.3	Results and Discussion . . . . .	97
6.3.1	Permeation mechanism of NMDG . . . . .	97
6.3.2	Permeation mechanism of Spermidine . . . . .	100
6.4	Conclusion . . . . .	101
7	CONCLUSIONS AND PERSPECTIVES	103
	BIBLIOGRAPHY	105
	Appendices	115
A	GLYCINE RECEPTOR $\alpha 1$ CORE ATOMS	116
B	COMPUTATIONAL ELECTROPHYSIOLOGY DATA (TMD-ONLY)	117
C	WATER EQUILIBRIUM PROFILES OF GLYR $\alpha 1$ CRYO-EM STRUCTURES	120
D	HOLE PROFILE OF ANIONIC PLGIC STRUCTURES	121
E	COMPUTATIONAL ELECTROPHYSIOLOGY DATA ( <i>full-length</i> )	122
F	(MIS)USE OF BROWNIAN DYNAMICS FOR COMPUTATIONAL ELECTROPHYSIOLOGY	123

## ACRONYMS

---

<b>5-HT</b>	5-hydroxytryptamine (Serotonin)
<b>5-HT<sub>3</sub>R</b>	Serotonin type 3 Receptor
<b>ACh</b>	Acetylcholine
<b>AChBP</b>	Acetylcholine Binding Protein
<b>AMPA</b>	alpha-amino-3-hydroxy-5-methyl-4-isoxazolepropionic acid
<b>ATP</b>	Adenosine Triphosphate
<b>BBK</b>	Brünger-Brooks-Karplus
<b>BD</b>	Brownian Dynamics
<b>CBD</b>	Cannabidiol
<b>CGenFF</b>	CHARMM General Force Field
<b>CHARMM</b>	Chemistry at Harvard Molecular Mechanics
<b>cMD</b>	conventional Molecular Dynamics
<b>CNS</b>	Central Nervous System
<b>cryo-EM</b>	Cryo-Electron Microscopy
<b>CSV</b>	Comma-Separated Values
<b>ECD</b>	Extracellular Domain
<b>ELIC</b>	<i>Erwinia chrysanthemi</i> Ligand-gated Ion Channel
<b>GA</b>	General Anesthetics
<b>GABA</b>	$\gamma$ -Aminobutyric acid
<b>GABA<sub>A</sub>R</b>	GABA type A Receptor
<b>GaMD</b>	Gaussian accelerated Molecular Dynamics
<b>GHK</b>	Goldman–Hodgkin–Katz
<b>GLIC</b>	Gloeobacter Ligand-Gated Ion Channel
<b>GluCl</b>	Glutamate-gated Chloride Channel
<b>GlyR</b>	Glycine Receptor
<b>GPCR</b>	G Protein-Coupled Receptor
<b>GPU</b>	Graphics Processing Unit
<b>GRALL</b>	Glycine Receptor Allosteric-Ligands Library
<b>HTS</b>	High-throughput screening
<b>ICD</b>	Intracellular Domain
<b>iGluR</b>	Ionotropic Glutamate Receptor

<b>I-V</b>	current-voltage
<b>IVM</b>	Ivermectin
<b>LJ</b>	Lennard-Jones
<b>LGIC</b>	Ligand-Gated Ion Channel
<b>MAM</b>	4,4'-bis(maleimido-glycine)azobenzene
<b>MD</b>	Molecular Dynamics
<b>ML</b>	Machine Learning
<b>MWC</b>	Monod-Wyman-Changeux
<b>nAChR</b>	nicotinic Acetylcholine Receptor
<b>NAM</b>	Negative Allosteric Modulator
<b>NAMD</b>	Nanoscale Molecular Dynamics
<b>NMDA</b>	N-Methyl-D-aspartic acid
<b>NMDG<sup>+</sup></b>	N-Methyl-D-glucamin
<b>NMR</b>	Nuclear magnetic resonance
<b>NPT</b>	isothermal–isobaric
<b>NVE</b>	microcanonical
<b>NVT</b>	canonical
<b>P2XR</b>	ATP-gated P2X ionotropic receptor
<b>PAM</b>	Positive Allosteric Modulator
<b>PB</b>	Poisson-Boltzmann
<b>PBC</b>	Periodic Boundary Conditions
<b>PCA</b>	Principal Component Analysis
<b>PIGS</b>	Progress-Index Guided Sampling
<b>pLGIC</b>	pentameric Ligand-Gated Ion Channel
<b>PME</b>	Particle-Mesh Ewald
<b>PNP</b>	Poisson-Nernst-Planck
<b>POPC</b>	1-Palmitoyl-2-oleoylphosphatidylcholine
<b>RMSD</b>	Root-Mean-Square Deviation
<b>SMILES</b>	Simplified Molecular Input Line Entry Specification
<b>SPD<sup>3+</sup></b>	Spermidine
<b>THC</b>	Tetrahydrocannabinol
<b>TMD</b>	Transmembrane Domain
<b>TPA<sup>+</sup></b>	tetrapropyl ammonium
<b>v-HTS</b>	Virtual high-throughput screening
<b>WT</b>	Wild Type
<b>ZAC</b>	Zinc-activated ion channel

## INTRODUCTION

---

This thesis aims to explore the synaptic transmission at the level of the ionotropic receptors using molecular dynamics simulations and computational electrophysiology. Before going into the details of the research carried out during the past three years, we will introduce the needed concepts starting from the neurons.

### 1.1 SIGNAL TRANSMISSION IN NEURONS

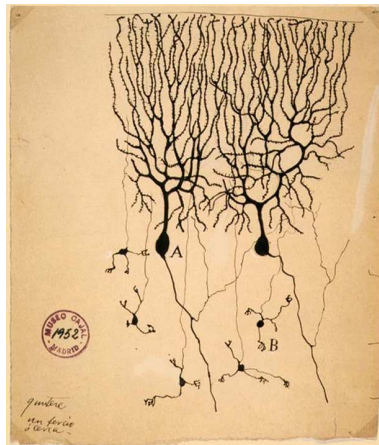
Our journey is taking place in the Central Nervous System (CNS) which includes the brain and the spinal cord, although we will primarily discuss the human nervous system, most of the basic elements that will be presented here are transferable to other animals. The CNS role is to collect, process and transmit information from and to all parts of the body in the vast majority of multicellular animals (Purves et al. 2015). The most famous cell in the nervous system is, of course, the nerve cell, i.e., the neuron. It is not surprising that the neuron, with its elementary function in the CNS, is all about signal transmission. In this section, we will describe the neuronal architecture and the basics of electric signal transmission within nerve cells.

#### 1.1.1 *Neurons*

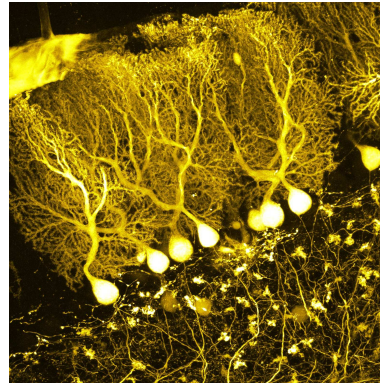
The central role of the neurons in the CNS was acknowledged in the late 19<sup>th</sup> century by Santiago Ramón y Cajal using and improving the silver staining process developed by Camillo Golgi to visualize the nervous cells under a microscope (López-Muñoz et al. 2006) (see Figure 1.1). Cajal described each element as "an absolutely autonomous canton", which became later the neuron doctrine (López-Muñoz et al. 2006). Although Golgi disagreed on Cajal's conclusions, they got in 1906 the first shared Nobel Prize of physiology or medicine "in recognition of their work on the structure of the nervous system." The term *neuron* was finally introduced in 1891 by Heinrich Wilhelm Waldeyer to describe the fundamental unit of the nervous system (Finger 1994).

The number of neurons in the brain is highly diverging between species from a simple organism like the nematode worm *Caenorhabditis elegans* which has only 302 neurons to the human brain with ~85 billion neurons (Bartheld et al. 2016).

One of the striking attribute of the neuron specialization into communication is their branching out (see Figure 1.2). The branched expansions of the nerve cell are called dendrites. The dendrites are the most common target for afferent synaptic contact from other neurons. The number of dendrites is profoundly different between neuron type. Some neurons have no dendrites and are only innervated by one or a few other neurons, but some neurons might have a "forest" of dendrites, increasing the complexity of the innervation.



(a) Drawing of Purkinje cells (A) and granule cells (B) from pigeon cerebellum by Santiago Ramón y Cajal, 1899; Instituto Cajal, Madrid, Spain.



(b) Cerebellar Purkinje cells expressing tdTomato. Confocal microscope image. Source of Wikimedia Commons, by BrainsRusDC, 2017; CC BY 4.0.

Figure 1.1 – Images of neurons one century apart.

The contact between two neurons is called a synapse and is located most of the time on the dendrites. In general, there is no physical contact between the two neurons forming the synapse and this extracellular space is named the synaptic cleft. On the side of the incoming signal there is the pre-synaptic termination and on the other side the post-synaptic one. As mentioned above, the number of synapses a neuron will have depends on its dendrite ramification and can be between 1 and 100,000 (Drachman 2005).

The input signals from afferent neurons are integrated and processed into an output signal that is propagated inside the axon, which is the specialized part of the neuron for signal conduction. The axon is an extension of the neuron that is  $\sim 100\ \mu\text{m}$  in length, or even more in specific neuron type, e.g., the sensory neuron that goes in the toe can be 1.5 m long. Neurons with short axons like in the brain are called interneurons, and the ones with longer axons that reach further target are the projection neurons.

### 1.1.2 An electric signal

As described above, neurons have a particular architecture to transmit a signal to each other and the rest of the body. This signal arises from a change in electrical potential difference between the two sides of the cellular membrane. Although all cells have a membrane potential, neurons are specialized in the modification of this potential to encode and transmit signals. All neurons have a negative resting potential that is sustained by the living cell and is between  $-40$  and  $-90\ \text{mV}$ , this value often around  $-65\ \text{mV}$  (Lewis et al. 2011). Electric signal might arise from an external stimulus in sensory neuron (i.e., receptor potential) or during the activation of a synapse (i.e., synaptic potential), they implies a short (few ms) and relatively small variation ( $\sim\text{mV}$ ) in the membrane potential which is termed graded potential (Hille 2001). Graded potentials are the neuron's response to inputs it collects.

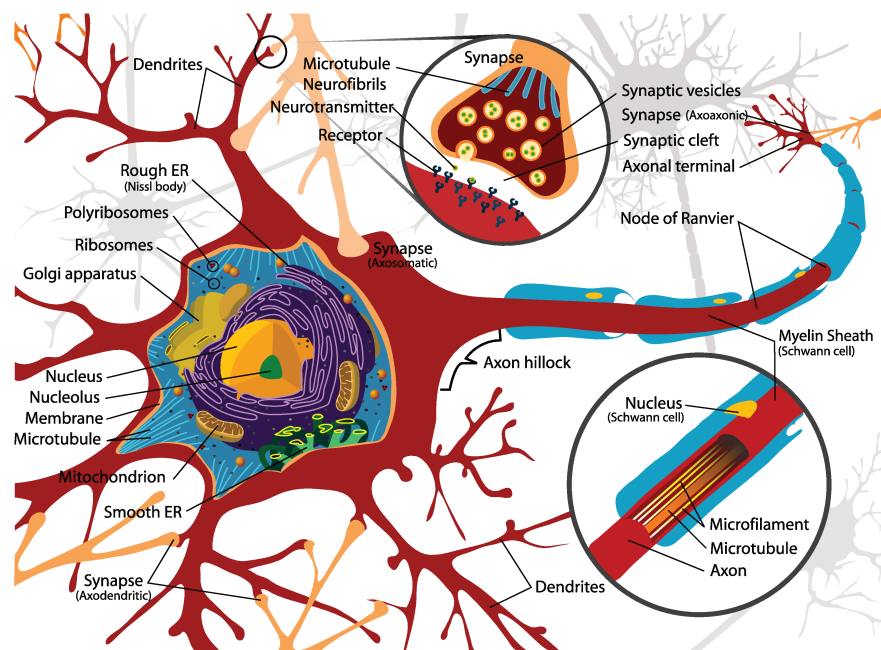


Figure 1.2 – A schematic representation of a neuron. From Wikipedia Commons, 2007.

The integration of the information within the neuron happens during the summation of all the graded potential arising at the dendrites or the soma of the neuron. The summation happens at the basis of the axon where the trigger zone of the action potential is located (i.e., the axon hillock, see Figure 1.2). The action potential (or spike) is the electric signal that the neuron sends within its axon as an output. They are used to carry the signal over a long distance to other neurons and also to reach the targets in the body, like the muscle for example.

If the membrane potential becomes more negative than the resting potential, it is called hyperpolarization which has an inhibitory effect on the action potential. On the other side, if the membrane potential is becoming less negative, it is a depolarization.

From the summation of the graded potential, neurons will or will not generate an action potential or spike that propagates within the axon. When enough depolarization is accumulated to reach a threshold potential (it is often around  $-50$  mV (Platkiewicz and Brette 2010)), then the action potential is triggered. After ignition of the action potential, the membrane potential quickly rises to positive values (up to  $40$  mV (Purves et al. 2015)) before equally abruptly going down to an even lower value than the resting potential called the refractory period (see Figure 1.3).

The action potential has an all-or-none property, the amplitude of the action potential is independent of the intensity of the depolarization of the membrane that triggers it, assuming that the depolarization is enough to reach the threshold. The action potential is then propagated along the axon with a constant amplitude and duration. In summary, the electric signal that is transmitted within the axon is the propagation of a membrane depolarization that is sustained by a net flux of ion across adjacent membrane patches.

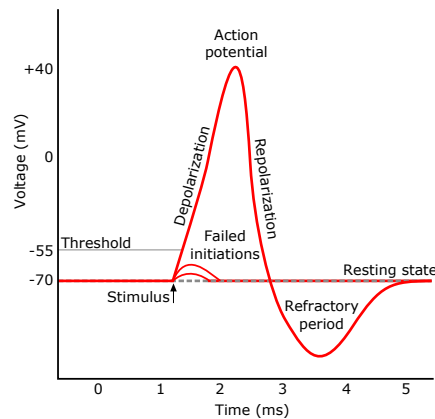


Figure 1.3 – A schematic representation of an action potential. From Wikipedia Commons.

### 1.1.3 The ionic basis for membrane potential

The membrane potential is the difference in electric potential between the interior and the exterior of the cell. These electric potentials are coming from: (i.) the concentration gradient for specific ions across the membrane and (ii.) the selective permeability of the membrane to these ions. Two protein families are involved in these processes: (i.) transporters to maintain the gradients and (ii.) ion channels for ion-specific permeability.

Transporters and ion-channels are working antagonistically. However, they are generating the resting, graded and action membrane potentials.

We consider the simplified example of two compartments containing a KCl solution and separated by an impermeable membrane and some ion channels embedded in it that are selectively permeable to  $K^+$  (see Figure 1.4). If the two compartments have an equally concentrated ionic solution, there will be no net flux of  $K^+$  and no membrane potential, although some cation will randomly permeate in both directions. Then, if we decide to concentrate one compartment ten times more than the other one, there will be a flux of  $K^+$  in the direction of the chemical gradient, from the more concentrated to the less concentrated compartment. As soon as some  $K^+$  start to directionally cross the membrane an electrical gradient (i.e., membrane potential) start to arise that opposes to the chemical gradient due to a separation of charges on both sides of the membrane. The compartment that was less concentrated become more positively charged because of the selectivity of the membrane for cations. At some point, the system will reach the electrochemical equilibrium where the membrane potential exactly opposes the concentration gradient. At this point, there is no more directionality in the permeation of the  $K^+$  ions.

Importantly, the number of  $K^+$  that have to cross the membrane to rise the membrane potential is relatively small (about  $10 \times 10^{-12}$  mol, i.e.,  $10^{12}$   $K^+$  ions per  $cm^2$  of membrane, or 1  $K^+$  per  $100 \text{ nm}^2$  of membrane (Purves et al. 2015)). It implies that the concentration of the extracellular and intracellular solutions remains globally constant and that the electroneutrality of these solutions is preserved. The charge separation that generates the membrane potential is definitively constrained to the vicinity of the membrane.

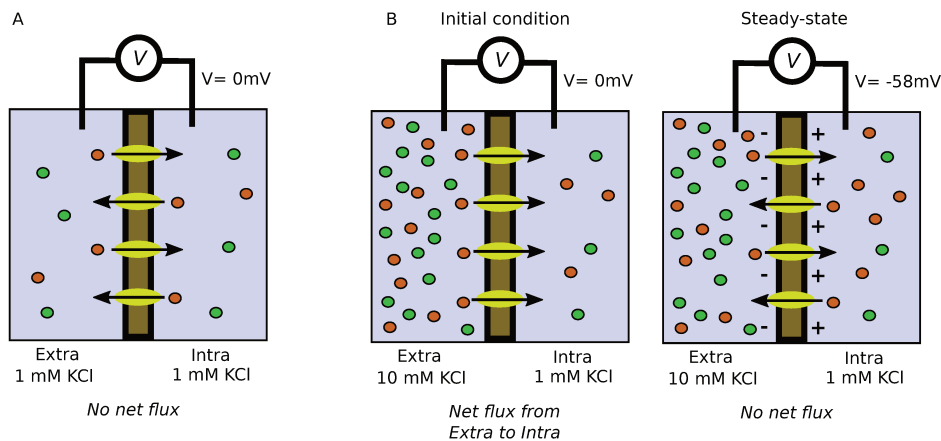


Figure 1.4 – The electrochemical gradient. In this example the membrane is selectively permeable to K<sup>+</sup>.

#### 1.1.4 Generation and propagation of the action potential

The propagation of the action potential was historically studied in the giant axon of the veined squid (*Loligo forbesii*) by Alan Lloyd Hodgkin and Andrew Huxley using the voltage clamp technique (Hodgkin et al. 1952). For this discovery, they got the Nobel Prize of Medicine or Physiology in 1963 "for their discoveries concerning the ionic mechanisms involved in excitation and inhibition in the peripheral and central portions of the nerve cell membrane." This Nobel Prize was also shared with John Carew Eccles for his work on the synapse.

The voltage clamp technique allowed Hodgkin and Huxley to measure the membrane permeability (i.e., the electric current) as a function of the membrane potential. Using this technique, they first demonstrated that within the axon, the depolarization is followed by a short-lasting inward current (entry of cations or exit of anions from the cell), finally changing into a long-lasting outward current (see Figure 1.5). On the contrary, a hyperpolarization does not affect the level of the axon. This experiment demonstrates that the membrane permeability to ions in the axon is voltage-dependent and that depolarization is necessary to promote the generation of an action potential.

Using channel blockers, it was possible to pharmacologically identify the Na<sup>+</sup> and K<sup>+</sup> channels, as responsible for the action potential (Moore et al. 1967; Armstrong and Binstock 1965), see Figure 1.5. It was subsequently shown that upon reaching the firing threshold, Na<sup>+</sup> channels activate quickly, promoting an inward current (i.e., Na<sup>+</sup> enter the cell) that depolarize in a burst fashion the membrane. A maximum potential is reached for several reasons, (i.) the voltage is near the equilibrium potential for Na<sup>+</sup> which implies that an opposite electric force slows the Na<sup>+</sup> current, (ii.) Na<sup>+</sup> channels start to inactivate, decreasing the inward current, (iii.) K<sup>+</sup> channels start to open allowing an outward current (i.e., K<sup>+</sup> ion leaving the cell). Due to the decrease of the inward current in favor to the outward current the membrane progressively repolarize until the outward current overcome the inward current,

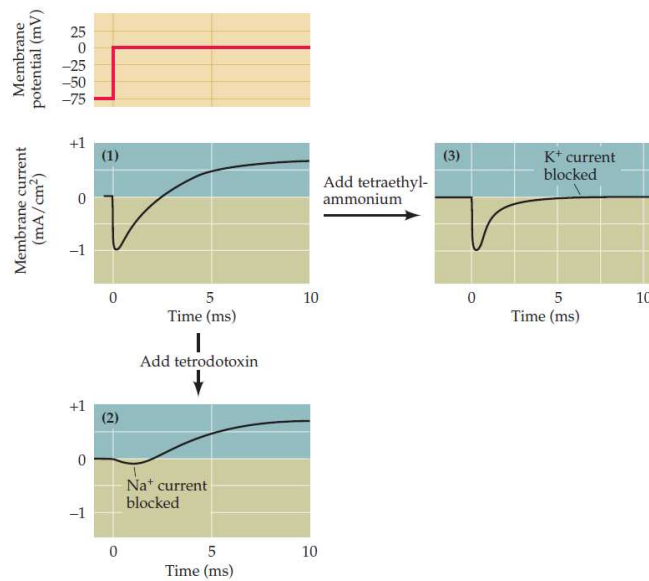


Figure 1.5 – The action potential is triggered by a depolarization of the membrane (top). It is composed of two successive components that can be blocked by pharmacological agents (middle). Indeed, tetrodotoxin blocks voltage-gated  $\text{Na}^+$  channels (bottom), and tetraethyl-ammonium blocks voltage-gated  $\text{K}^+$  channels (right). From Purves et al. 2015.

which finally inactivates the  $\text{K}^+$  channels and leads to the refractory period which is the time necessary for  $\text{Na}^+$  to recover from inactivation.

The existence of the refractory period (because of ion channel *desensitization* (Katz and Miledi 1965)) is also essential mechanistically because it assures the directionality of the propagation by preventing the depolarization of membrane patches recently fired. Additionally, it limits the frequency of firing that an axon can have.

In summary, due to its voltage-dependence, the action potential is all-or-nothing, self-sustained and regenerative. Thus, its amplitude and duration are properties of the excitable membrane and not of the stimulus. On the contrary, graded potentials scaled with the magnitude of the stimulus.

## 1.2 THE CHEMICAL SYNAPSES

The human brain is constituted of about 85 billion neurons with various degree of inter-connection between them. The complexity and efficiency of these connections are achieved by the synapses (i.e., the function contact between neurons). There is two kind of synapses, the electrical and the chemical ones. The electrical synapse is faster because it is constituted of a gap junction which is a mechanical and electrically conductive link between neurons. It is much shorter (i.e. 2 – 4 nm (Maeda et al. 2009)) in comparison to chemical synapses (i.e. 20 – 40 nm (McCann et al. 2003)) and the output signal can only be equal or smaller in intensity than the input. It is, however, bidirectional and highly efficient (~0.1 ms) when the neuronal system need the fastest connection possible (e.g., defensive reflexes).

In the following document, we will only consider the chemical synapses. Within this type of synapse, no electrical current flows from one neuron to the other. However, the action potential on the pre-synaptic neuron permits the release of chemical compounds (i.e., the neurotransmitters) that flow through the synaptic cleft to reach the post-synaptic neuron. On the post-synaptic membrane, they will bind to the neurotransmitter's receptors. Upon binding of neurotransmitters, the receptors will open directly or indirectly ion-channels to depolarize or hyperpolarize the membrane. Ultimately, graded potential newly generated might eventually trigger an action potential that will activate other synapses.

### 1.2.1 Neurotransmitters

The idea that chemical signal might propagate an electrical one between neurons was heavily debated during the first half of the 20<sup>th</sup> century (Haider 2007). However, Otto Loewi was the first in 1921 to carry out an experiment supporting this hypothesis (Loewi 1921). He isolated two frog hearts, one with the vagus nerves and the other without it. This nerve is controlling the heart rate. By electrically stimulating the nerve, the heart attached to it beat slower. Then, by taking some of the solution around the beating heart, and by applying it to the second heart without vagus nerves, the second heart beats at the same lower rate as the first one. This experiment showed that some chemical compounds released by the vagus nerves in the solution were controlling the heart rate. Otto Loewi initially named this unknown chemical "Vagusstoff," before being identified as Acetylcholine (ACh). The first neurotransmitter was identified. Subsequently, he was awarded the Nobel Prize of Physiology or Medicine in 1936, jointly with Henry Hallett Dale "for their discoveries relating to chemical transmission of nerve impulses."

Nowadays, more than 100 chemical compounds were identified as neurotransmitters (Purves et al. 2015). Neurotransmitters have to respect the three following conditions: (i.) The chemical compound has to be present in the pre-synaptic neuron as well as the enzymes and precursors. However, this condition is necessary but not sufficient since several neurotransmitters are present in all neurons because they are required for protein synthesis (e.g., glutamate, glycine, aspartate). (ii.) The chemical compound has to be released upon pre-synaptic depolarization of the membrane, and the release has to be dependent on the calcium concentration. (iii.) The chemical compound has to bind to some receptors expressed on the post-synaptic membrane. In other words, the same response must be obtained on the post-synaptic membrane when the chemical is experimentally placed on it or if the pre-synaptic neuron was stimulated.

There is two main kind of neurotransmitters, the small molecules, and the neuropeptides, see Figure 1.6. Most of the small molecules neurotransmitters are directly synthesized in the pre-synaptic termination, where they are generally stocked in small vesicles (40 – 60 nm) before being released (Qu et al. 2009). In opposition, neuropeptides are synthesized in the cell body and packed into large vesicles (90 – 250 nm), their vesicles are transported toward the pre-synaptic termination using kinesin (Pol 2012).

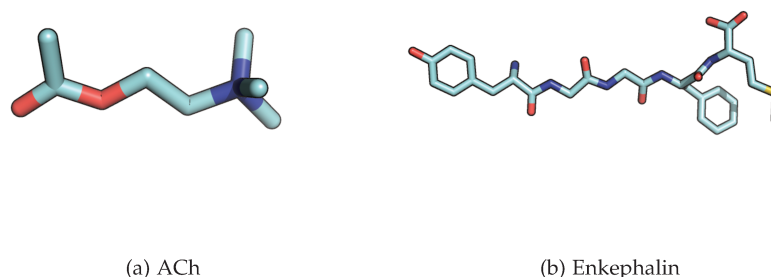


Figure 1.6 – There is two main families of neurotransmitter, the small-molecule neurotransmitters, e.g., ACh (left), and the neuropeptides, e.g., enkephalin. ACh binds to the nicotinic and muscarinic ACh receptors. Enkephalin binds to the  $\delta$  and  $\mu$  opioid receptors.

There are several chemical groups, and functions (excitatory or inhibitory) within the neurotransmitters.

### 1.2.2 Release of neurotransmitter from the pre-synaptic neuron

In the fifties, Bernard Katz and coworkers demonstrated that neurotransmitters (ACh at the neuromuscular junction in their case) are released by "quantal," i.e., there is a minimum amount of neurotransmitters that can be released (one quanta), and larger releases are numbers of quantal units (Fatt and Katz 1952; Castillo and Katz 1954). For this work, Katz won a shared Nobel Prize of Physiology or Medicine in 1970 with Ulf von Euler and Julius Axelrod "for their discoveries concerning the humoral transmitters in the nerve terminals and the mechanism for their storage, release, and inactivation." In 1979, Heuser, Reese, and coworkers morphologically demonstrated that the quantal released of neurotransmitter is correlated with the number of vesicles fused with the pre-synaptic membrane (Heuser et al. 1979). The quanta of ACh measured at the neuromuscular junction correspond to a vesicle containing about 10,000 molecules ( $\sim 100$  mM of ACh inside the vesicle).

During the experiments of Katz and coworkers, the importance of calcium was already highlighted in the synaptic transmission. They showed that the decrease in extracellular  $\text{Ca}^{2+}$  concentration is responsible for the decrease in the post-synaptic membrane potential. A decrease in neurotransmitter vesicle exocytosis caused this effect. The existence of a voltage-gated calcium channel in the pre-synaptic membrane was hypothesized by Katz and Ricardo Miledi and later confirmed by Rudolfo Llinás (Llinás et al. 1981). Ultimately, it was shown by pharmacologically blocking the calcium channels that the release of the neurotransmitter was prevented as well as the post-synaptic response (Augustine et al. 1985).

Although  $\text{Ca}^{2+}$  is controlling the release of all neurotransmitter, the kinetic is not the same depending on their nature. Vesicles containing small molecules are near the membrane and are quickly released (in  $\sim 0.5$  ms) after activation of the calcium channels (Südhof 2012). In opposition, vesicles containing neuropeptides needs several salves of action potential overs

few seconds to be released, undoubtedly because this type of vesicles is located further from the membrane.

### 1.2.3 Neurotransmitters receptors

The existence of some *receptive substance* able to bind specific drug or transmitter to activate or inhibit nerve cells was first theorized by John Newport Langley in 1905 (Langley 1905). However, this kind of receptors remained elusive until 1970 (Changeux et al. 1970a; Changeux et al. 1970b). We know yet that neurotransmitter receptors are proteins embedded in the phospholipidic membrane of the post-synaptic cell. They have an extracellular domain that is located in the synaptic cleft and that bind the neurotransmitters.

There are two families of receptors (see Figure 1.7), depending on their mode of signal transmission. The ionotropic receptors use a straightforward mode of signal transmission with the extracellular neurotransmitter-binding domain allosterically linked to the ion channel  $\sim 60 \text{ \AA}$  away. They have the particularity to combine the functions of neurotransmitter binding and ion conduction within the same protein. For that reason, they are also named Ligand-Gated Ion Channel (LGIC) and will be discussed in detail in this thesis. On the other side, there are the metabotropic receptors that are indirectly linked to ion channels through signal transduction (i.e., G proteins) and are accordingly named G Protein-Coupled Receptor (GPCR).

Both receptor families will generate post-synaptic membrane potential that might be excitatory or inhibitory, depending on the selectivity of the ion-channels they are controlling. The difference between the two families is the kinetics involved in the transmission of the signal. On one side, LGICs are very fast to transmit the signal, i.e., the postsynaptic current is measured about 2 – 3 ms after the entry of the action potential in the pre-synaptic termination (Augustine and Eckert 1984; Sabatini and Regehr 1999). At the same time, the current evoked by LGICs are quite short-lasting (i.e., few ms (Katz and Miledi 1965)). On the other side, GPCRs are relatively slow to transmit the signal because they are initiating a cascade of protein-protein interactions before the ion-channel opening. The time scale of current raised by GPCRs are from 100 ms to minutes or even hours (Hille 2001; Purves et al. 2015). Interestingly, a neurotransmitter can activate at the level of a single synapse both signaling pathways to promote a fast and a slow answer from the post-synaptic neuron.

### 1.2.4 Postsynaptic membrane potentials

After neurotransmitters binding to the receptors, ion channels will activate. An ion channel will typically stay only briefly open (a couple of ms (Katz and Miledi 1965)) and will promote a quite small electric current (few pA (Hille 2001)). However, the simultaneous release of millions of neurotransmitters in the synaptic cleft allows for the activation of thousands of receptors and subsequently, thousand of ion channels. Altogether, there is a large accumulated current (hundred of nA) arising from the sum of all the unitary ones. This postsynaptic current is ultimately responsible for the change in postsynaptic membrane potential.

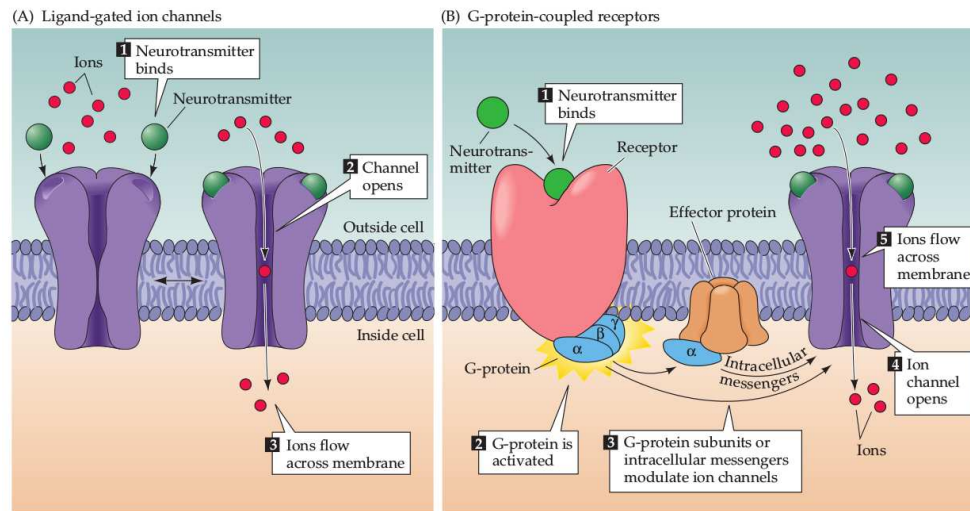


Figure 1.7 – Families of neurotransmitter receptors. (A) Ionotropic receptor, or LGIC. Both functions of neurotransmitter-binding and ionic diffusion through the membrane are hosted by a single protein which is why they are faster to transmit the signal than metabotropic receptors. (B) Metabotropic receptors or GPCR. They indirectly control the opening of ion channels through G proteins. From Purves et al. 2015.

As mentioned earlier the postsynaptic membrane potential can be either excitatory or inhibitory. The nature of the postsynaptic membrane potential is dependent on the selectivity of the ion channels that are open upon the neurotransmitter binding. By exploring the nature of the ionic current permeating the membrane during the activation of a synapse, it is possible to measure the membrane potential at which there is no net flux of ions because the chemical potential of ions across the membrane is equal the electrical potential. The value of the membrane potential at equilibrium is called the reverse potential because the direction of the current will change when this value is crossed. Knowing the intracellular and extracellular ionic concentration, it is possible to compute the equilibrium potential using the Nernst equation ( $-100$ ,  $-50$ , and  $+70$  mV for  $K^+$ ,  $Cl^-$ , and  $Na^+$  respectively). A synapse is selective for one ion if its reverse potential is equal to the equilibrium potential of that ion. If the measured reverse potential differs from the equilibrium potential of a single ion, it means that the current is composed of a combination of ion flux.

We can understand that a neurotransmitter's action is to activate ion channels in order to displace the membrane potential toward the reverse potential of those channels. In general, activation of ion channels upon neurotransmitter binding will promote a change in conductance that will evoke a postsynaptic current. This current will change the postsynaptic potential. This postsynaptic potential is depolarizing if its value is more positive than the resting potential or hyperpolarizing if it is the opposite.

Assuming that the threshold for ignition of the action potential is around  $-40$  mV (Hille 2001), a postsynaptic potential is excitatory if the reversing potential of the activated channels is more positive than  $-40$  mV and inhibitory if it is more negative than this threshold. In other

words, an excitatory postsynaptic potential will increase the probability of firing an action potential, in contrary to inhibitory postsynaptic potential which decreases this probability.

With the apparition of postsynaptic potentials and their summation over multiple synapses, the signal is integrated, and if the threshold is reached, an action potential is fired toward the next neuron.

### 1.3 LIGAND-GATED ION CHANNELS FOR FAST CHEMICAL SYNAPSES

The fast chemical synapses are mediated by LGICs and are located in all the nervous system in addition to the neuromuscular junction where they transmit the signal in the millisecond timescale. This family of receptors is particularly crucial in fast chemical synapses because they answer to the binding of neurotransmitter by direct gating of ion movement across the membrane and by generating electrical signals (i.e., postsynaptic potentials). The neurotransmitter controlling these receptors are typically ACh, 5-hydroxytryptamine (Serotonin) (5-HT), glutamate, glycine,  $\gamma$ -Aminobutyric acid (GABA) or Adenosine Triphosphate (ATP) (Hille 2001).

The most well-known receptor is undoubtedly the nicotinic Acetylcholine Receptor (nAChR), identified by Changeux et al. 1970a; Changeux et al. 1970b. Subsequently, the nAChR remained the best-studied ion channel with the first unitary current measured in patch clamp by Neher and Sakmann 1976, first purified receptor by Weill et al. 1974, the first receptor to have the complete amino-acid and gene sequence determined by Noda et al. 1984. Finally, the nAChR was the first to be imaged in by Brisson and Unwin 1985.

#### 1.3.1 *Ligand-Gated Ion Channels Diversity*

LGICs might be classified according to their selectivity or their quaternary organization. In human, a group of cation-selective (i.e., excitatory) ion channels is formed by the nAChR, the Serotonin type 3 Receptor (5-HT<sub>3</sub>R), the Zinc-activated ion channel (ZAC), the Ionotropic Glutamate Receptor (iGluR)s, and the ATP-gated P2X ionotropic receptor (P2XR). On the opposite, a group of anion-selective (i.e., inhibitory) channels is composed of the GABA type A Receptor (GABA<sub>A</sub>R) and the Glycine Receptor (GlyR).

An alternative classification based on the quaternary organization of the previous ion channels depicts their lack of evolution relationship, see Figure 1.8. There is a family of pLGICs composed by 5-HT<sub>3</sub>R, nAChR, GABA<sub>A</sub>R, GlyR, and ZAC. This family is also alternatively named Cys-loop receptors because they have a defining loop formed by a disulfide bond in the extracellular domain. However, their prokaryotic ancestors lack this bonds (Tasneem et al. 2005) explaining why the name pLGICs is preferred nowadays. Of note, more recently the alternative *Pro-loop receptors* was proposed by Jaiteh et al. 2016 because of a conserved Proline residue. iGluRs are tetrameric assemblies. They are all excitatory and glutamate-gated channels, but they can be divided into four subfamilies depending on their pharmacology or sequence similarity (i.e., alpha-amino-3-hydroxy-5-methyl-4-isoxazolepropionic acid (AMPA),

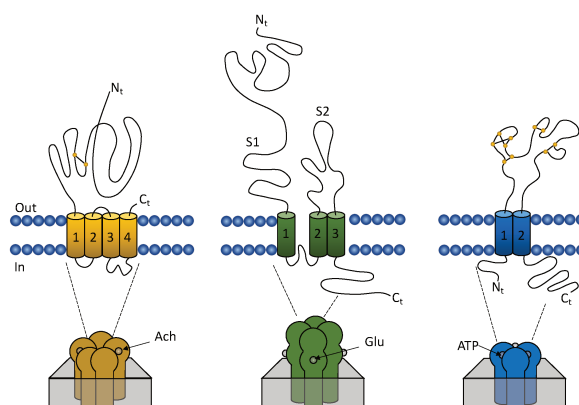


Figure 1.8 – Schematic organization of the three families of ionotropic receptors (LGICs). From the left to right, there is the pLGICs, the iGluRs, and the P2XR . Adapted from Lemoine et al. 2012.

kainate, N-Methyl-D-aspartic acid (NMDA) and  $\delta$  receptors). The third and last family is composed by the P2XR that form trimeric assemblies.

The opening of LGICs is principally controlled by the binding of neurotransmitters to orthosteric binding sites; however, several endogenous, exogenous, modulators can bind to allosteric sites and modify the receptor functions.

Several genes encode the subunits within each family of LGIC. The diversity found in each group is responsible for a wide range of receptors and subsequently, multiple pharmacology and functions.

### 1.3.2 Pentameric Ligand-Gated Ion Channels diversity

The pLGIC family is widely expressed in multicellular animals from invertebrates to mammal including humans. They are extensively studied from the structural and pharmacological point of view since their identification in 1970. However, only about a decade ago, few pLGICs orthologs were identified in bacterial species (Tasneem et al. 2005). Thanks to the discovery of prokaryotic receptors, it was possible to solve the first high-resolution structures of a full-length pLGICs in 2008 and 2009 (Hilf and Dutzler 2008; Bocquet et al. 2009). Following this success, the first structure at an atomic resolution of a eukaryotic channel was obtained in 2011 (Hibbs and Gouaux 2011). Finally, recent advances in structural biology permit to solve many more eukaryotic channels including human ones (P. S. Miller and Aricescu 2014; Huang et al. 2015; Huang et al. 2017b; Huang et al. 2017a; Zhu et al. 2018; Walsh et al. 2018; P. Miller et al. 2018) (see Figure 1.9). Nowadays all pLGIC have high-resolution structures for at least one subunit (apart for ZAC for which not much is known). Even some human heteromeric structures are solved thanks to Cryo-Electron Microscopy (cryo-EM) (Zhu et al. 2018; Walsh et al. 2018; P. Miller et al. 2018). In addition to the structural characterization of all pLGICs members, the availability of structures for the same channel captured in multiple conformations (Du et al. 2015; Bocquet et al. 2009; Sauguet et al. 2014; Hibbs and Gouaux

2011; Althoff et al. 2014) is critical to understand the biophysical and pharmacological properties of this family.

Overall pLGICs are expressed in virtually all neurons, and for that reason, they have a pivotal role in most of the CNS functions, including sensory and motor processes, memory and attention, pain and rewards, central autonomous control and cognition (Nemecz et al. 2016). Due to their broad involvement in the CNS, it is unfortunately not a surprise to have them involved in many diseases such as epilepsy (Steinlein 2012), hyperekplexia (Lynch 2004), autism (Dineley et al. 2015), schizophrenia (Braat and Kooy 2015), Alzheimer's disease (James and Nordberg 1995), addictions (Molander and Söderpalm 2005).

pLGICs are large (150 to 300 kDa) protein complexes forming a 5-fold symmetrical arrangement made by identical or homologous subunits. The axis of symmetry forms the ion pore that is perpendicular to the membrane. Binding of neurotransmitters in the extracellular domain initiates a transition (i.e., gating) that trigger the opening of the ion pore (Hille 2001). Prolonged exposure to neurotransmitter will promote a desensitized state (Katz and Thesleff 1957) that is different from the resting state (Gielen and Corringer 2018), although both are non-permeable to ion.

While pLGICs are predominately responsible for a synaptic and *phasic* transmission (Katz and Miledi 1973), they are also involved in an extrasynaptic and *tonic* regulation taking place at low-concentration of nonvesicular neurotransmitter (Betz and Laube 2006) and modulating the neuronal development for example.

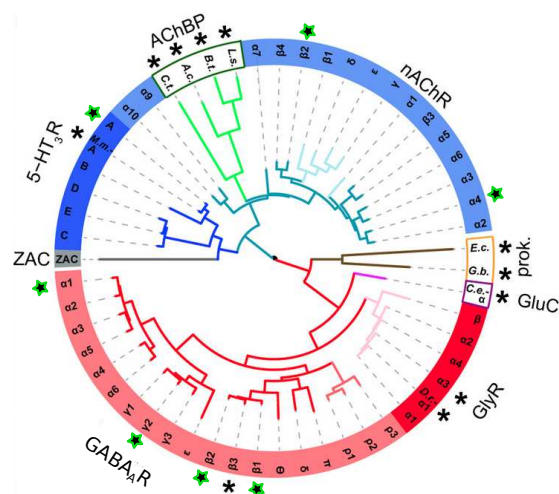


Figure 1.9 – Phylogeny of pLGICs. Adapted from Nemecz et al. 2016. Black stars correspond to available high-resolution structures. Green stars correspond to the structures made available after the publication of the original article. Of note, all the green stars refer to heteromeric channels although the black ones refer to homomeric channels (apart for the human 5-HT<sub>3</sub>R<sub>A</sub> which is green but homomeric).

## 1.4 THE GLYCINE RECEPTOR

Two teams demonstrated the glycine-mediated hyperpolarization in 1967 (Curtis et al. 1967; Werman et al. 1967) and the next year they both showed that this hyperpolarization is due to an increase in  $\text{Cl}^-$  conductance (Curtis et al. 1968; Werman et al. 1968). Following research on the receptor responsible for the action of glycine led to the identification of the GlyR as a member of the pLGIC family. GlyR was first purified in 1982 by Betz and colleagues from the rat spinal cord (Pfeiffer and Betz 1981; Pfeiffer et al. 1982). Later, in 1987, Betz et al. also successfully cloned the first GlyR (Grenningloh et al. 1987).

Overall, the activation of GlyR allows a flux of  $\text{Cl}^-$  to cross the membrane in the direction of the electrochemical gradient. In mature neurons, GlyR is an inhibitory receptor because the  $\text{Cl}^-$  equilibrium potential is more negative than the resting potential of those neurons. However, in embryonic neurons, the concentration gradient of  $\text{Cl}^-$  is inverted and the activation of GlyR promotes a depolarization.

One of the first pharmacological tools to identify GlyR was strychnine (Dutertre et al. 2012a), see Figure 1.10. This highly toxic alkaloid can bind to GlyR with a high-affinity and act as a competitive antagonist on it (Lynch 2004). At low concentration, it might be used as a doping substance to enhance the performance, but at higher concentration, it is a particularly deadly substance ( $\text{LD}_{50}$  for human within the oral route is about 100 mg (Palatnick et al. 1997)) that was commercialized as a pesticide against birds and rodent.

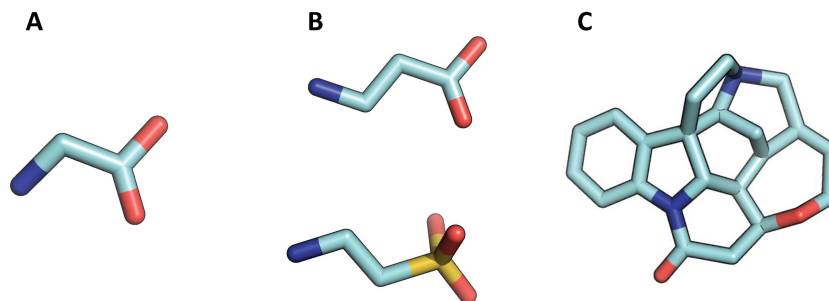


Figure 1.10 – (A) Glycine is the endogenous agonist of GlyR. (B)  $\beta$ -alanine (top) and taurine (bottom) are natural partial-agonists. (C) Strychnine is a selective antagonist of GlyR.

## 1.4.1 Diversity and function

In comparison to other pLGICs that have many subunit genes (nAChR has 17 and  $\text{GABA}_A\text{R}$  has 20), the GlyR found in vertebrate are less diverse with only five different subunits (in humans GlyR has just four subunits) (Lynch 2004). There is 4 different  $\alpha$  subunits ( $\alpha 1 - \alpha 4$ ) of 40 kDA. All the GlyR $\alpha$  are highly homologous and share high sequence similarity (i.e.,>

80%). The  $\alpha 4$  subunit seems to be missing in human and rat although it is found in mouse and chicken for example. The  $\beta$  subunit is larger (58 kDa) and display less amino-acid sequence identity with respect to  $\alpha 1$  (~47%).

GlyR $\alpha$  can form homomeric receptors that are functional although their properties are different from most of the *in vivo* receptors, meaning that the majority of the *in vivo* GlyR is formed of heteromeric assemblies (Bormann et al. 1987). However, GlyR $\beta$  cannot form functional receptors on their own. Concerning the stoichiometry of the GlyR assemblies *in vivo*, it was thought to be  $3\alpha : 2\beta$  (Burzomato et al. 2003) but more recent publications propose  $2\alpha : 3\beta$  (Yang et al. 2012). This information is crucial because photoaffinity labeling with [H3]strychnine showed that GlyR $\alpha$  subunits carry critical elements for ligand binding (Graham et al. 1983). It does not mean that GlyR $\beta$  is just a structural subunit since it has a determinant role in intracellular trafficking and clustering of the receptor at the postsynaptic level (Kneussel and Betz 2000). This function is notably granted by the high affinity of the GlyR $\beta$  subunit for the gephyrin protein which is in charge of the postsynaptic anchoring to the cytoskeleton (Maas et al. 2006).

From immunocytochemical studies and analysis of knock-out mice, it has been possible to identify the physiological functions of GlyR isoforms and their distribution within the mammalian CNS. Most pieces of evidence suggest that glycinergic synapses are located in the spinal cord motor reflex pathways, in the spinal cord pain sensory pathways, the retina, and various brainstem nuclei (Lynch 2004). In a few other cases, GlyR has been identified on the presynaptic side where it acts as an excitatory receptor, increasing the release of neurotransmitter (Lynch 2004). During the developmental phase, there is a switch from  $\alpha 2$  to  $\alpha 1$ . The switch toward the adult subunits is completed around 20 days after birth. In opposition to the  $\alpha 1$  subunit that is wide-spread within the previously cited area, the  $\alpha 3$  subunit is less expressed and restricted to the respiratory network of the brain stem and the superficial laminae of the dorsal horn, where it inhibits the propagation of nociceptive signals. The  $\beta$  subunit is expressed during all stage of development and adulthood forming heteromeric receptors. Due to the unique gephyrin binding-site presents on  $\beta$  subunits, the general idea is that heteromeric  $\alpha 1\beta$  or  $\alpha 3\beta$  receptors are found on the postsynaptic side, whereas homomeric  $\alpha 1$ ,  $\alpha 2$  and  $\alpha 3$  receptors are located pre- or extra-synaptically (Zeilhofer et al. 2018).

#### 1.4.2 Pathology and Pharmacology

The post-synaptic inhibition promoted by glycinergic transmission is crucial in many neuronal processes including motor control, muscle tone, and sensory processing. Due to the broad implication of glycinergic inhibition in physiological processes, GlyR malfunctions are responsible for several neurological disorders including hyperekplexia, temporal lobe epilepsy, autism, addiction, and chronic inflammatory pain which impacts 1/5 of the world-wide human population (Lynch et al. 2017).

#### 1.4.2.1 *Hyperekplexia*

Hyperekplexia is a rare and hereditary disease also named startle disease because it is characterized by an exaggerated startle reflex in response to unexpected stimuli. Mutations in genes encoding for GlyR $\alpha$ 1 and GlyR $\beta$  are the major causes of the disease. Upon the ~70 mutations identified, most of them are loss-of-function mutations (Bode and Lynch 2014). However, and surprisingly, some of them are gain-of-function mutations but still result in the same disease phenotype. The conventional treatment consists of enhancing the GABAergic inhibition with a benzodiazepine in order to compensate for the malfunctioning glycinergic transmission (Lynch et al. 2017).

#### 1.4.2.2 *Chronic Inflammatory Pain*

The first step of the pain pathway corresponds to the signal transmission from the nociceptors in several tissues to the spinal cord dorsal horn. Interestingly, the synaptic inhibition in the most superficial laminae of the dorsal horn is almost exclusively mediated by GlyR $\alpha$ 1 and GlyR $\alpha$ 3 in equal proportion (Lynch et al. 2017). Based on this evidence, the role of the glycinergic inhibition in the regulation of pain seems quite straightforward. Indeed, experiments show that pharmacological agents able to potentiate the GlyR's function are effective to treat inflammatory pain in animals (Lu et al. 2018). The cost of chronic pain in the USA was estimated to \$600 billion/year (Gaskin and Richard 2012). Unfortunately, available treatments have numerous side effects, and the current epidemics of opioid drugs is devastating in North America. For that reason, there is a critical need for novel efficient and selective pain-killers, possibly targeting GlyR $\alpha$ 1 – 3.

#### 1.4.2.3 *Autism*

Autism spectrum disorders are highly prevalent in the population (i.e., 1/68 birth), and are characterized by pathological trouble with social interaction and communication (Sztainberg and Zoghbi 2016). Some microdeletions and missense mutations in the gene encoding the prenatal GlyR $\alpha$ 2 were identified as a probable cause for autism spectrum disorders. However, due to the prenatal incidence of GlyR $\alpha$ 2, it seems difficult to pharmacologically target this receptor as a treatment for autism (Lynch et al. 2017).

#### 1.4.2.4 *Alcoholism*

It is well known that GlyR is positively modulated by ethanol at relevant concentration (Molander and Söderpalm 2005). Indeed, GlyR is involved in the intoxicating effects of alcohol such as the loss-of-righting reflex in mice, which can be antagonized by strychnine (Williams et al. 1995). Additionally, a mutation that disrupts the ethanol-binding site in GlyR $\alpha$ 1 in mice provides resistance to ethanol (Findlay et al. 2002). Finally, there is evidence that extrasynaptic GlyR in nucleus accumbens is involved in addiction mechanism of alcohol, but also nicotine and Tetrahydrocannabinol (THC) (Jonsson et al. 2014). Overall, modulation of GlyR seems to be a possibility to treat toxic and addictive effects of ethanol.

1.4.2.5 *Drugs availability*

Drug name	FDA status	Usage	Selective for GlyR	Action
Glycine	Approved	Many	no	Agonist
Taurine	Approved	Parenteral nutrition therapy	no	Partial Agonist
Zinc	Approved	Many	no	PAM
Methoxyflurane	Approved	Anesthetic	no	PAM
Enflurane	Approved	Anesthetic	no	PAM
Desflurane	Approved	Anesthetic	no	PAM
Isoflurane	Approved	Anesthetic	no	PAM
Halothane	Approved	Anesthetic	no	PAM
Sevoflurane	Approved	Anesthetic	no	PAM
THC	Approved	Alleviate severe pain	no	PAM
Cannabidiol (CBD)	Approved	Alleviate severe pain	no	PAM
Ginkgo biloba	Approved	Anti-dementia	no	PAM
Atropine	Approved	Anti poisoning by nerve agent and pesticide	no	Antagonist
Lindane	Withdrawn	Treatment of infestation by <i>Sarcoptes scabiei</i> or pediculosis capitis	no	Antagonist (pore blocker)
Thiocolchicoside	Experimental	Muscle-relaxant	no	Antagonist
Picrotoxin	Experimental	Antidote in poisoning by CNS depressants	no	Antagonist (pore blocker)

Table 1.1 – Drugs acting on GlyR. From DrugBank (Wishart et al. 2006; Wishart et al. 2018) (after manually removing drugs targeting the NMDA-sensitive glycine receptor).

So far, no drugs targeting selectively the Glycine Receptor is available on the market although many drugs act on GlyR in addition to other receptors (see Table 1.1). Interestingly, Bregman and coworkers discovered a novel family of potentiator of GlyR, i.e., tricyclic sulfonamides (Bregman et al. 2017). Hit optimization led to compounds AM-1488 and AM-3607, with good potency and pharmacokinetic properties, in addition to a decent selectivity over other receptors (Bregman et al. 2017). Of note, GlyR $\alpha$ 3 was cocrystallized with AM-3607 and the structure of the complex solved by X-ray (Huang et al. 2017b; Huang et al. 2017a). Overall, there is still a need to discover or design small molecules with potent and selective activity on GlyR in order to improve notably the therapeutics for the treatment of chronic inflammatory pains or addictions.

1.4.3 *Structure*

The general topology of GlyR is shared with other pLGICs, which means that the receptor is forming a pseudo-symmetrical arrangement of the five subunits around a central ion pore (see Figure 1.11). Similarly to other pLGICs, the GlyR has a large N-terminal domain which is extracellular and often referred to as the Extracellular Domain (ECD). This domain is also forming the orthosteric binding-site for glycine and strychnine. Then, a Transmembrane Domain (TMD) is formed by four  $\alpha$ -helices (i.e., TM<sub>1-4</sub>), with the TM<sub>2</sub> delimiting the ion

pore around the axis of symmetry. A long and poorly conserved intracellular section connects the TM<sub>2</sub> and TM<sub>3</sub> and is referred to as the Intracellular Domain (ICD). This domain contains notably phosphorylation sites and other sites for communication with cytoplasmic factors.

Due to the high structural similarity between pLGICs, the first models of GlyR were obtained by homology modeling from high-resolution structures of nAChR (Yevenes et al. 2006), Acetylcholine Binding Protein (AChBP) (Speranskiy et al. 2007) and lately Glutamate-gated Chloride Channel (GluCl) (Dutertre et al. 2012b). More recently several experimentally obtained models for GlyR appeared. First, the TMD was modeled in 2013 using Nuclear magnetic resonance (NMR) spectroscopy and electron micrographs on human GlyR $\alpha$ 1-TMD constructs (Mowrey et al. 2013). Then, in 2015 was solved by X-ray the human GlyR $\alpha$ 3 bound to strychnine in an apparently closed state (Huang et al. 2015). At the same time, three structures of zebrafish GlyR $\alpha$ 1 were solved by cryo-EM in the presence of strychnine, glycine only, or glycine and the potentiator Ivermectin (IVM) (Du et al. 2015). The three structures are displaying various levels of ion pore opening. Last, in 2017 new structures were solved by X-ray of the human GlyR $\alpha$ 3 bound to glycine and potentiator IVM and/or AM-3607 (Huang et al. 2017b; Huang et al. 2017a). All the structures obtained on human GlyR $\alpha$ 3 display a certainly non-conducting ion pore.

To date, no heteromeric GlyR assemblies have been solved, but very recent and promising developments have been made by raising antibodies that target specifically one of the subunits in order to disrupt the pseudo-symmetry with the antigen-binding fragment and to allow high-resolution particle alignment. This methodology have been successfully applied to the heteromeric nAChR (Walsh et al. 2018) and GABA<sub>A</sub>R (Phulera et al. 2018; Zhu et al. 2018). For that reason, we might expect that heteromeric GlyR $\alpha$ 1 $\beta$  and GlyR $\alpha$ 3 $\beta$  being solved by X-ray or cryo-EM soon. An additional challenge for structural biologists would also be to solve the ICD, for which the structure remains mostly elusive in pLGICs (apart for the 5-HT<sub>3</sub>R) because of the low sequence and length similarities.

#### 1.4.3.1 Extracellular Domain

From the NH<sub>2</sub>-terminal extremity, each subunit contains a short  $\alpha$ -helix parallel to the membrane. Then, a series of ten  $\beta$ -sheets compose the rest of the ECD. The neurotransmitter-binding site (i.e., the orthosteric binding site) is located at the subunits interface, similarly to other pLGICs, see Figure 1.12. The principal subunit ((+)-side) is contributing via its loops A, B and C to the binding pocket, whereas the complementary subunit ((-)-side) shares the middle of its  $\beta$ -strands (i.e., loop D, E, and F). The general view is that the degree of openness of the loop C is responsible for the activation of the receptor. An open loop C is correlated with a resting receptor, whereas a closed loop is related to its active state (Yu et al. 2014). Glycine is stabilized within its binding site via hydrogen bonds between its carboxylate moiety and the side chains of Arg65 and Ser129 from the (-)-side as well as Thr204 from the (+)-side, similarly to the glutamate in GluCl. Another shared interaction within pLGIC is the cation- $\Pi$  interaction with the Phe207 from the (+)-subunit and the amino group of Glycine. Additionally, experiments and simulations showed that a water molecule is mediating an H-bound interaction between the amino group of glycine and the side chain of Glu157 and

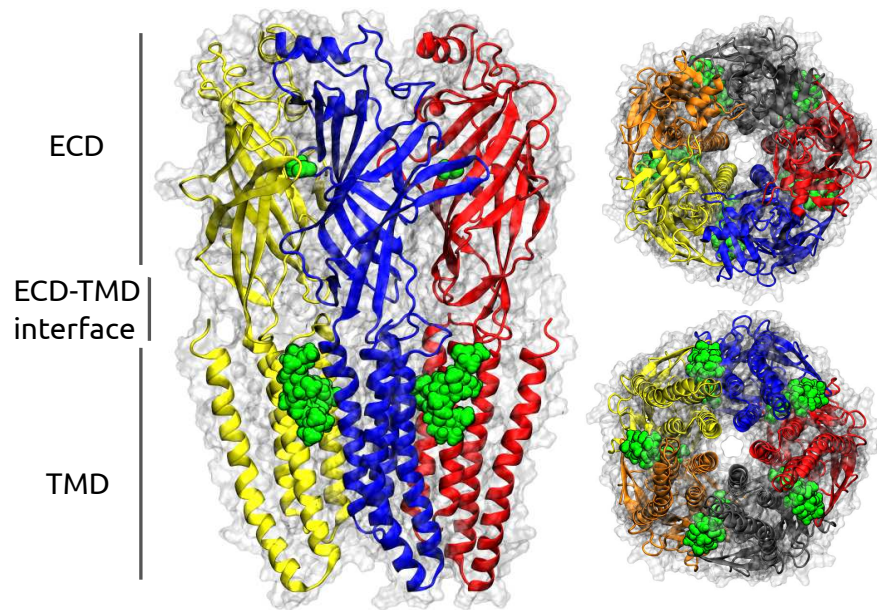


Figure 1.11 – Overall architecture of GlyR $\alpha$ 1. GlyR is composed of five similar subunits, with a central ion pore. The ECD is responsible for the neurotransmitters-binding, the signal is transmitted toward the ECD-TMD interface, and finally the channel opens the *gate* located in the TMD. In green are represented the Glycine (in the ECD) and the IVM (in the TMD).

the main chain of Ser158 from the principal subunit (Huang et al. 2017b; Yu et al. 2014). Interestingly, this water molecule occupies the positions of the amino nitrogen of glutamate and the amidinium nitrogens of benzamidine in GluCl and GABA $\text{A}$ R, respectively. Overall the orthosteric binding site is structurally highly conserved within anionic pLGICs, despite the variability in the sequence (P. S. Miller and T. G. Smart 2010) which is responsible for the different ligand selectivity.

A particularity of the GlyR is the presence of a potentiator-binding site at the top of the ECD (Huang et al. 2017b; Huang et al. 2017a), which has not been observed in other pLGICs yet. A tricyclic sulfonamide compound (AM-3607) can bind to this pocket at the interfaces between subunits and to positively potentiate the effect of glycine. The pocket is defined by the  $\alpha_1 - \beta_1$  loop and the loop B from the (+)-side, in addition to the  $\alpha$ -helix and the  $\beta_2 - \beta_3$  loop from the (-)-side, see Figure 1.13. In opposition to the orthosteric binding site which is buried, this pocket displays a hydrophobic side formed by residues Tyr161(+), Phe32(+), Arg29(+), Asp84(-), Pro10(-), Phe13(-), Leu13(-), Tyr78(-), Leu83(-), and another side where the ligand is exposed to the solvent.

Interestingly, this potentiator-binding site is relatively close ( $\sim 10 \text{ \AA}$ ) to the orthosteric binding site, and the loop B is involved in both ligands interactions. Not surprisingly for an allosteric binding site, some critical residues described here are not conserved in other pLGICs but the GlyR $\alpha$ 1/3 subunits. This lack of conservation within pLGICs is responsible for the high selectivity of these compounds for GlyR $\alpha$ .

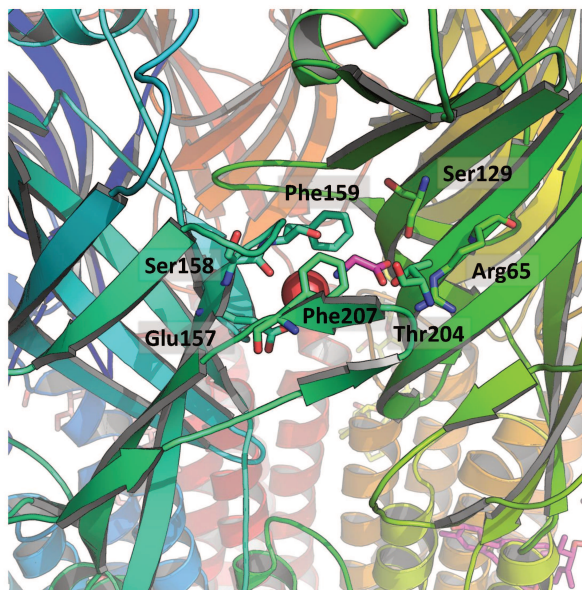


Figure 1.12 – Orthosteric binding site with Glycine bind, as observed in GlyR $\alpha$ 3 X-ray structure (Huang et al. 2017b). Of note, a water molecule was crystallized in the binding site, mediating the interaction with Glu157 and Ser158.

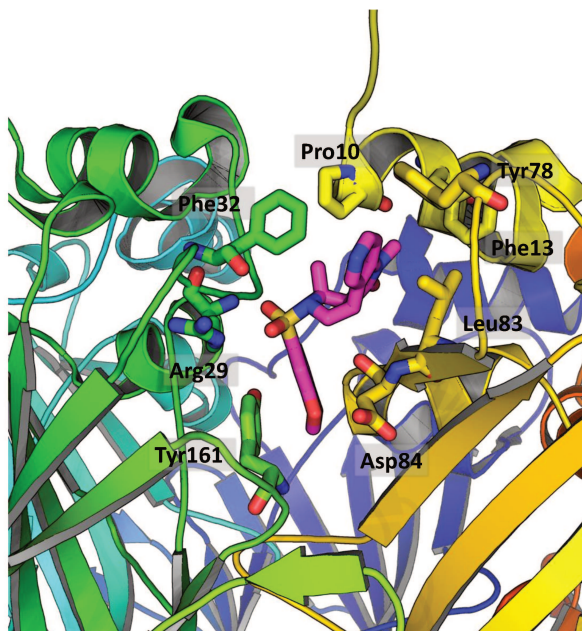


Figure 1.13 – Binding site of AM-3607, i.e., tricyclic sulfonamide compounds, as observed in GlyR $\alpha$ 3 X-ray structure (Huang et al. 2017b).

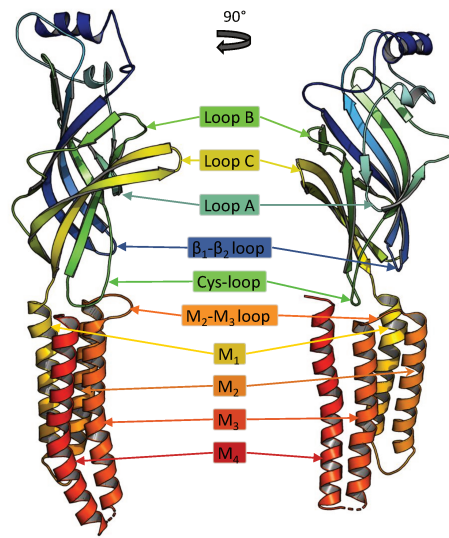


Figure 1.14 – Representation of one GlyR subunit. Names are displayed for the most important elements constituting the subunit.

#### 1.4.3.2 Transmembrane Domain

The TMD is topologically completely conserved within pLGICs with 4  $\alpha$ -helices embedded in the membrane, perpendicularly to it. Each helix is about 30 Å in length (i.e., the size of the phospholipid bilayer).

The TM<sub>2</sub> helix has the most striking effect on the function since it is lining the ion pore and its sequence is directly controlling the channel properties such as conductance and selectivity. Overall, the five TM<sub>2</sub> helices form a symmetric and pentameric arrangement with the water-filled channel in the middle of it. This observation arises from the exclusively homomeric high-resolution structures that exist to date for the GlyR receptors. Of note, the very recent structures of heteromeric GABA<sub>A</sub>R receptors seems to challenge this idea of complete symmetry in the TM<sub>2</sub> arrangement, but functional studies based on those models are missing. The TM<sub>2</sub> residues are numbered according to the conventional system where the residues at position 1' were supposed to be at the cytoplasmic end of TM<sub>2</sub> and 19' to the extracellular side (C. Miller 1989). However, since this initial numbering, the X-ray and cryo-EM structures showed that the TM<sub>2</sub> helices expand from -2' to 20' in GlyR (Du et al. 2015; Huang et al. 2015) (see Figure 1.15).

The loop that connects the TM<sub>2</sub> and TM<sub>3</sub> (i.e., M<sub>2</sub>-M<sub>3</sub> loop) is spanning at the ECD-TMD interfaces. It is ~10 amino-acids in length and has a critical role in the transmission of the signal between the two domains (Martin et al. 2017). Located in the middle of this loop, there is a Proline (i.e., Pro275) that is so conserved within pLGICs that some authors suggested the name of Pro-loop receptors in reference to pLGICs (Jaiteh et al. 2016).

The M<sub>3</sub>-M<sub>4</sub> loop is a very long one that is 86 and 130 residues in length in  $\alpha$  and  $\beta$  subunits, respectively, and that corresponds to the ICD. Although this domain will be discussed in the

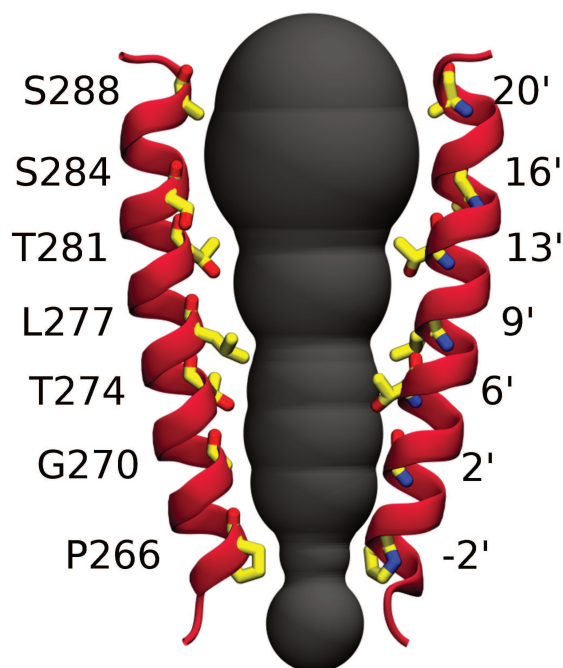


Figure 1.15 – Pore lining residues in GlyR $\alpha$ 1, in addition to their *prime* notation.

next paragraph, we can note that for crystallization purposes, the GlyR structures solved by X-ray or cryo-EM have a very short loop of 4 residues that is similar to the one found in the bacterial pLGIC, *Gloeobacter* Ligand-Gated Ion Channel (GLIC). However, the replacement of the long ICD by the shorter loop impact only mildly the function of the channel (Moraga-Cid et al. 2015; Jansen et al. 2008).

The binding-site of several allosteric modulators, such as neurosteroids, cannabinoids, ethanol, and general anesthetics, is located in the TMD. In GlyR $\alpha$ 1 and  $\alpha$ 3, only the binding-pocket of IVM is experimentally solved, see Figure 1.16. This deep inter-subunit cavity, and the critical residues (Ser267 and Ala288) is also conserved in GluCl and GABA $\Lambda$ R (Huang et al. 2017a).

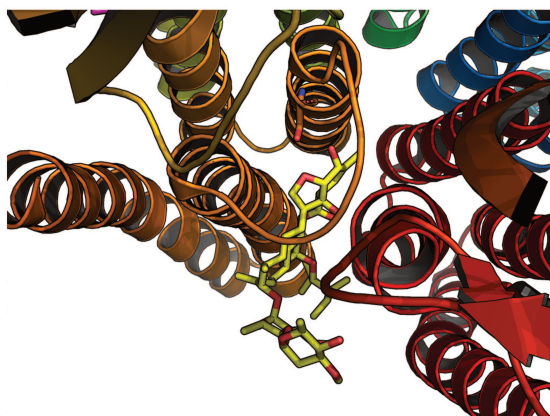


Figure 1.16 – Inter-subunit binding pocket of IVM in GlyR $\alpha$ 3.

### 1.4.3.3 Intracellular Domain

Due to the lack of high-resolution structures of the GlyR ICD, its structure remains elusive and speculative. Hopefully, the 5-HT<sub>3</sub>R was recently solved (Hassaine et al. 2014; Basak et al. 2018b; Basak et al. 2018a; Polovinkin et al. 2018) with a fragment of its ICD including two  $\alpha$ -helices named MA and MX. Interestingly and contrarily to the ECD, the ICD seems to be sterically close at its end. However, the helices are forming lateral portals that are water-filled and lined by charged residues that are controlling the conductance (Kelley et al. 2003; Langlofer and Villmann 2016). Due to the impact of these residues on the conductance, it is reasonable to speculate that they are forming the exit route for ions entering the cell. Unfortunately, the large sequence diversity in the pLGIC's ICD prevents us from doing accurate homology modeling and to provide any atomistic details on the structure of GlyR's ICD.

Of note, the gephyrin binding domain is present in GlyR $\beta$  subunit only. This domain is 18 amino acids in length and located in the middle of the ICD.

### 1.4.4 Ion pore properties

Pore properties are numerous and widely accessible from electrophysiology experiments. They are particularly important for this thesis because they are directly related to the function of the LGIC, they are responsible for the signal transmission at the synaptic level. Pore properties are the most diverse characteristic of pLGICs, and even at the level of receptor subunits, change in residue sequence have striking effects on those properties. For that reason, pore properties are advantageous to identify the nature of an ion channel or, the relevance of an ion channel model with respect to its physiological behavior.

Selectivity between anion and cation is one these properties and is a generic way to classify ion channels. GlyR is an anionic channel with a ~25-fold preference for chloride over sodium (Moorhouse et al. 2002). This high selectivity for anions over cations explains why the reversal potential of GlyR is very close to equilibrium potential of the Cl<sup>-</sup> anions. According to mutation studies, the selectivity filter for cation vs. anion is located at the bottom of the TM<sub>2</sub> helices (Cymes and Grosman 2016). The mutant A-1'E is sufficient for the charge selectivity reversal ( $P_{Cl^-}/P_{Na^+} = 0.34$ ) but the double mutant A-1'E + P-2  $\delta$  strengthens that effect ( $P_{Cl^-}/P_{Na^+} = 0.13$ ) (Keramidas et al. 2002). The double mutant GlyR is also permeable to divalent cation and organic cation as big as tetrapropyl ammonium (TPA<sup>+</sup>). Based on this permeability to polyatomic cations, the pore diameter of the double mutant was estimated to 8.3 Å, in close agreement with the cationic pore of mouse nAChRs (8.4 Å) (Keramidas et al. 2002).

The second property that has an essential physiological role is the conductance of the channel. The conductance corresponds to the ease at which ions cross the membrane through the ion channel. Single-channel experiments showed that the conductance of homomeric GlyR is ~86 and ~112 pS for  $\alpha 1$  and  $\alpha 2 - 3$  respectively (Bormann et al. 1993), which makes it one of the most conductive pLGICs. This particularity is quite useful to facilitate the (computational) electrophysiology recordings in comparison to other anionic pLGICs that have a conductance of few dozens pS (e.g., GABA<sub>A</sub>R or GluCl). However, the heteromeric

GlyR $\alpha\beta$  has a more modest conductance of  $\sim 42$  pS (Bormann et al. 1993). Interestingly, the difference in conductance between  $\alpha$  and  $\beta$  subunits is solely controlled by TM<sub>2</sub> residues, and mutation of TM<sub>2</sub> helix residues from  $\beta$  to  $\alpha$  ones allows to recover the higher conductance of GlyR $\alpha$  (Bormann et al. 1993). A final particularity of GlyR in respect to the conductance is the existence of several sub-conductive states, which are states that are less frequent than the main one, and also less conductive. GlyR $\alpha$  have sub-conductive states in a range between 112 and 19 pS. Again, mutations in the TM<sub>2</sub> residues seems to control the number and the frequency of the sub-conductance states observed between GlyR subunits (Bormann et al. 1993). Sub-conductive behavior is also observed in other pLGICs (e.g., GABA<sub>A</sub>R or nAChR), and it is a known phenomenon in other ion channel families but not well understood from a structural point of view neither for its physiological importance.

Next, pLGICs and in particular the GlyR can be permeable to other ions. The permeability sequence of several common anions is well known. The permeability sequence in neuronal GlyR is  $\text{SCN}^- > \text{NO}_3^- > \text{I}^- > \text{Br}^- > \text{Cl}^- > \text{F}^-$  (Bormann et al. 1987). The order in this sequence corresponds to the order of ionic hydration energies of these anions. This important result implies that the highest barrier controlling anion permeation in GlyR correspond to removal of water from the solvation shell.

In addition to its permeability to monoatomic anions, the GlyR is also permeable to polyatomic anions (similarly to the GABA<sub>A</sub>R). Experiments with polyatomic anions were initially conducted in order to probe the size of the pore, at least at the level of its constriction point. This series of electrophysiological experiments permit to estimate a minimum pore diameter of 5.2 Å for the GlyR $\alpha 1$  (and 5.4 Å for GABA<sub>A</sub>R) (Bormann et al. 1987). To date, the permeability of pLGIC to small polyatomic ions was not questioned in the context of a possible physiological relevance at the synaptic level, but we note that such function is actively discussed in the P2XR family which is permeable to large cations, including natural ones (e.g., spermidine) but also drugs (Harkat et al. 2017).

#### 1.4.5 Gating mechanism

The signal transduction mechanism in pLGICs happens through the conversion of a chemical signal (i.e., neurotransmitter binding) into an electrical signal (i.e., synaptic polarization/depolarization). This transduction is achieved by an allosteric mechanism involving cooperativity between subunits (Cecchini and Changeux 2015) (see Figure 1.17). The binding of an extracellular neurotransmitter will stabilize an open channel that is passively conducting ions. The transition from a closed state in the absence of neurotransmitter toward an open state stabilized by neurotransmitter-binding is commonly named *gating* (Hille 2001) and corresponds to a quaternary rearrangement of the five subunits. The *gate* is located in the middle of the TM<sub>2</sub> helices, and in GlyR the Leu277 at position 9' is playing this role. Interestingly, recent studies showed that pLGIC have a second *gate* located at the bottom of the TM<sub>2</sub> and responsible for the desensitization of the channel upon prolonged exposure to neurotransmitters (Gielen and Corringer 2018).

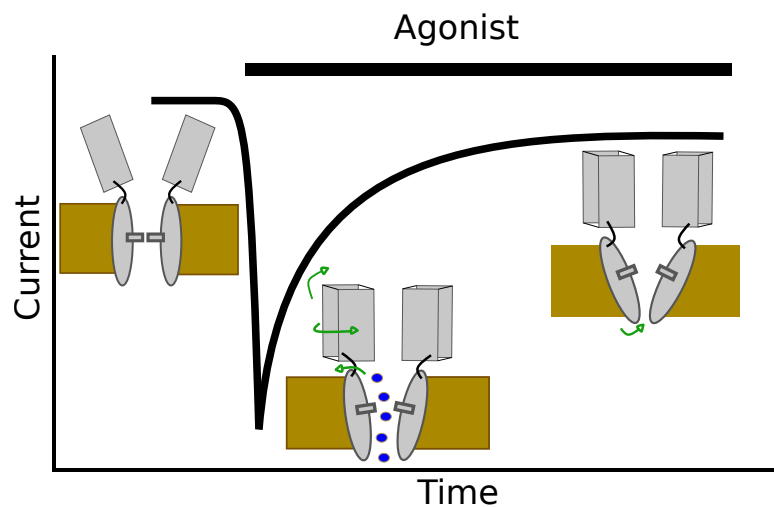


Figure 1.17 – Schematic representation of the three functional states with their associated current. Before application of agonist, channels are mostly in the resting state, and no current is measured. Upon application of agonist, a rapid quaternary motion elicits an open pore conformation. In the active state, a strong current can be measured. Finally, during prolonged exposure to agonist, channels will eventually desensitize and reach a novel non-conductive state.

Based on the available atomistic models, the gating transition seems to be initiated at the level of the neurotransmitter binding site, which is initially responsible for a change at the intersubunit interfaces. Current computational researches are still trying to describe the allosteric transition triggered by a change in intersubunit contacts in the ECD, leading to the opening of the ion pore  $\sim 60$  Å away (Lev et al. 2017; Martin et al. 2017).

The first motion involved in the gating transition was identified by Normal Mode Analysis and correspond to the *twisting* (Taly et al. 2005). It is a concerted and opposite rotation of the ECD and TMD around the ion pore axis. Subsequently, the model was refined by the availability of additional structures which permit to identify a second quaternary change corresponding to a radial expansion of the ECD, named *blooming* (Sauguet et al. 2014; Calimet et al. 2013) and a tertiary motion of  $M_2$  helices, describing an outward tilt. Finally, MD simulations (Calimet et al. 2013) and  $\phi$ -value (Gupta et al. 2017) analysis permit to understand better the link between the major changes described earlier and to propose a sequential view of the transition. Overall, the binding of the neurotransmitter stabilizes an un-bloomed ECD that does not directly impact the structure of the ion pore (Martin et al. 2017). However, the un-bloomed ECD is necessary to allow a complete twisting to take place. The twisting motion, in contrast to the blooming, is controlling the movement of the ion pore by modifying the ECD/TMD interface. In details, the twist controls the position of the  $\beta_1 - \beta_2$  loop relative to  $M_2$ - $M_3$  loop (i.e., the Pro-loop) which is ultimately responsible for the tilt of the  $M_2$  helices (Martin et al. 2017). In the resting state the  $M_2$  helices are straight, and upon activation, they tilt outward in order to open the gate in their middle (see Figure 1.18).

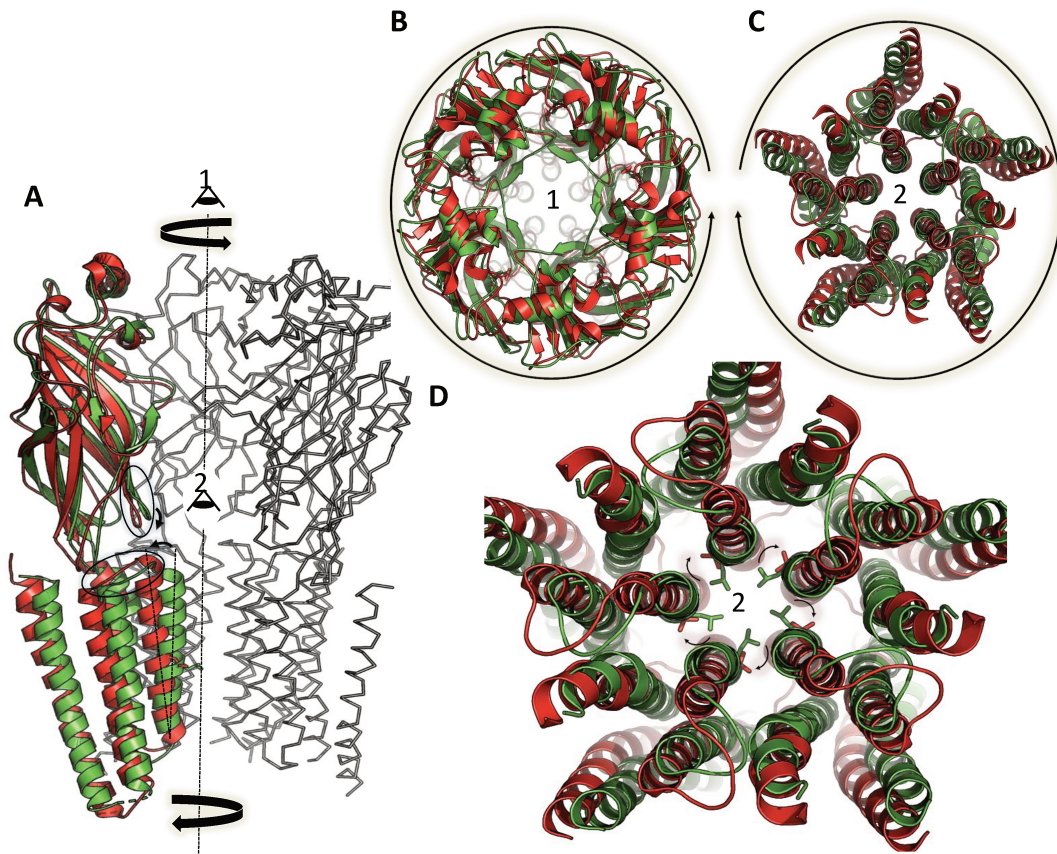


Figure 1.18 – Gating transition based on GlyR $\alpha$ 1 cryo-EM structures. The arrows are supporting the transition from the resting state (in green) toward the active state (in red). The structure captured in presence of the antagonist (strychnine) (PDB:3JAD) is displayed in green, and the structure captured in presence of the agonist (Glycine) and the positive modulator (IVM) (PDB:3JAF) is displayed in red. (A) Side-view shows circled in blue motion of the  $\beta_1 - \beta_2$  loop with respect to the  $M_2$ - $M_3$  loop. The two arrows highlighted in yellow represent the opposite rotation of the ECD with respect to the TMD, i.e., the twisting motion. (B) and (C) show the top view of the receptor from the apex of the channel and from the ECD-TMD interface, respectively (see the *eyes* annotation in (A)). (D) Top view on the TMD with stick representation of Leu277 that is forming the *gate*. The change in orientation of the  $M_2$  helices allow the Leu277 to orient toward and side and open the *gate* located in  $9'$ .

#### 1.4.6 *The functional-annotation problem*

Elucidating the molecular mechanism of gating is critical to rationally design drugs targeting pLGICs, but also to understand the effect of pathological mutations in human and to propose efficient treatment for them. To accurately model the transition mechanism between the resting/closed, the active/open and the desensitized/closed states we rely on the representative structures of each state. The end-point structures of such models of gating are nowadays based on x-ray/cryo-EM structures. However, the current explosion in the number of structures solved experimentally, and the structural heterogeneity of these structures ignited a debate about their functional-state annotation.

This thesis started the same year as the publication of three cryo-EM structures of GlyR $\alpha$ 1 (Du et al. 2015). Among the three structures, one was evidently assigned to the resting state (PDB:3JAD), but the two other ones (i.e., PDB:3JAE and 3JAF) could represent the active state. Unfortunately, by raising doubts about the structural models of the three main states, it is also the relevance of the gating mechanisms based on these structures that can be questioned. Hopefully, the ion pore properties that were mentioned earlier are characteristic of a given channel active state and could be used for a functional-annotation purpose. Indeed, a representative structure of the active state should be able to reproduce the single-channel recording produced experimentally. Overall, ion channels are undoubtedly an excellent system to study because their single-molecule experiments are simple to set up and their primal functions are relatively easily accessible both experimentally, and computationally.

For that reason, we first aimed at solving the function-annotation problem for the GlyR $\alpha$ 1 active state, in order to clarify which cryo-EM structure is the most representative conformation of the active/open state. It is particularly important because the conformation privileged by the authors of the structure is dissimilar, at the level of the TMD, to the previously known active conformation in pLGICs (i.e., in GLIC and GluCl). This observation supposes that, at least in GlyR, the final step of the channel gating, i.e., the pore opening, might differ from what was previously known.

In order to address this problem, we will describe in this thesis how computational methods, such as Molecular Dynamics, can help to provide structural annotation in LGIC. By probing the ion pore function of a given structure and comparing the results to experiments, we might assess the physiological relevance of proposed gating mechanisms. This objective was achieved in GlyR $\alpha$ 1 (Chapter 3) and in P2XR (Chapter 6).

After having reported on the GlyR structure compatible with the active state, we will explore one elementary part of the synaptic transmission, i.e., the ion permeation mechanism and pathways through the pore of GlyR (Chapter 4). An original observation concerning the role of P2XR in the synaptic transmission will also be reported (Chapter 6).

Finally, we will propose to develop a novel methodology to discover drugs targeting pLGICs using the functional-state annotation arising from the precedent chapters. This methodology, named *state-based pharmacology*, will aim at maximizing the binding free-energy difference for one state over the other, in order to optimize the modulatory effect of small-

molecule compounds, in agreement with the Monod-Wyman-Changeux (MWC) model of allostery (Chapter 5).

## THEORY

This thesis relies mainly on the use of computational approaches to understand in particular the interactions between the structure of a channel and the ionic diffusion through it. For that purpose, many models might be used, ranging from the macroscopic ones based on a continuum approach to the microscopic ones that are based on all-atom simulations.

## 2.1 MODELING ION DIFFUSION AND PERMEATION

Michael Faraday introduced in 1834 the word *ion* ("going" in Greek) to describe the charged species that travel between electrodes via an aqueous solution. In our case, we will be particularly interested in estimating the current of individual ions through the ion pore of ionotropic receptors. It is fundamental to be able to predict a current of ion for a given atomic channel structure because it is directly related to the macroscopic properties measured experimentally. Three levels of approximation are available for that purpose (Hille 2001; Chung and Corry 2005), continuum electrostatic models, simplified stochastic simulations or classical molecular dynamics.

2.1.1 *The Poisson-Nernst-Planck model*

The Poisson-Nernst-Planck (PNP) model is based on the mean-field approximation. Here, ions and water molecules are treated implicitly as continuous charge densities. These densities represent the averaged microscopic properties of ions. In the PNP model, the Nernst-Planck equation describes the ionic fluxes and the Poisson equation describes the position-dependent electrostatic potential of the system within a unified formalism. The Nernst-Planck equation describes the flux (i.e., current density)  $J_s$  (in unit:  $A.m^{-2}$ ) of an ion  $s$  from the combination of diffusion due to the concentration gradient (Fick's law) and the electrostatic potential gradient (Kohlrausch's law):

$$J_s = -z_s F D_s \left( \nabla c_s + \frac{F z_s c_s}{RT} + \nabla \phi \right) \quad (2.1)$$

where,  $z_s$ ,  $D_s$  ( $m^2.s^{-1}$ ),  $c_s$  ( $mol.m^{-3}$ ) are, respectively, the valence, the diffusion coefficient, and the local concentration of ion  $s$ . Additionally,  $F$  ( $C.mol^{-1}$ ),  $R$  ( $J.K^{-1}.mol^{-1}$ ),  $T$  (K), and  $\phi$  (V or  $J.C^{-1}$ ) are, respectively, Faraday's constant, the gas constant, the temperature, and the electric potential.

The Equation 2.1 results from the additivity of diffusion and electrophoretic motions. Of note, the equilibrium properties of this equation are demonstrated by choosing the condition  $J = 0$ , i.e., when there is no net flux, for which the Nernst-Planck equation integrates to the Nernst equation for equilibrium potentials (Hille 2001).

Most importantly,  $\phi$  arises from the protein's charges, the mobile ions, and the membrane potential. Using Poisson's equation, it is possible to determine the position-dependant electric potential. The PNP model consists of solving simultaneously the Poisson's equation and the Nernst-Planck equation. For most cases, the PNP equations have to be solved numerically (Kurnikova et al. 1999; Corry et al. 2000).

From the Nernst-Planck equation one may derivate the Goldman-Hodgkin-Katz (GHK) flux equation (Hille 2001) which permits to estimate in a easier way the flux  $J_s$  of an ion  $s$ :

$$J_s = -z_s^2 P_s \frac{V_m F^2}{RT} \frac{[s]_i - [s]_o \exp(-z_s V_m F/RT)}{1 - \exp(-z_s V_m F/RT)} \quad (2.2)$$

where,  $P_s$  ( $\text{m.s}^{-1}$ ) is the membrane permeability for the ion  $s$ ,  $V_m$  (V) is the membrane potential,  $[s]_i$  and  $[s]_o$  ( $\text{mol.m}^{-3}$ ) are the intracellular and extracellular concentration.

An essential difference between the two models is that GHK equation assumes a constant electric potential, which is not the case in PNP model. Indeed, by taking into account, the atomic description of the channel and the membrane through the Poisson's equation (Chung and Corry 2005), the PNP model estimate the local electric potential.

Finally, the PNP model (and GHK equation) permits to compute the steady-state ionic currents, which is comparable to the current measured by experimental electrophysiology.

However, there are some limitations to the use of continuum theory, especially in the context of narrow pores, like the one of LGICs. In particular, since ions are treated implicitly as average concentrations, both positive and negative fractional charges are present in each grid-cell of the calculations. The main effect of this treatment is the underestimation of the induced surface charges (Chung and Corry 2005). Yet, the induced surface charges are dominant forces, arising from ion-protein interactions, involved in the permeation process. The PNP models also suffer from the lack of ion-ion interactions, which might be important to represent the permeation process correctly. Lastly, having a fixed protein structure and assigned dielectric constants would play in disfavor of this methodology, but these limitations are shared with Brownian Dynamics.

Comparisons between several methodologies estimated the domain of applicability of PNP model to pores with radius larger than  $\sim 8 \text{ \AA}$  (Corry et al. 2000; Mamonov et al. 2003).

### 2.1.2 Brownian Dynamics

In 1905, Einstein introduced an alternative model of diffusion which relies on *random walk* (Einstein 1905). He demonstrated that his idea satisfies the Fick's law although based on stochastic elementary diffusion events. Brownian Dynamics (BD) is a model which use Einstein's idea on diffusion (microscopic view). Overall, BD maintains the Kohlraush's equation but replaces the Fick's law (macroscopic view).

Similarly to the PNP model, BD uses a continuum model to represent the solvent, implying the use of parameters such as frictional parameters of each ion and a dielectric constant. However, in BD the ions are explicitly treated, and their trajectories are integrated in time. The ionic diffusion is then driven by a random force representing the atomic collisions, and

the electric field arising from the membrane potential, the protein's charges, and the other ionic charges.

The ionic trajectories in BD might be computed using the Langevin equation for each particle  $i$  (Chung et al. 1998):

$$m_i a_i = z_i q_e \frac{d\phi}{dx} - f_i \frac{dx}{dt} + F_R \quad (2.3)$$

where  $m_i a_i$  corresponds to the product of the mass and the acceleration of a particle  $i$ . On the right-hand side of the Equation 2.3, the first term corresponds to the electric potential at the position of the ion  $i$ . The second term corresponds to a frictional force proportional to the velocity of the ion. Finally, the third term refers to random forces  $F_R$ , simulating stochastic collisions. In conclusion, the last two terms describe the effect of random collisions with the surrounding water which is treated implicitly in BD.

By solving at each time-step (usually between 2 to 10 fs), the Langevin equation of motion for each ion it is possible to trace the trajectory for all of them. Finally, after some microseconds, it is possible to count how many of them permeate through the channel and then compute from the ionic flux the single-channel conductance or selectivity.

Having a computationally inexpensive method to compute the current-voltage (I-V) curve for ion channels using explicit treatment of ions is a substantial advantage of the BD model. However, this technique still suffers from the drawback of having an implicit treatment of the solvent, which imposes to choose more or less arbitrarily a dielectric constant in the narrow environment constituting the ion pore. Additionally, this methodology is also relying on fixed protein structures which might be problematic when the order of magnitude of atomic thermal fluctuations is comparable to the pore radius (Allen et al. 2004), which is the case in narrow pores such as the ones of LGICs.

Because of the ease to obtain converged I-V curve using this technique at physiological conditions, we applied it to GlyR with mitigated success, certainly because of the limitations previously mentioned. Protocol, results and critical discussion thereof can be found in Appendix F. Of note, the BD methodology have been successfully applied to the bacterial pLGICs, GLIC and *Erwinia chrysanthemi* Ligand-gated Ion Channel (ELIC) in Song and Corry 2010.

### 2.1.3 Molecular Dynamics

Molecular Dynamics (MD) will be described in details in the next section because it is the main simulation technique used within this thesis. However, a brief introduction to MD will be given here and contextualized with respect to the previous two models for simulations of ionic currents.

In contrast to the previously mentioned models, the conventional MD simulations treat all atoms, including the solvent, the ions, the membrane, and the protein explicitly. The atomic trajectories are generated by numerically integrating over a short time-step (generally few fs) Newton's equation of motion for interacting atoms, using molecular mechanics force field:

$$m_i a_i = F_i = -\nabla_i U(r_1, \dots, r_N) \quad (2.4)$$

where  $U(r_1, \dots, r_N)$  corresponds to the many-body potential for atoms  $(r_1, \dots, r_N)$ .

In the context of ion permeation through narrow pores, this simulation technique has the advantage to overcome limitations of BD by avoiding to define the dielectric constant for continuum media explicitly. Additionally, all types of interactions are taken into account, and all atoms are free to move.

While more accurate than previously cited methods, MD also has significant drawbacks to compute ion channel conductance. First, this method is computationally costly in comparison to BD because hundreds of thousands of atoms have to be treated in comparisons to the few hundreds of ions in BD. Of note, the computational cost can be alleviated by running shorter simulations (few hundreds of nanoseconds), but in parallel on Graphics Processing Unit (GPU)-node, in order to reach more consistently the microsecond timescale required for proper evaluation of the conductance in some ion channels (see Chapter 3). Indeed, since ion permeation event are mostly independent event it does make sense to simulate on the multi-nanoseconds timescale and to aggregate results over many parallel simulations. All details concerning our setup can be found in Chapter 3.

Apart from the classical discussion on the accuracy of the force field, two elements can particularly impact the accuracy of the measured ionic flux. First, the choice of water models, which implicitly modifies the diffusion coefficient of ions and the dielectric constant. Second, the lack of explicit polarizability in most of the conventionally used force fields. Of note, no clear benchmark exists for the moment on the actual impact of both water model and polarizability on the computed currents accuracy. For example, for simulations carried out in NaCl solution, none of the available water models seem to reproduced accurately the diffusion coefficient of the ions (Patra and Karttunen 2004), which is indeed critical for the measured current.

## 2.2 MOLECULAR DYNAMICS SIMULATIONS

### 2.2.1 *The potential energy function*

To run MD simulations, one has to solve Newton's equation of motion described in Equation 2.4. In that perspective, MD relies on the definition of a potential energy function  $U$  and the calculation of its first derivative, i.e., the force or gradient. In the context of this thesis, we will describe the Chemistry at Harvard Molecular Mechanics (CHARMM) (Best et al. 2012; Vanommeslaeghe et al. 2010) potential energy function  $U_{\text{CHARMM}}$  which is the only one that we used in our simulations.

The energy function can be defined generally as the addition of bonded  $U_{\text{bonded}}$  and non-bonded  $U_{\text{non-bonded}}$  energy terms:

$$U_{\text{CHARMM}} = U_{\text{bonded}} + U_{\text{non-bonded}} \quad (2.5)$$

The interaction between nearest chemically bonded atoms consist in the addition of several terms, i.e., bound stretching, angle bending, Urey-Bradley, dihedral, improper dihedral, and CMAP (Mackerell et al. 2004) energy terms:

$$U_{\text{bonded}} = U_{\text{bond}} + U_{\text{angle}} + U_{\text{UB}} + U_{\text{dihedral}} + U_{\text{improper}} + U_{\text{CMAP}} \quad (2.6)$$

with:

$$\begin{aligned} U_{\text{bonded}} = & \sum_{\text{bonds}} K_b (b - b^0)^2 \\ & + \sum_{\text{angles}} K_\theta (\theta - \theta^0)^2 \\ & + \sum_{\text{Urey-Bradley}} K_{\text{UB}} (S^{1-3} - S^{1-3,0})^2 \\ & + \sum_{\text{dihedrals}} K_\phi (1 + \cos(n\phi - \delta)) \\ & + \sum_{\text{impropers}} K_\omega (\omega - \omega^0)^2 \\ & + \sum_{\text{residues}} u_{\text{CMAP}}(\Phi, \Psi) \end{aligned} \quad (2.7)$$

where  $b$  corresponds to the bond length between consecutive atoms,  $\theta$  the angle between three consecutive atoms,  $S^{1-3}$  the distance between atoms 1 and 3 of the angle terms,  $\phi$  the dihedral angle between four consecutive atoms,  $\omega$  the improper dihedral angles between four non-consecutive atoms. The CMAP term corresponds to a *cross-term* for the  $\phi$  and  $\psi$  (backbones dihedral angles) values. Other standard values (e.g.  $b^0$ ,  $\theta^0$ ), or force constants (e.g.  $K_b, K_\theta$ ) correspond to parameters in the force field that are specific to each atom types.

The non-bounded interactions are described as the addition of the Lennard-Jones (LJ) and Coulomb interactions energy terms:

$$U_{\text{non-bonded}} = U_{\text{LJ}} + U_{\text{elec}} \quad (2.8)$$

with:

$$\begin{aligned} U_{\text{non-bonded}} = & \sum_{\text{nonb.pairs}} \epsilon_{ij} \left[ \left( \frac{r_{ij}^{\text{min}}}{r_{ij}} \right)^{12} - 2 \left( \frac{r_{ij}^{\text{min}}}{r_{ij}} \right)^6 \right] \\ & + \sum_{\text{nonb.pairs}} \frac{q_i q_j}{4\pi\epsilon_0 r_{ij}} \end{aligned} \quad (2.9)$$

where  $r_{ij}$  corresponds to the distance between atoms  $i$  and  $j$ .  $\epsilon$  and  $r^{\text{min}}$  are force field parameters corresponding to the energy wells depth, and the inter-atomic distance which minimizes the interaction energy, respectively. In CHARMM, for mixture of atom type use  $\epsilon_{ij} = \sqrt{\epsilon_i \epsilon_j}$  (geometric mean), and  $r_{ij}^{\text{min}} = (r_i^{\text{min}} + r_j^{\text{min}})/2$  (arithmetic mean). The so-called  $\text{LJ}^{6-12}$  potentials are used to approximate the van der Waals forces. Because van der Waals interactions are most relevant at short range, they are spatially-truncated at a given cut-off

distance in order to decrease the computational cost of the pair-wise calculations. In practice, a *switching* function is used to smooth the energy profile at the vicinity of the cut-off distance.

The electrostatic interactions are computed for all non-bounded pairs of atoms with  $q_i$  and  $q_j$  the charges on atoms  $i$  and  $j$ . The parameter  $\epsilon_0$  refers to the vacuum permittivity. Because of the  $1/r$  behavior of the electrostatic interactions, no truncation is possible without introducing errors. For that reason, the periodicity of the system introduced by the Periodic Boundary Conditions (PBC) is exploited to alleviate the computational cost of computing the full electrostatic interaction using the smooth Particle-Mesh Ewald (PME) (Essmann et al. 1995).

### 2.2.2 Numerical integration

The Verlet integrator was the first method used to integrate Newton's equation of motion (Hairer et al. 2003). It has the advantage over Euler method to be stable numerically and time reversible at no extra cost. The Verlet integrator connects the positions  $r_i$  of a set of particles, with their positions  $r_{i+1}$  after a short time-step  $\Delta t$  using a Taylor expansion of Newton's second law (Equation 2.4) written in the differential form:

$$\begin{aligned} r_{i+1} &= r_i + \frac{\partial r}{\partial t}(\Delta t) + \frac{1}{2} \frac{\partial^2 r}{\partial t^2}(\Delta t)^2 + \frac{1}{6} \frac{\partial^3 r}{\partial t^3}(\Delta t)^3 + \dots \\ &= r_i + v_i(\Delta t) + \frac{1}{2} a_i(\Delta t)^2 + \frac{1}{6} b_i(\Delta t)^3 + \dots \end{aligned} \quad (2.10)$$

where  $v_i$ ,  $a_i$ , and  $b_i$  correspond to the velocities, the accelerations, and hyper-accelerations, respectively. It is also possible to obtain the positions  $r_{i-1}$ , one time-step earlier by substituting  $\Delta t$  by  $-\Delta t$ :

$$r_{i-1} = r_i - v_i(\Delta t) + \frac{1}{2} a_i(\Delta t)^2 - \frac{1}{6} b_i(\Delta t)^3 + \dots \quad (2.11)$$

By adding Equation 2.10 to Equation 2.11 we can obtain the Verlet integrator:

$$\begin{aligned} r_{i+1} &= (2r_i - r_{i-1}) + a_i(\Delta t)^2 + \dots \\ a_i &= -\frac{1}{m_i} \frac{dU}{dr_i} \end{aligned} \quad (2.12)$$

Finally, the integrator permits to predict the positions after a time-step  $\Delta t$ , knowing the current and previous positions, as well as the current accelerations. Of note, in Equation 2.12 the hyper-acceleration term  $b_i$  disappears, implying the correctness of the equation to the third order.

In Nanoscale Molecular Dynamics (NAMD) (i.e., the MD code used in this thesis) the Verlet integrator is used for microcanonical (NVE) simulations (Phillips et al. 2005). Although the natural ensemble of MD simulations is the NVE, it is possible to generate canonical (NVT) or isothermal-isobaric (NPT) ensemble using *thermostat* and *barostat* (F. Jensen 2007). However, the use of such *heat bath* or *pressure bath* to control directly the amount of energy by modifying

the velocities do not produce the correct NVT or NPT ensemble unless the Nosé-Hoover methods are used (F. Jensen 2007).

Alternatively, the NVT ensemble can be generated in NAMD using the Brünger-Brooks-Karplus (BBK) integrator (Brünger et al. 1984). Here, the system is stochastically coupled to an energy reservoir. The Langevin equation (Equation 2.3) can be rewritten to make apparent the terms relative to the random forces and the velocity-dependent friction:

$$m_i a_i = F_i - \gamma v_i + \sqrt{\frac{2\gamma k_b T}{m_i}} R(t) \quad (2.13)$$

where  $\gamma$  is the friction coefficient,  $k_b$  the Boltzmann constant, and  $R(t)$  a univariant Gaussian random process. Yet, the coupling to the reservoir is achieved by adding energy to the system through the random force and removing energy via the friction term (F. Jensen 2007).

Inserting the Equation 2.13 in the Verlet method (Equation 2.12) it is possible to derive the BBK integrator (Phillips et al. 2005):

$$r_{i+1} = r_i + \frac{1 - \gamma\Delta t/2}{1 + \gamma\Delta t/2}(r_i - r_{i-1}) + \frac{1}{1 + \gamma\Delta t/2}\Delta t^2 \left[ m^{-1}F(r_i) + \sqrt{\frac{2\gamma k_b T}{\Delta m_i}} Z_i \right] \quad (2.14)$$

where  $Z_i$  corresponds to a set of Gaussian random variables of zero mean and variance one. Typically, if one uses an algorithm to constrain H-bound, such as SHAKE (Ryckaert et al. 1977), it is possible to choose a time-step  $\Delta t = 2$  fs.

Of note, the NPT ensemble can be generated using several methods, including, in NAMD, a combination of Nosé-Hoover methods for constant pressure control (Martyna et al. 1994) and piston fluctuation implemented in Langevin dynamics (Feller et al. 1995a).

### 2.3 COMPUTATIONAL ELECTROPHYSIOLOGY

We already discussed in Chapter 1 the necessity for living cells to have an electric potential difference across the membrane, and that one of the main function of a neuron is to modify the potential difference in response to intercellular signals. In cells, the ionic distribution on both sides of the membrane is actively produced by pumps and transporters. However, it is possible to experimentally apply a potential difference across the membrane using electrodes and to measure the resulting currents. This electrophysiological technique is termed voltage clamp. In both physiological or experimental conditions, the membrane potential arises from a small charge imbalance at the vicinity of the membrane although the system as a whole is electroneutral. The charge imbalance  $Q$  (in Coulomb) is related to the membrane potential  $V_m$  (in Volt) through the membrane capacitance  $C$  (in Farad):

$$Q = V_m C \quad (2.15)$$

The cell membrane composed of a phospholipid bilayer behaves accordingly to the parallel-plate model of the capacitor with its capacitance  $C$ :

$$C = \frac{\epsilon_0 \epsilon A}{d} \quad (2.16)$$

with  $\epsilon_0$  ( $\text{F}\cdot\text{m}^{-1}$ ) the vacuum permittivity,  $\epsilon$  the membrane's relative permittivity (i.e., the dielectric constant),  $A$  the area of the capacitor ( $\text{m}^2$ ). Since the physiological membrane capacitance per unit area is  $\sim 1 \mu\text{F cm}^{-2}$  (Liang et al. 2017; Delemotte et al. 2008), an imbalance of only one electric elementary charge will result in a membrane potential of 100 mV for a membrane capacitance  $C = Q/V_m = 1.602 \times 10^{-19}/0.1 = 1.602 \times 10^{-18} \text{ F}$ . According to experiments, the capacitance per area is  $C/A = 1 \mu\text{F cm}^{-2} = 1 \times 10^{-2} \text{ F m}^{-2}$ , then  $A = C/(1 \times 10^{-2}) = 1.602 \times 10^{-16} \text{ m}^2 = 1.602 \times 10^4 \text{ \AA}^2$ , which corresponds to a membrane patch of  $127 \times 127 \text{ \AA}$ . Thus, physiological membrane potentials of  $\sim 50 - 100 \text{ mV}$  correspond to a small charge imbalance for the affordable size for a simulation box.

Of note, using Equation 2.16 it is also possible to approximate the dielectric constant of a physiological membrane to  $\epsilon \approx 4$  for a lipid bilayer of  $\sim 35 \text{ \AA}$ .

To date, there exists two methods to model a membrane potential that are applicable to all-atom MD simulations, the ion imbalance (J. N. Sachs et al. 2004; Delemotte et al. 2008; Kutzner et al. 2011; Kutzner et al. 2016), and the constant electric field (Roux 1997; Roux 2008; Gumbart et al. 2012).

### 2.3.1 Ion imbalance

In the framework of this method, the membrane potential arises from a charge imbalance on each side of the membrane, similarly to the physiological cause in cells. Due to the presence of PBC in all-atom MD simulations, there is a need to have two compartments that are physically separated. This separation can be achieved by adding an air slab (Delemotte et al. 2008) or a second membrane bilayer (J. N. Sachs et al. 2004; Kutzner et al. 2011) in the direction normal to the membrane. Then, the desired membrane potential is applied by defining a charge imbalance using the Equation 2.15. However, in the presence of ion channels embedded in the membrane, the differential potential would tend to disappear upon ion translocation. To overcome this issue, the latest developments of the ion imbalance method introduced a technique to perform the ion/water exchange between the two compartments in order to maintain the desired charge imbalance (Kutzner et al. 2016). The ion imbalance method as the advantage to be straightforwardly linked to the membrane potential and does not rely on mathematical approximation. However, this technique is limited to net charge imbalance which quickly represents several hundreds of mV for the standard simulation box sizes used nowadays.

### 2.3.2 Constant electric field

Benoit Roux developed in 1997 a modified Poisson-Boltzmann (PB) theory to model the membrane potential using a continuum electrostatic representation of its effect (Roux 1997). However, this methodology was not suited to introduce a membrane potential in all-atom MD simulations, in particular, the ones using PBC.

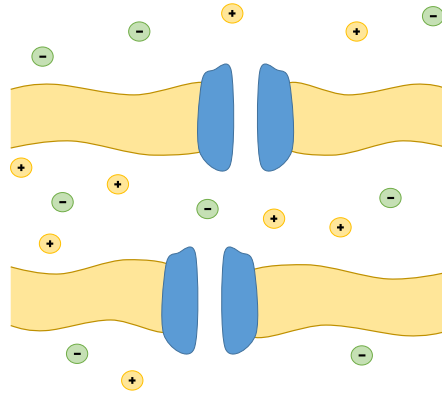


Figure 2.1 – Schematic representation of the ion imbalance method with two compartments separated by two membranes, in order to generate a charge separation resulting in a membrane potential.

Crozier and coworkers proposed to use a constant electric field applied along the  $z$ -axis on all particles in order to represent a membrane potential for all-atoms MD using PBC (Crozier et al. 2001). The constant electric field is supposed to model the effect of the metallic electrode because of the response of mobile water and ions to that applied field. Finally, they proposed the membrane potential to be equal to the drop in applied potential across the unit-cell (Crozier et al. 2001):

$$E_z = V_m/L_z \quad (2.17)$$

Where  $E_z$  corresponds to the applied electric-field,  $L_z$  is the size of the simulation box in the  $z$  direction and  $V_m$  the resulting membrane potential (Aksimentiev and Schulten 2005). The application of a uniform electric field perpendicular to the membrane to all charges composing the system was exemplified by Askimentiev and Schulten to compute the conductance of  $\alpha$ -hemolysin in all-atom MD (Aksimentiev and Schulten 2005). However, it is only later that Benoit Roux demonstrated theoretically the relationship between constant electric field and the resulting membrane potential (Roux 2008) from the analysis of its modified PB theory (Roux 1997). The constant electric field used in all-atom MD simulations was shown to be equivalent to the effect a membrane potential imposed on infinite baths via metallic electrodes connected to an electromotive force (Roux 2008).

In a review, Gumbart and coworkers supported, with all-atom MD simulations, the theoretical demonstration that the membrane voltage represented by a constant electric field is solely dependent on the size of the unit cell along the  $z$ -axis, and not by the thickness of the membrane, neither by the membrane geometry (Gumbart et al. 2012). They showed that the bulk medium reorganizes itself in order to reduce the magnitude of the external electric field. This non-uniform reorganization of the bulk medium produces a reaction field from the electrostatic interactions treated by PME. Finally, the summation of the external field and the reaction field results in the total field which is of biological interest (see Figure 2.2). The immobile and insulating medium formed by the membrane becomes the place

where the change in potential is focused in order to separate the bulk phases. Overall, this methodology permits to produce a non-periodic membrane potential from the application of a constant electric field to MD simulations with PBC on a system with only one, continuous bulk compartment.

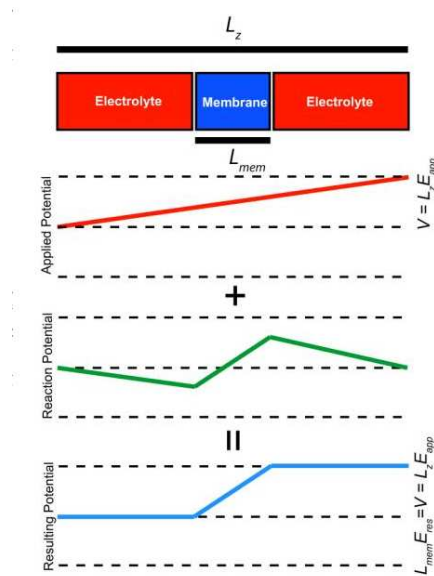


Figure 2.2 – Schematic representation of the constant electric field method in all-atom MD simulation with PBC. From Gumbart et al. 2012.

Recently, a review of the two techniques has shown that although they are based on entirely different theoretical grounds, both of them provide an equally accurate representation of the membrane potential (Melcr et al. 2016).

## AN ION PERMEABLE STATE OF THE GLYCINE RECEPTOR CAPTURED IN SILICO

---

### 3.1 INTRODUCTION

pLGICs can adopt at least three distinct functional states which can be characterized experimentally (Cecchini and Changeux 2015). A resting state in the absence of neurotransmitter where the ion channel is closed. An active state promoted by the binding of neurotransmitter where the ion channel is open and permeable. Upon long exposure to the neurotransmitter, the receptor eventually adopts a desensitized state where the channel is closed and impermeable to ion (Katz and Thesleff 1957). Although, the impermeability to ion is a shared property of *closed* states, their structures, and affinities for the neurotransmitter are distinct (Gielen et al. 2015). The gating mechanism commonly refers to the transition from the resting state to the active state (Hille 2001).

Ideally, one could derive most of the relevant properties of pLGICs knowing the atomistic structures of all these states and the molecular mechanisms that interconnect them. The knowledge that could be extracted from such data includes the rationalization of human mutations and the design of novel therapeutics targeting brain disorders.

GlyR seems in that respect the appropriate receptor to study because its structures have been solved for a couple of isoforms (homomeric receptors  $\alpha 1$  and  $\alpha 3$ ), in the presence of several ligands, agonist, antagonist, and two Positive Allosteric Modulator (PAM)s (Du et al. 2015; Huang et al. 2015; Huang et al. 2017b; Huang et al. 2017a). From the pathological point of view, GlyR malfunctions are involved in many brain disorders, and its mutations in human are responsible for hyperekplexia (startle disease) (Dutertre et al. 2012a; Lynch et al. 2017). Additionally, recent studies show that pharmacological modulation of GlyR is highly efficient to treat chronic inflammatory pain (Lynch et al. 2017; Lu et al. 2018).

High-resolution structures of the GlyR $\alpha 1$  captured by cryo-EM (Du et al. 2015) show that the antagonist strychnine can stabilize a conformation that is physically close to Chloride anion ( $\text{Cl}^-$  radius = 1.8 Å (Nightingale 1959)) with a minimum radius of 1.4 Å at the level of the constriction point in the middle of the ion pore. This conformation is compatible with previously captured Resting structures of pLGICs, GLIC at pH7 (Sauguet et al. 2014) and GluCl-apo (Althoff et al. 2014). The same study depicts a conformation stabilized by the agonist Glycine and the PAM IVM with a pore radius of 2.4 Å at the constriction point which is moved to the bottom of the pore. This conformation is quite similar to the structures of GluCl with L-glutamate and IVM (Hibbs and Gouaux 2011) or GLIC at pH4 (Bocquet et al. 2009) which were assigned as representatives of the Active state. Finally, the authors captured for the first time a widely open conformation with a minimum pore radius of 4.4 Å in the presence of Glycine only. Due to its unprecedentedly wide ion pore, the authors annotated it as the true representation of the Active state because it is the sole structure that would allow

the permeation of Chloride anion and its full hydration shell (hydrated  $\text{Cl}^-$  radius = 3.3 Å (Nightingale 1959)) (Du et al. 2015). In the following thesis, the Gly-bound structure will be termed *wide-open* and the Glycine and IVM -bound structure *semi-open*. Based on the novel annotation of the *wide-open* structure made by the authors they reinterpreted the *semi-open* structure and all its relatives as a low-conductive or desensitized conformations. Of note, the most recent X-ray structures of GlyR $\alpha$ 3 with the PAM AM-3607, with (Huang et al. 2017a) and without IVM (Huang et al. 2017b) are more similar to the *semi-open* conformation and were subsequently annotated as desensitized.

Because of the uniqueness of the *wide-open* structure in the pLGIC superfamily, its physiological relevance is debated (Nemecz et al. 2016).

Experimentally, the function of the GlyR can be probed by electrophysiology, especially in single channel setup. I-V measurement from single-channel experiments can provide several properties of the open ion pore including conductance and selectivity. More precisely it is known that the conductance of GlyR $\alpha$ 1 main Active state is equal to 86 pS in outside-out patches at symmetric 145 mM NaCl concentration (Bormann et al. 1993). Additionally, it exists several sub-conductive states with conductance values ranging from 18 to 64 pS (Bormann et al. 1993). Analysis of the permeability ratio between Chloride and a series of polyatomic anions permits to probe a minimum pore radius of 2.6 Å (Bormann et al. 1987). The corresponding permeability sequence corresponds to chloride > formate > bicarbonate > acetate, with phosphate and propionate being non-permeable (Bormann et al. 1987). Finally, whole-cell electrophysiological recordings with different NaCl concentration in the external solution allowed to measure the permeability of  $\text{Cl}^-$  versus  $\text{Na}^+$  of ~25 which depicts a strong selectivity of the GlyR for the chloride anions (Keramidas et al. 2002). Overall, we have an ensemble of properties that characterize the active state pore conformation, and that could serve as stringent functional restrains for the structure of the GlyR active state.

Computational approaches are suited to recover the properties of the available structures to annotate them functionally or to question their relevance (Howard et al. 2017). Providing a structure-function relationship would correspond to reproducing the functional properties of a state measured experimentally using the corresponding structural model in silico.

The most popular computational approach to functionally annotate ion channel structure, including the software HOLE (O. S. Smart et al. 1996), aims at measuring the physical dimension of the pore to categorize it as *open* or *closed*. Although the geometrical measurement is suited to annotate closed structures where constriction point is smaller than the permeating ions, it is more complicated to annotate an open channel structure because of pore dewetting. Such dewetting, named hydrophobic gating (Beckstein and Sansom 2006), may result in channel impermeability even when the pore radius is larger than water or ions. Based on the importance of the pore hydration in the annotation of the open channel structure, a three-level dynamic annotation has been recently proposed to probe the function more accurately (Trick et al. 2016) than static methods such as HOLE. This methodology was then applied to GlyR $\alpha$ 1 structures captured by cryo-EM to conclude that the antagonist-bound conformation is representative of the Resting state because of a strong dewetting in the middle of the pore, the *wide-open* is fully hydrated and corresponds to the active state, and the *semi-open* is

less hydrated at the bottom of the pore and depicts a desensitized conformation. However, this annotation assumes that the three tested conformations are physiologically relevant and correspond to the three functional states of the GlyR. If it is clear that the *wide-open* is more hydrated and could accommodate more easily anion permeation in comparison to *semi-open*, it is not clear if the *wide-open* structure is physiologically relevant because there is no straightforward comparison to experiments for water densities. Indeed, the physiological relevance of the *wide-open* structure was questioned by a joint effort of X-ray crystallography and MD simulations of GLIC and GlyR $\alpha$ 1 which showed evidence in favor of the *semi-open* structure being representative of the active state (Gonzalez-Gutierrez et al. 2017). From the computational perspective, the demonstration was notably done by showing the *wide-open* structure permeability to chloride anion, even in the presence of the channel blocker picrotoxin.

In this chapter, we used an original combination of simulations techniques (see Figure 3.1) including conventional MD, computational electrophysiology, and polyatomic anion permeability. Our goal is to design in-silico experiments that can be directly compared to wet-lab experiments in order to provide functional annotation of the GlyR $\alpha$ 1 structures that do not rely on the assumption that the cryo-EM structures are all physiologically relevant, and that goes behind a simple comparison between conformations.

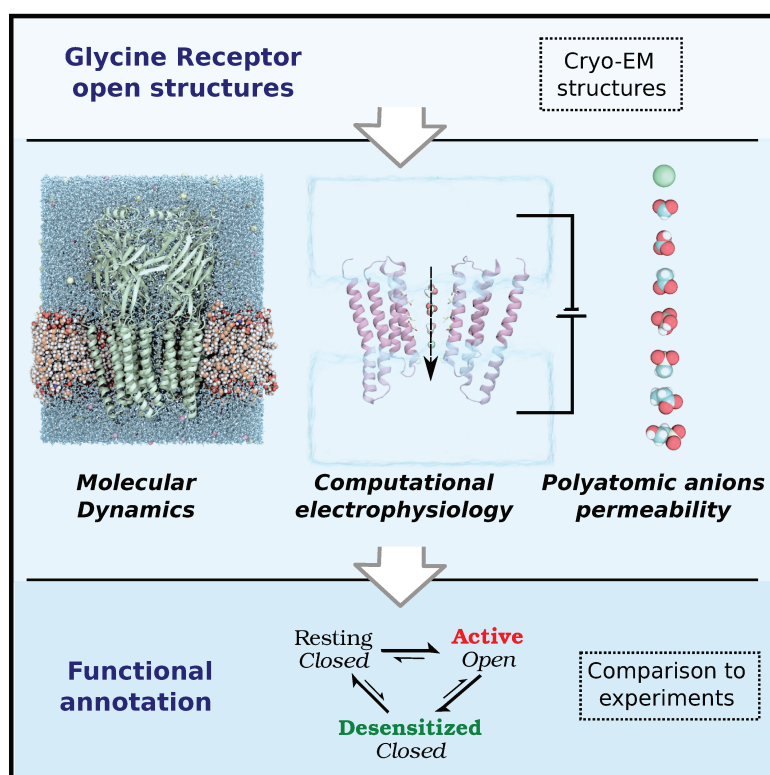


Figure 3.1 – Schematic representation of the computational experiments we designed to probe the function of cryo-EM structures of the GlyR $\alpha$ 1. From Cerdan et al. 2018.

## 3.2 METHODS

**STRUCTURES PREPARATION** Initial coordinates were extracted from the cryo-EM reconstructions of the Zebrafish GlyR $\alpha$ 1 in the *wide-open* (PDB:3JAE) and the *semi-open* (PDB:3JAF) states. The M<sub>3</sub>-M<sub>4</sub> loop, which was missing in the *wide-open* structure, was reconstructed by the program MODELLER (Sali and Blundell 1993) using the *semi-open* structure as a template. Complete models including hydrogens were built using the program CHARMM (Brooks et al. 2009) with the CHARMM 27 force field (Mackerell 2004) and the CHARMM 36 lipid parameter set (Klauda et al. 2010) to model the energetics.

The protonation state at pH7 of the titrable residues was determined by pK<sub>a</sub> calculations based on continuum electrostatics (Bashford and Karplus 1990) and the multi-site titration approach (Bashford and Karplus 1991). Continuum electrostatic calculations were performed by solving the linearized PB equation in 3D with the Adaptive PB Solver (Baker et al. 2001) through the Karlsberg+ package (Kieseritzky and Knapp 2008). The protonation probability of the titratable groups was obtained by Monte Carlo optimization, as implemented in the Karlsberg2 program (Kieseritzky and Knapp 2008). pK<sub>a</sub> values were derived from titration curves for each titratable site calculated by sampling the protonation probability at 300 K over a pH range from -2 to 16 by increments of 0.1 pH units. The dielectric constant used for the solvent is 80. A charge density corresponding to a solution of 150 mM of NaCl was used to account for mobile ions. Lastly, the membrane was mimicked using a slab of 30 Å in thickness and a dielectric constant of 4. The membrane was centered on the TM<sub>2</sub> helices. For the *wide-open* structure, the following residues were predicted in the non-standard (deprotonated) form at pH7: D100, D113, D164, D339, K297, and K362. For the *semi-open* structure, they were: D113, D164, D339, K209, K297, and K362.

Parameters for the allosteric modulator IVM were obtained using the CHARMM General Force Field (CGenFF) through the PARACHEM website (Vanommeslaeghe et al. 2010). In both structures, the coordinates of the endogenous agonist Glycine were missing. Initial coordinates for Glycine were modeled by manual docking to the orthosteric site using the binding mode of L-glutamate in the X-ray structure of GluCl active (PDB:3RIF) as a template. After several ns of MD relaxation, a binding mode with a water molecule mediating the interaction with the protein was stabilized similarly to what was previously suggested in the literature (Yu et al. 2014; Huang et al. 2017b).

**SYSTEMS SETUP** To prepare the system for MD, the protocol proposed by Calimet et al. 2013 was followed. In short, complete models for the *wide-open* and *semi-open* structures of GlyR $\alpha$ 1 were embedded in a lipid bilayer composed of 1-Palmitoyl-2-oleoylphosphatidylcholine (POPC). The POPC bilayer was preequilibrated in NPT ensemble at 303 K with the CHARMM 36 lipid parameter and downloaded from J. Klauda's resources webpage (<https://chbe.umd.edu/jbklau-da/memb.html>). The membrane patch was replicated 3 × 3 with CHARMM to fit the protein width. Next, the protein was inserted in the membrane with VMD and lipids or water molecules within 1 Å to the protein were removed. The system was then neutralized by adding 20 and 10 Cl<sup>-</sup> ions, for the *wide-open* and *semi-open* respectively, and solvated us-

ing a 150 mM NaCl in TIP3P water in a rectangular box of  $120 \times 120 \times 140 \text{ \AA}$  using VMD (Humphrey et al. 1996). The resulting setups include 203,131 atoms for the *wide-open* (328 lipids, 43,716 water molecules, 123  $\text{Na}^+$  and 144  $\text{Cl}^-$ ) and 204,344 atoms (329 lipids, 43,855 water molecules, 124  $\text{Na}^+$  and 134  $\text{Cl}^-$ ) for the *semi-open* simulations, respectively (see Figure 3.2).

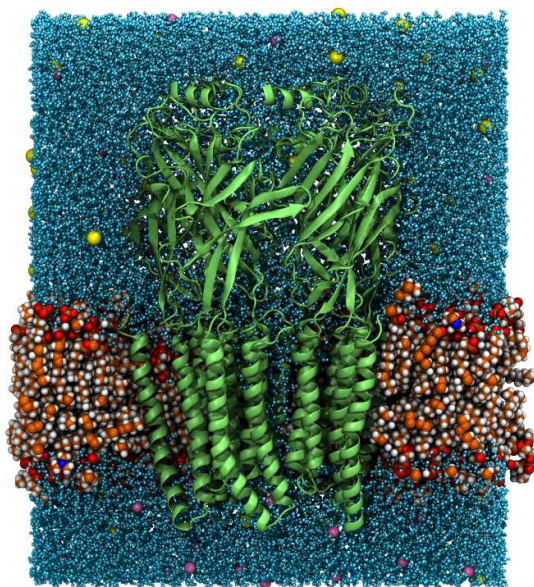


Figure 3.2 – Global view of the MD simulation box containing the GlyR $\alpha$ 1 in the *semi-open* conformation (PDB: 3JAF), embedded in a POPC bilayer, with explicit TIP3P water molecules and 150 mM of NaCl for a total of  $\sim 200,000$  atoms.

**MD SIMULATIONS** Constant temperature and pressure MD simulations were carried out using NAMD 2.12 (Phillips et al. 2005) within PBC.

The nonbonded potential function was truncated at a cutoff distance of  $12 \text{ \AA}$  for short range-range interactions, and a switching distance of  $10 \text{ \AA}$  was used to smooth the electrostatics and van der Waals interaction energies between  $10$  and  $12 \text{ \AA}$ . Long-range electrostatic interactions were computed by the PME method using a grid spacing of  $1 \text{ \AA}$ .

Initially, 5,000 steps of energy minimization using a sophisticated conjugate gradient were performed at constant volume in the presence of harmonic positional restraints with force constants of 10 and  $1 \text{ kcal mol}^{-1} \text{ \AA}^{-2}$  were applied to the protein backbone and side-chain heavy atoms, respectively.

The minimized coordinates are then used to start the heating procedure in the NPT ensemble. The SHAKE algorithm (Ryckaert et al. 1977) is applied to all covalent bond with hydrogens. A time-step of 2 fs is used to integrate each step of the MD simulation. The Langevin thermostat was used to control the temperature with a damping coefficient equal

to 1 and  $0.1 \text{ ps}^{-1}$  for the heating/equilibration and production phases, respectively. The constant pressure was assured by Langevin piston Nose-Hoover method in NAMD (Feller et al. 1995b). The pressure target is set to 1.013 25 bar, with a barostat oscillation period of 100 fs and a damping time scale of 50 fs. The Langevin piston temperature is naturally similar to the one set for the thermostat. The dimension of the unit cell was kept constant in the x-y plan while allowing fluctuation along the z-axis perpendicular to the membrane.

The heating procedure brings the system from 0 to 300 k in 600 ps by increasing the temperature incrementally by 2 K every 4 ps.

In the initial simulations, the systems were equilibrated at 300 K and 1 atm for 2 ns while gradually removing positional restraints on the protein heavy-atoms, followed by unbiased MD production.

**IMPROVED EQUILIBRATION** Because of the poor stability of the *wide-open* structure with the *standard* equilibration protocol we introduce a *gentle* one using the following procedure. Additional simulations of the *wide-open* state were carried out by introducing symmetry restraints on the pentameric organization with force constants of 0.25 and  $1.0 \text{ kcal mol}^{-1} \text{ \AA}^{-2}$  for the ECD and TMD, respectively, using the `symmetryRestraints` module in NAMD and torsional restraints on the  $\chi_1$  angle of Leu277 (at position 9') with half-harmonic boundary potentials at 280 and 300 deg (force constant  $0.1 \text{ kcal mol}^{-1} \text{ deg}^{-2}$ ) to keep the hydrophobic chain of Leu277 away from the pore lumen. Torsional restraints were implemented using the `colvars` module in NAMD (Fiorin et al. 2013). In these runs, the equilibration was elongated from 2 to 10 ns, followed by 50 ns of biased MD with torsional restraints on Leu277 (position 9') before unbiased production.

**PERFORMANCES OF UNBIASED MD SIMULATIONS** Production runs of the  $\sim 200,000$  atoms systems were executed on Haswell CPUs (E5 2690 V3) at a rate of  $\sim 25 \text{ ns day}^{-1}$  using 504 CPU-cores. For a total of  $\sim 1.2 \mu\text{s}$  of cumulated simulations using  $\sim 600,000$  CPU-hours.

**COMPUTATIONAL ELECTROPHYSIOLOGY SETUP** Three protein structures, i.e., the *wide-open* and *semi-open* cryo-EM reconstructions and a representative structure of the *MD-open* state, were analyzed. The *MD-open* representative structure state was selected as the snapshot in the original unbiased-MD with the lowest Root-Mean-Square Deviation (RMSD) to the average *MD-open* model; see below the structural average of the *MD-open* model. To control the robustness of our results, we produced a second model of the *MD-open* state called *MD-open2*. This second model corresponds to the centroid of the cluster formed by the snapshots in the original unbiased-MD with a pore radius between 2.4 and  $2.5 \text{ \AA}$ , in order to cover the most frequently sampled pore radius.

To perform the sampling of permeation events in all-atom MD the same system setup presented above was used with a few modifications to improve the efficiency of the calculations (see Figure 3.3). First, the ECD of the protein was removed, which reduced the system size to approximately one half. Second, one of the following set of positional restraints were applied to preserve the structure of the TMD during the production runs: (i) Light restrains applied

on the protein backbone with force constant of  $1 \text{ kcal mol}^{-1} \text{ \AA}^{-2}$ , (ii.) Heavy restraints with  $40 \text{ kcal mol}^{-1} \text{ \AA}^{-2}$  on the protein backbone and  $1 \text{ kcal mol}^{-1} \text{ \AA}^{-2}$  on the heavy-atoms, or (iii.) Fixed with the same restraints as Heavy but with the heavy atoms of the P266 fixed.

In comparison to our previous equilibration protocol, the restraints are kept constant during the 2 ns-long MD simulation.

Production runs were performed in the NVT ensemble in the presence of a physiological NaCl concentration of 145 mM and a constant electric field perpendicular to the membrane,  $E_z$ . The introduction of an electric field generates a membrane potential  $V_m$  (Roux 2008) that increases the permeation probability on the simulation timescale. In this setup,  $E_z$  is applied to all atoms along the Z component and is related to the membrane potential as:

$$E_z = V_m/L_z \quad (3.1)$$

Where  $L_z$  is the size of the simulation box in the Z direction. The electric field was introduced using the External Electric Field module in NAMD. The value of  $E_z$  was set to generate a membrane potential of 150 or 250 mV.

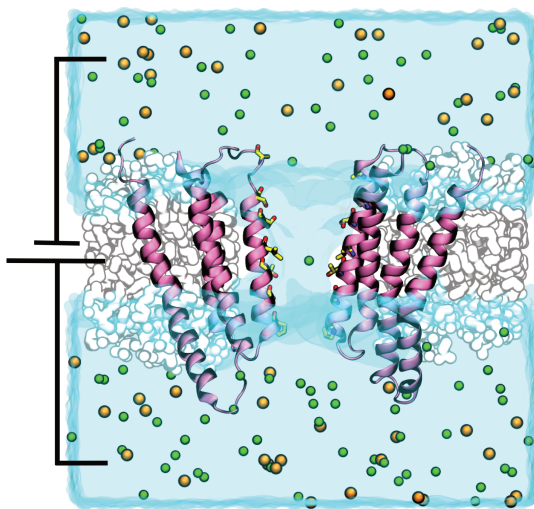


Figure 3.3 – The *MD-open* state devoid of the ECD and embedded in a POPC bilayer with an explicit treatment of the water and 145 mM ionic concentration (sodium in orange and chloride in green) is shown. The removal of the ECD reduces the size of the system to approximately one half; confront  $\sim 95,000$  (reduced) with  $\sim 200,000$  (original) atoms. This system is the one used in addition to the external electric field to represent a membrane potential of 150 and 250 mV.

**ESTIMATION OF THE CURRENTS** Estimates of the anionic and cationic currents per simulation were obtained by counting the number of anions or cations permeating the pore per nanosecond using the FLUX module in Wordom (Seeber et al. 2007; Seeber et al. 2011). The total current  $I$  is computed from the summation of permeation events within triplicate simulations for each setup (structure/restraints/voltage). Currents are given  $\pm$  the error  $\sigma$  assuming a Poisson distribution of the permeation events such that  $\sigma = I/\sqrt{N}$  with  $N$  the number of

events (Sotomayor et al. 2007). The conductance  $g$  is computed as  $g = I/V_m$  with  $V_m$  the applied voltage.

Channel selectivity, i.e., the probability of chloride versus sodium permeation, was calculated from the current ratio (i.e., anionic over cationic) in simulations where the NaCl concentration was increased to 1 M in order to increase the permeation probability.

To quantify the effect of the water model, an alternative system of the *wide-open* conformations was build using TIP4P/2005 water molecules (Abascal and Vega 2005).

The summary of simulations setup and data collection is available in Table 3.1, Table 3.2 in Appendix B.2.

**PERFORMANCES OF THE COMPUTATIONAL ELECTROPHYSIOLOGY SETUP** All the simulations of the reduced-system in the presence of an electric field were carried out on the hybrid compute-node IBM S822LC (2× IBM POWER8 processors + 4× NVIDIA Tesla P100 GPU s). This architecture allowed us to reach  $\sim 50 \text{ ns day}^{-1} \text{ node}^{-1}$  with the NAMD 2.13 version, for a total of  $\sim 5.5 \mu\text{s}$  of cumulated simulations using 2,640 GPU-node-hours. Similar performances were reached on Intel CPUs + 4× NVIDIA GTX 1080ti.

**POLYATOMIC ANION PERMEABILITY** To measure the permeability to polyatomic anions of the *wide-open* and *MD-open* structures, we used the same simulation setup as presented above. Only the Heavy-restrains were applied to both structures, the ionic concentration was increased to 1 M and the equilibrated  $\text{Cl}^-$  ions replaced by one of the polyatomic anions, see Figure 3.4. As for IVM, CGenFF parameters for the polyatomic anions (formate, bicarbonate, acetate, phosphate, methanesulfonate, isethionate, propionate) were generated using the PARACHEM website. The applied membrane voltage  $V_m$  is 150 and 250 mV for the *wide-open* and *MD-open* structure, respectively.

The permeability is computed as a ratio between the number of permeation events per ns of polyatomic anions  $X^-$  and  $\text{Cl}^-$ .

Details on the number of permeation events per anion and per structure are given in Appendix B.2, page 119.

Similarly, simulations were carried out on the IBM S822LC compute nodes, for a total of  $\sim 2.6 \mu\text{s}$  cumulated simulations using 1,248 GPU-node-hours.

**HOLE ANALYSIS** The configuration of the ion pore in anionic pLGICs available from X-ray, cryo-EM, and MD simulations was compared using the program HOLE (O. S. Smart et al. 1996). The following structures were analyzed: (i.) the GlyR $\alpha$ 1 in complex with strychnine (PDB:3JAD) or glycine with (PDB:3JAF) and without (PDB:3JAE) ivermectin; (ii.) the GlyR $\alpha$ 3 in complex with strychnine (PDB:5CFB) or glycine and the allosteric potentiator AM-3607 with (PDB:5VDH) and without (PDB:5TIO) ivermectin; (iii.) the GluCl in complex with glutamate and ivermectin (PDB:3RIF) or with ivermectin only (PDB:3RHW); and (iv.) the GABA $_A$ R in complex with the agonist benzamidine (PDB:4COF). All these structures were aligned using PyMol (Schrödinger 2015) and their hydrogens generated by the same software. The HOLE profiles were produced using an efficient implementation in the program Wordom

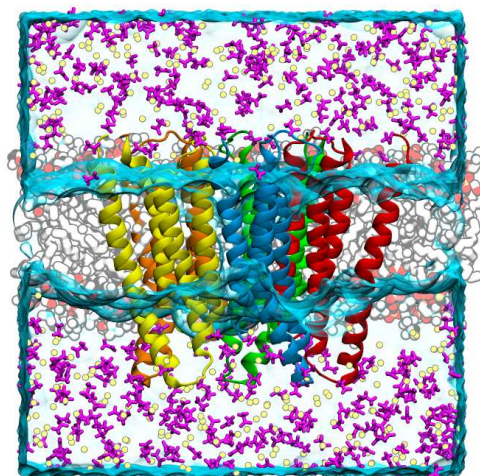


Figure 3.4 – Snapshot of the simulation box corresponding to the *reduced* system. The *MD-open* state devoid of the ECD and embedded in a POPC bilayer with 1 M ionic concentration (sodium in yellow and the polyatomic anion, here acetate, in magenta) is shown. This system is the one used in addition to the external electric field to estimate the conductance or probe the permeability of the ion channel to polyatomic anions.

(Seeber et al. 2007; Seeber et al. 2011) with incremental steps of  $0.1 \text{ \AA}$ . Average HOLE profiles per cluster were computed with Numpy (Jones et al. 2001) in a Python script. The mean value was calculated for each value of  $Z \pm$  the standard deviation.

**STRUCTURAL AVERAGE OF THE *md-open* MODEL** To illustrate the *MD-open* state, two structural models were built from averaging structures over the MD trajectory. The first model (*MD-open*) was produced by averaging over a series of consecutive snapshots taken from a 10 ns stretch of the *wide-open* simulation after re-opening, i.e., the local rearrangement of the TMD sampled at 200 ns. The second model (*MD-open-sym*) was obtained from the *MD-open* structure by overlapping all subunits and computing an average. This average subunit was then superimposed to the individual subunits in the original structure to obtain a symmetric model. Trajectory manipulation and structural averaging were carried out using the software Wordom.

**WATER DENSITY INSIDE THE PORE OF GLYR** According to Trick et al. 2016, one could compute free-energy profiles from water molecule distribution in MD simulation at equilibrium. For that purpose, we first computed the water density by extracting water molecule positions within a cylinder centered on the pore using MDanalysis (Gowers et al. 2016; Michaud-Agrawal et al. 2011). Then, we converted the positions into a density using the histogram

function of Numpy. Finally, the water density is converted into a free-energy profile using the Boltzmann relation between free-energy and probability of being at a certain position:

$$P_z = 1/Z e^{(-F_z/(k_b T))} \quad (3.2)$$

With  $P_z$  the probability of being at a given position  $z$ ,  $Z$  the partition function,  $F_z$  the free-energy at that position,  $k_b$  the Boltzmann constant and  $T$  the temperature. Since the probability is proportional to  $n_z$ , the density of water molecule at a certain position we obtain:

$$E_z = -k_b T \ln(n_z) + k_b T \ln(C) \quad (3.3)$$

With  $C$ , an arbitrary constant chosen by requiring the value of the free-energy being zero at the extremities of the profile. The whole computations were done within a Python script by analyzing MD trajectories of 50 ns. For all structures, positional restrains on the backbone and heavy-atoms were applied in order to prevent structural modification of the pore profile during the simulations timescale.

### 3.3 RESULTS AND DISCUSSION

#### 3.3.1 Structural stability of the ion channels

The first property that we investigated is the stability of the cryo-EM structures of the GlyR $\alpha$ 1 in all-atom MD with an explicit treatment of the solvent and the membrane environment. We chose to simulate the GlyR embedded in a more physiological environment composed of a bilayer of phospholipids POPC when the cryo-EM structures were captured after solubilization in detergent. In a first attempt, we used the *standard* 2 ns equilibration followed by 50 and 250 ns of unbiased MD for the *wide-open* and *MD-open* structure, respectively.

**GLOBAL OBSERVABLES OF THE STRUCTURES** By looking at the global observable such as twisting and blooming angles such as defined by Martin and coworkers (Martin et al. 2017), we can observe an increase of the twist angle in both simulations in respect to the cryo-EM structures. This increase is particularly marked for the *wide-open* conformation. However, the blooming angle remains constant for both conformation and close to their initial value. Of note, the twisting and blooming angles observed in both *wide-open* and *semi-open* simulations (see Figure 3.5) are consistent with the ones measured in simulations of GluCl bound to L-glutamate and IVM (Martin et al. 2017).

So far, and based on global observable we cannot distinguish between the structural dynamics of both GlyR conformations, and they are both compatible with conformations of other pLGICs that are supposed to be in an active state.

**CHARACTERIZATION OF THE ION PORE GEOMETRY** The more *stringent* characterization of an open state is of course the observation its *open* pore. As mentioned previously, the first structural clues of an *open* pore come from its geometry. For that reason, we will now pay

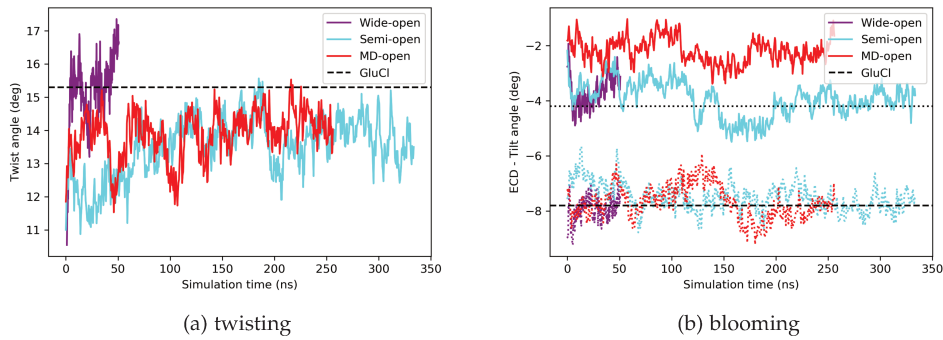


Figure 3.5 – Twisting and blooming angle in GlyR. Concerning the blooming angles, the continuous lines correspond to polar angle and the dotted lines to azimuthal angle. GluCl values come from Martin et al. 2017.

attention to the organization of the  $M_2$  helices forming the ion pore and the actual geometry of this pore.

Concerning the orientation of the  $M_2$  helices defined by Calimet and coworkers (see Figure 3.6), the *semi-open* original structure is highly similar to GluCl and GLIC active-like conformations, and the values of the azimuthal and polar tilt remain overall constant during the simulations (see Figure 3.6).

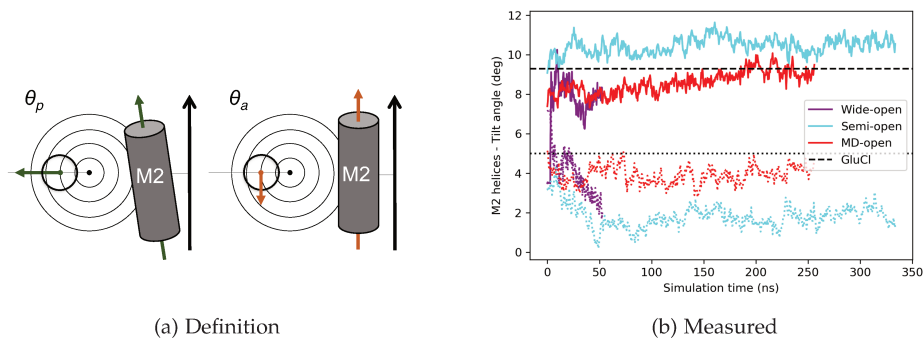


Figure 3.6 – (a) Polar and azimuthal tilt of the  $M_2$  helices in respect to the center of the ion pore. Adapted from Calimet et al. 2013. (b) Continuous lines correspond to polar angle and the dotted lines to azimuthal angle. GluCl values come from Martin et al. 2017.

On the contrary, the *wide-open* structure was captured in a unique organization of the  $M_2$  helices and subsequently, of the ion pore, in respect to other members of the pLGIC family. Overall, the values of the azimuthal and polar tilt of the  $M_2$  helices are interverted in comparison to the *semi-open* and the other active-like structures. This particular orientation of the  $M_2$  helices in the *wide-open* structure is responsible for the unprecedented wide pore. However, the original orientation of the  $M_2$  helices found in the *wide-open* structure is not stable at all in our MD simulation and interconverts immediately with the orientation of the

*semi-open* structure (see Figure 3.6). We will next see the impact of this change in orientation on the radius of the pore.

The results in Figure 3.7 show that upon removal of the positional restraints on heavy-atoms during the 2 ns-long equilibration phase, both ion pores collapse at the bottom of  $M_2$  helices (i.e., the  $-2'$  position). The collapsing is already observed during the minimization of the *semi-open* structure which minimum pore radius (i.e., the radius at the constriction point) decreased from 2.38 Å to 2.09 Å. These results demonstrate that both GlyR $\alpha$ 1 *open*-like structures are unstable in unbiased MD. Worst, both ion pores remain on average too tight to accommodate the passage of a chloride anion (see Figure 3.7). For that reason, both simulations led to physically *closed* ion pores.

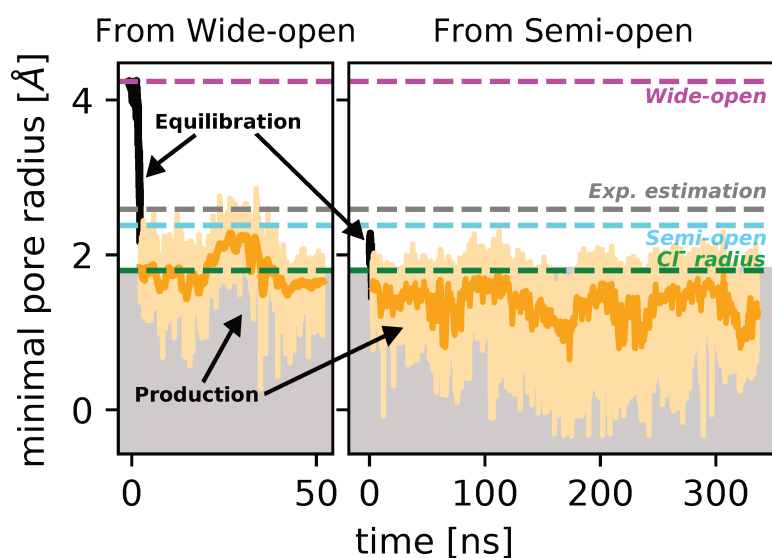


Figure 3.7 – Pore collapse of the *wide-open* and *semi-open* structures of GlyR $\alpha$ 1 in explicit solvent/membrane MD. The time series of the pore radius at position  $-2'$  is shown for the *wide-open* (left) and the *semi-open* (right) structures. Corresponding values measured in the cryo-EM reconstructions (3JAE for *wide-open*, and 3JAF for *semi-open*), the experimental estimate of the pore size (Rundström et al. 1994), and the ionic radius of chloride (Nightingale 1959) are indicated by dashed lines. From Cerdan et al. 2018.

To test the robustness of this finding, we used simulation repeats with different initial conditions such as initial velocities, protonation states, or harmonic restraints on the residues forming the  $M_2$  helices. However, none of the tested conditions, nor protocols were able to stabilize, even marginally, the ion pores close to their initial geometries (see Figure 3.8).

**CHASING THE OPEN PORE** In order to find the appropriate way to stabilize of the GlyR $\alpha$ 1 open pore, we focused on the *wide-open* structure because its initial wideness was more promising in comparison to the *semi-open* structure which already lost  $\sim 13\%$  of its radius after the energy-minimization. Additionally, the stabilization of this new orientation of the pore-lining helices would be of extremely valuable to assert on its physiological relevance.

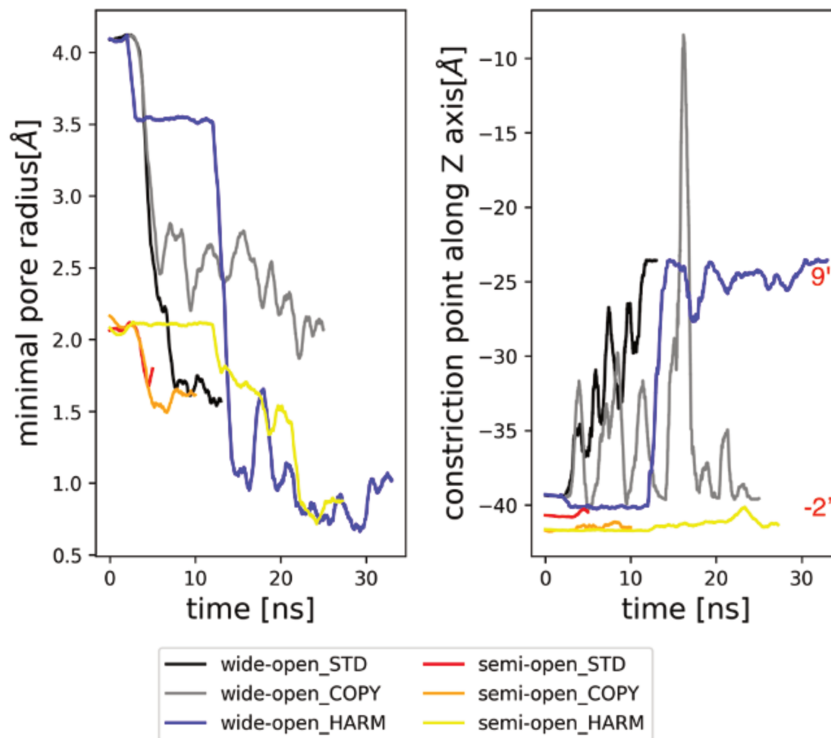


Figure 3.8 – The configuration of the pore captured by the *wide-open* and *semi-open* structures is unstable in explicit solvent/membrane MD independently of the simulation conditions. The time series of the pore radius (left) and the position of the constriction point (right) are shown for three independent runs per structure. Simulation repeats started with different initial velocities (COPY), a standard protonation state of the titrating residues (STD), or gently equilibrated (10 ns) in the presence of harmonic restraints on the pore-lining helices (HARM) consistently exhibit fast pore collapsing. Interestingly, the analysis on the right shows that the ion pore shuts at the position 9' (resting gate) when starting with the *wide-open* structure, whereas it shuts at the position -2' (desensitization gate (Gielen and Corringer 2018)) when starting with the *semi-open* structure. The position of residues at -2' and 9' are indicated in red. From Cerdan et al. 2018.

To obtain a stable open pore we incorporated knowledge from the previous failure, and the literature. During the previous simulations of the *wide-open* conformation, we systematically observed an important loss of symmetry in the M<sub>2</sub> helices position and orientation during the massive reorganization that happens after the constraints removal. For that reason, we introduced a symmetry restrains on the pentameric organization during the equilibration. Also, and following the observations from Yuan and coworkers (Yuan et al. 2016), we introduced torsional restrains on the  $\chi_1$  angles of L277 at the position 9' in order to keep these hydrophobic side-chains away from the pore lumen. Both these restrains were applied during an elongated (10 ns) equilibration. Next, the torsional restrains remained applied for the following 50 ns. Lastly, all restrains were removed, and the system was simulated for 300 ns of unbiased MD.

The results from this *gentle* equilibration protocol are displayed in Figure 3.9.A and indicate that although the collapsing is slower (black line), still the simulation converges toward a *closed*-like ion pore (orange line) which is non-permeable to chloride anymore. However, about 200 ns after the end of the equilibration, the simulation captured a spontaneous transition toward a wider *open*-like pore configuration (blue line). This *re-opening* is stable for more than 100 ns and correspond to a conformation compatible with the *semi-open* cryo-EM structure, with a constriction point located at the -2' level which is  $\sim 2.4$  Å in radius.

Visual inspection of the MD-trajectory revealed that the spontaneous transition responsible for the *re-opening* corresponds to the outward tilt of one the M<sub>2</sub> helices that was still in a *wide-open*-like orientation. Subsequently, the helix tilting permits to its attached bulky P266 (-2' residue) to move inward and to form back a circle with the other prolines (see Figure 3.9.B). Overall, the newly adopted configuration of the M<sub>2</sub> helices corresponds to an almost symmetric one, which is similar to the organization in the *semi-open* structure. Strikingly, at 240 ns, i.e., 40 ns after the reorganization responsible for a widening of the pore, a chloride anion spontaneously permeated through the TMD (see Figure 3.9.C). Although anecdotal at this point, this permeation event is still an important observation because it probes the ion pore permeability to chloride. Based on the stability in MD and the ion-permeability of this conformation we chose to named it *MD-open* throughout the text.

Importantly, the relevance of the *MD-open* conformation is supported by a simulation repeat using the same relaxation protocol which leads to *MD-open*-replica (see Figure 3.10). This simulation replica captured independently a pore configuration that is equally wide and stable as the initially captured *MD-open* structure. In opposition to the initial simulation, *MD-open*-replica could be characterized immediately at the end of the relaxation, i.e., 60 ns after the beginning of the simulation. Additionally, *MD-open*-replica did not host spontaneous chloride permeation during the 200 ns of unbiased MD. However, the similitudes in geometry are striking within the two *MD-open* configurations, with similar pore radius ( $\pm 0.1$  Å), see Figure 3.10. Interestingly, although the hole profiles (see Figure 3.10.B) are equivalent, the local arrangements of the P266 at the level of the constriction point in -2' are slightly different, highlighting both local asymmetry and flexibility of the gate.

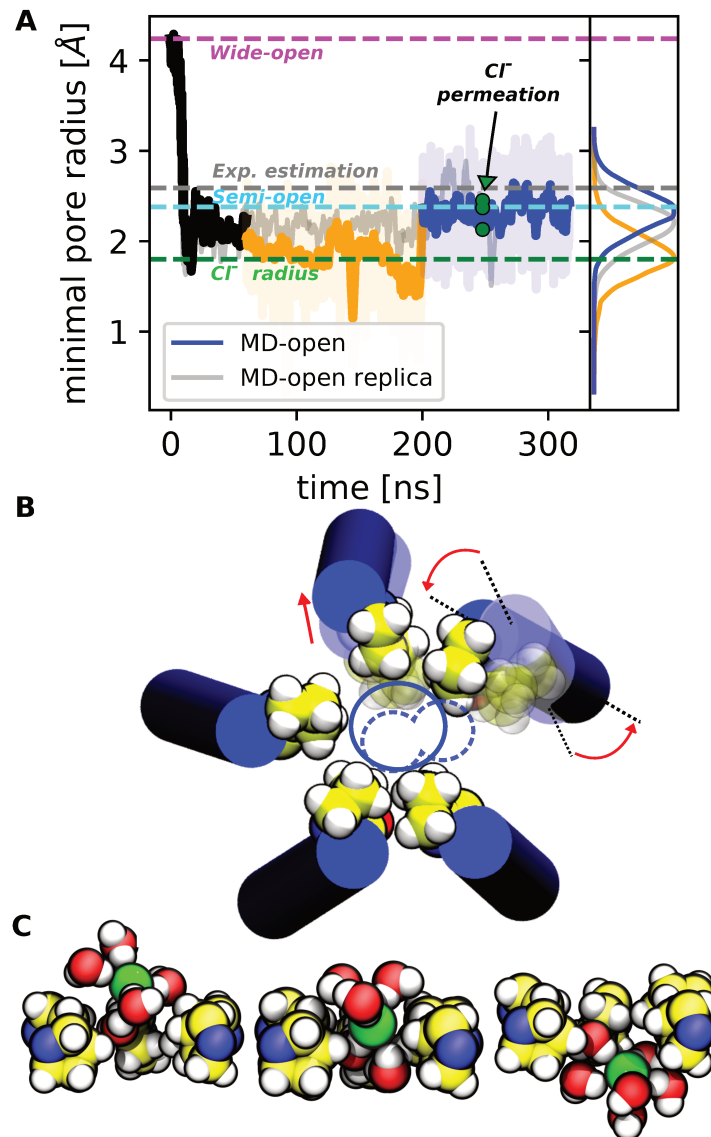


Figure 3.9 – The spontaneous transition to a structurally stable and chloride permeable open state captured by MD. (A) The time series of the pore radius at position  $-2'$  is shown along the simulation of the *wide-open* structure equilibrated with symmetry restraints. The color code is the same as in Figure 3.7. Strikingly, after 200 ns the simulation captures a spontaneous transition to an open pore configuration (*MD-open*) that is stable over  $> 100$  ns (blue line), it is significantly more open (confront orange and blue statistical distributions), and it is permeable to chloride (green dots). The simulation repeat at the end of the gentle equilibration captured the same open-pore configuration that is stable over  $> 150$  ns (grey line). (B) Structural rearrangement of the pore-lining helices to the *MD-open* structure. The outward tilting of the last  $M_2$  helix results in the inward displacement of proline 266 at position  $-2'$ , which results in a more globally symmetric orientation of the  $M_2$  helices, but in a locally asymmetric and chloride-permeable  $-2'$  gate. Overall, the *MD-open* state is structurally similar to the *semi-open* structure; see Table 3.4. (C) The anisotropic organization of the first hydration shell around chloride during its spontaneous translocation at the constriction point (P266). From Cerdan et al. 2018.

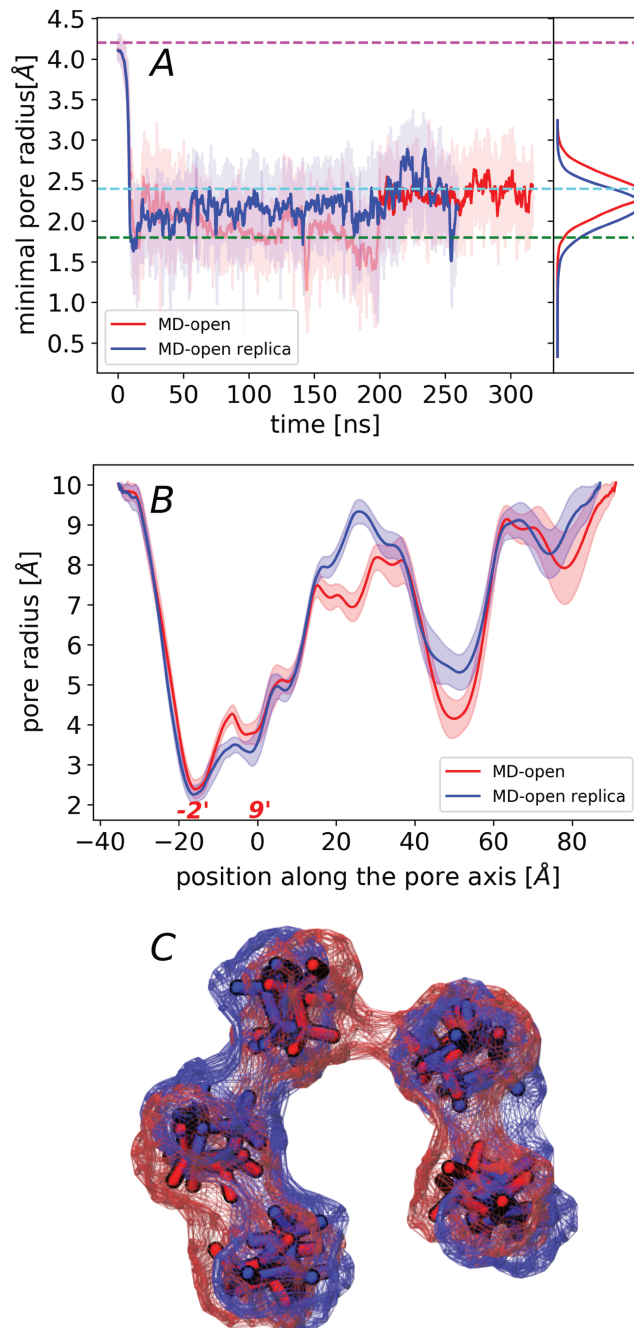


Figure 3.10 – The spontaneous transition to a structurally stable and chloride permeable open state captured by MD and its replica. (A) The time series of the pore radius at position  $-2'$  is shown along the simulation of the *wide-open* structure equilibrated with symmetry restraints. The color code is the same as in Figure 3.7. The replica remained directly open at the end of the *gentle* relaxation from the *wide-open* and is stable for at least 200 ns. (B) Hole profiles for the *MD-open* state and its replica. The solid line corresponds to the average value after 200 ns (pore re-opening) in *MD-open* and after 60 ns (beginning of the unbiased simulation) in *MD-open* replica; in transparent  $\pm$  the standard deviation. (C) Comparison of the P266 at the gate in  $-2'$ . The surface was computed with a probe of 1.4 Å. Both structures are captured in a similarly open conformation with an asymmetry in the organization of the residues that lowered the hydrophobicity and allows the permeation of anions. From Cerdan et al. 2018.

COMPARISON OF *md-open* AND *semi-open* Previously we mentioned that the global organization in the  $M_2$  helices in *MD-open* (and *MD-open-replica*) are quite similar, *in average*, to the one found in *semi-open*. However, a unique feature of the *MD-open* configuration is the local structural asymmetry of the pore at the level of P266 forming the constriction point. This feature is observed in both replica and is possibly responsible for the stability of the pore in comparison to the perfectly symmetric *semi-open* structure. The local asymmetry of such bulky residues prevents an optimal packing that is observed in the *semi-open* structure simulation, right after the energy-minimization. Overall, it is reasonable to think that the quaternary transition (twisting motion) responsible for the change in the orientation of the five  $M_2$  helices from the resting to the active state may lead to some asynchronicity in the inward motion in P266, and then to a local asymmetry from non-optimal packing.

From a functional point of view, we can also find interesting differences between the *MD-open* and *semi-open* organization of the  $-2'$  residues. The non-optimal packing is also responsible for an increase of the water accessibility or *wetting* of the ion pore with a minimal variation of its geometric radius. To quantify that observation we used the methodology proposed by Trick et al. 2016 to estimate the free-energy barrier for water permeation based on the water probability distribution along the pore. The robustness of our implementation of the method was tested on the three cryo-EM structures of the GlyR $\alpha$ 1, and we found results in perfect quantitative agreement with the original authors of the method (see Appendix C.1).

Our analysis shows that upon similarity in HOLE profile of *MD-open* and *semi-open* cryo-EM structures, the MD-relaxed conformation has a free-energy barrier for water that is  $\sim 3.5$  kJ mol $^{-1}$  lower in respect to the *semi-open* structure (see Figure 3.11). This result demonstrates that symmetric organization of the pore, although equivalent in radius, is less permeable to water, and arguably to anions. In fact, because of the stability and permeability of the local asymmetry captured in both *MD-open* configuration, we could hypothesize on the functional relevance of such feature in comparison to the fully symmetric organization that exists in the *semi-open* structure. Of note, it is clear that such free-energy profiles for water permeability along a pore is helpful to compare the effect of pore-lining residue organization, but it is impossible to conclude on the physiological relevance of multiple *open* states, since the quantity measured cannot be compared to experimental data.

Lastly, analysis of the chloride permeation event (see Figure 3.9) indicates that the number of water molecules forming the first hydration shell around the anion remained globally constant during the crossing of the constriction point. However, the hydration shell adopts an anisotropic dumbbell shape around the anion during the translocation which might be assisted by the asymmetric organization of the P266 residues. The observation of this spontaneous event would suggest that ion translocation in the pore of GlyR $\alpha$ 1 can happen even if the constriction is as narrow as 2.4 Å in average. In conclusion, an ion pore radius larger than 3.3 Å, corresponding to the fully hydrated chloride (Nightingale 1959), is not strictly required to permit ion permeation in GlyR $\alpha$ 1.

To summarize, we showed that none of the GlyR $\alpha$ 1 cryo-EM structures are stable in all-atom MD simulation, but a *gentle* relaxation from the *wide-open* structure may capture a transition toward a stable *MD-open* conformation. This newly characterized conformation is

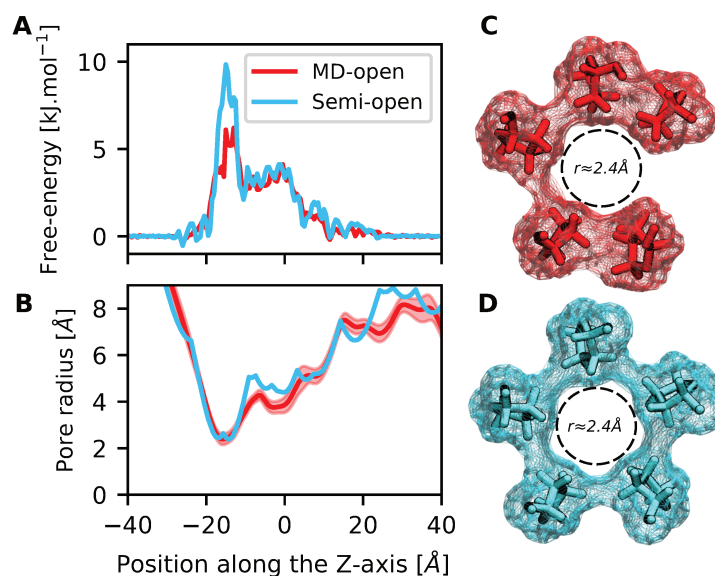


Figure 3.11 – Comparison of the free-energy profiles for water permeation in the GlyR $\alpha$ 1 structures. Free-energy profiles for water permeation based on Boltzmann inversion of the water density sampled by the molecular dynamics (Trick et al. 2016). Simulated trajectories of 50 ns were analyzed to compute the water density within the pore. (A) *semi-open* and *MD-open* (both with high harmonic restraints on the position of the heavy atoms). At the level of the constriction point (i.e.,  $-2'$  position), the energetic barrier is reduced by  $\sim 3.5 \text{ kJ mol}^{-1}$  from *semi-open* to *MD-open*. (B) Comparison of the HOLE profiles obtained for *semi-open* (cyan) versus *MD-open* (red). Unlike the free-energy profiles for water permeation, the HOLE profiles are strikingly similar. (C) and (D) provide representations of the  $-2'$  residues (P266) with the corresponding surfaces computed with a probe size of  $1.4 \text{ \AA}$  in *MD-open* and *semi-open*, respectively. The asymmetric arrangement of the prolines in the *MD-open* state allows water molecules to sneak through adjacent residues. Overall, these structures highlight the importance of the local asymmetry of the P266 residues to modulate the hydrophobicity of the pore at the  $-2'$  gate. From Cerdan et al. 2018.

more similar to the *semi-open* structure but displayed a local asymmetry in the P266 positions. This asymmetry might be the cause of the relative stability of the *MD-open* conformation in comparison to the *semi-open* structure and was shown to facilitate the water permeation through the pore. In the next section, we will explore in depth the ionic permeability of the three GlyR $\alpha$ 1 structures, i.e., *wide-open*, *semi-open* and *MD-open*.

### 3.3.2 Permeability to Chloride anions and conductance

The function of pLGICs is to open an ion pore in response to neurotransmitter binding. An open ion pore can be probed experimentally using electrophysiology, and in particular single-channel setup. The main properties that one can measure in single-channel electrophysiology are the conductance and the anion/cation selectivity. Such properties are related to the unitary current measured through a particular ion pore at a given voltage. For that reason, we designed computational electrophysiology experiments to compare the conductance and ionic selectivity of the three GlyR $\alpha$ 1 *open* structures with data present in the literature (Bormann et al. 1993; Keramidis et al. 2002).

Due to the instability of the *wide-open* and *semi-open* structures in MD simulation we chose to apply harmonic restraints on the atomic position of the backbone heavy-atoms (see *Methods* for more details). For the sake of comparison, the same had to be applied to the *MD-open* structures. Since all tested structures were already harmonically restrained we took the opportunity to devoid the GlyR from its ECD in order to reduce by half the size of the simulation cell and subsequently, double the performances of our simulations (see Figure 3.3 for setup representation). Lastly, we applied a constant electric field to represent the membrane voltage (Roux et al. 2004). In our *in silico* experiments we estimated the conductance as the ration between the current, i.e., the number of ion permeation over a unit of time, and the membrane voltage.

The experiments we compare to were conducted by Bormann and coworkers (Bormann et al. 1993) in single-channel outside-out patch-clamp with 145 mM NaCl. *By design* we incorporated some deviations with the original experiments. First, the receptors are devoid from its ECD and ICD in our simulations. However, experiments have shown that the characteristic ( $\sim 86$  pS) conductance of GlyR $\alpha$ 1 is preserved even if the ICD is removed (Duret et al. 2011; Moroni et al. 2011a) or if the ECD is changed for the of GLIC (Duret et al. 2011) which conductance is only few pS. Second, harmonic restraints on some atoms position had to be introduced for the previously mentioned reason. Although, it is difficult to infer on the impact of such approximation we tried to account for it by running simulations with multiple degrees of restraints, and to control their effect on the ion pore flexibility (see Appendix B.1). Third, the membrane voltage we can afford to apply to have a sufficient sampling of permeation events during our simulation time is double (150 mV) in comparison to the range of voltage tested experimentally ( $\pm 80$  mV). However, the GlyR $\alpha$ 1 is not known to rectify, i.e., change in conductance in function of the voltage (Raltschev et al. 2016)) and our simulations in the range [150 : 250 mV] show a linear evolution of the measured current, and then a constant conductance, i.e., no rectification (see Appendix B.2). Altogether, this evidence

supports the idea that results obtained from our *in silico* setup should be comparable with experimental data obtained on GlyR $\alpha$ 1.

We collected statistics of hundreds of ion permeation in triplicate simulations at physiologically relevant conditions, i.e, membrane voltage of 150 mV and symmetric 145 mM NaCl concentration, to converge on the conductance and selectivity of the three tested structures (see Table 3.1, Table 3.2, and Appendix B.2 for details).

Structure	Permeation Events	Current (pA)	Conductance (pS)	Selectivity ( $P_{Cl^-} / P_{Na^+}$ )
<i>wide-open</i>	128	$62.0 \pm 0.8$	413	18
<i>semi-open</i>	0	0	N.D.	N.D.
<i>MD-open</i>	31	$3.5 \pm 0.6$	23	N.D.
<i>MD-open2</i>	17	$2.9 \pm 0.7$	19	N.D.

Table 3.1 – Computational electrophysiology for three open structures of GlyR $\alpha$ 1. The numerical results were obtained from all-atom MD of the TMD applying a membrane potential of 150 mV and a symmetrical 145 mM concentration of NaCl. Currents were computed by counting the number of ions permeating the pore over a period of time. Uncertainties were estimated assuming a Poisson distribution of the permeation events such that  $\sigma = I/\sqrt{N}$  with I the current and N the number of events (Sotomayor et al. 2007)). Ion conductance was estimated as the current over the membrane potential. The selectivity was measured from the non-directional permeation probability of  $Cl^-$  versus  $Na^+$  in simulations at 150 or 250 mV and 1 M concentrations to increase the sampling of rare  $Na^+$  permeation events. The selectivity of the *MD-open* state was not determined as no permeant  $Na^+$  was observed on the simulation time scale. Simulations details are available in Appendix B.2 and Table 3.2.

Structure	Voltage (mV)	Duration (ns)	Number of $Cl^-$ permeation	Number of $Na^+$ permeation	Selectivity ( $P_{Cl^-} / P_{Na^+}$ )
<i>wide-open</i>	150	162	109	6	18.6
<i>MD-open</i>	250	118	15	0	N.D.

Table 3.2 – Selectivity at 1 M NaCl concentration measured by computational electrophysiology of GlyR $\alpha$ 1. The selectivity is estimated by the permeability ratio between  $Cl^-$  and  $Na^+$ . Simulations were carried out at 1 M concentration because no  $Na^+$  permeation events were captured during simulations at 145 mM.

Our *in silico* electrophysiology experiments permit to measured conductance of 413 pS for the *wide-open*, 23 pS for *MD-open*, and no current for the *semi-open* structure. In comparison to the  $\sim 86$  pS measured experimentally for the main open state of the GlyR $\alpha$ 1, none of the tested structure was able to reproduce the physiological behavior of the main conductive state accurately. However not all the structures are equally wrong.

First, the *wide-open* is 5-fold more conductive than the most conductive state of GlyR $\alpha$ 1. In addition to this observation, we tried to take into account the effect of the water model. By using TIP4P/2005 instead of TIP3P the conductance decreased to 228 pS (see Appendix B.2), which is still 2.5-fold more conductive than experiments, although the TIPT4P/2005 model would tend to underestimate the diffusion coefficient of chloride (Patra and Karttunen 2004)

and the dielectric constant as well (Abascal and Vega 2005), which would altogether underestimate the conductance. Second, the *semi-open* structure is shown to be completely impermeable to chloride anion in physiological conditions. Since its constriction point tends to collapse, we tried a different level of restrains until we fixed the atomic position of the P266 into the original cryo-EM ones. Also, we repeated the simulation at a stronger 250 mV membrane voltage. In all cases, and for a total of near 2  $\mu$ s we observed no chloride permeation (see Appendix B.2). Of note, we investigated increasingly non-physiological membrane voltage for dozens of ns and observed chloride permeating through the pore of *semi-open* at 1 V. Third and last, the *MD-open* structure is permeable to chloride anions in physiological conditions, consistently with the spontaneous permeation observed during the unbiased MD. However, its conductance is three to four lower the value of 86 pS for the main conductive state of GlyR $\alpha$ 1. Additional analysis at 250 mV or using an alternative representative structure, i.e., *MD-open2* confirm the robustness of our observation (see Table 3.1 and Appendix B.2). Of note, the GlyR $\alpha$ 1 display experimentally a set of sub-conductive states, ranging from 18 to 86 pS, which seems to be a property of the M<sub>2</sub> helices sequence (Bormann et al. 1993). Nevertheless, it is not trivial to assign the *MD-open* conformation to a sub-conductive state, or a representative of the main conductive state which conductance would be reduced by the use of harmonic restrains, especially when we showed in Figure 3.8 and Figure 3.11 the functional relevance of the dynamical asymmetry.

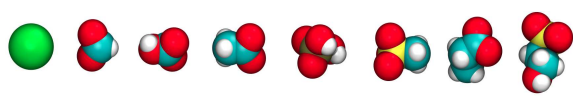
Strikingly, and despite the similarity in the ion pore conformation of *semi-open* and *MD-open* our analysis can discriminate between the two conformations. More importantly, the computational electrophysiology confirms the suggestion made by the water equilibrium profile (see Figure 3.11) that the local and dynamic asymmetry observed in *MD-open* is not only able to facilitate the *wetting* of the pore, but is also responsible for the ionic permeability. However, the computational electrophysiology experiment provides a clear answer to the permeable/impermeable annotation, and in which extend the structure are permeable in comparison to experiments when the water equilibrium profile was only able to rank the structure based on how *wet* they are. In summary, our experiment shows that the local organization of the residues at the  $-2'$  is critical for ion permeation in GlyR $\alpha$ 1 at the physiological condition, in qualitative agreement with mutagenesis study (D. J. S. Lee et al. 2003).

Concerning the ionic selectivity between anion and cation our results suggest that both *wide-open* and *MD-open* structures are highly selective for chloride over sodium in qualitative agreement with experiments (Keramidas et al. 2002) (see Table 3.2), although it is difficult to infer on the quantitative accuracy of our analysis due to the extremely low current expected from sodium, i.e., 25-fold smaller than current from chloride. Perhaps surprisingly, our results show that even the *wide-open* structure which is several folds too conductive preserved a strong selectivity for anion over cation, which indicates that the selectivity filter is not strongly correlated to the geometric radius at the  $-2'$  level.

The *semi-open* structure being non-permeable to chloride definitively excludes it definitively from the candidate of the representative structure of the GlyR $\alpha$ 1 active state. We will in the next section have an even more stringent test to compare the *wide-open* and *MD-open* structures to experiments using polyatomic anions.

## 3.3.3 Permeability to polyatomic anions and selectivity

In this section, we will investigate the permeability of GlyR $\alpha$ 1 *wide-open* and *MD-open* ion pore to a series polyatomic anions. Permeability to polyatomic ion was initially designed to probe the size of the constriction point (Bormann et al. 1987; D. J. S. Lee et al. 2003), which resulted in an estimation of  $\sim 2.6$  Å in radius for the GlyR $\alpha$ 1. However, and surprisingly, such data remained utterly unexploited (to the best of our knowledge) from a computational point of view to annotate the available structures. The series of anions available for GlyR $\alpha$ 1 includes three smaller ones (i.e., formate, bicarbonate, and acetate), which were shown to be permeable, and four larger ones (i.e., methanesulfonate, phosphate, propionate, and isethionate), which were shown to be non-permeable. A setup similar to the one used to compute the conductance was adapted to probe the permeability to polyatomic anions. For this purpose, a constant electric field was applied to represent a membrane voltage of 150 and 250 mV for the *wide-open* and *MD-open* structures, respectively. Additionally, the ionic concentration was increased to 1 M to enhance the probability of ion translocation, and the chloride anions were replaced by the polyatomic ones.



Anions	Wide-open	MD-open	Exp.
Chloride	1	1	1
Formate	0.65	1.39	0.33
Bicarbonate	0.37	0.17	0.11
Acetate	0.32	0.18	0.035
Phosphate	0.15	0	0
Methanesulfonate	0.38	0	0
Propionate	0.24	0	0
Isethionate	0.19	0	0

Figure 3.12 – Permeability ratio ( $P_{X^-/Cl^-}$ ) of polyatomic anions in the open structures of GlyR $\alpha$ 1. The permeability of seven polyatomic anions with increasing size (top) was investigated by all-atom MD of the *wide-open* and *MD-open* structures; see Figure 3.4 for an illustration of the simulation setup. For each anion, the permeability relative to chloride is given; relative permeability values were evaluated as the ratio between the polyatomic anion current (number of permeation events/ns) over the reference chloride current for each structure. Permeant ions are highlighted in green, the non-permeant ones in red. Experimental values were extracted from (Bormann et al. 1987; D. J. S. Lee et al. 2003). The simulations were carried out at 150 mV for the *wide-open* structure and 250 mV for *MD-open*. No permeation events were observed for the four largest anions in *MD-open* up to 1 V. Details on the number of permeation events per simulation are given in Table 3.3. From Cerdan et al. 2018.

Ion	<i>wide-open</i>	<i>MD-open</i>	<i>MD-open2</i>	<i>MD-open</i> Total
Chloride	109 (162)	25 (258)	16 (111)	41 (369)
Formate	44 (101)	20 (109)	8 (72)	28 (181)
Bicarbonate	23 (92)	2 (73)	2 (135)	4 (208)
Acetate	14 (66)	2 (113)	2 (86)	4 (199)
Phosphate	12 (116)	0 (100)	0 (74)	0 (174)
Methanesulfonate	16 (63)	0 (100)	0 (100)	0 (200)
Isethionate	6 (48)	0 (83)	0 (91)	0 (174)
Propionate	10 (62)	0 (66)	0 (86)	0 (152)

Table 3.3 – Permeations of polyatomic anions through the ion permeable structures of GlyR $\alpha$ 1. Number of permeation events in ( $\times$  ns) of all-atom MD simulation at 1 M ionic concentration and under a transmembrane potential of 150 and 250 mV for the *wide-open* and *MD-open* structures, respectively. In the case of the four largest anions the voltage was increased to 1 V for  $\sim$ 10 ns in triplicate simulations without enabling the permeability of *MD-open* to them. In total we sampled polyatomic anion permeations over 0.87 and 1.7  $\mu$ s for the *wide-open* and *MD-open*, respectively.

The results in Table 3.3 and Figure 3.12 show that the *wide-open* structure is permeable to the full range of anions, whereas the *MD-open* conformation is selectively permeable to the three smallest anions in qualitative agreement with the experiments (Bormann et al. 1987; D. J. S. Lee et al. 2003). Additionally, the *MD-open* structure remained selective for the smallest anions even when the membrane was raised to 1 V for a dozen ns, demonstrating the selectivity of this ion pore conformation. Although it is not clear why the *MD-open* structure is so permeable for formate and acetate relative to chloride, the qualitative agreement with the experiment is striking. Lastly, the lack of selectivity from the *wide-open* structure in our simulations strengthen the interrogations concerning its physiological relevance.

In summary, we showed that the *wide-open* structure is unable to selectively filter polyatomic anions based on their size, in contradiction to experiments, when the *MD-open* conformation displayed a qualitative agreement with the literature. Importantly, our analysis is based on permeation ratios (similarly to the literature (Bormann et al. 1987; D. J. S. Lee et al. 2003)) which are likely to be more robust to systematic errors due to the force field, water model, and or simulation setup. For that reason, we believe that polyatomic ion permeability should be used more routinely for the functional annotation of an ion channel, especially when the experimental data are available for many ion channels.

### 3.3.4 A novel structural annotation of the anionic pLGICs

Our analysis allowed us to propose that none of the currently available cryo-EM structures of GlyR $\alpha$ 1 are *true* representation of the active state of that ion-channel; the *wide-open* conformation being up to five times too conductive and non-selective to polyatomic anions, and the *semi-open* being simply not permeable to chloride in physiological conditions. By contrast, the *MD-open* conformation was spontaneously captured from the *gentle* relaxation from the *wide-open* structure, is stable when embedded in a membrane environment, is ion-

conductive and selective to polyatomic anions in qualitative agreement with patch-clamp electrophysiology data. Based on these functional results obtained *in silico*, we conclude that the *MD-open* structure provides the closest representation to the physiologically active state of the GlyR $\alpha$ 1. Despite our radical conclusion of the *wide-open* and *semi-open* structures, we note that our results are consistent with the recent simulations made by Trick et al. 2016, or Gonzalez-Gutierrez et al. 2017. However, we went further than previous simulation analysis by demonstrating the non-permeability of the *semi-open* structure, and by attributing this property to the symmetrical organization of the P266 at the level of the constriction point. Moreover, we proposed a rather *simple* simulation setup to stringently discard the too wide ion pore of the *wide-open* structure.

The structural analysis of the *MD-open* conformation unveils that the TMD features an overall symmetric organization of the pore-lining M<sub>2</sub> helices in average, which is remarkably similar to the organization observed in the *semi-open* cryo-EM structure (RMSD = 0.8 Å). However, the two structure differ mainly by their local arrangement of the P266 residues forming the constriction point. The local asymmetry in the -2' level featured by the *MD-open* conformation and represented by a sub-optimal packing of these bulky side-chains are not only responsible for the stability of the ion pore but also its enhanced permeability in respect to the *semi-open* structure by reducing the hydrophobicity of the gate.

It is presently unclear if the fully symmetric organization of the pore in the *semi-open* structure is a structural biology artifact by averaging out of electron densities during the molecular reconstruction, or is physiologically relevant and consistent with fast desensitization, and would require further investigation. Perhaps surprisingly, *MD-open* and *semi-open* ECDs are even more similar (RMSD = 0.6 Å, see Table 3.4) than their TMD which would difficulty explain the difference in pharmacology observed between the active and desensitized state of the GlyR $\alpha$ 1. Additionally, since cation pLGIC feature charged or polar residues to form the constriction point at the bottom of the pore (Cymes and Grosman 2016; Sine et al. 2010), which are more likely to promote a symmetric local organization without impairing its *wetting*, we predict that a local asymmetry of the pore is likely to be functionally relevant in anionic pLGICs, where the gate in -2' is solely formed by hydrophobic side-chains.

TMD/ECD	<i>wide-open</i>	<i>semi-open</i>	<i>MD-open</i>	<i>MD-open-sym</i>
<i>wide-open</i>	/	1.3/0.3	2.1/1.0	1.5/0.6
<i>semi-open</i>	1.3/0.3	/	1.5/1.0	0.8/0.6
<i>MD-open</i>	2.1/1.0	1.5/1.0	/	1.3/0.8
<i>MD-open-sym</i>	1.5/0.6	0.8/0.6	1.3/0.6	/

Table 3.4 – Structural similarity of the *semi-open* and *MD-open* structures. RMSD (in Å) between backbone core atoms (see Appendix A.1) of the TMD and ECD for the open structures of GlyR $\alpha$ 1. All the ECD are very similar (RMSD < 1 Å). Globally, *semi-open* and *MD-open-sym* are almost identical with RMSD of 0.64 and 0.84 Å for the ECD and TMD, respectively.

The characterization of a structurally stable conformation and ion permeable ion pore at physiological conditions, i.e., *MD-open*, allows for an original functional interpretation of the anionic pLGICs structures. Despite the difference in permeability that was measured by com-

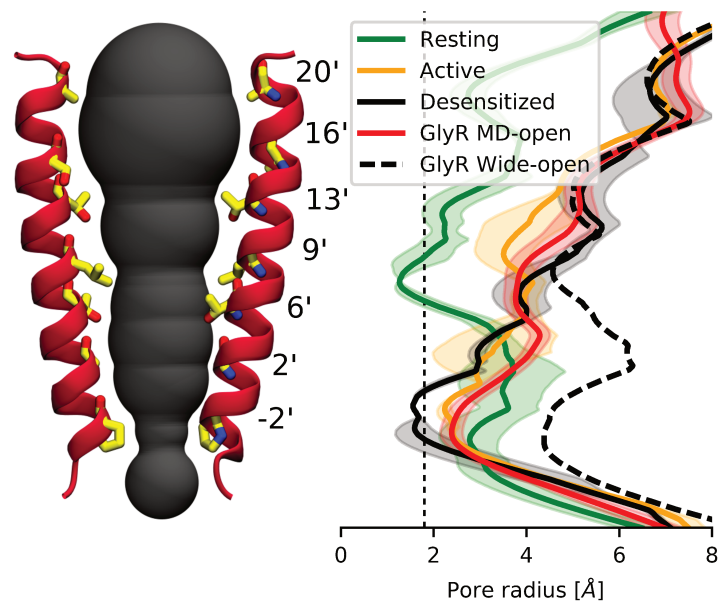


Figure 3.13 – Functional annotation of anionic pLGICs structures. On the left, the configuration of the open pore visualized by the *MD-open* state is shown. On the right, the HOLE profiles of currently available high-resolution structures of anionic pLGICs are compared to those obtained from the simulations of the *MD-open* (red) and the *wide-open* (black dashed) states. The vertical dashed line corresponds to the ionic radius of chloride. Based on this analysis and the simulation results on GlyR $\alpha$ 1 (i.e. MD stability, conductance, and polyatomic anion permeability), we conclude that there exist three structural clusters corresponding to: (i.) a closed-pore configuration at position 9' (resting); (ii.) a closed-pore configuration at position -2' (desensitized); and (iii.) an open-channel structure (active). The structures of GlyR $\alpha$ 1 and  $\alpha$ 3 in complex with strychnine, and GluCl-apo are consistent with the resting state. The structure of GlyR $\alpha$ 1 in complex with glycine and ivermectin and those of GluCl with L-glutamate and ivermectin bound or ivermectin alone visualize the active state. The structure of the GABA $\text{A}$ R in complex with benzamidine, and those of GlyR $\alpha$ 1 with glycine and AM-3607 bound or glycine, ivermectin and AM-3607 bound are desensitized channels. See Appendix D.1 for details. From Cerdan et al. 2018.

putational electrophysiology between the *semi-open* and *MD-open*, the striking structural similarity of these two conformations suggests that they are representative of the same functional state, i.e., the active state. This conclusion thus suggests that pLGICs ion-channels featuring the same arrangement of the  $M_2$  helices, i.e., GLIC at pH4 (Bocquet et al. 2009), GluCl with glutamate and ivermectin bound (Hibbs and Gouaux 2011), and GlyR with glycine and ivermectin bound (i.e., the *semi-open* structure) provide a reasonable model for the active state, which is likely to fail to capture the details controlling ion permeation, but might be accurate enough to explore the gating mechanism or for drug discovery purposes. Based on our analysis, where the *semi-open* and *MD-open* structures provide a reasonable model for the active state and the *wide-open* structure being a cryo-EM artifact, the comparative analysis of the experimental structures of anionic channels GlyR, GABA $_A$ R, and GluCl by HOLE reveals the existence of three major clusters, corresponding to the three functional states of pLGICs.

1. A *closed* ion pore conformation with a gate located in  $9'$ , consistent with the resting state.
  - a) GlyR $\alpha$ 1 bound to strychnine (Du et al. 2015)
  - b) GlyR $\alpha$ 3 bound to strychnine (Huang et al. 2015)
  - c) GluCl-apo (Althoff et al. 2014)
2. A *closed* ion pore conformation with a gate located in  $-2'$ , consistent with the desensitized state.
  - a) GlyR $\alpha$ 3 bound to glycine and AM-3607 (Huang et al. 2017b)
  - b) GlyR $\alpha$ 3 bound to glycine, AM-3607 and IVM (Huang et al. 2017a)
  - c) GABA $_A$ R bound to benzamidine (P. S. Miller and Aricescu 2014)
3. An *open* ion pore conformation corresponding to the active state.
  - a) GlyR $\alpha$ 1 bound to glycine and IVM (Du et al. 2015)
  - b) GluCl bound to IVM (Hibbs and Gouaux 2011)
  - c) GluCl bound to L-glutamate and IVM (Hibbs and Gouaux 2011)

Interestingly, this functional annotation supports the idea of dual gate (Gielen and Corringer 2018), which are located differently in the resting versus the desensitized state. Also, it suggests that pore-closing by desensitization versus *un-gating* (Martin et al. 2017), involve the polar reorientation of the pore-lining  $M_2$  helices in the opposite direction, i.e., a straighten for the *un-gating* versus a further tilting in the outward direction for the desensitization.

### 3.4 CONCLUSION

The synaptic transmission is notably mediated by pLGICs, which can interconvert between discrete states upon ligand-binding. Providing an atomistic description of the relevant functional states in physiological conditions is crucial to develop novel pharmaceutical strategies to cure brain disorders. With this work, we explored the structure of the GlyR $\alpha$ 1 physiological active state, and validate our findings by computational electrophysiology and polyatomic anion permeability simulations. We exemplified how this combination of simulation techniques

can be used as a tool for functional annotation of ion-channel, especially to compare multiple *open* ion pore conformation, which was not adequately tackled in the literature so far. In particular, we showed how MD could be used to identify and eventually correct structural artifact such as the *wide-open* conformation of GlyR $\alpha$ 1. The reason why a non-physiological structure was captured by cryo-EM is presently unclear, but the use of detergent for protein extraction and purification might be related to the problem. Of note, stabilization of artificially wide structures in detergent micelle was recently demonstrated in P2XR ion channel (Heymann et al. 2013; Habermacher et al. 2016). Additionally, the work of Aricescu and coworkers have recently shown that the use of detergent in cryo-EM resulted in structural artifact at the level of the M<sub>2</sub> helices in heteromeric GABA<sub>A</sub>R, which can be fixed by adding lipids (P. Miller et al. 2018). The striking lack of structural stability of the *wide-open* and *semi-open* conformations in our MD simulation supports the idea that reliable characterization of ion channels structure should be done experimentally in a native membrane environment, especially for the resolution of active state structures. Also, our results exemplify how MD simulation could/should be used *a posteriori* for structure/function assessment in ion channels.

In conclusion, the results presented here indicate that the synergic use of high-resolution structural biology experiments (cryo-EM and X-ray crystallography) with all-atom MD simulations, is a powerful tool to solve the gating mechanism and its allosteric regulation in pLGICs. Our protocol permits to identify a conformation of the GlyR $\alpha$ 1 compatible with the known functional properties of its active state and suggests that non-symmetric organization of the residues forming the gate is crucial for ion-permeation in physiological conditions by reducing the hydrophobicity of the pore with minimal variation of the pore radius. Since anionic pLGICs gates are mainly hydrophobic, and proline residues at the  $-2'$  position are vastly conserved, we hypothesized that this feature is also mandatory for ion permeation in other members of the anionic pLGICs family.

ELUCIDATION OF THE ION PERMEATION MECHANISM IN GLYCINE RECEPTOR

---

## 4.1 INTRODUCTION

In the previous chapter, we demonstrated the physiological relevance of the *MD-open* conformation to represent the active state of GlyR. This annotation is based on the overall stability of its ion pore in unbiased MD simulations and qualitative agreement with experiments concerning its conductance and selectivity to small poly-atomic anions. However, the in-silico electrophysiological experiments that we carried out were based only on the structure of the TMD. For that reason, we missed the potential impact of the flexibility of the ion pore, because we restrained the atomic positions after removing the ECD. Additionally, we assumed that the highest free-energy barriers controlling ion permeation are located in the TMD and thus imposing the limitation to the conductance. Here, we propose to explore the permeability of the *full-length* receptor, i.e., ECD and TMD, we are still missing the ICD.

## 4.2 METHODS

All the simulation setups used in this chapter were already introduced in the previous chapter, i.e., modeling, MD simulations parameters, force-field, constant electric field. For that reason, they will not be detailed here, but the reader might refer to Chapter 3, section *Methods*. However, the simulations that were carried out for that chapter are summarized in Table 4.1. Additionally, more detailed report on the computational electrophysiology results can be found in Appendix E.1 and E.2.

Concerning the analysis, i.e., ionic flux, currents, errors, and hole profiles, they were computed similarly as in the Chapter 3.

Additionally, we used the MOLE plugin (Petřek et al. 2007) within the visualization program PyMol (Schrödinger 2015), to probe the existence of tunnels in GlyR structures. A probe radius of 1.8 Å was used, in order to reproduce the size of a chloride anion (Nightingale 1959). Tunnels were computed using the energy minimized *wide-open* structure of GlyR $\alpha$ 1 and the snapshot named *MD-open*<sub>7</sub>.

To track which permeation pathway was taken by chloride anions in hundreds of permeation events, we wrote a *Tcl* script to be executed in VMD (Humphrey et al. 1996). Overall, our algorithm tracks all ions that enter or leave the ECD vestibule. Then, it reports on the direction of the ion, i.e., entering or leaving the vestibule, and the pathway that was used by the ion, i.e., the TMD, the apex of the ECD, or one of the five lateral portals. Of note, each of the five portals is treated as an independent pathway, and statistics are reported per portal.

Lastly, the sequence alignment of all human pLGICs was done with Clustal Omega (Sievers et al. 2011) within EMBL-EBI web server (McWilliam et al. 2013).

ID	Structure	Length (ns)	Simulation type	Membrane potential (mV)
<i>MD-open</i> preparation	<i>wide-open</i>	50	<i>gentle</i> relaxation	0
<i>MD-open</i> sampling	<i>MD-open</i>	400	unbiased MD	0
<i>MD-open</i> <sub>1</sub>	<i>MD-open</i> <sub>1</sub>	~200	electrophysiology	±250 and ±150
<i>MD-open</i> <sub>2</sub>	<i>MD-open</i> <sub>2</sub>	~200	electrophysiology	±250 and ±150
<i>MD-open</i> <sub>3</sub>	<i>MD-open</i> <sub>3</sub>	~200	electrophysiology	±250 and ±150
<i>MD-open</i> <sub>4</sub>	<i>MD-open</i> <sub>4</sub>	~200	electrophysiology	±250 and ±150
<i>MD-open</i> <sub>5</sub>	<i>MD-open</i> <sub>5</sub>	~200	electrophysiology	±250 and ±150
<i>MD-open</i> <sub>6</sub>	<i>MD-open</i> <sub>6</sub>	~200	electrophysiology	±250 and ±150
<i>MD-open</i> <sub>7</sub>	<i>MD-open</i> <sub>7</sub>	~200	electrophysiology	±250 and ±150
<i>MD-open</i> <sub>8</sub>	<i>MD-open</i> <sub>8</sub>	~200	electrophysiology	±250 and ±150
<i>MD-open</i> <sub>9</sub>	<i>MD-open</i> <sub>9</sub>	~200	electrophysiology	±250 and ±150
<i>MD-open</i> <sub>10</sub>	<i>MD-open</i> <sub>10</sub>	~200	electrophysiology	±250 and ±150
<i>MD-open</i> <sub>K120E<sub>1</sub></sub>	<i>MD-open</i> <sub>1</sub>	~200	electrophysiology	±250
<i>MD-open</i> <sub>K120E<sub>2</sub></sub>	<i>MD-open</i> <sub>2</sub>	~200	electrophysiology	±250
<i>MD-open</i> <sub>K120E<sub>3</sub></sub>	<i>MD-open</i> <sub>3</sub>	~200	electrophysiology	±250
<i>MD-open</i> <sub>K120E<sub>4</sub></sub>	<i>MD-open</i> <sub>4</sub>	~200	electrophysiology	±250
<i>MD-open</i> <sub>K120E<sub>5</sub></sub>	<i>MD-open</i> <sub>5</sub>	~200	electrophysiology	±250
<i>MD-open</i> <sub>K120E<sub>6</sub></sub>	<i>MD-open</i> <sub>6</sub>	~200	electrophysiology	±250
<i>MD-open</i> <sub>K120E<sub>7</sub></sub>	<i>MD-open</i> <sub>7</sub>	~200	electrophysiology	±250
<i>MD-open</i> <sub>K120E<sub>8</sub></sub>	<i>MD-open</i> <sub>8</sub>	~200	electrophysiology	±250
<i>MD-open</i> <sub>K120E<sub>9</sub></sub>	<i>MD-open</i> <sub>9</sub>	~200	electrophysiology	±250
<i>MD-open</i> <sub>K120E<sub>10</sub></sub>	<i>MD-open</i> <sub>10</sub>	~200	electrophysiology	±250
<i>wide-open</i>	<i>wide-open</i>	20	electrophysiology	±1000, ±750, ±500, ±350, ±250, ±150

Table 4.1 – Simulations summary. If a number  $x$  of voltages are reported in the *Membrane potential* columns it means that  $x$  simulations have been run, each one for a duration of  $t$  ns (*Length* columns). *MD-open*<sub>1:10</sub> refer to the ten snapshots randomly extracted from the last 50 ns of the simulation *MD-open sampling*.

## 4.3 RESULTS AND DISCUSSION

## 4.3.1 Exploration of full-length GlyR conductance

To confirm the reproducibility of our modeling leading to the *MD-open* conformation we restarted, again, from the *wide-open* cryo-EM structure and employed the *gentle* relaxation leading to *MD-open*, see Chapter 3 for all details. After the equilibration procedure, unbiased MD simulation was carried out to reach a total of 450 ns, see Figure 4.1.

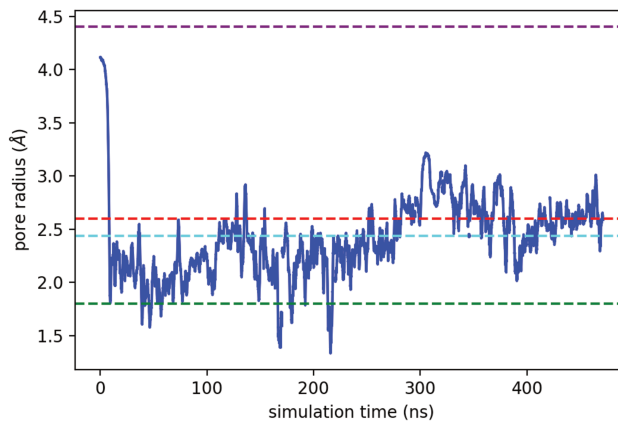


Figure 4.1 – Minimum pore radius, i.e., pore radius at the level of the constriction point, as a function of the simulation time. Only the running average over 100 consecutive points is plotted. Cyan and purple dashed lines correspond to minimal pore radius in *semi-open* (PDB:3JAF), and *wide-open* (PDB:3JAE) cryo-EM structures (Du et al. 2015), respectively. The green line corresponds to the radius of a chloride anion (Nightingale 1959), and the red line corresponds to the minimal pore radius estimated experimentally with poly-atomic anions (Bormann et al. 1987).

Interestingly, during the last 50 ns of that simulation, the constriction seems to converge, in average, on the experimentally predicted minimum pore radius in GlyR $\alpha$ 1, see the red line in Figure 4.1. This part of the trajectory was further analyzed by producing the average pore-profile over the last 50 ns, see Figure 4.2. From this analysis, we can see that the pore-profile is completely compatible with the active state cluster that we proposed in the previous chapter (Figure 3.13). Moreover, the mean pore radius at the constriction point is 2.67 Å, with a standard deviation of 0.32 Å. This minimum pore radius is in excellent agreement with the prediction made by Bormann et al. 1987, based on the permeability to poly-atomic anions. Also, the significant standard deviation is also highlighting the dynamical behavior of the gate which might assist the hydration of the constriction point, and facilitating the ion permeation.

Based on these observations, we choose to randomly extract ten snapshots from the last 50 ns in order to perform computational electrophysiology. This ten snapshots will be restarted

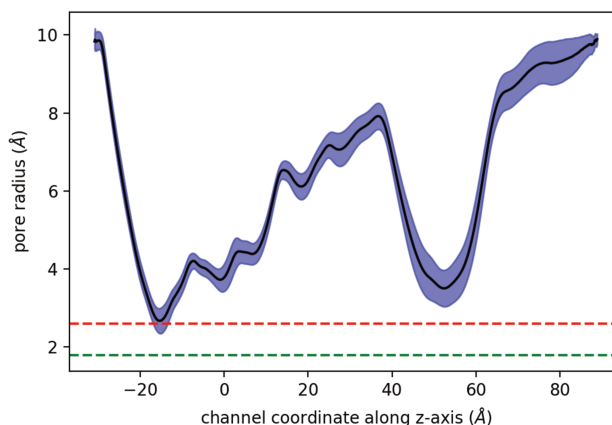


Figure 4.2 – Pore profile computed from the last 50 ns of the main 450 ns trajectory. The black line corresponds to the mean pore radius over the 50 ns. The area filled in blue corresponds to  $\pm$  the standard deviation. The red and green dashed lines represent the experimentally estimated minimum pore radius of GlyR $\alpha$ 1 (Bormann et al. 1987) and the radius of a chloride anion (Nightingale 1959), respectively.

with random velocities before starting to apply a constant electric field, see Chapters 2 and 3 for details on the constant electric field methodology.

In order to produce a faithful I-V-curve computationally, we used the previously extracted snapshots to accumulate sampling at  $\pm 150$  and  $\pm 250$  mV over hundreds of nanoseconds per replica, per voltages. The results are presented in Figure 4.3 (blue curve). For the comparison, we also introduced in this figure the results obtained in the previous chapter, based on the analysis of the constrained TMD-only GlyR $\alpha$ 1 in the *MD-open* conformation (red curve). All details concerning the simulations and their results are available in Appendix E.1.

From here, some observations can be made by the comparison of the two I-V-curves.

First, the curve computed from the TMD-only structure is somewhat linear (red curve) in comparison to the *full-length* structure (blue line). This first result might be explained by the asymmetry introduced in the structure by adding the ECD on one side of the channel, and nothing on the intracellular side.

Second, starting from  $\pm 250$  mV the current passing through the channel is increased in the *full-length* structure with respect to the TMD-only. Apart from the addition of the ECD, the *full-length* also benefits from the absence of harmonic restraints on the atomic positions that we used to preserve the channel conformation in the previous chapter. Here, the increase in conductance seems more likely related to the restored flexibility of the pore-lining residues than to the addition of the ECD.

Lastly, in the *full-length* simulations, the inward current at negative voltages, i.e., entry of positive charge in the intracellular compartment, or here, the exit of negative charges from the intracellular compartment, is larger than the outward current at positive voltages. The ratio of  $P_{Cl^-}(-250 \text{ mV})$  over  $P_{Cl^-}(250 \text{ mV})$  is equal to 2.16. Overall, it means that chloride

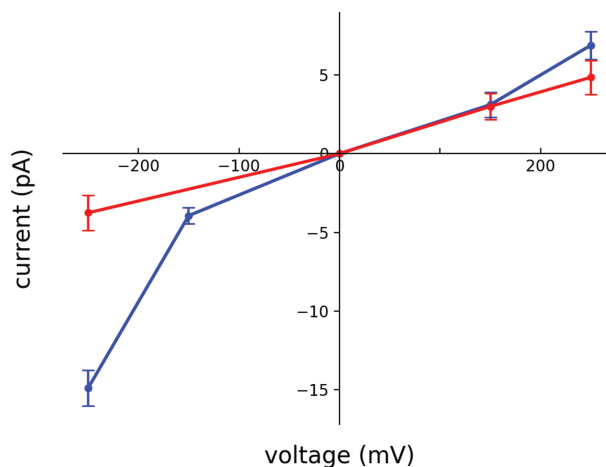


Figure 4.3 – I-V-curves produced by computational electrophysiology in all-atom MD with a constant electric field. Results are reported for the unconstrained *full-length* GlyR $\alpha$ 1 and constrained TMD-only, in blue and red, respectively. Current is measured as the number of ionic permeation per unit of time, the error bar arises from uncertainties estimation by assuming a Poisson distribution of the permeation events such that  $\sigma = I/\sqrt{N}$  with I the current and N the number of events (Sotomayor et al. 2007)). Simulations were carried out with symmetrical 145 mM NaCl.

will permeate two times more easily when they faced first the TMD, in comparison to the ECD.

This surprising observation suggests that the ECD is hindering the permeation of chloride anion in our simulations. It is interesting to note that the ECD is widely accessible from the bulk, according to its wide entry at the apex of the channel ( $3.5 - 4 \text{ \AA}$ ), see Figure 4.2.

In order to further probe the effect of the ECD on the conductance, we employed the *wide-open* structure (PDB:3JAE) (Du et al. 2015). Even though we demonstrated the probable artefactual status of this structure on the previous chapter, its use might be useful to collect statistics since it displays a very large conductance. Since the effect of the ECD seems to appears particularly at high voltage (from  $\pm 250 \text{ mV}$ ), we broadened the range to the non-physiological values of  $\pm 1 \text{ V}$  for the *wide-open* GlyR $\alpha$ 1 structure. Results are presented in Figure 4.4.

Strikingly, the unrealistic *wide-open* conformation displays a completely asymmetric I-V-curve when the *full-length* structure is used, see Figure 4.4. At negative voltages, the inward current is still extremely high, meaning that chloride can easily leave the intracellular compartment. However, the ionic flux at positive voltages, i.e., anions diffusing from the extracellular toward the intracellular domain is almost null. This latter observation is strikingly different from the results obtained in the previous chapter on the TMD-only structure of the *wide-open* conformation, reported in Figure 4.4 with the cyan line.

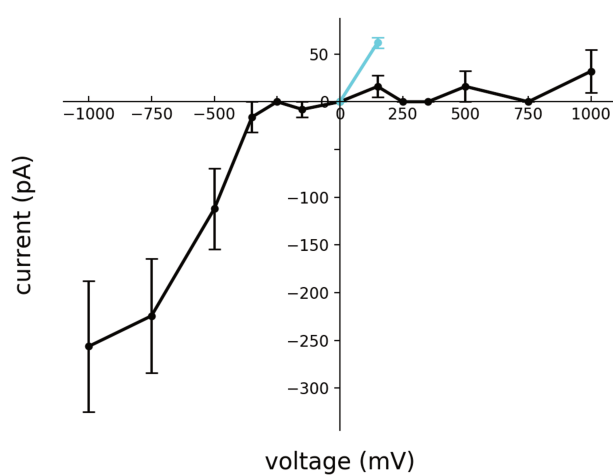


Figure 4.4 – I-V-curves produced by computational electrophysiology in all-atom MD with a constant electric field. Results are reported for the heavily constrained (see Chapter 3 for details) *wide-open* GlyR $\alpha$ 1 (PDB:3JAE) (Du et al. 2015). For information, the current measured through the TMD-only structure of the *wide-open* conformation, is reported here in cyan (see details in Chapter 3). Current is measured as the number of ionic permeation per unit of time, the error bar arises from uncertainties estimation by assuming a Poisson distribution of the permeation events such that  $\sigma = I/\sqrt{N}$  with I the current and N the number of events (Sotomayor et al. 2007)). Simulations were carried out with symmetrical 145 mM NaCl.

Surprisingly, the ECD in the *wide-open* cryo-EM structure is not only decreasing the permeation rate of chloride, as observed in the *MD-open* conformation (Figure 4.3), but it is completely preventing the entry of chloride from the extracellular to the intracellular compartments. This observation is even more intriguing by considering that the opening at the apex of the channel is even wider (around 6 Å) in the cryo-EM structure (Du et al. 2015), than it is in the *MD-open* conformation (3.5 – 4 Å), see Figure 4.2.

In summary, we showed using computational electrophysiology on GlyR $\alpha$ 1 *full-length* structure that the flexibility of the pore-lining residue possibly enhances the conductance of the channel, and that the ECD introduces an asymmetry in the measured current depending on the sign of the applied voltage. The ECD conformation captured in the *MD-open* structure seems to partially impair the permeation of chloride diffusing from the extracellular toward the intracellular compartment, although the ECD conformation in the *wide-open* cryo-EM structure is almost impermeable to chloride under positive voltage.

In the next section, we will investigate the structural origin of this asymmetry in the measured currents.

#### 4.3.2 Identification of a novel main permeation pathway

Driven by the surprising observations made in the previous section, we investigated the chloride permeation pathway across the membrane at both positive and negative voltages. By visual inspection of some trajectories, we observed that independently of the voltages, the anions are preferentially using lateral *portals* located at the subunit-subunit interfaces in the ECD to enter or leave the vestibule, see Figure 4.5. The portals are located right below the orthosteric binding site and involve residues from many loops of both (+) and (-)-subunits, see Figure 4.5.

To explore automatically the ECD portals in the GlyR structures, we used the program MOLE (Petřek et al. 2007) interfaced in PyMol (Schrödinger 2015). We used a probe with a radius equal to the chloride radius, i.e., 1.8 Å (Nightingale 1959). The tunnel detection analysis was executed for the *MD-open* and the cryo-EM *wide-open* structures of GlyR $\alpha$ 1, see Figures 4.6 and 4.7.

For the *MD-open* structure, the software correctly detected the main ion-channel (Figure 4.6), formed by the TMD section (in pink), and the vestibule with its exit at the apex of the channel (in yellow). In addition to this central section, the program detected three lateral portals that connect the vestibule with the extracellular bulk. The positions of the automatically detected portals are in agreement with the location of the portals that we identified by visual inspection of the trajectories, compare Figures 4.5 and 4.6. The identified tunnels are not normal to the membrane but are oriented in such a way that the tunnels start right below the C-loop and terminate near to the ECD-TMD interface, where the vestibule is the widest. However, based on this structure, only three portals are detected as wholly opened.

Using the same parameters on the analysis of the cryo-EM *wide-open* structure (Figure 4.7), we could not detect any tunnel connecting the bulk to the vestibule through lateral portals.

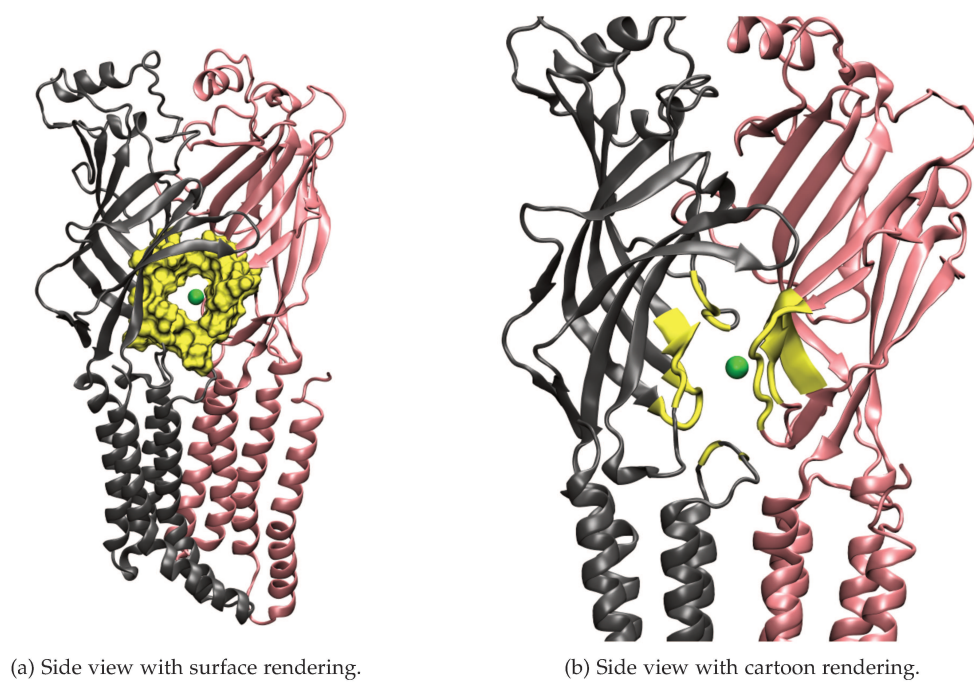


Figure 4.5 – Representation of the residues lining the ECD lateral portals.

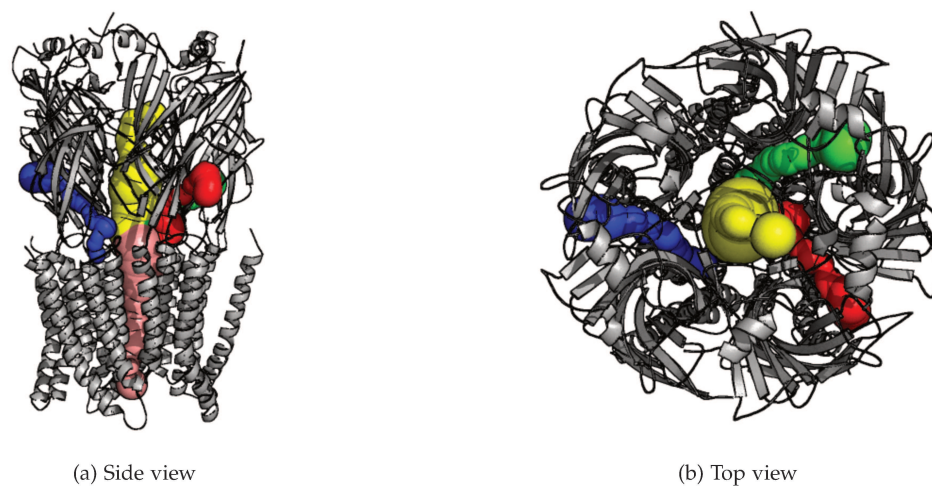


Figure 4.6 – Portals computed by MOLE with a probe radius of  $1.8 \text{ \AA}$  in the *MD-open* structure.

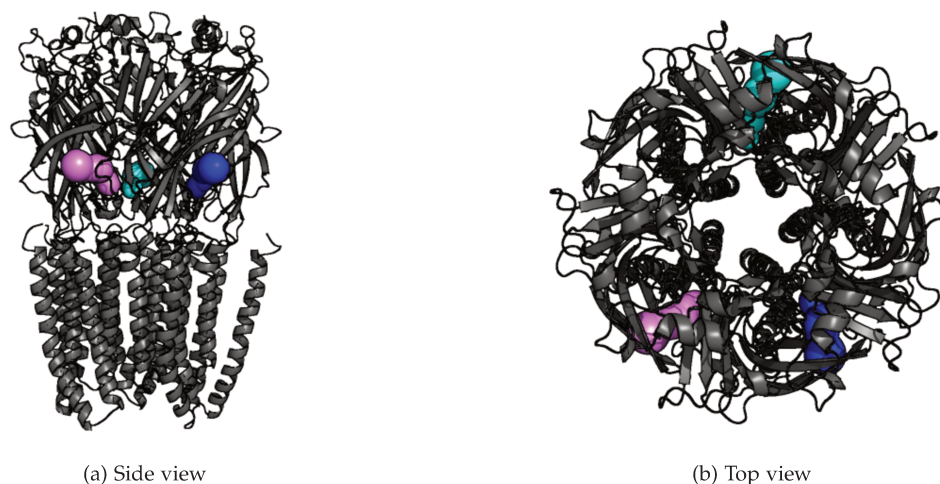


Figure 4.7 – Portals computed by MOLE with a probe radius of  $1.8 \text{ \AA}$  in the cryo-EM *wide-open* structure.

However, the entry of the tunnels was detected in three out of five interfaces, but none of them were sufficiently wide to accommodate the passage of chloride anion at the inner end of the portals.

Interestingly, the structural observation of closed portals in the cryo-EM structure of GlyR $\alpha$ 1 correlates nicely with the impermeability of the structure under positive voltages, when chloride have first to enter into the vestibule, before permeating through the ion pore. This observation also suggests that lateral portals have to be open in order to allow chloride anions to enter in the vestibule, implying that anions do not enter by the apex of the channel.

Additionally, inspection of the trajectories at negative voltages shown that permeating anions could easily go through the TMD section and then were *trapped* in the vestibule. None of them were able to exit the vestibule through the portals, but few of them eventually exited by the apex of the channel, when they were too many in the vestibule. Indeed, our permeation detection algorithm records a permeation event when an ion crosses the membrane through the pore, but going from the intracellular compartment to the vestibule is enough to be detected. For that reason, the cryo-EM structure was probed as highly permeable at negative voltages and almost not permeable at positive voltages. Most of the permeation events recorded at negative voltages were not bulk-to-bulk translocation.

Next, we developed a novel algorithm in VMD to detect the permeation pathway used by chloride anions to enter or exit the vestibule, i.e., by the apex of the channel or by one of the five lateral portals. Results are presented in Table 4.2.

From the Table 4.2, we can make two observations. First, the *apex* pathway is marginally used ( $\sim 5\%$  of the ionic flux) in comparison to the lateral portals (all five accumulated represent  $\sim 95\%$  of the flux). Second, only three portals, i.e., Portal<sub>1,2,3</sub>, are significantly permeable to chloride. Interestingly, they correspond to the three tunnels automatically detected by MOLE, see Figure 4.6.

Pathway	Number of permeation event	Proportion of ionic traffic (%)
Apex	12	4.6
Portal <sub>1</sub>	66	25.6
Portal <sub>2</sub>	4	1.6
Portal <sub>3</sub>	24	9.3
Portal <sub>4</sub>	151	58.5
Portal <sub>5</sub>	1	0.4
Total	258	100

Table 4.2 – Statistics collected at  $\pm 250$  mV for the ten replicas. Portals<sub>1–5</sub> refers to the five different interfaces where they are located. The apex pathway corresponds to the central opening at the top of the ECD.

Altogether this results support the idea that having an open ion pore at the TMD level is not enough to be ion conductive, the lateral portals in the ECD also have to be *open* since the apical entry of the ion-channel is only marginally used by chloride anions.

Indeed, the *wide-open* structure is impermeable at positive voltages, because its lateral portals are closed. Additionally, the lower conductance of the *MD-open* conformation at positive voltages might come from the fact that not all portals are fully open.

The reason for which the lateral portals are not all equally *open* or permeable is for the moment unclear. One hypothesis is that the memory of the cryo-EM structure, where all portals are *closed*, still partially persists in some of the interfaces. Indeed, we sampled ten replicas for some hundreds of nanoseconds each, but we lack longer ( $> 1 \mu\text{s}$ ) simulations to understand the functional dynamics of these portals.

In summary, we showed in this section that the functional annotation of an ion-channel, or at least the evaluation of its permeability, should take into account not only the free-energy barriers located in the TMD but also the ones introduced by the lateral portals in the ECD. Indeed, the structure-function relationship concerning the permeability of the ECD seems to be more complicated than it looks like at first sight because the widely opened apex of the channel is not, according to our simulations, the main permeation pathway for chloride anions. On the contrary, chloride anions use mostly (i.e.,  $\sim 95\%$ ) narrow tunnels located at the subunit-subunit interfaces, below the C-loop, to enter and exit the vestibule.

#### 4.3.3 A mutation that closes the portals

There is a recent increase in the mention of these portals in the literature. First, P. S. Miller and Aricescu 2014 mentioned it as a possible modulatory site in the GABA<sub>A</sub>R. Then, Di Maio et al. 2015 presented MD results based on 5-HT<sub>3</sub>R, where few sodium cations could permeate through the lateral portals. Based on this observation they conclude that it might be an alternative pathway for ion translocation. Finally, Zhu et al. 2018; Phulera et al. 2018 observed the portals in heteromeric GABA<sub>A</sub>R, and Hu et al. 2018 in STELIC. All the three articles published this year, refer to the portals as a potential alternative pathway for ions.

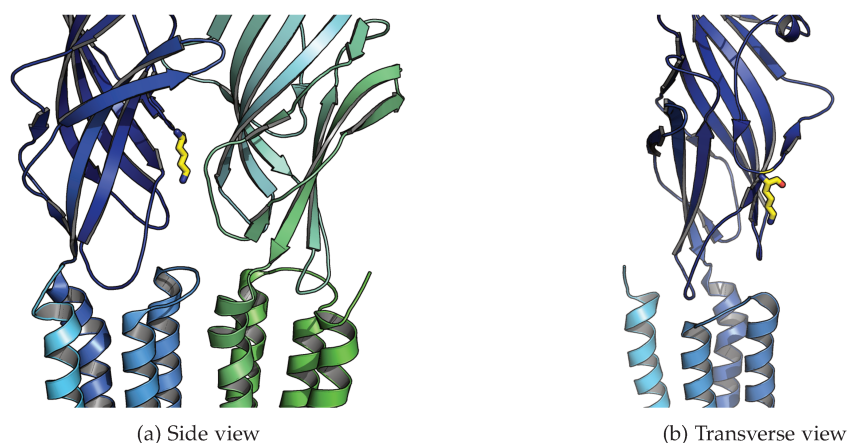


Figure 4.8 – Views on the location of the residue K120 in GlyR $\alpha$ 1. Overall, the residue is located in the middle of the portals when viewed from the front. A transverse view indicates that the residue is positioned at the inner side of the portals, next to the vestibule.

However, nothing more was known about these portals apart from rather quick structural descriptions.

By reviewing the literature on the ECD-located residues involved in the modulation of the conductance in GlyR, we found the amino-acid K120 that affects the conductance (Moroni et al. 2011b; Brams et al. 2011) and is located at the inner termination (vestibule side) of the portals, see Figure 4.8.

In Moroni et al. 2011b, they report on an asymmetric reduction of the conductance by reversing the residue charge (K120E) in GlyR $\alpha$ 1. Interestingly, the conductance at positive voltages, i.e., the diffusion of chloride from the extracellular toward the intracellular compartment, was reduced by 72.4%, when it was only reduced by 22% at negative voltages.

However, Moroni et al. 2011b explained the effect of the mutation K120E on the conductance by invoking the formation of a ring of charged residues lining the vestibule and preventing the vertical diffusion of chloride anions, i.e., from the apex to the bottom of the channel, or the opposite. Although the origin of the asymmetry was not further explained.

In order to rationalize the effect of the mutation on GlyR $\alpha$ 1 conductance, and to provide atomistic details on the origin of the asymmetry, we reproduced the mutant K120E starting from the previously used snapshots from GlyR *MD-open* conformations. The permeability of the mutant structures was tested by computational electrophysiology, and results are shown in Figure 4.9.

According to our simulations (Figure 4.9), the effect of the mutation K120E observed *in silico* has a similar trend to the one observed experimentally (Moroni et al. 2011b). Indeed, the reduction of the measured current is asymmetrical depending on the sign of the applied voltage. However the effect recorded computationally is stronger than the experimental one, i.e., we computed a reduction of the inward current of 24.9% (22% experimentally) and a reduction of the outward current of 91.3% (72.4% experimentally). Of note, at positive voltages,

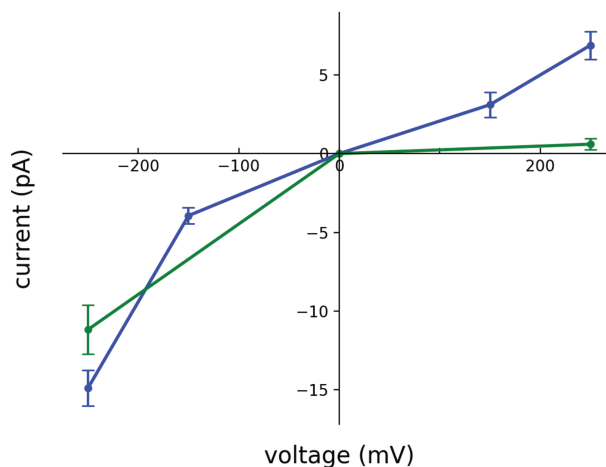


Figure 4.9 – I-V-curves produced by computational electrophysiology in all-atom MD with a constant electric field. Results are reported for the unconstrained *full-length* GlyR $\alpha$ 1 and the unconstrained *full-length* mutant K120E, in blue and green, respectively. Current is measured as the number of ionic permeation per unit of time, the error bar arises from uncertainties estimation by assuming a Poisson distribution of the permeation events such that  $\sigma = I/\sqrt{N}$  with I the current and N the number of events (Sotomayor et al. 2007)). Simulations were carried out with symmetrical 145 mM NaCl.

we measured a tiny current (0.60 pA) associated with a significant error ( $\pm 0.35$  pA), which arises from the insufficient sampling of permeation events in small conductance channels.

In our simulations, the mutant K120E impairs the permeation rate through the lateral portals. Indeed, in the mutant, the chloride permeation rate through the ECD portals decreased by a factor of 20 for outward current and a by a factor of 7 for the inward current. In contradiction to the hypothesis made by Moroni et al. 2011b the mutant K120E slightly enhance the longitudinal pathway by doubling the small permeation rate through the apex for inward current.

The asymmetric effect of the mutation on the current can be explained based on our atomistic simulations. Indeed, the charge reversal of the residue at the position 120 closes the inner end of the portals, introducing a large free-energy barrier impairing the free diffusion of chloride. At positive voltage, chloride anions first face this newly introduced barrier, and most of them could not enter the vestibule. However, at negative voltages the anions permeate as freely as in the Wild Type (WT) through the membrane via the TMD, but then are *trapped* in the vestibule, facing the same free-energy barrier that prevents anions to enter the vestibule at positive voltages. At negative voltages, the density of anions is increasing inside the vestibule over time because the membrane potential prevents the backward motion of anions through the ion pore. Finally, the increasing anionic density in the vestibule results in a decrease in the free-energy barrier imposed by the mutation. In summary, the height of

the free-energy barrier introduced by the mutant is indirectly voltage-dependent since it is modulated by the resulting local density of anions in the vestibule.

One original observation that we made but that was not reported in the experimental research article (Moroni et al. 2011b) is related to the selectivity of the channel. One might think that a charge reversal of residues controlling the conductance might change the selectivity of the channel. It is indeed slightly the case, the computed selectivity for chloride decreased in the mutant when computed as the ratio of the anionic over cationic currents. However, the change in the measured ratio is solely due to the decreased anionic permeability. The mutation K120E did not significantly increase the cationic current. This critical observation supports the idea that the *main* selectivity filter is located in the TMD (see selectivity of the TMD-only structures in Chapter 3), but that charged residues lining the lateral portals are exploited to *optimize* the permeability of the ion type of interest.

Additional predictions could arise from this work, especially to confirm the main role of the lateral portals in the ion translocation in opposition to the apical pathway. Indeed, it could be possible to mutate residues at the outer end of the portal, next to the protein surface, in such a way that the mutated residues close the tunnels. Such an experiment would still test the relevance of this permeation pathway but without modifying the longitudinal pathway. Such residues have to be identified.

In summary, we shown in this section that a mutation identified experimentally (Brams et al. 2011; Moroni et al. 2011b), is *gating* the inner end of the ECD lateral portals. Our simulations are in quantitative agreement with experiment concerning the asymmetrical effect of the mutation on the conductance. Moreover, we explained the asymmetric effect by a local change in chloride density within the vestibule. Lastly, our simulations revealed a role of the portals on the optimization of chloride permeability.

#### 4.4 CONCLUSION

Several conclusions can be drawn from our analysis of the ECD lateral portals.

First, it is still not clear if the various degree of opening in the portals observed in our *MD-open* conformation is physiologically relevant or if it is a residual artifact from the cryo-EM structure in which all portals are closed to chloride. Indeed, because we are studying a homopentamer we should expect on average, and over a longer time-scale, a homogeneity of the permeation rates within the fives portals, which was not the case here. However, the need of *open* lateral portals to observe ion translocation was exemplified here, using the *wide-open* cryo-EM structure.

Of note, the sub-conductive states observed in GlyR (Bormann et al. 1993) seems not to be related to the ECD portals, because their frequencies are controlled by residues in the M<sub>2</sub> helices, but since no other structural or functional information is available concerning the sub-conductive behavior in GlyR, we shouldn't rule out this eventuality especially because the M<sub>2</sub>-M<sub>3</sub> loop (linked to the M<sub>2</sub> helix position) is partially involved in the formation of the portals.

Second, we proposed that the ECD lateral portals are the main permeation pathway for ion translocation in GlyR, in opposition to the long-lasting view of a purely longitudinal route via the apex of the ECD. This new model for ion translocation implies that the structure-function relationship, or functional annotation, of a given ion-channel structure, should take into account the *openness* of the lateral portals in addition to the organization of the ion pore, in order to conclude on the possible conductive state of that channel.

Third, we possibly identified the main permeation pathway for chloride and revealed that lateral portals might restrict the permeability because of their geometries, or mutated residues lining their tunnels. These observations imply to take into account a novel free-energy barrier along the ion translocation in GlyR. The identification of this new barrier, which might not be directly modulated by the membrane potential because of its location in the ECD, should be incorporated in any model based on the permeation rate theory (Hille 2001; Sigg 2014).

Fourth, the charged residue K120 that was reported earlier (Brams et al. 2011; Moroni et al. 2011b), and reanalyzed here, is strikingly conserved in all human anionic pLGICs, with a charge inversion between anionic and cationic channels, see Figure 4.10.

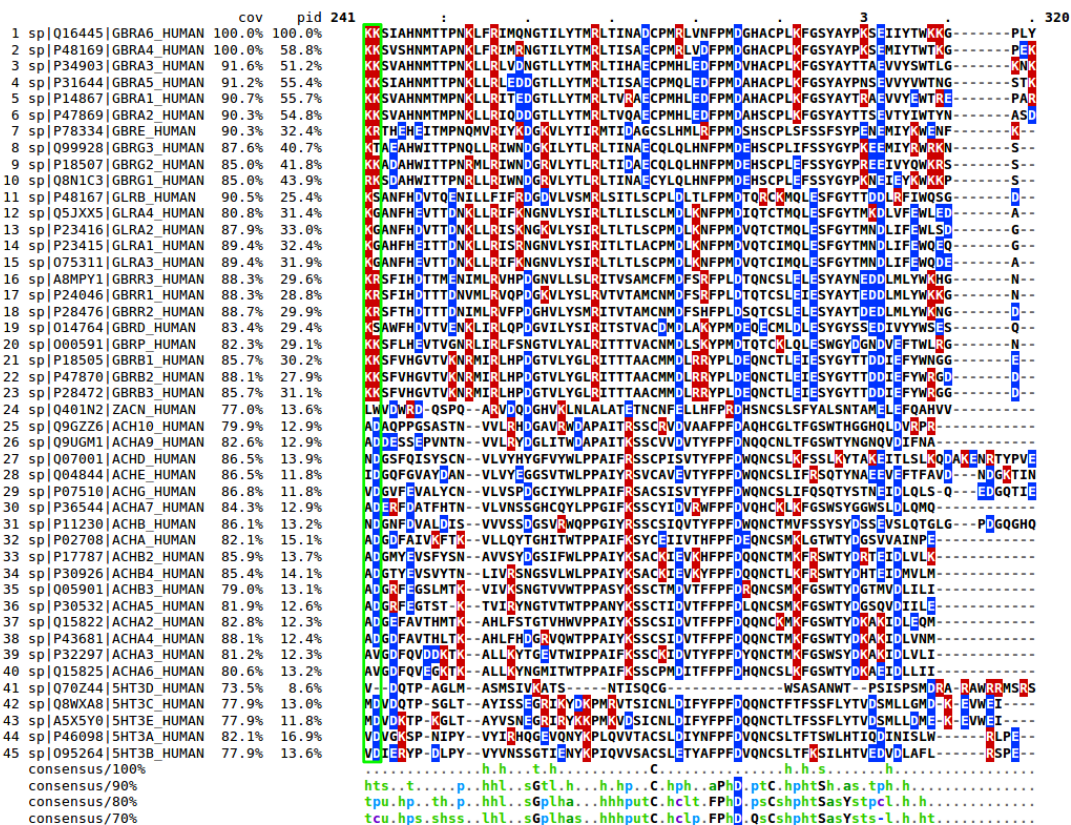


Figure 4.10 – Multiple alignment of all anionic (top) and cationic (bottom) human pLGICs produced with Clustal Omega (Sievers et al. 2011). The charged residues located at the inner end of the ECD lateral portals are boxed in green.

It is interesting to note here that GlyR is particular within the anionic pLGICs because it is one of the few channels to have only one charged residue when the vast majority of the anionic pLGICs have two adjacent positively charged residues at the inner end of the lateral portals (see Figure 4.10). Additionally, the cationic pLGICs also have a single charged residue but at the adjacent position to the one found in GlyR, i.e., position 121 in our numbering. According to the hypothesis that K120 in GlyR helps at *optimizing* the channel permeability for chloride, we can propose that this behavior is shared in anionic pLGICs due to its strict conservation, and opposite effect is observed in cationic channels.

Lastly, the emerging mechanism of ion translocation through lateral portals in the ECD is now strikingly similar to the one happening in the ICD. Unfortunately, the lack of high-resolution structures in the presence of the ICD of GlyR or anionic pLGICs, in general, prevents us from testing our hypothesis computationally. However, the recent structures of human 5-HT<sub>3</sub>R (Basak et al. 2018b; Basak et al. 2018a; Polovinkin et al. 2018) confirmed the existence of lateral portals in the ICD. Interestingly, these ICD portals are also lined by charged residues that profoundly impact the channel conductance in 5-HT<sub>3</sub>R (Kelley et al. 2003). Strikingly, at a similar position, charged residues also modulate the conductance in GlyR (Carland et al. 2009), and most importantly in an asymmetric way, similar but opposite to the mutation K120E in the ECD, i.e., at the ICD level, the mutations reduce more importantly the inward current (chloride efflux) than the outward current (chloride influx). Additionally, the mutations in the ICD portals were reported to have a little effect on the selectivity (Carland et al. 2009), similarly to what we measured computationally in the ECD.

Despite the structural differences between ECD and ICD, it seems that both domains host lateral portals that are possibly used as main ion translocation pathways. Charged residues lining the portals in both domains seem to positively modulate the permeability of anions in GlyR WT, but negatively the permeability of cations in 5-HT<sub>3</sub>R WT (Kelley et al. 2003). Overall, charged residues located at these positions participate to the conductive properties of pLGICs without interfering much with the selectivity of the channels.

In conclusion, based on our simulations of the *full-length* GlyR $\alpha$ 1 in the *MD-open* conformation, we propose that lateral portals, located in the ECD, are the main permeation pathways for chloride anions. These portals can be *gated* at least by the charged residue at the position 120; a mechanism which seems to be shared in anionic and possibly cationic human pLGICs. In GlyR, the effect of the mutations in ECD and ICD lateral portals have strikingly similar effects, which is why we suggest to unify the role of ECD and ICD on the ionic conductance modulation.

## TOWARD A STATE-BASED PHARMACOLOGY FOR GLYCINE RECEPTOR

---

This final chapter concerning GlyR is a mixture of results, on-going research, and perspective. It is also a direct application of the results obtained in Chapter 3 and Chapter 4, on the functional annotation and the exploration of the active state, respectively.

### 5.1 INTRODUCTION

At rest, the ion channel is closed. Binding of neurotransmitter elicits a rapid isomerization to the active state, which opens a transmembrane pore that allows the diffusion of ions. Prolonged exposure to high levels of agonist eventually results in a time-dependent decrease of the current named desensitization, which involves the transition to a closed-channel form thought to be structurally different from the resting state. Several models have been proposed for the ligand-gated ion-channel activation and desensitization. Among them, the MWC model (Monod et al. 1965) postulates that allosteric pLGICs exist in reversible equilibrium between distinct quaternary states, i.e., a resting state, an active open-channel state, and one or several high-affinity desensitized state(s) with a shut ion pore, and that a conformational selection (or shift of conformers population) takes place upon binding of agonist, antagonist, or modulators (Changeux and Edelstein 2005). In this view, agonist binding shifts the equilibrium to the active state, whereas antagonist binding shifts it to the resting state. Importantly, all the states pre-exist and ligand binding is only responsible for the conformational selection of one state over the others. Very recent single-channel electrophysiology of mutated nAChR demonstrated that the MWC model provides a perfect description of ion-channel activation in pLGICs (Nayak and Auerbach 2017).

The whole pLGIC super-family is a crucial target for pharmacological drugs. In humans, nAChRs are targets of systemically applied pharmacological agents (Taly et al. 2009). They are blocked by curare, hexamethonium and toxins present in the venoms of snakes and shellfishes (Nasiripourdori et al. 2011), and their reaction to neuromuscular blocking agents is routinely used in anesthesia (Tassonyi et al. 2002). Pharmacological modulation of nAChR is also currently developed for the treatment of Alzheimer's, Parkinson's, schizophrenia, depression, and tobacco addiction (Taly et al. 2009), and eventually the establishment of personalized medicine (Tsuang et al. 1998; Zigmond et al. 2014). GABA<sub>A</sub>R are the target of benzodiazepines, that potentiate their function to promote anxiolytic effect, sedation and muscle relaxation, and are a key target for General Anesthetics (GA) (Möhler 2011). GlyRs play a critical role in motor coordination, and essential sensory functions including vision and audition and have been since long recognized as pharmacological targets for chronic pain, autism, and the startle disease (see Chapter 1 for the review). Therefore, the rational design

of small-molecule compounds able to activate (agonists), inhibit (antagonists), or modulate the function of pLGICs are crucial to develop pharmacological strategies in humans.

A wide panel of small-molecule compounds modulates the function of GlyRs by binding at topographically distinct sites (see Figure 5.1). First, the orthosteric site corresponds to the binding site of the endogenous neurotransmitter glycine. This site is located within the ECD at the interface between subunits, halfway between the apex of the receptor and the membrane, as revealed by the cryo-EM structure of the GlyR $\alpha$ 1 in complex with glycine (Du et al. 2015). This site also binds strychnine, a competitive antagonist, as well as the partial agonists taurine and  $\beta$ -alanine. Also, several allosteric sites have been identified on the experimentally captured 3D structures (see Figure 5.1). It exists a series of synthetic compounds from Amgen exemplified by AM-3607 that binds at the ECD subunit interface above the orthosteric site (named "sulfonamide pocket" in the following text) (Huang et al. 2017b; Huang et al. 2017a). Additionally, divalent cations such as Zinc can bind nearby the ECD-TMD interface (Huang et al. 2017b; Huang et al. 2017a). Finally, IVM, a natural compound acting as a potent PAM, can bind to the TMD at the interface between subunits (named accordingly "IVM pocket") (Du et al. 2015; Huang et al. 2017a). Besides, GlyRs are modulated, typically potentiated, by a large variety of compounds thought to bind to the TMD, including cannabinoids, neuroactive steroids, GA, and alcohols. Although the binding site(s) of these molecules have not been demonstrated in GlyRs, their binding site was identified by X-ray crystallography of other pLGICs, notably the binding site(s) of GA on GLIC (Nury et al. 2011; Sauguet et al. 2013a; Fourati et al. 2018), and of neurosteroids on the TMD of the GABA $_A$ R (Laverty et al. 2017; P. S. Miller et al. 2017). Furthermore, tropeines were recently shown to bind the orthosteric site of 5-HT $_3$ R (Basak et al. 2018b). Unfortunately, no pLGIC structure was solved in the presence of cannabinoids, but mutagenesis experiments identified one essential residue for binding in the middle of M $_3$  helices in GlyR (Xiong et al. 2012) and GABA $_A$ R (Bakas et al. 2017).

In Chapter 3, we proposed a functional annotation of the anionic pLGICs structures based on their classification within three clusters. Having representative structures of the three main functional states, it becomes feasible to explore the pharmacology of each state. Since the physiological relevance of the available structures was already tackled, it allows us to confidently evaluate the state-dependent binding affinity of small-molecule compounds to predict their modulatory role, i.e., PAM, or Negative Allosteric Modulator (NAM).

In this perspective, the annotated crystallographic structures will be complemented by a MD-generated ensemble of structures for each state. Additionally, a chemical library of known modulators of GlyR will be compiled in order to validate our methodology.

## 5.2 METHODS

**COMPILATION CHEMICAL LIBRARY** Molecules were manually extracted from the literature and drawn with MarvinSketch (Marvin 17.27, 2017, ChemAxon, www.chemaxon.com). Particular care was taken to respect the stereoisomerism of each molecule. Next, Simplified Molecular Input Line Entry Specification (SMILES) were produced for all molecules using

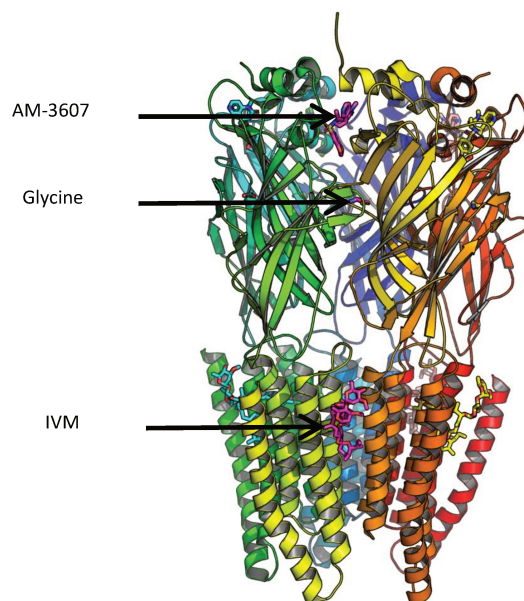


Figure 5.1 – Structure of GlyR $\alpha$ 3 bound to AM-3607, Glycine, and IVM.

MarvinSketch. SMILES is a convenient 2D molecular format which preserves the chirality. Since SMILES are ASCII strings, they are easy to incorporate in any database format and can be easily read by most cheminformatics software.

The Glycine Receptor Allosteric-Ligands Library (GRALL) is structured for the moment in the Comma-Separated Values (CSV) format. With each row being a different molecule entry. Columns are separating the relevant information:

*Name, SMILES, Chemical family, Binding pocket, Experimental measurement type (unit), Experimental measurement value for GlyR $\alpha$ 1, Experimental measurement value for GlyR $\alpha$ 3, Effect on GlyR $\alpha$ 1, Effect on GlyR $\alpha$ 3, Reference*

*Chemical families* are, for the moment, based on the description made of the molecules in the original articles reporting them, e.g., IVM analogs, cannabinoids, neurosteroids. However, for most of the newly discovered compounds, this information is missing because the identification arises from a High-throughput screening (HTS) or Virtual high-throughput screening (v-HTS) procedure. To overcome this problematic, cheminformatics or Machine Learning (ML) techniques will be used in the future to merge novel compounds to existent families or to create new ones if the chemical diversity is too important.

*Binding pockets* is a descriptor with less class than *Chemical family*. Indeed, several *Chemical families* can bind the same pocket. For the moment, we assumed that a *Chemical family* cannot bind to several pockets. *Binding pockets* classification arises from the structures of GlyR $\alpha$ 1 and GlyR $\alpha$ 3 for the orthosteric pocket, the sulfonamide pocket, and the IVM pocket. Structures of other pLGICs in addition to mutation experiments, permit to classify pockets for cannabinoids, neurosteroids, GA/ethanol, and pore blockers. Recently, a novel 5-HT $_3$ R structure

solved with tropisetron (tropein family), permits to identify the antagonist binding site of tropeines in the receptor orthosteric pocket. Because of the lack of structure of GlyR bound to all classes of modulators, *Binding pockets* can be rather elusive for half of them (i.e., neurosteroids, GA, and cannabinoids and refer more to an area of interest, than to actual pockets). However, this classification is particularly useful to order the database and later on to filter chemical libraries of interest at the beginning of a *v*-HTS campaign using chemoinformatics or ML techniques.

The sections *Effect on GlyR $\alpha$ 1* and *Effect on GlyR $\alpha$ 3* are simplifications of the sections relative to the experimental measurements of the activity. Because activities are reported in numerous ways (e.g., EC<sub>50</sub>, IC<sub>50</sub>, Ki, maximal potentiation, mean potentiation), they are not easy to use in order to classify compounds. For that reason, we converted actual experimental data into the simplified *Effect* sections based on the type and the value of the measurements. There is three only three classes: positive, or negative modulators, and decoys. Decoys are compounds for which the modulatory effect on GlyR was measured, but is null.

**LIGAND BASED MACHINE LEARNING** In order to apply some ML procedures to GRALL, we will need to prepare the small-molecule structures starting from their SMILES. The ligands preparation pipeline was done with KNIME software (Berthold et al. 2008).

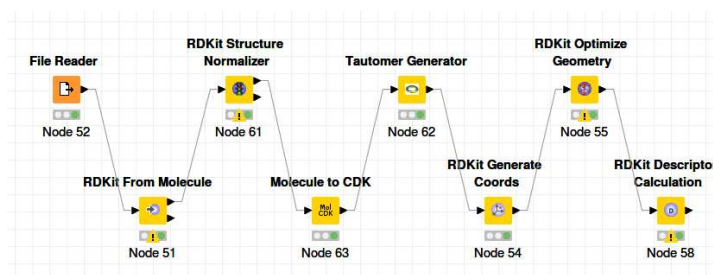


Figure 5.2 – Ligands preparation pipeline before ML.

The molecular manipulations are achieved with RDKit (RDKit: Open-source cheminformatics; <http://www.rdkit.org>) within a KNIME pipeline (see Figure 5.2). First, the molecular structures are normalized according to the standards of RDKit; then molecules are converted in the CDK internal format (Steinbeck et al. 2003). This later conversion allows us to apply the AMBIT-tautomer procedure to enumerate all tautomer and select the most viable one (Kochev et al. 2013). Then, 3D coordinates are generated, and the geometries are optimized using the MMFF94 force field (Halgren 1996). Finally, all the 177 descriptors (2D and 3D) from CDKit are computed for all molecules.

GRALL's chemical space was explored using two different ML techniques: Principal Component Analysis (PCA) and regression analysis.

In order to assess the chemical space of GRALL, the DrugBank (Wishart et al. 2018) subset containing the approved small-molecule drugs (2388 compounds) were prepared using the previously described procedure, and corresponding descriptors were computed. The PCA was achieved using all the 2D and 3D descriptors previously computed for the GRALL and the DrugBank subset. The analysis was done with the Scikit-learn library (Pedregosa et al.

2011) in Python. First, all descriptors were scaled between zero and one. Second, the PCA was computed using the normalized descriptors. Lastly, the first two components were plotted with Matplotlib (Hunter 2007), and points from GRALL were colored based on the *Binding pocket* classification, otherwise DrugBank's compounds were colored with a single color.

Using a regression technique, two models were built to classify compounds based either on their *Effect* (PAM, NAM, or decoys), or their *Binding pocket*. For that purpose, we used the program WEKA (Witten et al. 2017), embedded in a KNIME pipeline. In WEKA, the class "classification via regression" (Frank et al. 1998) was executed, using the M5 algorithm for regression (Quinlan 1992).

Due to the relatively small number of compounds, the quality of the generated models was assessed using the *leave-one-out* cross-validation procedure. It is an exhaustive method, i.e., which divide the dataset into training and validation set in all possible ways to train and test the model accuracy. Successively, one compound is used as a validation set when all the other compounds are in the training set, until all compounds were tested.

Two metrics were used to evaluate the quality of the models. The accuracy is defined as  $ACC = \frac{TP+TN}{P+N}$ , where TP, TN, P, and N refer to, True Positives, True Negatives, Positives, and Negatives, respectively. Cohen's kappa is defined as  $\kappa = \frac{ACC-RAND}{1-RAND}$  where ACC and RAND corresponds to the agreement, and random agreement, respectively. Landis and Koch 1977 characterized  $\kappa$  values < 0 as indicating no agreement and 0–0.20 as slight, 0.21–0.40 as fair, 0.41–0.60 as moderate, 0.61–0.80 as substantial, and 0.81–1 as almost perfect agreement. Of note,  $\kappa$  values can be negative and would describe a model doing worst than random.

## 5.3 RESULTS AND DISCUSSION

### 5.3.1 *The Glycine Receptor Allosteric-Ligand Library*

Starting from the recent reviews on the modulation of GlyR function by small-molecule compounds (Lynch et al. 2017; Zeilhofer et al. 2018), it has been possible to collect manually all the published chemicals and their modulatory effects from the cited articles. Extracted data was compiled into a database named GRALL. The information recovered from our analysis of the literature go well beyond the molecules cited in the two initial reviews, and correspond to 159 small-molecule compounds with experimental activity data on GlyR $\alpha$ 1 or  $\alpha$ 3. Structures and bioactivities were extracted from the following list of articles: Maksay 1998; Maksay et al. 2001; Chesnoy-Marchais and Cathala 2001; Ahrens et al. 2004; Hejazi 2005; Yang et al. 2007; Yang et al. 2008a; Yang et al. 2008b; Maksay et al. 2009; A. A. Jensen et al. 2010; Liu et al. 2010; Lynagh and Lynch 2010a; Lynagh and Lynch 2010b; Lynagh et al. 2011; Yévenes and Zeilhofer 2011; Yévenes and Zeilhofer 2011; Islam and Lynch 2012; Balansa et al. 2013b; Balansa et al. 2013a; Wells et al. 2015; Maleeva et al. 2015; Lara et al. 2016; Stead et al. 2016; Sadek et al. 2017; Chakka et al. 2017; Bregman et al. 2017.

Interestingly, most of the recent research articles reporting on GlyR modulators used HTS (Balansa et al. 2013b; Balansa et al. 2013a; Stead et al. 2016; Bregman et al. 2017) and v-HTS (Wells et al. 2015; Chakka et al. 2017). This trend is of course supported by the need to explore

novel and diverse chemical libraries to identify original chemical probes or lead-compounds, based on unexploited chemical scaffolds. However, both v-HTS campaigns did not use the functional state information but considered either a single structure (in addition to ligand-based techniques) (Chakka et al. 2017) or an ensemble of structures constituting only the active state (Wells et al. 2015).

Importantly, all known modulator of GlyR lack of potency, selectivity, or good ADME-T properties (Sparling and DiMauro 2017). However, one recent example contradicts this generality, i.e., the sulfonamide family demonstrates decent potency and selectivity over other pLGICs. In particular, the compounds AM-3607 has an 11-fold potentiation of Glycine affinity in GlyR $\alpha$ 3 $\beta$  at 0.1  $\mu$ M (Huang et al. 2017b), which makes it one of the most efficient potentiators of pLGICs (Sparling and DiMauro 2017). Overall, these observations justify the use of HTS and v-HTS to discover new fragments and scaffolds, able to modulate GlyRs selectively.

In order to propose a rational drug-discovery protocol to target the GlyR, we first aimed at compiling a chemical library (i.e., GRALL), to benchmark our methodology. The composition of GRALL can be found in Table 5.1. In total, 159 compounds were collected. Three of them are agonists or partial agonists, and one is an antagonist. These four compounds are known to bind the orthosteric binding site. Other molecules are split between three categories: PAM, NAM, and Decoys, see *Methods*.

Potent small-molecule compounds are reported for GlyR $\alpha$ 1 or  $\alpha$ 3. This distinction also serves as a category for the ligands classification.

Lastly, molecules are categorized based on their probable binding sites (see Figure 5.3). Apart from the compounds identified by HTS, the binding site annotation follows the *Chemical family* categories. However, for one *Chemical family*, i.e., Glutamate (and its analogs) not much is known about their binding site. Of note, a recent 5-HT<sub>3</sub>R structure was captured with tropisetron (tropeine family) bound to the orthosteric binding site. This observation supports the idea that tropeines could bind the orthosteric site of GlyR. Following the same reasoning, one might think that Glutamate and its analogs could bind the orthosteric site of GlyR since they do the same in GluCl, but in contrary to tropeines, no mutations experiments support that eventuality.

Type	GlyR $\alpha$ 1	GlyR $\alpha$ 3
Orthosteric agonist	3	3
Orthosteric antagonist	1	1
PAM	81	40
NAM	31	20
Decoys	29	23
Sub-total	145	87
Total	159	
Known binding location	75	53

Table 5.1 – The number of known compounds with experimental activity against GlyR $\alpha$ 1 and  $\alpha$ 3 classified by type is shown. Information on the binding sites comes from X-ray/cryo-EM structures or mutation experiments. Some ligands are shared between  $\alpha$ 1 and  $\alpha$ 3 GlyR.

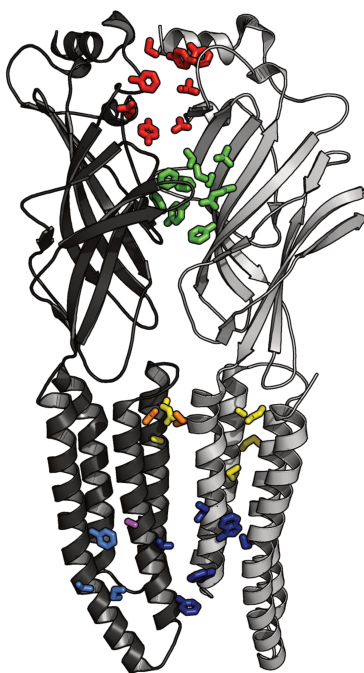


Figure 5.3 – All putative binding sites location in GlyR. Binding sites for channel-blockers are not displayed. Side-chains involved in the binding of small-molecules compounds are represented in sticks and colored accordingly to each binding site. The sulfonamide pocket is represented in red, the orthosteric binding site in green, the IVM pocket in orange, the GA/ethanol pocket(s) in yellow, the single residue identified in the cannabinoid binding site is represented in purple, and the two possible binding sites for neurosteroids are colored in blue.

After this report on the pharmacological modulation of GlyR and the classification of GlyR's modulators, we aimed at measuring the chemical space occupied by GRALL in respect to approved small-molecule drugs from DrugBank (Wishart et al. 2018). Using PCA based on 177 molecular descriptors from RDKit we annotated compounds from GRALL and DrugBank separately. Also, compounds from GRALL were labeled based on their putative binding site, see Figure 5.4. Interestingly, the PCA is showing that GRALL and DrugBank approved small-molecule drugs share mostly their chemical space since there is a substantial overlap of the data points. However, IVM and its analogs seem to be entirely different from known drugs, implying possible challenges to target this pocket with drug-like compounds, yet novel chemical scaffolds binding this pocket could be discovered.

Concerning GRALL, the *Chemical families* and putative *Binding sites* are quite well separated by the PCA. Most groups are correctly clustered on the PCA, but the pore blockers and the cannabinoids. Concerning the cannabinoids it might be interesting to split the family in two, depending if they are endogenous or exogenous cannabinoids since the chemistry of the two sub-families is quite different. Unfortunately, cannabinoids are not only chemically diverse,

but their binding site is also one of the less defined structurally, making it more challenging to target rationally.

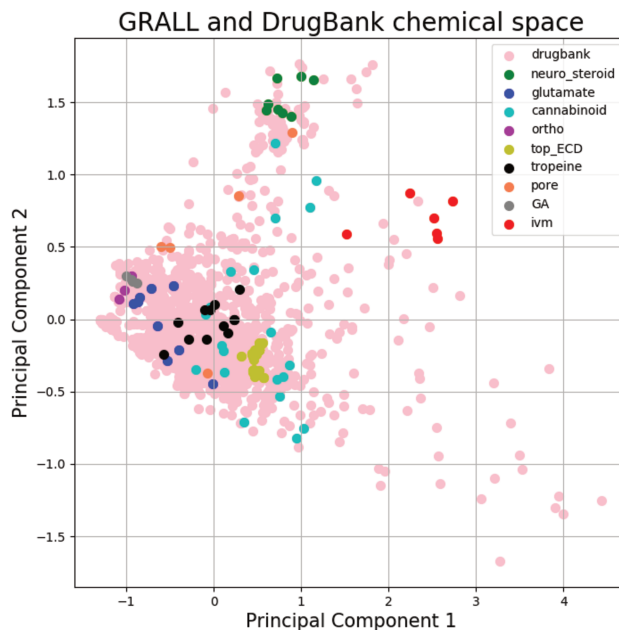


Figure 5.4 – PCA applied to GRALL and DrugBank approved small-molecule drugs in order to access their chemical diversity. All DrugBank compounds are colored in pink. GRALL compounds are colored based on their putative binding sites.

In addition to PCA, we used another ML techniques, i.e., classification via regression, to classify the ligands present in GRALL. Using the same set of descriptors as the ones used in the PCA, we built two models. The first one was built to predict the putative *Binding sites*, see Table 5.2.

Overall, the model is relatively predictive according to Cohen’s kappa (Landis and Koch 1977),  $\kappa > 0.81$ , see Table 5.2. However, there is a notable difference in the accuracy of the model depending on the binding site which is predicted. Neurosteroids, IVM analogs, GA, and sulfonamides are extremely well classified. Two third of the cannabinoids and pore blockers are well predicted, but only half of the glutamate analogs and the tropeines. Surprisingly, none of the orthosteric ligands are correctly predicted by the model. Interestingly, the moderate accuracy in the prediction of some binding sites correlate well with the dispersion of the data point representing these families on the PCA, see Table 5.2 and Figure 5.4, apart for the orthosteric ligands, which are well clustered in the PCA but are wrongly predicted by the model.

This predictive model might have several applications. First, one may use it to propose a binding site for compounds obtained from HTS for which no extra information is available. The predictions of the model might be compared to the binding sites predicted by docking algorithm or ranking based on free-energy estimations. Additionally, the model could be

Pocket	TP	FP	TN	FN	Accuracy	Cohen's kappa
Pore blockers	6	0	97	2		
Cannabinoids	18	5	79	3		
Glutamate	7	4	92	2		
Neurosteroids	8	1	96	0		
IVM	6	0	99	0		
GA	4	1	100	0		
Sulfonamides	35	1	69	0		
Tropeines	7	2	91	5		
Orthosteric	0	0	103	2		
Overall					0.87	0.83

Table 5.2 – Results of the model for the pocket prediction for GlyR $\alpha$ 1 ligands with identified binding site.

applied as a filter to restrict the chemical space of a library before docking, in order to focus the search on specific binding sites.

Then, a second model was built to classify the ligands based on their modulatory effect on GlyR $\alpha$ 1, see Table 5.3. Here, in contradiction with the previous model, the predictive power of the model is low, according to Cohen's kappa equal to 0.25 (i.e., "slight" agreement). Overall predictions are bad for all three categories (i.e., positives, and negative modulators, or decoys). It is indeed not surprising that general rules to predict the effect of a small-molecule compound, independently of its binding site, are very difficult to define. Indeed, the difference between positive or negative modulators is pocket-based. According to this observation, one should build a model discriminating between positive and negative modulators per pocket. However, the considerable imbalance of known positive vs. negative modulators per pocket (i.e., pockets are mostly occupied by only one of the two categories), makes the production of such model impossible for the moment.

Modulation type	TP	FP	TN	FN	Accuracy	Cohen's kappa
Positive	50	24	19	8		
Negative	11	10	65	15		
Decoy	1	5	79	16		
Overall					0.61	0.25

Table 5.3 – Results of the model for the modulation types prediction for ligands with experimental effect measured on GlyR $\alpha$ 1.

In conclusion, the use of ML techniques (e.g., PCA or regression) could already be used on a database containing ~150 ligands, to predict relatively accurately the binding sites of novel small-molecule compounds, or to filter libraries. However, the prediction of the modulatory effect with ligand-based techniques seems to be unfeasible for the moment, and justify the need to employ structure-based approaches.

### 5.3.2 A Drug Design protocol for Allosteric Protein

The recent X-ray and cryo-EM determinations of GlyR (and other pLGICs) in complex with modulatory ligands have provided a detailed topological map of the modulatory sites, which is key to search for modulators. Moreover, the ability to functionally annotate GlyR structures by MD permits to generate a conformational ensemble per functional state of the receptor. Following the MWC model of allostery, we will explore the opportunity to design PAM and NAM by screening for compounds that maximize the differential binding affinity for one conformational state of the receptor over the others, rather than optimizing it for a single conformation of the receptor. This strategy aims at the development of a new *state-based* pharmacological approach for GlyR.

From here, we will present very recent results or experiments that are currently on-going. This section is part of the perspectives.

#### 5.3.2.1 Generation of representative structures: On-going work

According to our work plan, we would need representative structures or ensembles of structures for all three functional states of GlyR. Structures obtain by cryo-EM (Du et al. 2015) or X-ray crystallography (Huang et al. 2015; Huang et al. 2017b; Huang et al. 2017a) can, of course, be used in the *v*-HTS procedure, but the instabilities in simulations, and the possible artifacts reported in Chapter 3 and 4 might justify the use of complementary structures or ensembles generated by MD. This alternate way to produce structure is particularly relevant in our case since we already proposed in Chapter 3 a methodology to functionally annotate them. For that reason, the functional states represented by the newly generated structures might be used in our state-based drug discovery approach.

The active state of GlyR $\alpha$ 1 was already largely sampled by conventional Molecular Dynamics (cMD) (several  $\mu$ s), as presented in Chapter 4. Indeed, the function of the sampled conformations was probed by *in silico* electrophysiology. Since the ion-channel remained permeable in qualitative agreement with experiments during the simulations time scale, we can conclude that the sampled conformations are constituting the active state ensemble. Because it is unfeasible to do ensemble docking and free-energy rescoring over all frames produced during MD simulations, one remaining task is to propose representative structures. This task can be achieved by doing structural clustering for each binding pocket, and choosing cluster centers as representative structures (Tian et al. 2014). The clustering has not been done yet.

Concerning the resting state, the exhaustive sampling of representative structures might be more challenging than it was for the active state, according to recent simulations of GluCl (Martin et al. 2017). Indeed, it was shown that GluCl-apo, displays a structurally diverse and highly asymmetric ECD in comparison to available experimental structures of GluCl or other pLGICs in the resting state. Based on this observation we proposed to investigate the conformational ensemble of GlyR $\alpha$ 1 resting state in the absence of strychnine (i.e., apo). Using long (1  $\mu$ s) of both cMD, or Gaussian accelerated Molecular Dynamics (GaMD) (Miao et al. 2015). Of note, the boost used in GaMD to allow an accurate reweighting of the trajectory was so small that no particular enhancement of the sampling was observed in comparison

to the cMD. Interestingly, both runs sampled two openings of subunit-subunit interfaces in the ECD, see Figure 5.5. The twist angle during the cMD simulation, is relatively close to the values measured in GluCl-apo, see Figure 5.6 (left). However, the small ECD opening observed in both runs are not sufficient to promote a large blooming motion, such as the one observed in GluCl-apo, see Figure 5.6 (right).

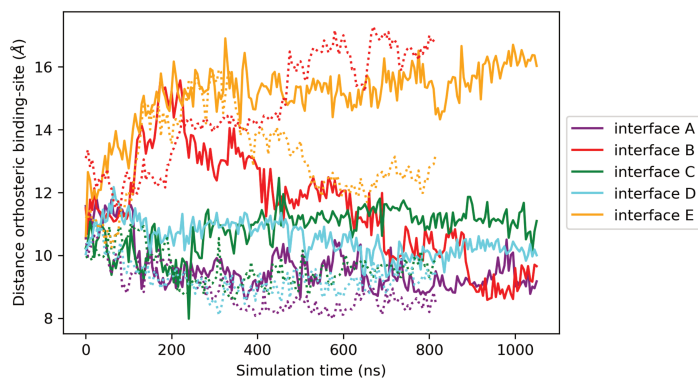


Figure 5.5 – Opening of the ECD interfaces during GlyR-apo simulations. The distance is measured at the level of the orthosteric binding site, between the  $C\alpha$  of residues in the loop B ((+)-side) and  $\beta_2$  ((-)-side), see Cecchini and Changeux 2015. Solid lines correspond to angles measured during the cMD simulation and dotted lines to the GaMD simulation. Colors are annotating the five subunit-subunit interfaces.

It is not clear for the moment if the unusually large motion observed in GluCl is a particularity of this channel, or if the sampling of apo-GlyR $\alpha$ 1 was not long enough. It is particularly difficult to answer to this question since the conformational ensemble and heterogeneity of the pLGICs resting state is vastly unexplored for the moment, which justifies extensive efforts in that direction.

To tackle this problem, we recently started to use another enhanced sampling technique, i.e., Progress-Index Guided Sampling (PIGS) (Bacci et al. 2015). This technique has the advantage to be unsupervised but needs the definition of metrics to measure the distance between structures. Then, PIGS relies on an information bias, instead of an energetic one, in order to enhance the sampling on a region of interest. In our case we defined inter-atomic distances at the subunit interfaces in the ECD in order to focus the sampling on the *blooming* motion (i.e., radial expansion of the ECD).

In the context of drug discovery and the generation of representative structures before docking, it is particularly important to avoid as much as possible the use of energetic bias because reweighting is then non-trivial and the physiological relevance of the sampled structures is unsure. In the case of PIGS, sampling follows natural fluctuations of the protein dynamics but distorts the kinetics because of the information bias. Although the proper kinetic can be recovered by doing Markov State Modelling, we will not necessarily need to do this task in order to have relevant structures describing the resting state of GlyR. Simulations using PIGS are currently on-going but it is too early to report on any relevant results.

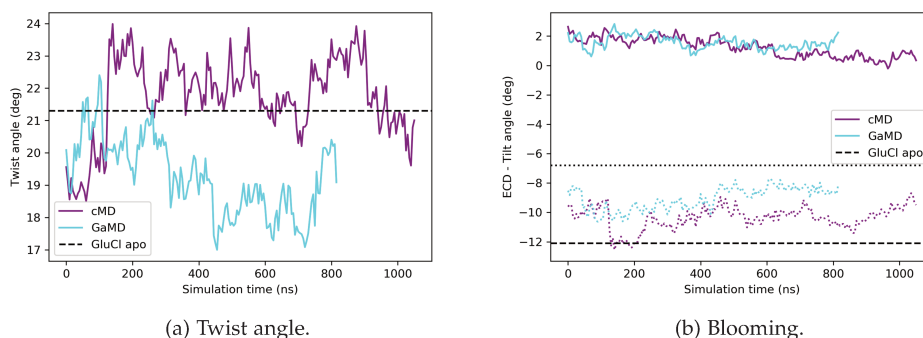


Figure 5.6 – Angles computed during GlyR-apo simulations in comparison to GluCl-apo (Martin et al. 2017). The horizontal lines refer to average values measured in GluCl-apo simulation (Martin et al. 2017). In (b), the solid lines corresponds to polar tilt of the ECD, and dotted lines to its azimuthal tilt.

Lastly, the production of the desensitized state ensemble might be as tedious as the production of the resting state, because few structural information is yet available. It seems that most of the structural changes between active and desensitized states happen in the lower part of the TMD (see Chapter 3 and Gielen and Corringer 2018). For that reason, the structural exploration of the desensitized state, starting from GlyR $\alpha$ 3 structures in the presence of AM-3607, that we classify as desensitized (see Chapter 3), will be of particular interest. Additionally to cMD, the exploration of this state might be enhanced by the use of techniques such as PIGS, by focusing the sampling on the bottom of the TMD. This work is planned for the near future.

### 5.3.2.2 State-based drug discovery: Perspectives

The perspectives of the project are to merge the information coming from the various subpart, i.e., the functional annotation (see Chapter 3), the ensembles of structures (see Chapter 4 for the active state and Chapter 5 for the resting state), and the library of known modulators (Chapter 5).

According to the functional annotation of anionic pLGICs, we proposed to generate three structural ensembles, corresponding to the three states populated by GlyR. Each ensemble will be clustered based on the binding sites geometries, then a series of representative structures will be chosen to rationalize the drug-discovery procedure. From here, it will be possible to explore in details the state-dependence in the structures of the binding sites and their featured interactions.

Lastly, the relevance of the representative structures, picked-up for each state, will be validated using our chemical library of known modulators (GRALL). This step will also be the occasion to make sure that our binding affinity estimator, e.g., MM/GBSA (Genheden and Ryde 2015) implemented in our in-house drug-design workflow, named *ChemFlow*, is appropriate to rank known modulators over decoys.

Our final goal will be to provide an automated pipeline to do ensemble docking and free-energy rescoring for all three functional states, and to prioritize compounds based on the maximization of the  $\Delta\Delta G_b$  (difference of binding free-energy), in order to predict compounds with strong modulatory effect and to predict their effect, i.e, positive vs. negative allosteric modulators. Indeed, maximizing the  $\Delta\Delta G_b$  should be a way to rationally design ligands able to shift equilibrium efficiently between all functional states, see Figure 5.7, in agreement with MWC model of allostery.

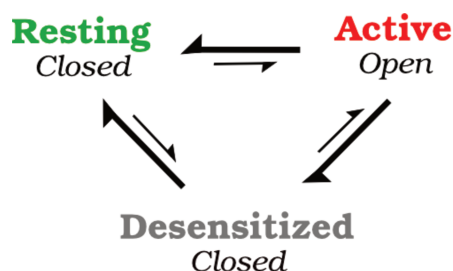


Figure 5.7 – Three-state model for pLGICs.

We note that the prediction of agonist vs. antagonist is a challenging task for computational approaches, although a recent methodology which takes advantage from the binding sites differences between active and inactive states in nuclear receptors and GPCR was able to prioritize agonists over antagonists (Lakkaraju et al. 2015).

Overall, we are still producing the representative structures for each state and preparing our pipeline. For that reasons, we have no result to show concerning the computation of  $\Delta\Delta G_b$ .

#### 5.4 CONCLUSION

The allosteric modulators developed here will have potential applications for the treatment of diseases related to the GlyR, including hyperekplexia. Of major interest, glycinergic interneurons in the spinal cord are key components of a spinal gate for pain and itch. The known role of GlyR $\alpha$ 1 and  $\alpha$ 3 in inflammatory pain and its more recently identified broader implications in pain modulation are also supported by the analgesic effects of THC, the primary psychoactive component of cannabis, and derivatives, such as 5-desoxy-THC and 1-desoxy-THC, that retain activity toward GlyR $\alpha$ 3 but do not bind to the CB<sub>1</sub> receptor (Xiong et al. 2011).

The development of a novel paradigm for the rational design of positive and negative allosteric modulators in pLGICs more generally (i.e., including nAChR and GABA<sub>A</sub>R), here termed *state-based* pharmacology, will have a significant impact not only on the academic community but also the industry and ideally, benefits to the society; the World Health Organization has predicted 82 million patients living with a form of dementia by 2030 (World-Health-Organization 2017). Thus, despite its fundamental character, the current research and their perspectives aim at establishing approaches to tackle, on the long run, neurological disorders like Alzheimer's, Parkinson's, schizophrenia, depression, and chronic pain, to pro-

vide a first answer to one of the toughest medical and economic challenge facing the global population.

PERMEATION MECHANISM OF ORGANIC CATIONS IN TRIMERIC P2X RECEPTOR

---

## 6.1 INTRODUCTION

This chapter is part of a joint effort from experimental biology and computational electrophysiology to investigate the existence of *dilated* pore in the P2XR, and lead to a shared publication with the team of Thomas Grutter of an *Article* in PNAS (Harkat et al. 2017). After a short contextualization of the project, only my results concerning the simulations will be reported here, other relevant results being cited from the published *Article*.

P2XRs are a family of cation-permeable trimeric ligand-gated ion-channels. They are activated by the extracellular ATP. Seven subtypes exist for this receptor family (P2X<sub>1-7</sub>R) and form homo- and heterotrimers. P2XRs are formed by two transmembrane helices, constituting the central ion pore. The two helices, named TM<sub>1</sub> and TM<sub>2</sub>, are linked by the ECD which is also where the ATP-binding sites are located. The P2XRs are expressed in a variety of animals and tissues. The receptors are implicated in the synaptic transmission and can be found on both the pre- and postsynaptic sides. They are involved in the physiological process in all nervous systems (central, peripheral and autonomous) to modulate the cardiac rhythm, vascular tone, pain sensation, hearing, tasting, and neurotransmitter release (North 2002; Vassort 2001; Chizh and Illes 2001).

Upon activation by ATP, the gating transition happens in the millisecond timescale and promote the opening of the ion pore to small inorganic cations, like Na<sup>+</sup>, K<sup>+</sup> and Ca<sup>2+</sup>. The single-channel conductance of P2XRs for small inorganic cation is actually quite high, with recorded values form ~10 to ~50 pS (Ding and F. Sachs 1999a; Evans 1996). This functional open state, which is relevant in the context of signal transduction is often referred to as I<sub>1</sub> state (Khakh and North 2012). However, some P2XRs are also known to populate a second open state, named I<sub>2</sub>, upon prolonged ATP exposure. Interestingly, I<sub>2</sub> displays a time-dependent pore widening, termed pore *dilation* (Virginio et al. 1999; Khakh et al. 1999; Rokic and Stojilkovic 2013). Of note, I<sub>2</sub> is thought to be permeable to large organic cations such as N-Methyl-D-glucamin (NMDG<sup>+</sup>), or ethidium bromide (YO-PRO-1) (Khakh and North 2012). Because of the larger size of the organic cations in respect to the inorganic ones, they are thought to be impermeable in I<sub>1</sub> (Browne et al. 2013). On the contrary, a recent study tends to show that changes in apparent permeability of NMDG<sup>+</sup> relative to Na<sup>+</sup>, is due to a change in intracellular concentration of these ions during patch-clamp recordings, rather than pore *dilation* (Li et al. 2015). This observation is at least consistent with the lack of crystal structures or single-channel experiments supporting the dilated state I<sub>2</sub> (Ding and F. Sachs 1999b; Riedel et al. 2007). The subject of our project was to challenge further the existence, and the physiological relevance of the dilated stated in P2XR by various techniques.

From their work, our collaborators, notably showed that using outside-out patch-clamp experiments in single-channel conditions, the P2X<sub>2</sub>R is simultaneously permeable to Na<sup>+</sup> and NMDG<sup>+</sup> (Harkat et al. 2017). By optimizing the patch-clamp recording setup they were able to measure the NMDG<sup>+</sup> conductance to  $3.3 \pm 0.6$  pS which is one-fold less permeable than Na<sup>+</sup> ( $44 \pm 8$  pS) (Harkat et al. 2017). Overall, the kinetics of gating is in the millisecond time scale, but the permeation rate is about ten times lower for large organic cations in comparison to small inorganic ones.

Additionally, our collaborators re-used their *opto-tweezer* strategy (Habermacher et al. 2016) to probe the molecular mechanism responsible for a pore opening permeable to NMDG<sup>+</sup>. By using three photo-linkers of various sized (named 4,4'-bis(maleimido-glycine)azobenzene (MAM)<sub>1-3</sub>) either in a vertical position or horizontal one along the pore, they were able to control with light the gating of the pore. Interestingly, all mutants were still responsive to ATP and permeable to NMDG<sup>+</sup>. Moreover, the mutants that were permeable to NMDG<sup>+</sup> by light-gating, were also permeable to Na<sup>+</sup>, supporting the idea that the molecular mechanism responsible for the permeability of both cations are similar (Harkat et al. 2017). Of note, among the 11 combinations that were permeable to Na<sup>+</sup> upon light-gating, three of them were not permeable to NMDG<sup>+</sup>. But the physiological relevance of such *partially-open* state is presently unclear (Harkat et al. 2017).

Since the permeation mechanism itself seems to be the reason for different kinetics between Na<sup>+</sup> and NMDG<sup>+</sup>, we proposed to use MD simulations to investigate it.

## 6.2 METHODS

The modeling of the zf-P2X<sub>4</sub>R in the presence of the MAM photo-linkers was produced and relaxed by my colleague Nicolas Calimet, and all details can be found in (Harkat et al. 2017).

The double mutant with MAM<sub>2</sub> linking residues 336 and 353 (equivalent to 328 – 345 in r-P2X<sub>2</sub>R) displayed an excellent representativity of the physiological ATP-gated open pore (Harkat et al. 2017). For that reason, this model relaxed with MAM<sub>2</sub> in the *cis* conformation was used as a model for the open state of the P2X<sub>4</sub>R, since strong doubts were emitted (Heymann et al. 2013; Habermacher et al. 2016) concerning the physiological relevance of the X-ray structure of this receptor (Hattori and Gouaux 2012). In order to probe the permeability of organic cations, a couple of modifications were introduced in respect to the original model. First, the MAM<sub>2</sub> linkers were removed, while keeping the mutated residues 336 and 353 into cysteines, in order to mimic more closely the physiological conditions. Since the initial models of the ion pore were only transiently stable without positional restrains (Habermacher et al. 2016), we would need to maintain such restrains. Then, we profited from the situation to remove the ECD and to fuse the two part of the TMD by a peptide bond between D59 and F333. This *optimization* allowed a reduction of the simulation box from ~140,000 atoms to ~90,000 atoms, hence, focusing the sampling on permeation events through the ion pore. Similar MD protocol was used as in Chapter 3 and 4 for GlyR. The simulation boxes were initially solvated with either 0.15 or 1 M of NaCl. Na<sup>+</sup> were replaced by either NMDG<sup>+</sup>,

YO-PRO-1<sup>2+</sup>, or Spermidine (SPD<sup>3+</sup>). The number of chlorides was adjusted in function of the cation nature in order to preserve the system's electroneutrality. Parameters for the three organic cations were obtained with CGenFF web-server. The constant electric field method was used to impose a membrane potential of  $-2$ ,  $-1.5$ , and  $-1$  V. Analysis of ion permeation mechanism was done with Tcl scripting in VMD. We defined two observables to describe the mechanism of permeation. First, the end-to-end distance corresponds to the distance between the two terminal carbons of NMDG<sup>+</sup> and was computed for each trajectory frames. Second, the horizontality is computed by selecting a vector from the center of mass of the molecule to the terminal carbon linked to the nitrogen, and then computing the complement of the polar angle. Finally, the center-of-mass of permeant cations is plotted in function of the two other observables.

### 6.3 RESULTS AND DISCUSSION

#### 6.3.1 Permeation mechanism of NMDG

In order to investigate the permeation mechanism of NMDG<sup>+</sup> through an open conformation of zf-P2X<sub>4</sub>R (see *Methods*) we choose to use all-atom MD in the presence of a membrane potential arising from the application of a constant electric field. To observe some permeation events in a short time scale (i.e.,  $< 50$  ns) we applied a series of high membrane potentials (i.e.,  $-1$ ,  $-1.5$ ,  $-2$  V) with an ionic concentration of 0.15 or 1 M. First and foremost, our simulation demonstrated a consistent permeability of the open model of zf-P2X<sub>4</sub>R to both Na<sup>+</sup> and NMDG<sup>+</sup> (See Figure 6.1 and Table 6.1).

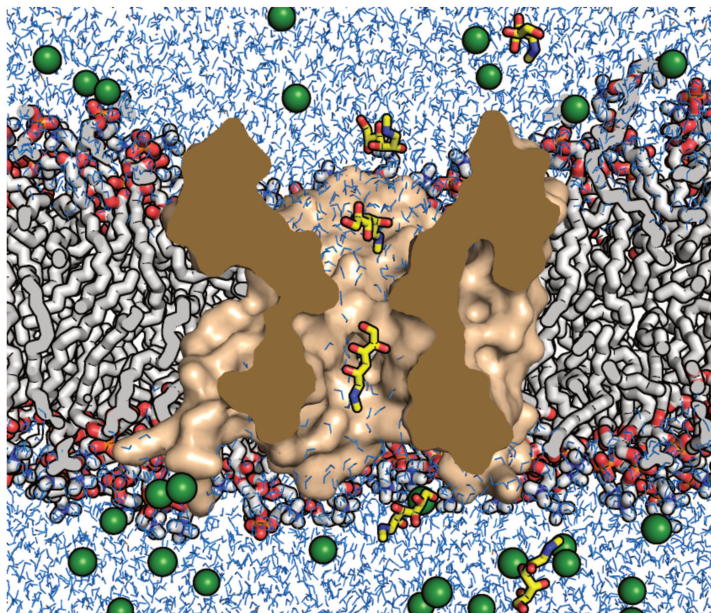


Figure 6.1 – Series of snapshots during the permeation of NMDG<sup>+</sup> through the TMD of zf-P2X<sub>4</sub>R in all-atom MD simulation, in presence of a constant electric field.

Within this condition, we could roughly estimate that the conductance of  $\text{NMDG}^+$  is about one order of magnitude lower than the one of  $\text{Na}^+$ . However, this analysis is rather qualitative due to the small number of events and the high membrane potential used to enhance the sampling (see Table 6.1).

Voltage (V)	Concentration (M)	Number of $\text{NMDG}^+$ permeation (in $\times \text{ns}$ )	Number of $\text{Na}^+$ permeation (in $\times \text{ns}$ )
-2	0.15	2 (10)	N.D.
-1.5	0.15	3 (10)	N.D.
-1	0.15	1 (25)	N.D.
-1	1	3 (45)	11 (20)

Table 6.1 – Summary of the permeation events of  $\text{Na}^+$  and  $\text{NMDG}^+$  in the open pore conformation of zf-P2X<sub>4</sub>R.

This interesting founding is qualitatively supporting by the single-channel electrophysiological experiments of our collaborators that showed similar relative permeation rates between  $\text{Na}^+$  and  $\text{NMDG}^+$ . The usefulness of our approach is to be able to extract a mechanism of permeation from the all-atom MD trajectories.

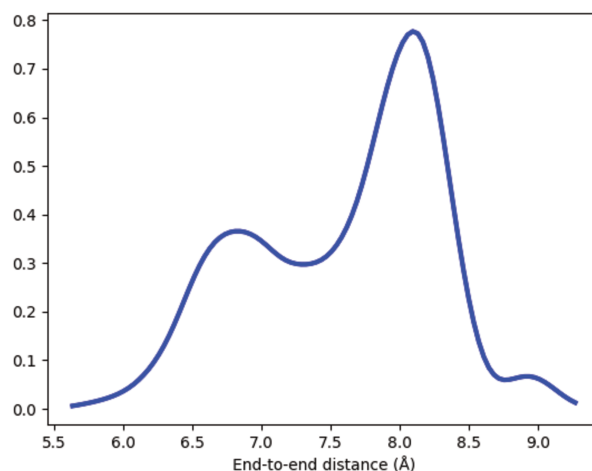


Figure 6.2 – Probability density of the *end-to-end* distance of  $\text{NMDG}^+$  during a control simulation (500 ns) of one cation in explicit solvent.

According to the control simulation of  $\text{NMDG}^+$  in solution, two conformations can be spontaneously populated. The newly designed observable *End-to-End* distance (see *Methods*) allow us to characterize this two states, see Figure 6.2. On the contrary, the second observable, i.e., the horizontality is not informative since the molecule is free to rotate.

In order to elucidate the mechanism of permeation, we computed at each frame of the trajectories the two observables for all permeant  $\text{NMDG}^+$  molecules (see Figure 6.3).

Of note, it is interesting to observe that both the elongation and orientation of the  $\text{NMDG}^+$  molecules are untouched by the electric field, when the cation is in the bulk environment

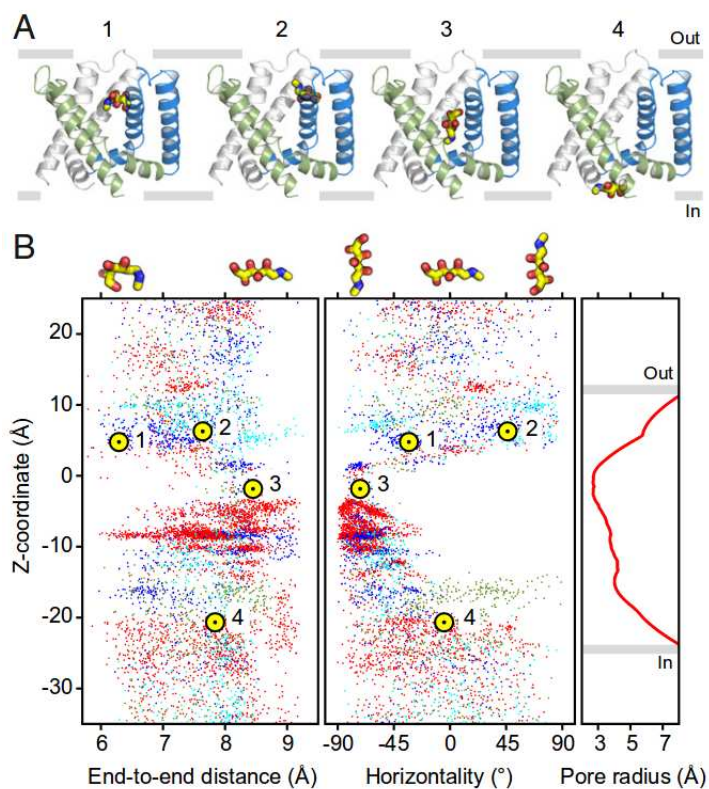


Figure 6.3 – (A) Selection of snapshot depicting the various stage of the permeation of one NMDG<sup>+</sup> molecule through the open pore of zf-P2X<sub>4</sub>R. (B) Molecular mechanism of the NMDG<sup>+</sup> permeation. (Left) *End-to-end* distance of NMDG<sup>+</sup>. (Middle) *horizontality* of NMDG<sup>+</sup> measured as the angle formed between the longitudinal axis of the cation and the axis normal to the membrane. (Right) HOLE profile of zf-P2X<sub>4</sub>R open conformation after 50 ns of equilibration. From Harkat et al. 2017.

(see Figure 6.3 for  $z > 10$  or  $z < -20$  Å). This observation is critical because it supports the idea that even a strong membrane potential (from  $-1$  to  $-2$  V) can preserve the permeation mechanism, although the high of the free-energy barriers will be lowered significantly.

From Figure 6.3 it is clear that NMDG<sup>+</sup> molecules have to undergo under a stringent selectivity filter at the level of the constriction point in the zf-P2X<sub>4</sub>R ion pore. More precisely, NMDG<sup>+</sup> permeation is only possible when the cation is in a fully extended form ( $d > 7.5$  Å), in addition to be in a vertical orientation with the charged nitrogen facing downward along the electrochemical gradient ( $\theta < -50^\circ$ ), see Figure 6.3. The analysis of this two observables allowed us to describe the constriction point of P2X<sub>4</sub>R playing a role of conformational and orientational filter on against the permeation of NMDG<sup>+</sup>. It is obvious that small inorganic cations, such as Na<sup>+</sup>, cannot be described by these two observables since they are monoatomic and fully isotropic. This observation implies that the conformational and orientational barriers only exist for NMDG<sup>+</sup> and not for Na<sup>+</sup> which permits to provide a qualitative explanation for the order of magnitude difference in the permeation kinetic observed in simulation and experimentally. NMDG<sup>+</sup> has to sample many conformations and orientations before to being able to initiate the permeation along the pore of zf-P2X<sub>4</sub>R, which hinders its permeability and supports its low unitary single-channel conductance in respect to Na<sup>+</sup>. Altogether, our results are consistent with the idea that the open-channel state elicited by MAM is permeable to organic and inorganic cations. Also, our data provide an atomistic description of the permeation mechanism.

Of note, we were not able, in contrary to experiments, to observe permeation of YO-PRO-1 through the membrane. Two reasons can explain this observation. First, the time scale of our simulations was rather short ( $< 50$  ns), which might be insufficient to allow the permeation of large molecules such as a fluorescent dye. Second, we observed in simulation an important effect of aggregation of the dye, due to its chemical nature, which prevent permeation through the pore.

### 6.3.2 Permeation mechanism of Spermidine

After having demonstrated that rapid activation of P2XRs allows the permeation of organic cations, our colleagues proposed to investigate the permeability of natural organic cations. They chose to study the permeability of P2XRs to Spermidine, which is a positively charge organic cation of similar size to NMDG<sup>+</sup>. It is interesting to note that Spermidine is a natural polyamine known to module the function of many ion channels (Guerra et al. 2016), which is of principal interest in the context of synaptic transmission.

First, and in agreement with our experimental collaborators, we showed that spermidine could permeate through the open pore of zf-P2X<sub>4</sub>R. Interestingly our simulations showed that at a similar membrane potential, spermidine is about seven-fold faster to permeate than NMDG<sup>+</sup>, despite their similar size. Of note, at physiological pH, we estimated that spermidine would carry three positive charges (SPD<sup>3+</sup>) in comparison to NMDG cation, which carries only one charge. For that reason, it might be delicate to directly compare the permeation rate for spermidine with the one of NMDG<sup>+</sup>. What is clear, however, is that the complex

mechanism hindering the permeation of  $\text{NMDG}^+$  almost vanish in the case of spermidine. In fact, due to the molecular structure of spermidine, we can anticipate that both conformational and orientational selectivity vanish. First, the spermidine is almost symmetric and carry a charged nitrogen at both extremities which allow the spermidine to go through the pore in a vertical orientation but irrespectively to the terminal part of the molecule facing downward. Additionally, the presence of two charged at the extremities, and one in the middle, of the molecule would favor and elongated conformation because of charge-charge repulsion. In conclusion, the chemical nature of spermidine bypass the conformational and orientational selection applied to  $\text{NMDG}^+$  and could explain its higher permeation rate in respect to  $\text{NMDG}^+$ . On the other side, the impact of the number of positive charges on spermidine on the permeation is not clear and might have been tackled by repeating the simulations with  $\text{SPD}^{2+}$ .

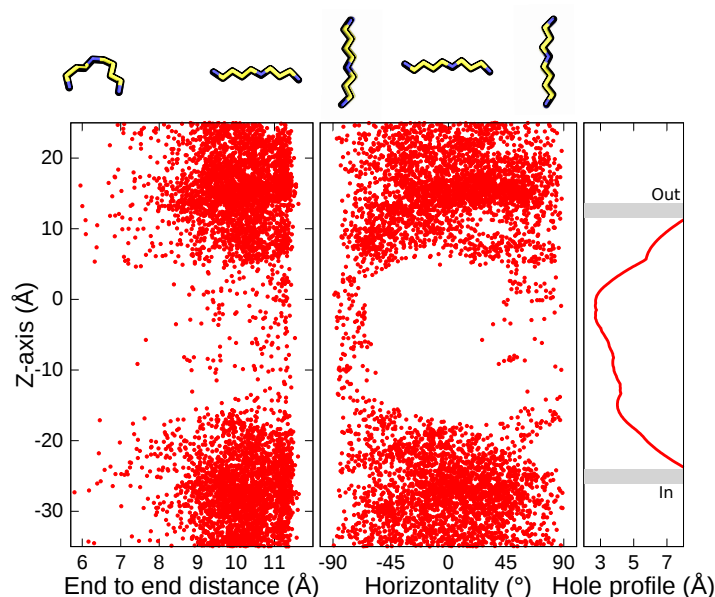


Figure 6.4 – Molecular mechanism of the  $\text{SPD}^{3+}$  permeation through the open-pore of zf-P2X<sub>4</sub>R. (Left) *End-to-end* distance of  $\text{SPD}^{3+}$ . (Middle) *horizontality* of  $\text{SPD}^{3+}$  measured as the angle formed between the longitudinal axis of the cation and the axis normal to the membrane. (Right) HOLE profile of zf-P2X<sub>4</sub>R open conformation after 50 ns of equilibration.

This result might be significant since it would uncover a novel signaling role for P2XRs in which large organic molecules, such as spermidine, can rapidly permeate through the ATP-gated ion pore.

#### 6.4 CONCLUSION

The current paradigm in favor of the pore dilation in ionotropic purinergic receptor states that during prolonged exposition to ATP the ion pore will become increasingly wider until the pore can accommodate the permeation of large organic cation such as  $\text{NMDG}^+$  or

YO-PRO-1. However, a recent study went against this view and showed that P2XRs rapidly present a NMDG<sup>+</sup> current, without a slow phase, corresponding to the pore dilation (Li et al. 2015). Our collaborative work is consistent with this study, and altogether, they strongly demonstrate that the open-state reached in milliseconds after ATP exposure is immediately permeable to organic cations, such as NMDG<sup>+</sup>, in strong contraction to earlier beliefs. This finding is consistent with the X-ray structures of the open-pore conformation available for zf-P2X<sub>4</sub>R (Hattori and Gouaux 2012) and the human P2X<sub>3</sub>R (Mansoor et al. 2016) receptors. Indeed, the minimal cross-section of NMDG<sup>+</sup> ( $6 \times 6 \times 12.5 \text{ \AA}$ ) is smaller than the diameter of the pore at the constriction point (7 and  $6.4 \text{ \AA}$  in zf-P2X<sub>4</sub>R and h-P2X<sub>3</sub>R, respectively). However, we investigated the permeability of the improved model of the open-pore of zf-P2X<sub>4</sub>R (Habermacher et al. 2016), stabilized in the presence of three vertically cross-linked MAM<sub>2</sub> molecules. This decision was motivated by the instability of the X-ray structure in simulation and its possibly non-physiological arrangement of the TMD (Heymann et al. 2013; Habermacher et al. 2016). Besides, the conformation adopted by the ion pore in the presence of MAM<sub>2</sub> can be accurately controlled experimentally, which allows a straightforward interpretation of both experimental and computational results on the permeation of organic cations. Indeed, both experimentally (Harkat et al. 2017) and computationally, we showed that the open-pore conformation adopted by P2XRs vertically cross-linked by MAM<sub>2</sub> molecules is permeable to large organic cation (i.e., NMDG<sup>+</sup> and SPD<sup>3+</sup>). Also, our simulations permit to identify the origins of the smaller unitary current of NMDG<sup>+</sup> in respect to Na<sup>+</sup> and SPD<sup>3+</sup>.

In conclusion, our results and the ones of Li et al. 2015 are going against the paradigm of pore dilation in P2XRs, supporting the idea that the first open state reached during activation is already permeable to organic cations and do not undergo a time-dependent widening, supposedly increasing the permeability to organic cations. Finally, by identifying spermidine, a natural polyamine cation involve in ion-channel regulation, we propose that the P2XRs might be involved in alternative signaling pathways. Notably, the P2XRs were recently used to deliver membrane-impermeable drugs in the retina (Tochitsky et al. 2016), exploiting their wide-pore, opening novel route for drug delivery.

CONCLUSIONS AND PERSPECTIVES

---

Ionotropic receptors are widely expressed in the central nervous system and play a crucial role in the fast chemical synapses. Because of their central role in the physiological function of the central nervous system, they are also implicated in many of the neurological disorders that afflict humans. For that reason, it is necessary to aim at developing novel therapeutics for that disorders, targeting the ionotropic receptors.

To rationally develop small-molecule compounds able to modulate the function of allosteric protein such as these receptors, it is needed to have faithful models of the protein in its physiological conformations. We have access to a broad set of experimentally solved structures representing pentameric ligand-gated ion channels, although the most recent structures display an important heterogeneity. The novel GABA<sub>A</sub>R structures are dissimilar because of their heteromeric nature (Phulera et al. 2018; Zhu et al. 2018). Two recently published structures of 5-HT<sub>3</sub>R were annotated as representative of the active state (Basak et al. 2018a; Polovinkin et al. 2018), however, they are not structurally identical, at the level of the TMD. The GlyR $\alpha$ 1 suffered from a similar problem since two structures solved by cryo-EM could have been compatible with an open state (Du et al. 2015).

Because it is infeasible to build a clear three-state model of the gating mechanism in pentameric ligand-gated ion channels, using several and sometimes, different representation of the active state, one need to prune the available structures. For that reason, we used Molecular Dynamics and computational electrophysiology to reproduce *in silico* the single-channel experiments carried out in *wet lab*. Ion channels are, indeed, one of the best systems to study their function at the single-molecule scale, both experimentally and computationally.

In Chapter 3, we showed that none of the experimentally solved cryo-EM structures of GlyR $\alpha$ 1 can reproduce the physiological function of the ion pore in its active state. However, we captured and characterized a novel model of GlyR $\alpha$ 1, featuring a local and dynamical asymmetry in the organization of the residues forming the gate, which reproduce best the single-channel properties. Based on these results, it has been possible to elaborate a functional annotation of anionic pLGICs, highlighting the three physiological states.

In Chapter 4, we pursued our investigation on the GlyR $\alpha$ 1 active state, using the *full-length* receptor. We demonstrated the major role of lateral portals located in the ECD to permit the synaptic transmission. Indeed, in GlyR the apex of the channel seems mostly impermeable to chlorides which have to permeate through these lateral openings. We also reexplored the impact of a mutation that can *gate* these portals. Finally, we proposed a unified role of the ECD and ICD on the conductance modulation; which is appended to their known role on ligand-binding and intracellular trafficking, respectively.

In Chapter 5, we employed the previous results on the functional-annotation of structures to propose an original *state-based pharmacology* protocol. This methodology relies on the existence of functionally annotated structures representing the three states populated by pLGIC

and to prioritize small-molecule compounds that maximize the  $\Delta\Delta G_b$  for one state over the other, in order to promote a population shift, in agreement with MWC model of allostery. For that purpose, we compiled a chemical library of known small-molecule modulators of the function of GlyR $\alpha 1 - 3$ . Besides, we started *in silico* to produce an ensemble of representative structures for the three states. This work is currently in production for the resting state and has to be similarly processed for the desensitized one.

Lastly, in Chapter 6, we used computational electrophysiology to provide an atomistic description of the permeation mechanism of large organic cations through the open-pore of P2X<sub>4</sub>R. This atomistic view on the permeation mechanism helped at interpreting the low unitary current of organic cations with respect to the inorganic ones. Additionally, we participated in the identification of the natural organic cation spermidine, which is permeable in P2XR open pore and capable of modulating the function of several ion channels. This critical finding extends the role of P2XR in synaptic transmission.

To conclude, the work presented in this thesis helps at understanding the fundamental role of ionotropic receptors in the synaptic transmission. This work also strengthens the relevance of gating mechanisms that are based on structures that can be functionally annotated.

We will continue to explore the permeation mechanism in pLGICs, especially with the future release of anionic pLGICs structure in the presence of the ICD. It is, indeed, particularly important to have access to the protein physiological construct in order to propose a complete permeation mechanism, and to confidently explore the desensitized state.

Despite its fundamental aspect, our work is directly related to sensible applications in the context of drug design. Because of the significant implication of pLGICs on human brain disorders, it is ethically needed to invest effort into that direction, especially since several big pharmaceutical industries interrupted, in the past years, their investment in their neuroscience departments. The GlyR is a particularly relevant target to treat chronic inflammatory pains. This affliction is poorly treated for the moment, and the commercially available drugs have significant side-effects and are often misused, resulting in the opioids epidemics in North America. For all these reasons, our primary focus is now to complete our protocol for *state-based pharmacology*, in order to propose a novel paradigm for drug discovery in allosteric protein.

## BIBLIOGRAPHY

---

- Abascal, J. L. F. and C. Vega (2005). "A general purpose model for the condensed phases of water: TIP4P/2005". In: *The Journal of Chemical Physics* 123.23, p. 234505.
- Ahrens, J., G. Haeseler, M. Leuwer, B. Mohammadi, K. Krampfl, R. Dengler, and J. Bufler (2004). "2,6-Di-tert-butylphenol, a Nonanesthetic Propofol Analog, Modulates  $\alpha 1\beta$  Glycine Receptor Function in a Manner Distinct from Propofol". In: *Anesthesia & Analgesia* 99.1, pp. 91–96.
- Aksimentiev, A. and K. Schulten (2005). "Imaging alpha-hemolysin with molecular dynamics: ionic conductance, osmotic permeability, and the electrostatic potential map". eng. In: *Biophysical Journal* 88.6, pp. 3745–3761.
- Allen, T. W., O. S. Andersen, and B. Roux (2004). "On the Importance of Atomic Fluctuations, Protein Flexibility, and Solvent in Ion Permeation". In: *The Journal of General Physiology* 124.6, pp. 679–690.
- Althoff, T., R. E. Hibbs, S. Banerjee, and E. Gouaux (2014). "X-ray structures of GluCl in apo states reveal gating mechanism of Cys-loop receptors". In: *Nature* 512.7514, pp. 333–337.
- Armstrong, C. M. and L. Binstock (1965). "Anomalous Rectification in the Squid Giant Axon Injected with Tetraethylammonium Chloride". In: *The Journal of General Physiology* 48.5, pp. 859–872.
- Aryal, P., M. S. P. Sansom, and S. J. Tucker (2015). "Hydrophobic Gating in Ion Channels". In: *Journal of Molecular Biology*. Understanding Functions and Mechanisms of Ion Channels 427.1, pp. 121–130.
- Augustine, G. J., M. P. Charlton, and S. J. Smith (1985). "Calcium entry into voltage-clamped presynaptic terminals of squid." In: *The Journal of Physiology* 367, pp. 143–162.
- Augustine, G. J. and R. Eckert (1984). "Divalent cations differentially support transmitter release at the squid giant synapse". eng. In: *The Journal of Physiology* 346, pp. 257–271.
- Bacci, M., A. Vitalis, and A. Caflich (2015). "A molecular simulation protocol to avoid sampling redundancy and discover new states". In: *Biochimica et Biophysica Acta (BBA) - General Subjects* 1850.5, pp. 889–902.
- Bakas, T., P. van Nieuwenhuijzen, S. Devenish, I. McGregor, J. Arnold, and M. Chebib (2017). "The direct actions of cannabidiol and 2-arachidonoyl glycerol at GABAA receptors". In: *Pharmacological Research* 119, pp. 358–370.
- Baker, N. A., D. Sept, S. Joseph, M. J. Holst, and J. A. McCammon (2001). "Electrostatics of nanosystems: Application to microtubules and the ribosome". en. In: *Proceedings of the National Academy of Sciences* 98.18, pp. 10037–10041.
- Balansa, W., R. Islam, F. Fontaine, A. M. Piggott, H. Zhang, X. Xiao, T. I. Webb, D. F. Gilbert, J. W. Lynch, and R. J. Capon (2013a). "Sesterterpene glycinyl-lactams: A new class of glycine receptor modulator from Australian marine sponges of the genus Psammocinia". In: *Organic and Biomolecular Chemistry* 11.28, pp. 4695–4701.
- Balansa, W., R. Islam, D. F. Gilbert, F. Fontaine, X. Xiao, H. Zhang, A. M. Piggott, J. W. Lynch, and R. J. Capon (2013b). "Australian marine sponge alkaloids as a new class of glycine-gated chloride channel receptor modulator". In: *Bioorganic and Medicinal Chemistry* 21.14, pp. 4420–4425.
- Bartheld, C. S. von, J. Bahney, and S. Herculano-Houzel (2016). "The search for true numbers of neurons and glial cells in the human brain: A review of 150 years of cell counting". en. In: *Journal of Comparative Neurology* 524.18, pp. 3865–3895.
- Basak, S., Y. Gicheru, S. Rao, M. S. P. Sansom, and S. Chakrapani (2018a). "Cryo-EM reveals two distinct serotonin-bound conformations of full-length 5-HT<sub>3A</sub> receptor". In: *Nature* 563.7730, pp. 270–274.
- Basak, S., Y. Gicheru, A. Samanta, S. K. Molugu, W. Huang, M. la de Fuente, T. Hughes, D. J. Taylor, M. T. Nieman, V. Moiseenkova-Bell, and S. Chakrapani (2018b). "Cryo-EM structure of 5-HT<sub>3A</sub> receptor in its resting conformation". En. In: *Nature Communications* 9.1, p. 514.
- Bashford, D. and M. Karplus (1990). "pKa's of ionizable groups in proteins: atomic detail from a continuum electrostatic model". In: *Biochemistry* 29.44, pp. 10219–10225.
- Bashford, D. and M. Karplus (1991). "Multiple-site titration curves of proteins: an analysis of exact and approximate methods for their calculation". In: *The Journal of Physical Chemistry* 95.23, pp. 9556–9561.
- Beckstein, O. and M. S. P. Sansom (2006). "A hydrophobic gate in an ion channel: the closed state of the nicotinic acetylcholine receptor". en. In: *Physical Biology* 3.2, p. 147.
- Berthold, M. R., N. Cebron, F. Dill, T. R. Gabriel, T. Kötter, T. Meinl, P. Ohl, C. Sieb, K. Thiel, and B. Wiswedel (2008). "KNIME: The Konstanz Information Miner". In: Springer, Berlin, Heidelberg, pp. 319–326.
- Best, R. B., X. Zhu, J. Shim, P. E. M. Lopes, J. Mittal, M. Feig, and A. D. MacKerell (2012). "Optimization of the additive CHARMM all-atom protein force field targeting improved sampling of the backbone  $\phi$ ,  $\psi$  and side-chain  $\chi_1$  and  $\chi_2$  dihedral angles". In: *Journal of chemical theory and computation* 8.9, pp. 3257–3273.
- Betz, H. and B. Laube (2006). "Glycine receptors: recent insights into their structural organization and functional diversity". In: *Journal of Neurochemistry* 97.6, pp. 1600–1610.
- Bocquet, N., H. Nury, M. Baaden, C. Le Poupon, J.-P. Changeux, M. Delarue, and P.-J. Corringer (2009). "X-ray structure of a pentameric ligand-gated ion channel in an apparently open conformation". eng. In: *Nature* 457.7225, pp. 111–114.

- Bode, A. and J. W. Lynch (2014). "The impact of human hyperekplexia mutations on glycine receptor structure and function". In: *Molecular Brain* 7, p. 2.
- Bormann, J., O. P. Hamill, and B. Sakmann (1987). "Mechanism of anion permeation through channels gated by glycine and gamma-aminobutyric acid in mouse cultured spinal neurones." In: *The Journal of Physiology* 385, pp. 243–286.
- Bormann, J., N. Rundström, H. Betz, and D. Langosch (1993). "Residues within transmembrane segment M2 determine chloride conductance of glycine receptor homo- and hetero-oligomers." In: *The EMBO Journal* 12.10, pp. 3729–3737.
- Braat, S. and R. F. Kooy (2015). "The GABAA Receptor as a Therapeutic Target for Neurodevelopmental Disorders". eng. In: *Neuron* 86.5, pp. 1119–1130.
- Brams, M., E. A. Gay, J. C. Sáez, A. Guskov, R. van Elk, R. C. van der Schors, S. Peigneur, J. Tytgat, S. V. Strelkov, A. B. Smit, J. L. Yakel, and C. Ulens (2011). "Crystal Structures of a Cysteine-modified Mutant in Loop D of Acetylcholine-binding Protein". In: *Journal of Biological Chemistry* 286.6, pp. 4420–4428.
- Bregman, H., J. R. Simard, K. L. Andrews, S. Ayube, H. Chen, H. Gunaydin, A. Guzman-Perez, J. Hu, L. Huang, X. Huang, P. H. Krolikowski, S. G. Lehto, R. T. Lewis, K. Michelsen, P. Pegman, M. H. Plant, P. L. Shaffer, Y. Teffer, S. Yi, M. Zhang, J. Gingras, and E. F. DiMauro (2017). "The Discovery and Hit-to-Lead Optimization of Tricyclic Sulfonamides as Potent and Efficacious Potentiators of Glycine Receptors". In: *Journal of Medicinal Chemistry* 60.3, pp. 1105–1125.
- Brisson, A. and P. N. Unwin (1985). "Quaternary structure of the acetylcholine receptor". eng. In: *Nature* 315.6019, pp. 474–477.
- Brooks, B. R., C. L. Brooks, A. D. Mackerell, L. Nilsson, R. J. Petrella, B. Roux, Y. Won, G. Archontis, C. Bartels, S. Boresch, A. Caflisch, L. Caves, Q. Cui, A. R. Dinner, M. Feig, S. Fischer, J. Gao, M. Hodoscek, W. Im, K. Kuczera, T. Lazaridis, J. Ma, V. Ovchinnikov, E. Paci, R. W. Pastor, C. B. Post, J. Z. Pu, M. Schaefer, B. Tidor, R. M. Venable, H. L. Woodcock, X. Wu, W. Yang, D. M. York, and M. Karplus (2009). "CHARMM: the biomolecular simulation program". eng. In: *Journal of Computational Chemistry* 30.10, pp. 1545–1614.
- Browne, L. E., V. Compan, L. Bragg, and R. A. North (2013). "P2X7 receptor channels allow direct permeation of nanometer-sized dyes." In: *The Journal of neuroscience : the official journal of the Society for Neuroscience* 33.8, pp. 3557–66.
- Brünger, A., C. L. Brooks, and M. Karplus (1984). "Stochastic boundary conditions for molecular dynamics simulations of ST2 water". In: *Chemical Physics Letters* 105.5, pp. 495–500.
- Burzomato, V., P. J. Groot-Kormelink, L. G. Sivilotti, and M. Beato (2003). "Stoichiometry of recombinant heteromeric glycine receptors revealed by a pore-lining region point mutation". eng. In: *Receptors & Channels* 9.6, pp. 353–361.
- Calimet, N., M. Simoes, J.-P. Changeux, M. Karplus, A. Taly, and M. Cecchini (2013). "A gating mechanism of pentameric ligand-gated ion channels". In: *Proceedings of the National Academy of Sciences* 110.42, E3987–E3996.
- Carland, J. E., M. A. Cooper, S. Sugiharto, H.-J. Jeong, T. M. Lewis, P. H. Barry, J. A. Peters, J. J. Lambert, and A. J. Moorhouse (2009). "Characterization of the effects of charged residues in the intracellular loop on ion permeation in alpha1 glycine receptor channels". eng. In: *The Journal of Biological Chemistry* 284.4, pp. 2023–2030.
- Castillo, J. del and B. Katz (1954). "Quantal components of the end-plate potential". In: *The Journal of Physiology* 124.3, pp. 560–573.
- Cecchini, M. and J.-P. Changeux (2015). "The nicotinic acetylcholine receptor and its prokaryotic homologues: Structure, conformational transitions & allosteric modulation". In: *Neuropharmacology. The Nicotinic Acetylcholine Receptor: From Molecular Biology to Cognition* 96, Part B, pp. 137–149.
- Cerdan, A. H., N. É. Martin, and M. Cecchini (2018). "An Ion-Permeable State of the Glycine Receptor Captured by Molecular Dynamics". In: *Structure* 26.11, 1555–1562.e4.
- Chakka, N., K. L. Andrews, L. M. Berry, H. Bregman, H. Gunaydin, L. Huang, A. Guzman-Perez, M. H. Plant, J. R. Simard, J. Gingras, and E. F. DiMauro (2017). "Applications of parallel synthetic lead hopping and pharmacophore-based virtual screening in the discovery of efficient glycine receptor potentiators". In: *European Journal of Medicinal Chemistry* 137, pp. 63–75.
- Changeux, J.-P., M. Kasai, M. Huchet, and J. C. Meunier (1970a). "Extraction à partir du tissu électrique de gymnote d'une protéine présentant plusieurs propriétés caractéristiques du récepteur physiologique de l'acétylcholine". In: *CR Acad Sci Hebd Seances Acad Sci D* 270.23, pp. 2864–2867.
- Changeux, J.-P., M. Kasai, and C. Y. Lee (1970b). "Use of a snake venom toxin to characterize the cholinergic receptor protein". eng. In: *Proceedings of the National Academy of Sciences of the United States of America* 67.3, pp. 1241–1247.
- Changeux, J.-P. and S. J. Edelstein (2005). "Allosteric Mechanisms of Signal Transduction". In: *Science* 308.5727, pp. 1424–1428.
- Chesnoy-Marchais, D. and L. Cathala (2001). "Modulation of glycine responses by dihydropyridines and verapamil in rat spinal neurons". In: *European Journal of Neuroscience* 13.12, pp. 2195–2204.
- Chizh, B. A. and P. Illes (2001). "P2X receptors and nociception." In: *Pharmacological reviews* 53.4, pp. 553–68.
- Chung, S.-H. and B. Corry (2005). "Three computational methods for studying permeation, selectivity and dynamics in biological ion channels". en. In: *Soft Matter* 1.6, pp. 417–427.
- Chung, S.-H., M. Hoyles, T. Allen, and S. Kuyucak (1998). "Study of Ionic Currents across a Model Membrane Channel Using Brownian Dynamics". In: *Biophysical Journal* 75.2, pp. 793–809.
- Corry, B., S. Kuyucak, and S. H. Chung (2000). "Tests of continuum theories as models of ion channels. II. Poisson-Nernst-Planck theory versus brownian dynamics." In: *Biophysical journal* 78.5, pp. 2364–81.
- Crozier, P. S., D. Henderson, R. L. Rowley, and D. D. Busath (2001). "Model channel ion currents in NaCl-extended simple point charge water solution with applied-field molecular dynamics". eng. In: *Biophysical Journal* 81.6, pp. 3077–3089.

- Curtis, D. R., L. Hösl, and G. A. Johnston (1967). "Inhibition of spinal neurons by glycine". eng. In: *Nature* 215.5109, pp. 1502–1503.
- Curtis, D. R., L. Hösl, and G. a. R. Johnston (1968). "A pharmacological study of the depression of spinal neurones by glycine and related amino acids". en. In: *Experimental Brain Research* 6.1, pp. 1–18.
- Cymes, G. D. and C. Grosman (2016). "Identifying the elusive link between amino acid sequence and charge selectivity in pentameric ligand-gated ion channels". en. In: *Proceedings of the National Academy of Sciences* 113.45, E7106–E7115.
- Delemotte, L., F. Dehez, W. Treptow, and M. Tarek (2008). "Modeling Membranes under a Transmembrane Potential". In: *The Journal of Physical Chemistry B* 112.18, pp. 5547–5550.
- Di Maio, D., B. Chandramouli, and G. Brancato (2015). "Pathways and Barriers for Ion Translocation through the 5-HT<sub>3A</sub> Receptor Channel". en. In: *PLOS ONE* 10.10. Ed. by S. Barnes, e0140258.
- Dineley, K. T., A. A. Pandya, and J. L. Yakel (2015). "Nicotinic ACh receptors as therapeutic targets in CNS disorders". In: *Trends in Pharmacological Sciences* 36.2, pp. 96–108.
- Ding, S. and F. Sachs (1999a). "Single channel properties of P2X<sub>2</sub> purinoceptors." In: *The Journal of general physiology* 113.5, pp. 695–720.
- Ding, S. and F. Sachs (1999b). "Ion permeation and block of P2X(2) purinoceptors: single channel recordings." In: *The Journal of membrane biology* 172.3, pp. 215–23.
- Drachman, D. A. (2005). "Do we have brain to spare?" en. In: *Neurology* 64.12, pp. 2004–2005.
- Du, J., W. Lü, S. Wu, Y. Cheng, and E. Gouaux (2015). "Glycine receptor mechanism elucidated by electron cryo-microscopy". en. In: *Nature* 526.7572, pp. 224–229.
- Duret, G., C. V. Renterghem, Y. Weng, M. Prevost, G. Moraga-Cid, C. Huon, J. M. Sonner, and P.-J. Corringer (2011). "Functional prokaryotic–eukaryotic chimera from the pentameric ligand-gated ion channel family". en. In: *Proceedings of the National Academy of Sciences* 108.29, pp. 12143–12148.
- Dutertre, S., C.-M. Becker, and H. Betz (2012a). "Inhibitory Glycine Receptors: An Update". en. In: *Journal of Biological Chemistry* 287.48, pp. 40216–40223.
- Dutertre, S., M. Drwal, B. Laube, and H. Betz (2012b). "Probing the pharmacological properties of distinct subunit interfaces within heteromeric glycine receptors reveals a functional  $\beta\beta$  agonist-binding site". In: *Journal of Neurochemistry* 122.1, pp. 38–47.
- Einstein, A. (1905). "Über die von der molekularkinetischen Theorie der Wärme geforderte Bewegung von in ruhenden Flüssigkeiten suspendierten Teilchen". In: *Annalen der Physik* 322.8, pp. 549–560.
- Essmann, U., L. Perera, M. L. Berkowitz, T. Darden, H. Lee, and L. G. Pedersen (1995). "A smooth particle mesh Ewald method". In: *The Journal of Chemical Physics* 103.19, pp. 8577–8593.
- Evans, R. J. (1996). "Single channel properties of ATP-gated cation channels (P2X receptors) heterologously expressed in Chinese hamster ovary cells". In: *Neuroscience Letters* 212.3, pp. 212–214.
- Fatt, P. and B. Katz (1952). "Spontaneous subthreshold activity at motor nerve endings". In: *The Journal of Physiology* 117.1, pp. 109–128.
- Feller, S. E., Y. Zhang, R. W. Pastor, and B. R. Brooks (1995a). "Constant pressure molecular dynamics simulation: The Langevin piston method". In: *The Journal of Chemical Physics* 103.11, pp. 4613–4621.
- Feller, S. E., Y. Zhang, R. W. Pastor, and B. R. Brooks (1995b). "Constant pressure molecular dynamics simulation: The Langevin piston method". In: *The Journal of Chemical Physics* 103.11, pp. 4613–4621.
- Findlay, G. S., M. J. Wick, M. P. Mascia, D. Wallace, G. W. Miller, R. A. Harris, and Y. A. Blednov (2002). "Transgenic expression of a mutant glycine receptor decreases alcohol sensitivity of mice". eng. In: *The Journal of Pharmacology and Experimental Therapeutics* 300.2, pp. 526–534.
- Finger, S. (1994). *Origins of neuroscience: a history of explorations into brain function*. Oxford University Press, p. 462.
- Fiorin, G., M. L. Klein, and J. Héin (2013). "Using collective variables to drive molecular dynamics simulations". In: *Molecular Physics* 111.22–23, pp. 3345–3362.
- Fourati, Z., R. J. Howard, S. A. Heusser, H. Hu, R. R. Ruza, L. Sauguet, E. Lindahl, and M. Delarue (2018). "Structural Basis for a Bimodal Allosteric Mechanism of General Anesthetic Modulation in Pentameric Ligand-Gated Ion Channels". In: *Cell Reports* 23.4, pp. 993–1004.
- Frank, E., Y. Wang, S. Inglis, G. Holmes, and I. H. Witten (1998). "Using Model Trees for Classification". In: *Machine Learning* 32.1, pp. 63–76.
- Gaskin, D. J. and P. Richard (2012). "The economic costs of pain in the United States". eng. In: *The Journal of Pain: Official Journal of the American Pain Society* 13.8, pp. 715–724.
- Genheden, S. and U. Ryde (2015). "The MM/PBSA and MM/GBSA methods to estimate ligand-binding affinities." In: *Expert opinion on drug discovery* 10.5, pp. 449–61.
- Gielen, M. and P.-J. Corringer (2018). "The dual-gate model for pentameric ligand-gated ion channels activation and desensitization". eng. In: *The Journal of Physiology*.
- Gielen, M., P. Thomas, and T. G. Smart (2015). "The desensitization gate of inhibitory Cys-loop receptors". In: *Nature Communications* 6.
- Gonzalez-Gutierrez, G., Y. Wang, G. D. Cymes, E. Tajkhorshid, and C. Grosman (2017). "Chasing the open-state structure of pentameric ligand-gated ion channels". eng. In: *The Journal of General Physiology* 149.12, pp. 1119–1138.
- Gowers, R. J., M. Linke, J. Barnoud, T. J. E. Reddy, M. N. Melo, S. L. Seyler, J. Domański, D. L. Dotson, S. Buchoux, I. M. Kenney, and O. Beckstein (2016). "MD-Analysis: A Python Package for the Rapid Analysis of Molecular Dynamics Simulations". In: *Proceedings of the 15th Python in Science Conference*, pp. 98–105.
- Graham, D., F. Pfeiffer, and H. Betz (1983). "Photoaffinity-labelling of the glycine receptor of rat spinal cord". eng. In: *European Journal of Biochemistry* 131.3, pp. 519–525.
- Grenningloh, G., A. Rienitz, B. Schmitt, C. Methfessel, M. Zensen, K. Beyreuther, E. D. Gundelfinger, and H.

- Betz (1987). "The strychnine-binding subunit of the glycine receptor shows homology with nicotinic acetylcholine receptors". eng. In: *Nature* 328.6127, pp. 215–220.
- Guerra, G. P., M. A. Rubin, and C. F. Mello (2016). "Modulation of learning and memory by natural polyamines". In: *Pharmacological Research. Country in focus: Pharmacology in Brasil* 112, pp. 99–118.
- Gumbart, J., F. Khalili-Araghi, M. Sotomayor, and B. Roux (2012). "Constant electric field simulations of the membrane potential illustrated with simple systems". In: *Biochimica et biophysica acta* 1818.2, pp. 294–302.
- Gupta, S., S. Chakraborty, R. Vij, and A. Auerbach (2017). "A mechanism for acetylcholine receptor gating based on structure, coupling, phi, and flip". In: *The Journal of General Physiology* 149.1, pp. 85–103.
- Habermacher, C., K. Dunning, T. Chataigneau, and T. Grutter (2016). "Molecular structure and function of P2X receptors". In: *Neuropharmacology. Special Issue: Purines in Neurodegeneration and Neuroregeneration* 104, pp. 18–30.
- Haider, B. (2007). "The War of the Soups and the Sparks: The Discovery of Neurotransmitters and the Dispute Over How Nerves Communicate". In: *The Yale Journal of Biology and Medicine* 80.3, pp. 138–139.
- Hairer, E., C. Lubich, and G. Wanner (2003). "Geometric numerical integration illustrated by the StrmerVerlet method". In: *Acta Numerica* 12, S0962492902000144.
- Halgren, T. A. (1996). "Merck molecular force field. I. Basis, form, scope, parameterization, and performance of MMFF94". In: *Journal of Computational Chemistry* 17.5-6, pp. 490–519.
- Harkat, M., L. Peverini, A. Cerdan, K. Dunning, J. Beudez, A. Martz, N. Calimet, A. Specht, M. Cecchini, T. Chataigneau, and T. Grutter (2017). "On the permeation of large organic cations through the pore of ATP-gated P2X receptors". In: *Proceedings of the National Academy of Sciences of the United States of America* 114.19.
- Hassaine, G., C. Deluz, L. Grasso, R. Wyss, M. B. Tol, R. Hovius, A. Graff, H. Stahlberg, T. Tomizaki, A. Desmyter, C. Moreau, X.-D. Li, F. Poitevin, H. Vogel, and H. Nury (2014). "X-ray structure of the mouse serotonin 5-HT<sub>3</sub> receptor". eng. In: *Nature* 512.7514, pp. 276–281.
- Hattori, M. and E. Gouaux (2012). "Molecular mechanism of ATP binding and ion channel activation in P2X receptors". en. In: *Nature* 485.7397, pp. 207–212.
- Hejazi, N. (2005). "9-Tetrahydrocannabinol and Endogenous Cannabinoid Anandamide Directly Potentiate the Function of Glycine Receptors". In: *Molecular Pharmacology* 69.3, pp. 991–7.
- Heuser, J. E., T. S. Reese, M. J. Dennis, Y. Jan, L. Jan, and L. Evans (1979). "Synaptic vesicle exocytosis captured by quick freezing and correlated with quantal transmitter release". eng. In: *The Journal of Cell Biology* 81.2, pp. 275–300.
- Heymann, G., J. Dai, M. Li, S. D. Silberberg, H.-X. Zhou, and K. J. Swartz (2013). "Inter- and intrasubunit interactions between transmembrane helices in the open state of P2X receptor channels". en. In: *Proceedings of the National Academy of Sciences* 110.42, E4045–E4054.
- Hibbs, R. E. and E. Gouaux (2011). "Principles of activation and permeation in an anion-selective Cys-loop receptor". eng. In: *Nature* 474.7349, pp. 54–60.
- Hilf, R. J. C. and R. Dutzler (2008). "X-ray structure of a prokaryotic pentameric ligand-gated ion channel". en. In: *Nature* 452.7185, pp. 375–379.
- Hille, B. (2001). *Ion channels of excitable membranes*. Sinauer, p. 814.
- Hodgkin, A. L., A. F. Huxley, and B. Katz (1952). "Measurement of current-voltage relations in the membrane of the giant axon of Loligo". In: *The Journal of Physiology* 116.4, pp. 424–448.
- Howard, R. J., V. Carnevale, L. Delemotte, U. A. Hellmich, and B. S. Rothberg (2017). "Permeating disciplines: Overcoming barriers between molecular simulations and classical structure-function approaches in biological ion transport". eng. In: *Biochimica Et Biophysica Acta*.
- Hu, H., Á. Nemezc, C. Van Renterghem, Z. Fourati, L. Sauguet, P.-J. Corringer, and M. Delarue (2018). "Crystal structures of a pentameric ion channel gated by alkaline pH show a widely open pore and identify a cavity for modulation". eng. In: *Proceedings of the National Academy of Sciences of the United States of America*.
- Huang, X., H. Chen, K. Michelsen, S. Schneider, and P. L. Shaffer (2015). "Crystal structure of human glycine receptor- $\alpha_3$  bound to antagonist strychnine". eng. In: *Nature* 526.7572, pp. 277–280.
- Huang, X., H. Chen, and P. L. Shaffer (2017a). "Crystal Structures of Human GlyR $\alpha_3$  Bound to Ivermectin". In: *Structure* 25.6, 945–950.e2.
- Huang, X., P. L. Shaffer, S. Ayube, H. Bregman, H. Chen, S. G. Lehto, J. A. Luther, D. J. Matson, S. I. McDonough, K. Michelsen, M. H. Plant, S. Schneider, J. R. Simard, Y. Teffera, S. Yi, M. Zhang, E. F. DiMauro, and J. Gingras (2017b). "Crystal structures of human glycine receptor  $\alpha_3$  bound to a novel class of analgesic potentiators". eng. In: *Nature Structural & Molecular Biology* 24.2, pp. 108–113.
- Humphrey, W., A. Dalke, and K. Schulten (1996). "VMD: visual molecular dynamics". eng. In: *Journal of Molecular Graphics* 14.1, pp. 27–28, 33–38.
- Hunter, J. D. (2007). "Matplotlib: A 2D Graphics Environment". In: *Computing in Science Engineering* 9.3, pp. 90–95.
- Im, W., S. Seefeld, and B. Roux (2000). "A Grand Canonical Monte Carlo–Brownian Dynamics Algorithm for Simulating Ion Channels". In: *Biophysical Journal* 79.2, pp. 788–801.
- Islam, R. and J. W. Lynch (2012). "Mechanism of action of the insecticides, lindane and fipronil, on glycine receptor chloride channels". In: *British Journal of Pharmacology* 165.8, pp. 2707–2720. arXiv: 1603.03342.
- Jaiteh, M., A. Taly, and J. Hénin (2016). "Evolution of Pentameric Ligand-Gated Ion Channels: Pro-Loop Receptors". en. In: *PLOS ONE* 11.3, e0151934.
- James, J. R. and A. Nordberg (1995). "Genetic and environmental aspects of the role of nicotinic receptors in neurodegenerative disorders: Emphasis on Alzheimer's disease and Parkinson's disease". en. In: *Behavior Genetics* 25.2, pp. 149–159.
- Jansen, M., M. Bali, and M. H. Akabas (2008). "Modular Design of Cys-loop Ligand-gated Ion Channels: Functional 5-HT<sub>3</sub> and GABA  $\rho_1$  Receptors Lacking

- the Large Cytoplasmic M3M4 Loop". en. In: *The Journal of General Physiology* 131.2, pp. 137–146.
- Jensen, A. A., M. L. Bergmann, T. Sander, and T. Balle (2010). "Ginkgolide X is a potent antagonist of anionic Cys-loop receptors with a unique selectivity profile at glycine receptors". In: *Journal of Biological Chemistry* 285.13, pp. 10141–10153.
- Jensen, F. (2007). *Introduction to computational chemistry*. John Wiley & Sons, p. 599.
- Jones, E., T. Oliphant, P. Peterson, et al. (2001). *SciPy: Open source scientific tools for Python*.
- Jonsson, S., L. Adermark, M. Ericson, and B. Söderpalm (2014). "The involvement of accumbal glycine receptors in the dopamine-elevating effects of addictive drugs". eng. In: *Neuropharmacology* 82, pp. 69–75.
- Katz, B. and R. Miledi (1973). "The binding of acetylcholine to receptors and its removal from the synaptic cleft". In: *The Journal of Physiology* 231.3, pp. 549–574.
- Katz, B. and S. Thesleff (1957). "A study of the 'desensitization' produced by acetylcholine at the motor end-plate". en. In: *The Journal of Physiology* 138.1, pp. 63–80.
- Katz, B. and R. Miledi (1965). "The measurement of synaptic delay, and the time course of acetylcholine release at the neuromuscular junction". en. In: *Proc. R. Soc. Lond. B* 161.985, pp. 483–495.
- Kelley, S. P., J. I. Dunlop, E. F. Kirkness, J. J. Lambert, and J. A. Peters (2003). "A cytoplasmic region determines single-channel conductance in 5-HT<sub>3</sub> receptors". eng. In: *Nature* 424.6946, pp. 321–324.
- Keramidas, A., A. J. Moorhouse, K. D. Pierce, P. R. Schofield, and P. H. Barry (2002). "Cation-selective Mutations in the M2 Domain of the Inhibitory Glycine Receptor Channel Reveal Determinants of Ion-Charge Selectivity". In: *The Journal of General Physiology* 119.5, pp. 393–410.
- Khakh, B. S., X. R. Bao, C. Labarca, and H. A. Lester (1999). "Neuronal P2X transmitter-gated cation channels change their ion selectivity in seconds". In: *Nature Neuroscience* 2.4, pp. 322–330.
- Khakh, B. S. and R. A. North (2012). "Neuromodulation by extracellular ATP and P2X receptors in the CNS." In: *Neuron* 76.1, pp. 51–69.
- Kieseritzky, G. and E.-W. Knapp (2008). "Optimizing pKA computation in proteins with pH adapted conformations". en. In: *Proteins: Structure, Function, and Bioinformatics* 71.3, pp. 1335–1348.
- Klauda, J. B., R. M. Venable, J. A. Freites, J. W. O'Connor, D. J. Tobias, C. Mondragon-Ramirez, I. Vorobyov, A. D. MacKerell, and R. W. Pastor (2010). "Update of the CHARMM all-atom additive force field for lipids: validation on six lipid types". eng. In: *The Journal of Physical Chemistry. B* 114.23, pp. 7830–7843.
- Kneussel, M. and H. Betz (2000). "Clustering of inhibitory neurotransmitter receptors at developing postsynaptic sites: the membrane activation model". eng. In: *Trends in Neurosciences* 23.9, pp. 429–435.
- Kochev, N. T., V. H. Paskaleva, and N. Jeliazkova (2013). "Ambit-tautomer: An open source tool for tautomer generation". In: *Molecular Informatics* 32.5-6, pp. 481–504.
- Kurnikova, M. G., R. D. Coalson, P. Graf, and A. Nitzan (1999). "A lattice relaxation algorithm for three-dimensional Poisson-Nernst-Planck theory with application to ion transport through the gramicidin A channel". In: *Biophysical Journal* 76.2, pp. 642–656.
- Kutzner, C., H. Grubmüller, B. L. de Groot, and U. Zachariae (2011). "Computational Electrophysiology: The Molecular Dynamics of Ion Channel Permeation and Selectivity in Atomistic Detail". In: *Biophysical Journal* 101.4, pp. 809–817.
- Kutzner, C., D. A. Köpfer, J.-P. Machtens, B. L. de Groot, C. Song, and U. Zachariae (2016). "Insights into the function of ion channels by computational electrophysiology simulations". In: *Biochimica et Biophysica Acta (BBA) - Biomembranes*. New approaches for bridging computation and experiment on membrane proteins 1858.7, Part B, pp. 1741–1752.
- Lakkaraju, S. K., W. Yu, E. P. Raman, A. V. Hershfeld, L. Fang, D. A. Deshpande, and A. D. MacKerell (2015). "Mapping Functional Group Free Energy Patterns at Protein Occluded Sites: Nuclear Receptors and G-Protein Coupled Receptors". In: *Journal of Chemical Information and Modeling* 55.3, pp. 700–708.
- Landis, J. R. and G. G. Koch (1977). "The measurement of observer agreement for categorical data." In: *Biometrics* 33.1, pp. 159–74.
- Langley, J. N. (1905). "On the reaction of cells and of nerve-endings to certain poisons, chiefly as regards the reaction of striated muscle to nicotine and to curari". en. In: *The Journal of Physiology* 33.4-5, pp. 374–413.
- Langlhofer, G. and C. Villmann (2016). "The Intracellular Loop of the Glycine Receptor: It's not all about the Size." In: *Frontiers in molecular neuroscience* 9, p. 41.
- Lara, C. O., P. Murath, B. Muñoz, A. M. Marileo, L. S. Martín, V. P. San Martín, C. F. Burgos, T. A. Mariqueo, L. G. Aguayo, J. Fuentealba, P. Godoy, L. Guzman, and G. E. Yévenes (2016). "Functional modulation of glycine receptors by the alkaloid gelsemine". In: *British Journal of Pharmacology* 173.14, pp. 2263–2277.
- Lavery, D., P. Thomas, M. Field, O. J. Andersen, M. G. Gold, P. C. Biggin, M. Gielen, and T. G. Smart (2017). "Crystal structures of a GABAA-receptor chimera reveal new endogenous neurosteroid-binding sites". In: *Nature Structural & Molecular Biology* 24.11, pp. 977–985.
- Lee, D. J. S., A. Keramidas, A. J. Moorhouse, P. R. Schofield, and P. H. Barry (2003). "The contribution of proline 250 (P-2') to pore diameter and ion selectivity in the human glycine receptor channel". In: *Neuroscience Letters* 351.3, pp. 196–200.
- Lee, K. I., S. Jo, H. Rui, B. Egwolf, B. Roux, R. W. Pastor, and W. Im (2012). "Web interface for brownian dynamics simulation of ion transport and its applications to beta-barrel pores". en. In: *Journal of Computational Chemistry* 33.3, pp. 331–339.
- Lemoine, D., R. Jiang, A. Taly, T. Chataigneau, A. Specht, and T. Grutter (2012). "Ligand-Gated Ion Channels: New Insights into Neurological Disorders and Ligand Recognition". In: *Chemical Reviews* 112.12, pp. 6285–6318.
- Lev, B., S. Murail, F. Poitevin, B. A. Cromer, M. Baaden, M. Delarue, and T. W. Allen (2017). "String method solution of the gating pathways for a pentameric ligand-gated ion channel." In: *Proceedings of the Na-*

- tional Academy of Sciences of the United States of America 114.21, E4158–E4167.
- Lewis, R., K. E. Asplin, G. Bruce, C. Dart, A. Mobasher, and R. Barrett-Jolley (2011). “The role of the membrane potential in chondrocyte volume regulation”. en. In: *Journal of Cellular Physiology* 226.11, pp. 2979–2986.
- Li, M., G. E. S. Toombes, S. D. Silberberg, and K. J. Swartz (2015). “Physical basis of apparent pore dilation of ATP-activated P2X receptor channels”. In: *Nature Neuroscience* 18.11, pp. 1577–1583.
- Liang, W., Y. Zhao, L. Liu, Y. Wang, W. J. Li, and G.-B. Lee (2017). “Determination of Cell Membrane Capacitance and Conductance via Optically Induced Electrokinetics”. eng. In: *Biophysical Journal* 113.7, pp. 1531–1539.
- Liu, J., D. C. Wu, and Y. T. Wang (2010). “Allosteric potentiation of glycine receptor chloride currents by glutamate”. In: *Nature Neuroscience* 13.10, pp. 1225–1232.
- Llinás, R., I. Z. Steinberg, and K. Walton (1981). “Relationship between presynaptic calcium current and postsynaptic potential in squid giant synapse”. English. In: *Biophysical Journal* 33.3, pp. 323–351.
- Loewi, O. (1921). “Über humorale Übertragbarkeit der Herznervenwirkung”. In: *Pflüger's Archiv für die gesamte Physiologie des Menschen und der Tiere* 189.1, pp. 239–242.
- López-Muñoz, F., J. Boya, and C. Alamo (2006). “Neuron theory, the cornerstone of neuroscience, on the centenary of the Nobel Prize award to Santiago Ramón y Cajal”. In: *Brain Research Bulletin* 70.4, pp. 391–405.
- Lu, J., S. Fan, G. Zou, Y. Hou, T. Pan, W. Guo, L. Yao, F. Du, G. E. Homanics, D. Liu, L. Zhang, and W. Xiong (2018). “Involvement of glycine receptor  $\alpha 1$  subunits in cannabinoid-induced analgesia”. In: *Neuropharmacology* 133, pp. 224–232.
- Lynagh, T. and J. W. Lynch (2010a). “A glycine residue essential for high ivermectin sensitivity in Cys-loop ion channel receptors”. In: *International Journal for Parasitology* 40.13, pp. 1477–1481.
- Lynagh, T. and J. W. Lynch (2010b). “An improved ivermectin-activated chloride channel receptor for inhibiting electrical activity in defined neuronal populations”. In: *Journal of Biological Chemistry* 285.20, pp. 14890–14897.
- Lynagh, T., T. I. Webb, C. L. Dixon, B. A. Cromers, and J. W. Lynch (2011). “Molecular determinants of ivermectin sensitivity at the glycine receptor chloride channel”. In: *Journal of Biological Chemistry* 286.51, pp. 43913–43924.
- Lynch, J. W., Y. Zhang, S. Talwar, and A. Estrada-Mondragon (2017). “Glycine Receptor Drug Discovery.” eng. In: *Advances in pharmacology (San Diego, Calif.)* 79, pp. 225–253.
- Lynch, J. W. (2004). “Molecular Structure and Function of the Glycine Receptor Chloride Channel”. en. In: *Physiological Reviews* 84.4, pp. 1051–1095.
- Maas, C., N. Tagnaouti, S. Loeblich, B. Behrend, C. Lappe-Siefke, and M. Kneussel (2006). “Neuronal cotransport of glycine receptor and the scaffold protein gephyrin”. In: *The Journal of Cell Biology* 172.3, pp. 441–451.
- Mackerell, A. D. (2004). “Empirical force fields for biological macromolecules: Overview and issues”. en. In: *Journal of Computational Chemistry* 25.13, pp. 1584–1604.
- Mackerell, A. D., M. Feig, and C. L. Brooks (2004). “Extending the treatment of backbone energetics in protein force fields: Limitations of gas-phase quantum mechanics in reproducing protein conformational distributions in molecular dynamics simulations”. In: *Journal of Computational Chemistry* 25.11, pp. 1400–1415.
- Maeda, S., S. Nakagawa, M. Suga, E. Yamashita, A. Oshima, Y. Fujiyoshi, and T. Tsukihara (2009). “Structure of the connexin 26 gap junction channel at 3.5 Å resolution”. en. In: *Nature* 458.7238, pp. 597–602.
- Maksay, G., B. Laube, and H. Betz (2001). “Subunit-specific modulation of glycine receptors by neurosteroids”. In: *Neuropharmacology* 41.3, pp. 369–376.
- Maksay, G. (1998). “Bidirectional allosteric modulation of strychnine-sensitive glycine receptors by tropeines and 5-HT<sub>3</sub>serotonin receptor ligands”. In: *Neuropharmacology* 37.12, pp. 1633–1641.
- Maksay, G., B. Laube, R. Schemm, J. Grudzinska, M. Drwal, and H. Betz (2009). “Different binding modes of tropeines mediating inhibition and potentiation of  $\alpha 1$  glycine receptors”. In: *Journal of Neurochemistry* 109.6, pp. 1725–1732.
- Maleeva, G., S. Buldakova, and P. Bregestovski (2015). “Selective potentiation of alpha 1 glycine receptors by ginkgolic acid”. In: *Frontiers in Molecular Neuroscience* 8, p. 64.
- Mamonov, A. B., R. D. Coalson, A. Nitzan, and M. G. Kurnikova (2003). “The role of the dielectric barrier in narrow biological channels: a novel composite approach to modeling single-channel currents.” In: *Biophysical journal* 84.6, pp. 3646–61.
- Mansoor, S. E., W. Lü, W. Oosterheert, M. Shekhar, E. Tajkhorshid, and E. Gouaux (2016). “X-ray structures define human P2X<sub>3</sub> receptor gating cycle and antagonist action”. en. In: *Nature* 538.7623, pp. 66–71.
- Martin, N. E., S. Malik, N. Calimet, J.-P. Changeux, and M. Cecchini (2017). “Un-gating and allosteric modulation of a pentameric ligand-gated ion channel captured by molecular dynamics”. In: *PLoS Computational Biology* In press. In press.
- Martyna, G. J., D. J. Tobias, and M. L. Klein (1994). “Constant pressure molecular dynamics algorithms”. In: *The Journal of Chemical Physics* 101.5, pp. 4177–4189.
- McCann, F. E., B. Vanherberghen, K. Eleme, L. M. Carlin, R. J. Newsam, D. Goulding, and D. M. Davis (2003). “The Size of the Synaptic Cleft and Distinct Distributions of Filamentous Actin, Ezrin, CD43, and CD45 at Activating and Inhibitory Human NK Cell Immune Synapses”. en. In: *The Journal of Immunology* 170.6, pp. 2862–2870.
- McWilliam, H., W. Li, M. Uludag, S. Squizzato, Y. M. Park, N. Buso, A. P. Cowley, and R. Lopez (2013). “Analysis Tool Web Services from the EMBL-EBI”. In: *Nucleic Acids Research* 41.W1, W597–W600.
- Melcr, J., D. Bonhenry, Š. Timr, and P. Jungwirth (2016). “Transmembrane Potential Modeling: Comparison between Methods of Constant Electric Field and Ion Imbalance”. In: *Journal of Chemical Theory and Computation* 12.5, pp. 2418–2425.
- Miao, Y., V. A. Feher, and J. A. McCammon (2015). “Gaussian Accelerated Molecular Dynamics: Unconstrained Enhanced Sampling and Free Energy

- Calculation". In: *Journal of Chemical Theory and Computation* 11.8, pp. 3584–3595.
- Michaud-Agrawal, N., E. J. Denning, T. B. Woolf, and O. Beckstein (2011). "MDAnalysis: A toolkit for the analysis of molecular dynamics simulations". en. In: *Journal of Computational Chemistry* 32.10, pp. 2319–2327.
- Miller, C. (1989). "Genetic manipulation of ion channels: A new approach to structure and mechanism". In: *Neuron* 2.3, pp. 1195–1205.
- Miller, P. S. and A. R. Aricescu (2014). "Crystal structure of a human GABAA receptor". en. In: *Nature* 512.7514, pp. 270–275.
- Miller, P. S., S. Scott, S. Masiulis, L. De Colibus, E. Pardon, J. Steyaert, and A. R. Aricescu (2017). "Structural basis for GABAA receptor potentiation by neurosteroids". In: *Nature Structural & Molecular Biology* 24.11, pp. 986–992.
- Miller, P. S. and T. G. Smart (2010). "Binding, activation and modulation of Cys-loop receptors". In: *Trends in Pharmacological Sciences* 31.4, pp. 161–174.
- Miller, P., S. Masiulis, T. Malinauskas, A. Kotecha, S. Rao, S. Chavali, L. D. Colibus, E. Pardon, S. Hannan, S. Scott, Z. Sun, B. Frenz, G. Klesse, S. Li, J. Diprose, A. Siebert, R. Esnouf, F. DiMaio, S. Tucker, T. Smart, J. Steyaert, M. Babu, M. Sansom, J. Huiskonen, and R. Aricescu (2018). "Heteromeric GABAA receptor structures in positively-modulated active states". en. In: *bioRxiv*, p. 338343.
- Möhler, H. (2011). "The rise of a new GABA pharmacology". In: *Neuropharmacology* 60.7-8, pp. 1042–1049.
- Molander, A. and B. Söderpalm (2005). "Glycine receptors regulate dopamine release in the rat nucleus accumbens". eng. In: *Alcoholism, Clinical and Experimental Research* 29.1, pp. 17–26.
- Monod, J., J. Wyman, and J.-P. Changeux (1965). "On the nature of allosteric transitions: A plausible model". In: *Journal of Molecular Biology* 12.1, pp. 88–118.
- Moore, J. W., M. P. Blaustein, N. C. Anderson, and T. Narahashi (1967). "Basis of Tetrodotoxin's Selectivity in Blockage of Squid Axons". In: *The Journal of General Physiology* 50.5, pp. 1401–1411.
- Moorhouse, A. J., A. Keramidas, A. Zaykin, P. R. Schofield, and P. H. Barry (2002). "Single Channel Analysis of Conductance and Rectification in Cation-selective, Mutant Glycine Receptor Channels". In: *The Journal of General Physiology* 119.5, pp. 411–425.
- Moraga-Cid, G., L. Sauguet, C. Huon, L. Malherbe, C. Girard-Blanc, S. Petres, S. Murail, A. Taly, M. Baaden, M. Delarue, and P.-J. Corringer (2015). "Allosteric and hyperekplexic mutant phenotypes investigated on an  $\alpha 1$  glycine receptor transmembrane structure". en. In: *Proceedings of the National Academy of Sciences* 112.9, pp. 2865–2870.
- Moroni, M., I. Biro, M. Giugliano, R. Vijayan, P. C. Biggin, M. Beato, and L. G. Sivilotti (2011a). "Chloride ions in the pore of glycine and GABA channels shape the time course and voltage dependence of agonist currents". In: *The Journal of neuroscience : the official journal of the Society for Neuroscience* 31.40, pp. 14095–14106.
- Moroni, M., J. O. Meyer, C. Lahmann, and L. G. Sivilotti (2011b). "In glycine and GABA(A) channels, different subunits contribute asymmetrically to channel conductance via residues in the extracellular domain". eng. In: *The Journal of Biological Chemistry* 286.15, pp. 13414–13422.
- Mowrey, D., T. Cui, Y. Jia, D. Ma, A. M. Makhov, P. Zhang, P. Tang, and Y. Xu (2013). "Open-Channel Structures of the Human Glycine Receptor  $\alpha 1$  Full-Length Transmembrane Domain". In: *Structure (London, England : 1993)* 21.10.
- Nasiripourdori, A., V. Taly, T. Grutter, and A. Taly (2011). "From Toxins Targeting Ligand Gated Ion Channels to Therapeutic Molecules". In: *Toxins* 3.3, pp. 260–293.
- Nayak, T. K. and A. Auerbach (2017). "Cyclic activation of endplate acetylcholine receptors". In: *Proceedings of the National Academy of Sciences* 114.45, pp. 11914–11919.
- Neher, E. and B. Sakmann (1976). "Single-channel currents recorded from membrane of denervated frog muscle fibres". en. In: *Nature* 260.5554, pp. 799–802.
- Nemecz, Á., M. S. Prevost, A. Menny, and P.-J. Corringer (2016). "Emerging Molecular Mechanisms of Signal Transduction in Pentameric Ligand-Gated Ion Channels". In: *Neuron* 90.3, pp. 452–470.
- Nightingale, E. R. (1959). "Phenomenological Theory of Ion Solvation. Effective Radii of Hydrated Ions". In: *The Journal of Physical Chemistry* 63.9, pp. 1381–1387.
- Noda, M., S. Shimizu, T. Tanabe, T. Takai, T. Kayano, T. Ikeda, H. Takahashi, H. Nakayama, Y. Kanaoka, N. Minamino, K. Kangawa, H. Matsuo, M. A. Raftery, T. Hirose, S. Inayama, H. Hayashida, T. Miyata, and S. Numa (1984). "Primary structure of Electrophorus electricus sodium channel deduced from cDNA sequence". en. In: *Nature* 312.5990, pp. 121–127.
- North, R. A. (2002). "Molecular Physiology of P2X Receptors". In: *Physiological Reviews* 82.4, pp. 1013–1067.
- Nury, H., C. Van Renterghem, Y. Weng, A. Tran, M. Baaden, V. Dufresne, J.-P. Changeux, J. M. Sonner, M. Delarue, and P.-J. Corringer (2011). "X-ray structures of general anaesthetics bound to a pentameric ligand-gated ion channel". In: *Nature* 469.7330, pp. 428–431.
- Palatnick, W., R. Meatherall, D. Sitar, and M. Tenenbein (1997). "Toxicokinetics of Acute Strychnine Poisoning". In: *Journal of Toxicology: Clinical Toxicology* 35.6, pp. 617–620.
- Patra, M. and M. Karttunen (2004). "Systematic comparison of force fields for microscopic simulations of NaCl in aqueous solutions: Diffusion, free energy of hydration, and structural properties". en. In: *Journal of Computational Chemistry* 25.5, pp. 678–689.
- Pedregosa, F., G. Varoquaux, A. Gramfort, V. Michel, B. Thirion, O. Grisel, M. Blondel, P. Prettenhofer, R. Weiss, V. Dubourg, J. Vanderplas, A. Passos, D. Cournapeau, M. Brucher, M. Perrot, and É. Duchesnay (2011). "Scikit-learn: Machine Learning in Python". In: *J. Mach. Learn. Res.* 12, pp. 2825–2830.
- Petřek, M., P. Kořinová, J. Koča, and M. Otyepka (2007). "MOLE: A Voronoi Diagram-Based Explorer of Molecular Channels, Pores, and Tunnels". In: *Structure* 15.11, pp. 1357–1363.
- Pfeiffer, F. and H. Betz (1981). "Solubilization of the glycine receptor from rat spinal cord". eng. In: *Brain Research* 226.1-2, pp. 273–279.
- Pfeiffer, F., D. Graham, and H. Betz (1982). "Purification by affinity chromatography of the glycine receptor

- of rat spinal cord". eng. In: *The Journal of Biological Chemistry* 257.16, pp. 9389–9393.
- Phillips, J. C., R. Braun, W. Wang, J. Gumbart, E. Tajkhorshid, E. Villa, C. Chipot, R. D. Skeel, L. Kalé, and K. Schulten (2005). "Scalable molecular dynamics with NAMD". en. In: *Journal of Computational Chemistry* 26.16, pp. 1781–1802.
- Phulera, S., H. Zhu, J. Yu, D. P. Claxton, N. Yoder, C. Yoshioka, and E. Gouaux (2018). *Cryo-EM structure of the benzodiazepine-sensitive  $\alpha 1\beta 1\gamma 2S$  trimeric GABAA receptor in complex with GABA*. en.
- Platkiewicz, J. and R. Brette (2010). "A Threshold Equation for Action Potential Initiation". en. In: *PLOS Computational Biology* 6.7, e1000850.
- Pol, A. N. van den (2012). "Neuropeptide transmission in brain circuits". In: *Neuron* 76.1, pp. 98–115.
- Polovinkin, L., G. Hassaine, J. Perot, E. Neumann, A. A. Jensen, S. N. Lefebvre, P.-J. Corringer, J. Neyton, C. Chipot, F. Dehez, G. Schoehn, and H. Nury (2018). "Conformational transitions of the serotonin 5-HT<sub>3</sub> receptor". In: *Nature* 563.7730, pp. 275–279.
- Purves, D., G. J. Augustine, D. Fitzpatrick, J.-M. Coquery, N. Tajeddine, P. Gailly, A. Volterra, and M. Jeannerod (2015). *Neurosciences*. French. Louvain-la-Neuve: De Boeck Supérieur.
- Qu, L., Y. Akbergenova, Y. Hu, and T. Schikorski (2009). "Synapse-to-synapse variation in mean synaptic vesicle size and its relationship with synaptic morphology and function". en. In: *Journal of Comparative Neurology* 514.4, pp. 343–352.
- Quinlan, J. R. (1992). "LEARNING WITH CONTINUOUS CLASSES: Constructing Model Trees". In: *In 5th Australian joint conference on artificial intelligence* 92, pp. 343–348.
- Raltschev, C., F. Hetsch, A. Winkelmann, J. C. Meier, and M. Semtner (2016). "Electrophysiological Signature of Homomeric and Heteromeric Glycine Receptor Channels". en. In: *Journal of Biological Chemistry* 291.34, pp. 18030–18040.
- Riedel, T., G. Schmalzing, and F. Markwardt (2007). "Influence of Extracellular Monovalent Cations on Pore and Gating Properties of P2X<sub>7</sub> Receptor-Operated Single-Channel Currents". In: *Biophysical Journal* 93.3, pp. 846–858.
- Rokic, M. B. and S. S. Stojilkovic (2013). "Two open states of P2X receptor channels". In: *Frontiers in Human Neuroscience* 7, p. 215.
- Roux, B. (1997). "Influence of the membrane potential on the free energy of an intrinsic protein". eng. In: *Biophysical Journal* 73.6, pp. 2980–2989.
- Roux, B. (2008). "The Membrane Potential and its Representation by a Constant Electric Field in Computer Simulations". In: *Biophysical Journal* 95.9, pp. 4205–4216.
- Roux, B., T. Allen, S. Bernèche, and W. Im (2004). "Theoretical and computational models of biological ion channels". In: *Quarterly Reviews of Biophysics* 37.01, pp. 15–103.
- Rundström, N., V. Schmieden, H. Betz, J. Bormann, and D. Langosch (1994). "Cyanotriphenylborate: subtype-specific blocker of glycine receptor chloride channels". eng. In: *Proceedings of the National Academy of Sciences of the United States of America* 91.19, pp. 8950–8954.
- Ryckaert, J.-P., G. Ciccotti, and H. J. C. Berendsen (1977). "Numerical integration of the cartesian equations of motion of a system with constraints: molecular dynamics of n-alkanes". In: *Journal of Computational Physics* 23.3, pp. 327–341.
- Sabatini, B. L. and W. G. Regehr (1999). "Timing of Synaptic Transmission". In: *Annual Review of Physiology* 61.1, pp. 521–542.
- Sachs, J. N., P. S. Crozier, and T. B. Woolf (2004). "Atomistic simulations of biologically realistic transmembrane potential gradients". In: *The Journal of Chemical Physics* 121.22, pp. 10847–10851.
- Sadek, B., M. Oz, S. M. Nurulain, P. Jayaprakash, G. Latacz, K. Kieć-Kononowicz, and E. Szymańska (2017). "Phenylalanine derivatives with modulating effects on human  $\alpha 1$ -glycine receptors and anticonvulsant activity in strychnine-induced seizure model in male adult rats". In: *Epilepsy Research* 138, pp. 124–131.
- Sali, A. and T. L. Blundell (1993). "Comparative protein modelling by satisfaction of spatial restraints". eng. In: *Journal of Molecular Biology* 234.3, pp. 779–815.
- Sauguet, L., R. J. Howard, L. Malherbe, U. S. Lee, P.-J. Corringer, R. Adron Harris, and M. Delarue (2013a). "Structural basis for potentiation by alcohols and anaesthetics in a ligand-gated ion channel". In: *Nature Communications* 4.1, p. 1697.
- Sauguet, L., F. Poitevin, S. Murail, C. Van Renterghem, G. Moraga-Cid, L. Malherbe, A. W. Thompson, P. Koehl, P.-J. Corringer, M. Baaden, and M. Delarue (2013b). "Structural basis for ion permeation mechanism in pentameric ligand-gated ion channels". In: *The EMBO Journal* 32.5, pp. 728–741.
- Sauguet, L., A. Shahsavari, F. Poitevin, C. Huon, A. Menny, A. Nemeč, A. Haouz, J.-P. Changeux, P.-J. Corringer, and M. Delarue (2014). "Crystal structures of a pentameric ligand-gated ion channel provide a mechanism for activation". en. In: *Proceedings of the National Academy of Sciences* 111.3, pp. 966–971.
- Schrödinger, L. L. C. (2015). *The PyMOL Molecular Graphics System, Version 1.8*.
- Seeber, M., M. Cecchini, F. Rao, G. Settanni, and A. Caflisch (2007). "Wordom: a program for efficient analysis of molecular dynamics simulations". In: *Bioinformatics* 23.19, pp. 2625–2627.
- Seeber, M., A. Felling, F. Raimondi, S. Muff, R. Friedman, F. Rao, A. Caflisch, and F. Fanelli (2011). "Wordom: a user-friendly program for the analysis of molecular structures, trajectories, and free energy surfaces". eng. In: *Journal of Computational Chemistry* 32.6, pp. 1183–1194.
- Sievers, F., A. Wilm, D. Dineen, T. J. Gibson, K. Karplus, W. Li, R. Lopez, H. McWilliam, M. Remmert, J. Söding, J. D. Thompson, and D. G. Higgins (2011). "Fast, scalable generation of high-quality protein multiple sequence alignments using Clustal Omega." In: *Molecular systems biology* 7.1, p. 539.
- Sigg, D. (2014). "Modeling ion channels: past, present, and future." In: *The Journal of general physiology* 144.1, pp. 7–26.
- Sine, S. M., H.-L. Wang, S. Hansen, and P. Taylor (2010). "On the Origin of Ion Selectivity in the Cys-Loop Receptor Family". In: *Journal of molecular neuroscience : MN* 40.1-2, pp. 70–76.

- Smart, O. S., J. G. Neduvilil, X. Wang, B. A. Wallace, and M. S. Sansom (1996). "HOLE: a program for the analysis of the pore dimensions of ion channel structural models". *ENG. In: Journal of Molecular Graphics* 14.6, pp. 354–360, 376.
- Song, C. and B. Corry (2010). "Ion Conduction in Ligand-Gated Ion Channels: Brownian Dynamics Studies of Four Recent Crystal Structures". *In: Biophysical Journal* 98.3, pp. 404–411.
- Sotomayor, M., V. Vásquez, E. Perozo, and K. Schulten (2007). "Ion Conduction through MscS as Determined by Electrophysiology and Simulation". *In: Biophysical Journal* 92.3, pp. 886–902.
- Sparling, B. A. and E. F. DiMauro (2017). "Progress in the discovery of small molecule modulators of the Cys-loop superfamily receptors". *In: Bioorganic & Medicinal Chemistry Letters* 27.15, pp. 3207–3218.
- Speranskiy, K., M. Cascio, and M. Kurnikova (2007). "Homology modeling and molecular dynamics simulations of the glycine receptor ligand binding domain". *In: Proteins: Structure, Function, and Bioinformatics* 67.4, pp. 950–960.
- Stead, C., A. Brown, C. Adams, S. J. Nickolls, G. Young, J. Kammonen, D. Pryde, and D. Cawkill (2016). "Identification of Positive Allosteric Modulators of Glycine Receptors from a High-Throughput Screen Using a Fluorescent Membrane Potential Assay". *In: Journal of Biomolecular Screening* 21.10, pp. 1042–1053.
- Steinbeck, C., Y. Han, S. Kuhn, O. Horlacher, E. Luttmann, and E. Willighagen (2003). "The Chemistry Development Kit (CDK): An Open-Source Java Library for Chemo- and Bioinformatics". *In: Steinlein, O. K. (2012). "Ion Channel Mutations in Neuronal Diseases: A Genetics Perspective". In: Chemical Reviews* 112.12, pp. 6334–6352.
- Südhof, T. C. (2012). "Calcium Control of Neurotransmitter Release". *en. In: Cold Spring Harbor Perspectives in Biology* 4.1, a011353.
- Sztainberg, Y. and H. Y. Zoghbi (2016). "Lessons learned from studying syndromic autism spectrum disorders". *eng. In: Nature Neuroscience* 19.11, pp. 1408–1417.
- Taly, A., P.-J. Corringer, D. Guedin, P. Lestage, and J.-P. Changeux (2009). "Nicotinic receptors: allosteric transitions and therapeutic targets in the nervous system." *In: Nature reviews. Drug discovery* 8.9, pp. 733–50.
- Taly, A., M. Delarue, T. Grutter, M. Nilges, N. Le Novère, P.-J. Corringer, and J.-P. Changeux (2005). "Normal mode analysis suggests a quaternary twist model for the nicotinic receptor gating mechanism". *eng. In: Biophysical Journal* 88.6, pp. 3954–3965.
- Tasneem, A., L. M. Iyer, E. Jakobsson, and L. Aravind (2005). "Identification of the prokaryotic ligand-gated ion channels and their implications for the mechanisms and origins of animal Cys-loop ion channels". *In: Genome Biology* 6.1, R4.
- Tassonyi, E., E. Charpentier, D. Muller, L. Dumont, and D. Bertrand (2002). "The role of nicotinic acetylcholine receptors in the mechanisms of anesthesia." *In: Brain research bulletin* 57.2, pp. 133–50.
- Tian, S., H. Sun, P. Pan, D. Li, X. Zhen, Y. Li, and T. Hou (2014). "Assessing an Ensemble Docking-Based Virtual Screening Strategy for Kinase Targets by Considering Protein Flexibility". *In: Journal of Chemical Information and Modeling* 54.10, pp. 2664–2679.
- Tochitsky, I., Z. Helft, V. Meseguer, R. B. Fletcher, K. A. Vessey, M. Telias, B. Denlinger, J. Malis, E. L. Fletcher, and R. H. Kramer (2016). "How Azobenzene Photoswitches Restore Visual Responses to the Blind Retina". *In: Neuron* 92.1, pp. 100–113.
- Trick, J. L., S. Chelvaniththilan, G. Klesse, P. Aryal, E. J. Wallace, S. J. Tucker, and M. S. P. Sansom (2016). "Functional Annotation of Ion Channel Structures by Molecular Simulation". *In: Structure* 24.12, pp. 2207–2216.
- Tsuang, M. T., M. J. Lyons, J. M. Meyer, T. Doyle, S. A. Eisen, J. Goldberg, W. True, N. Lin, R. Toomey, and L. Eaves (1998). "Co-occurrence of abuse of different drugs in men: the role of drug-specific and shared vulnerabilities." *In: Archives of general psychiatry* 55.11, pp. 967–72.
- Vanommeslaeghe, K., E. Hatcher, C. Acharya, S. Kundu, S. Zhong, J. Shim, E. Darian, O. Guvench, P. Lopes, I. Vorobyov, and A. D. Mackerell (2010). "CHARMM general force field: A force field for drug-like molecules compatible with the CHARMM all-atom additive biological force fields". *eng. In: Journal of Computational Chemistry* 31.4, pp. 671–690.
- Vassort, G. (2001). "Adenosine 5'-Triphosphate: a P2-Purinergic Agonist in the Myocardium". *In: Physiological Reviews* 81.2, pp. 767–806.
- Virginio, C., A. MacKenzie, F. A. Rassendren, R. A. North, and A. Surprenant (1999). "Pore dilation of neuronal P2X receptor channels". *In: Nature Neuroscience* 2.4, pp. 315–321.
- Walsh, R. M., S.-H. Roh, A. Gharpure, C. L. Morales-Perez, J. Teng, and R. E. Hibbs (2018). "Structural principles of distinct assemblies of the human  $\alpha 4 \beta 2$  nicotinic receptor". *In: Nature* 557.7704, pp. 261–265.
- Weill, C. L., M. G. McNamee, and A. Karlin (1974). "Affinity-labeling of purified acetylcholine receptor from *Torpedo californica*". *eng. In: Biochemical and Biophysical Research Communications* 61.3, pp. 997–1003.
- Wells, M. M., T. S. Tillman, D. D. Mowrey, T. Sun, Y. Xu, and P. Tang (2015). "Ensemble-Based Virtual Screening for Cannabinoid-Like Potentiators of the Human Glycine Receptor  $\alpha 1$  for the Treatment of Pain". *In: Journal of Medicinal Chemistry* 58.7, pp. 2958–2966. arXiv: 15334406.
- Werman, R., R. A. Davidoff, and M. H. Aprison (1967). "Inhibition of motoneurons by iontophoresis of glycine". *eng. In: Nature* 214.5089, pp. 681–683.
- Werman, R., R. A. Davidoff, and M. H. Aprison (1968). "Inhibitory of glycine on spinal neurons in the cat". *eng. In: Journal of Neurophysiology* 31.1, pp. 81–95.
- Williams, K. L., A. P. Ferko, E. J. Barbieri, and G. J. DiGregorio (1995). "Glycine enhances the central depressant properties of ethanol in mice". *eng. In: Pharmacology, Biochemistry, and Behavior* 50.2, pp. 199–205.
- Wishart, D. S., Y. D. Feunang, A. C. Guo, E. J. Lo, A. Marcu, J. R. Grant, T. Sajed, D. Johnson, C. Li, Z. Sayeeda, N. Assempour, I. Iynkkaran, Y. Liu, A. Maciejewski, N. Gale, A. Wilson, L. Chin, R. Cummings, D. Le, A. Pon, C. Knox, and M. Wilson (2018). "DrugBank 5.0: a major update to the Drug-

- Bank database for 2018". eng. In: *Nucleic Acids Research* 46.D1, pp. D1074–D1082.
- Wishart, D. S., C. Knox, A. C. Guo, S. Shrivastava, M. Hassanali, P. Stothard, Z. Chang, and J. Woolsey (2006). "DrugBank: a comprehensive resource for in silico drug discovery and exploration". eng. In: *Nucleic Acids Research* 34.Database issue, pp. D668–672.
- Witten, I. H., E. Frank, M. A. Hall, and C. J. Pal (2017). *Data mining : practical machine learning tools and techniques*, p. 621.
- World-Health-Organization (2017). *Dementia*.
- Xiong, W., K. Cheng, T. Cui, G. Godlewski, K. C. Rice, Y. Xu, and L. Zhang (2011). "Cannabinoid potentiation of glycine receptors contributes to cannabis-induced analgesia." In: *Nature chemical biology* 7.5, pp. 296–303.
- Xiong, W., X. Wu, F. Li, K. Cheng, K. C. Rice, D. M. Lovinger, and L. Zhang (2012). "A common molecular basis for exogenous and endogenous cannabinoid potentiation of glycine receptors." In: *The Journal of neuroscience : the official journal of the Society for Neuroscience* 32.15, pp. 5200–8.
- Yang, Z., K. R. Aubrey, I. Alroy, R. J. Harvey, R. J. Vandenberg, and J. W. Lynch (2008a). "Subunit-specific modulation of glycine receptors by cannabinoids and N-arachidonyl-glycine". In: *Biochemical Pharmacology* 76.8, pp. 1014–1023.
- Yang, Z., K. R. Aubrey, I. Alroy, R. J. Harvey, R. J. Vandenberg, and J. W. Lynch (2008b). "Subunit-specific modulation of glycine receptors by cannabinoids and N-arachidonyl-glycine". In: *Biochemical Pharmacology* 76.8, pp. 1014–1023.
- Yang, Z., A. Ney, B. A. Cromer, H. L. Ng, M. W. Parker, and J. W. Lynch (2007). "Tropisetron modulation of the glycine receptor: Femtomolar potentiation and a molecular determinant of inhibition". In: *Journal of Neurochemistry* 100.3, pp. 758–769.
- Yang, Z., E. Taran, T. I. Webb, and J. W. Lynch (2012). "Stoichiometry and Subunit Arrangement of  $\alpha 1\beta$  Glycine Receptors As Determined by Atomic Force Microscopy". In: *Biochemistry* 51.26, pp. 5229–5231.
- Yévenes, G. E., G. Moraga-Cid, L. Guzmán, S. Haeger, L. Oliveira, J. Olate, G. Schmalzing, and L. G. Aguayo (2006). "Molecular determinants for G protein betagamma modulation of ionotropic glycine receptors." In: *The Journal of biological chemistry* 281.51, pp. 39300–7.
- Yévenes, G. E. and H. U. Zeilhofer (2011). "Allosteric modulation of glycine receptors". In: *British Journal of Pharmacology* 164.2, pp. 224–236.
- Yévenes, G. E. and H. U. Zeilhofer (2011). "Molecular sites for the positive allosteric modulation of glycine receptors by endocannabinoids". In: *PLoS ONE* 6.8. Ed. by D. Kendall, e23886.
- Yu, R., E. Hurdiss, T. Greiner, R. Lape, L. Sivilotti, and P. C. Biggin (2014). "Agonist and Antagonist Binding in Human Glycine Receptors". In: *Biochemistry* 53.38, pp. 6041–6051.
- Yuan, S., S. Filipek, and H. Vogel (2016). "A Gating Mechanism of the Serotonin 5-HT<sub>3</sub> Receptor". In: *Structure* 24.5, pp. 816–825.
- Zeilhofer, H. U., M. A. Acuña, J. Gingras, and G. E. Yévenes (2018). "Glycine receptors and glycine transporters: targets for novel analgesics?" eng. In: *Cellular and molecular life sciences: CMLS* 75.3, pp. 447–465.
- Zhu, S., C. M. Noviello, J. Teng, R. M. Walsh, J. J. Kim, and R. E. Hibbs (2018). "Structure of a human synaptic GABA A receptor". en. In: *Nature*, p. 1.
- Zigmond, M. J., J. T. Coyle, and L. P. Rowland (2014). *Neurobiology of brain disorders : biological basis of neurological and psychiatric disorders*. Academic Press.

# Appendices

# A

## GLYCINE RECEPTOR $\alpha 1$ CORE ATOMS

---

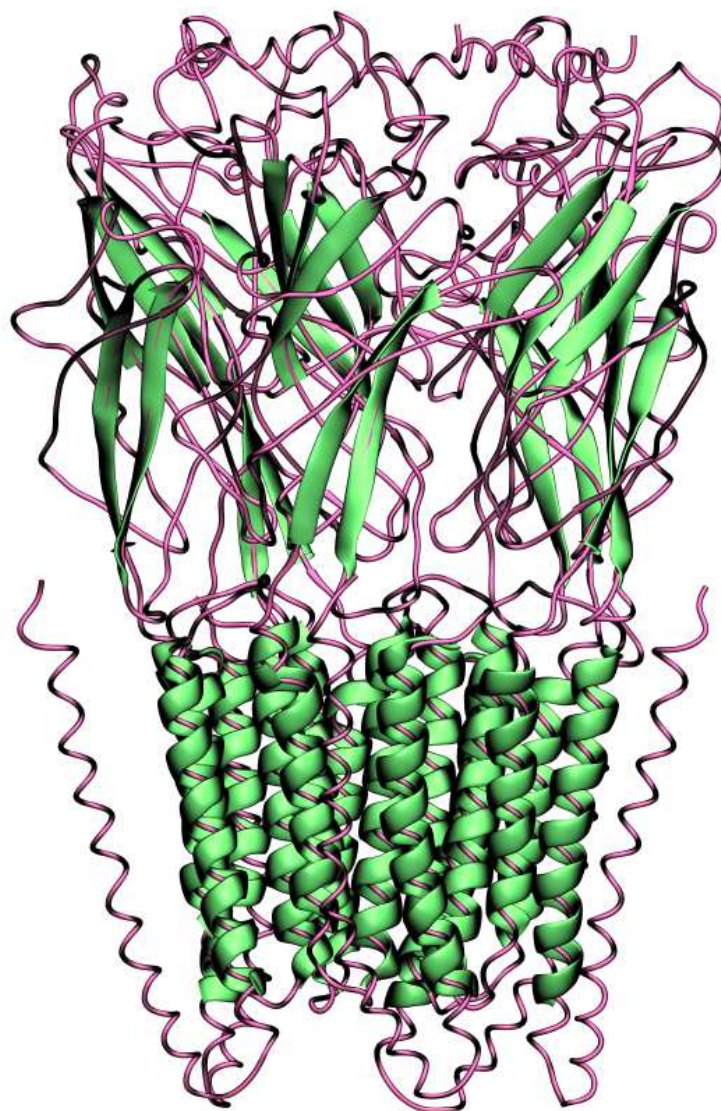


Figure A.1 – Core atoms of GlyR $\alpha 1$  in green. The definition is: (resid 54 to 60 or resid 78 to 84 or resid 142 to 147 or resid 165 to 174 or resid 225 to 233 or resid 241 to 258 or resid 265 to 288 or resid 297 to 322) based on Du et al. 2015 residue numbering.

# B

COMPUTATIONAL ELECTROPHYSIOLOGY DATA (TMD-ONLY)

---

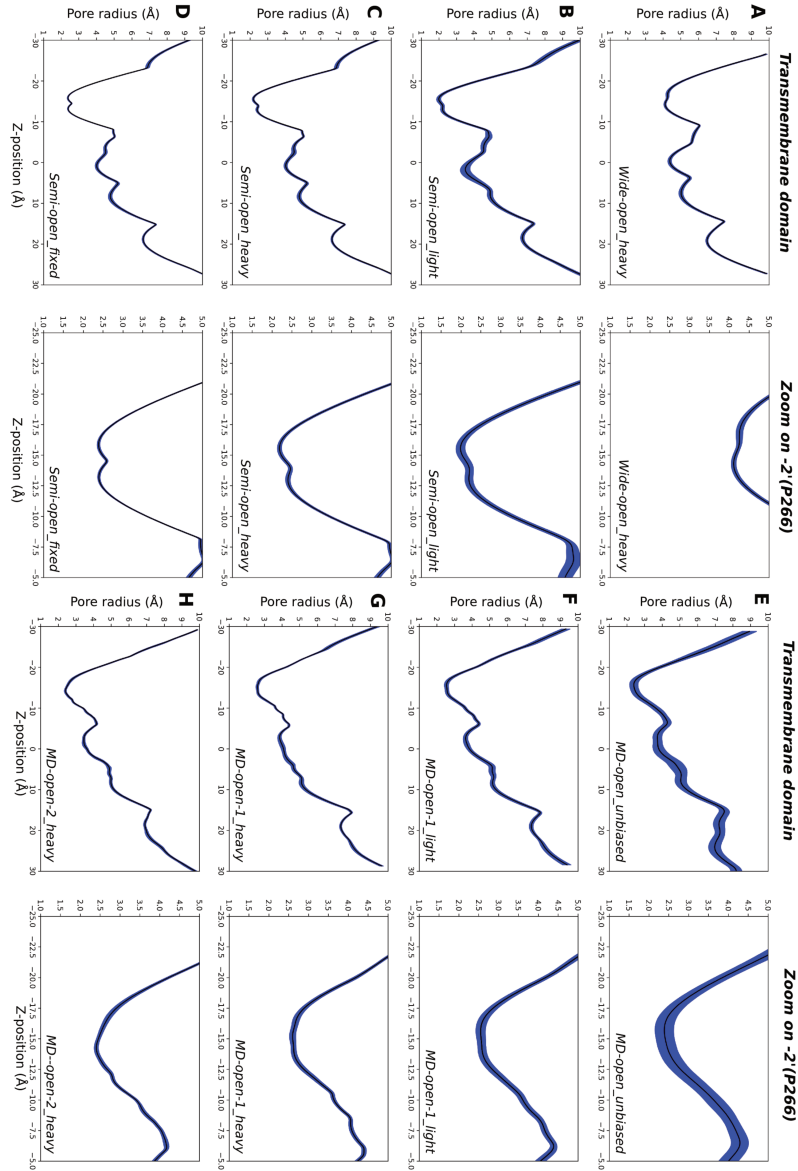


Figure B.1 – Related to Chapter 3. Hole-profiles of the *wide-open*, *semi-open* and *MD-open* structures during computational electrophysiology. The Hole-profiles during 50 ns-long MD trajectories were computed using the Wordom software. Data were analyzed within a Python script and represented as average value (black line)  $\pm$  the standard deviation (filled in blue). The averaged pore radius at the constriction point are: (A)  $4.14 \pm 0.06 \text{ \AA}$  for the *wide-open* with heavy restrains, (B)  $1.98 \pm 0.11 \text{ \AA}$  for the *semi-open* with light restrains, (C)  $2.18 \pm 0.05 \text{ \AA}$  for the *semi-open* with heavy restrains, and (D)  $2.38 \pm 0.03 \text{ \AA}$  for the *semi-open* with fixed restrains. (E)  $2.39 \pm 0.23 \text{ \AA}$  for the *MD-open* during unbiased-MD (Figure 3.g), (F)  $2.54 \pm 0.12 \text{ \AA}$  for the *MD-open* with light restrains, (G)  $2.59 \pm 0.08 \text{ \AA}$  for the *MD-open* with heavy restrains, and (H)  $2.40 \pm 0.05 \text{ \AA}$  for the *MD-open2* with heavy restrains.

Structure	Run	Restrains	Voltage (mV)	Water model	Duration (ns)	CF permeation events	CF /ns	Current (pA)	Error (pA)	Conductance (pS)
<b>Wide-open</b>	1	Heavy	150	TIP3P	86	32	/	/	/	/
	2				107	45	/	/	/	/
	3				138	51	/	/	/	/
	TOT				331	128	0.39	62.0	3.4	413.0
<b>Wide-open</b>	1	Heavy	150	TIP4P/2005	91	20	/	/	/	/
	2				111	24	/	/	/	/
	3				133	30	/	/	/	/
	4				126	25	/	/	/	/
	5				105	22	/	/	/	/
	TOT				566	121	0.214	24.3	3.1	228.3
<b>MD-open</b>	1	Light	150	TIP3P	236	1	/	/	/	/
	2				275	13	/	/	/	/
	3				234	4	/	/	/	/
	TOT				745	18	0.024	3.9	0.9	25.8
<b>MD-open</b>	1	Heavy	150	TIP3P	270	4	/	/	/	/
	2				241	4	/	/	/	/
	3				183	5	/	/	/	/
	TOT				693	13	0.019	3.0	0.8	20.0
<b>MD-open</b>	1	Heavy	250	TIP3P	177	11	/	/	/	/
	2				230	6	/	/	/	/
	3				254	3	/	/	/	/
	TOT				661	20	0.030	4.8	1.1	19.4
<b>MD-open2</b>	1	Heavy	150	TIP3P	161	1	/	/	/	/
	2				142	3	/	/	/	/
	3				161	4	/	/	/	/
	4				160	2	/	/	/	/
	5				161	4	/	/	/	/
	6				162	3	/	/	/	/
	TOT				947	17	0.018	2.88	0.7	19.2
<b>Semi-open</b>	1	Light	150	TIP3P	59	0	/	/	/	/
	2				116	0	/	/	/	/
	3				97	0	/	/	/	/
<b>Semi-open</b>	1	Heavy	150	TIP3P	161	0	/	/	/	/
	2				219	0	/	/	/	/
	3				212	0	/	/	/	/
<b>Semi-open</b>	1	Heavy	250	TIP3P	216	0	/	/	/	/
	2				166	0	/	/	/	/
	3				244	0	/	/	/	/
<b>Semi-open</b>	1	Fixed	250	TIP3P	62	0	/	/	/	/
	2				191	0	/	/	/	/
	3				124	0	/	/	/	/
	TOT				1867	0	0	0	/	0

Figure B.2 – Related to Chapter 3. Computational electrophysiology for the three open structures of GlyR $\alpha$ 1. Summary of the production runs carried out in all-atom MD in presence of a transmembrane potential and physiological 145 mM NaCl concentration. Permeation events were recorded using the FLUX module in the Wordom. Errors  $\sigma$  on the currents  $I$  are estimated as  $\sigma = I/\sqrt{N}$  with  $N$  the number of permeation events. We sampled a total of 331, 3046 and 1867 ns for the *wide-open*, *MD-open* and *semi-open*, respectively.

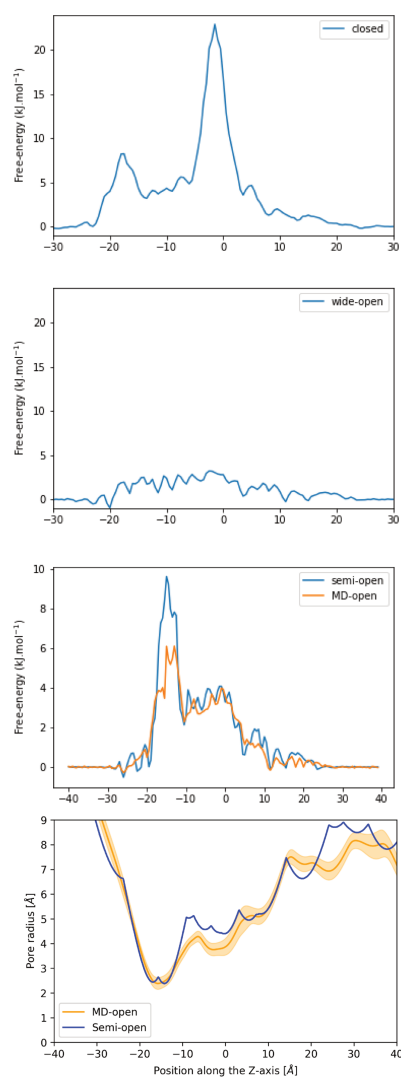


Figure C.1 – Comparison of the free-energy profiles for water permeation in the GlyR $\alpha$ 1 structures. Free-energy profiles for water permeation based on Boltzmann inversion of the water density sampled by the molecular dynamics (Trick et al. 2016). Simulated trajectories of 50 ns were analyzed to compute the water density within the pore. Our results for the three GlyR $\alpha$ 1 cryo-EM structures are in qualitative and quantitative agreements with the results obtained by the authors of the methods (Trick et al. 2016).

# D

## HOLE PROFILE OF ANIONIC PLGIC STRUCTURES

---

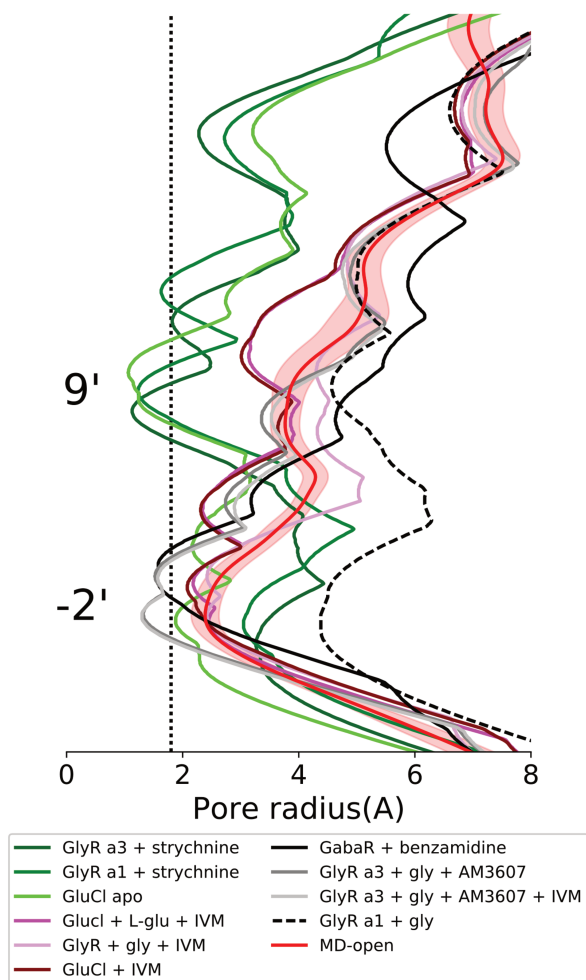


Figure D.1 – Hole profile of anionic pLGICs. Hole analysis the TMD of presently available high-resolution structures of anionic pLGICs. Colors represent the three clusters: shades of green for the resting structures, shades of red for active structures, shades of grey for desensitized structures. The vertical dashed line symbolizes the radius of a chloride.

COMPUTATIONAL ELECTROPHYSIOLOGY DATA (*FULL-LENGTH*)

Structure	250 mV (WT)	150 mV (WT)	-150 mV (WT)	-250 mV (WT)	250 mV (K120E)	-250 mV (K120E)
<i>MD-open</i> <sub>1</sub>	10 (167)	7 (205)	5 (503)	22 (195)	2 (157)	9 (161)
<i>MD-open</i> <sub>2</sub>	11 (200)	2 (174)	27 (554)	22 (196)	0 (55)	4 (161)
<i>MD-open</i> <sub>3</sub>	1 (58)	2 (188)	13 (416)	12 (155)	0 (127)	7 (127)
<i>MD-open</i> <sub>4</sub>	7 (165)	4 (205)	3 (500)	6 (230)	0 (165)	11 (111)
<i>MD-open</i> <sub>5</sub>	7 (150)	/	6 (281)	15 (249)	1 (150)	14 (150)
<i>MD-open</i> <sub>6</sub>	2 (42)	/	8 (266)	20 (250)	0 (150)	7 (150)
<i>MD-open</i> <sub>7</sub>	6 (163)	/	/	17 (193)	/	/
<i>MD-open</i> <sub>8</sub>	10 (163)	/	/	22 (191)	/	/
<i>MD-open</i> <sub>9</sub>	3 (160)	/	/	24 (188)	/	/
<i>MD-open</i> <sub>10</sub>	4 (174)	/	/	13 (198)	/	/
Total	61 (1442)	15 (772)	62 (2520)	173 (2045)	3 (804)	52 (860)
Selectivity ( $P_{Cl^-} / P_{Na^+}$ )	61	N.A.	N.A.	10.2	N.A.	6.5

Table E.1 – Related to Chapter 4. Computational electrophysiology results obtained on the unconstrained and *full-length* GlyR $\alpha$ 1 in the *MD-open* conformation. *MD-open*<sub>1:10</sub> refer to the ten snapshots randomly extracted during the initial unbiased simulation of the *MD-open* conformation, see Chapter 4 for details. The cells contain the number of chloride anion permeation events (in t ns). Each column is a different experimental condition, i.e., applied membrane voltage, or GlyR WT and mutant K120E. The selectivity is computed as the ratio between the number of permeating chloride and sodium. We wrote *N.A.* when no sodium permeation event was recorded.

Membrane potential mV	Duration (ns)	Chloride permeation events	Sodium permeation events
1000	10	2	0
750	10	0	0
500	10	1	0
350	10	0	0
250	10	0	0
150	20	2	0
-150	20	1	0
-250	10	0	0
-350	10	1	0
-500	10	6	1
-750	10	12	2
-1000	10	13	3

Table E.2 – Related to Chapter 4. Computational electrophysiology results obtained on the *heavily* constrained *full-length* GlyR $\alpha$ 1 in the *wide-open* cryo-EM structure.

*Methods*

To measure the conductance of an ion-channel structure, a statistically meaningful number of permeation events needs to be sampled at equilibrium, which requires  $\mu$ s sampling possibly at different membrane potentials. By modeling the movement of ions in the mean field of the protein/membrane environment, BD simulations provide an efficient strategy to explore ion conductance with a realistic implementation of concentration gradients and the membrane potential. Besides, since the ions are modeled explicitly, these simulations offer a microscopic interpretation of the phenomenon. In this report, BD simulations were carried out using the GCMC/BD software (Im et al. 2000), where the protein, the membrane and the water molecules are treated as a continuum, whereas the ions undergo diffusive dynamics with a time step of 10 fs. This approach is computationally inexpensive and grants  $\mu$ s sampling in a week or so on a single CPU-core.

Three protein structures, i.e., the *wide-open* and *semi-open* cryo-EM reconstructions and an average structure representative of the *MD-open* state, were analyzed. By running BD on the *wide-open* and *semi-open* structures, it was found that these structures were not permeable (similarly to all-atom simulations, see Chapter 4). To overcome this problem, chimeric structures for the *wide-open* and *semi-open* states were produced by merging the coordinates of both ECD relaxed by MD with those of the TMD extracted from the corresponding cryo-EM structures. This preparation allowed us to preserve the exact geometry of the cryo-EM reconstructions at the level of the pore with minor but necessary reorientation of charged residues in the ECD to make it ion permeable. To probe the behavior of the *MD-open* state, two structural models were built. The first model (*MD-open*) was produced by averaging over a series of consecutive snapshots taken from a 10 ns stretch of the *wide-open* simulation after re-opening, i.e., the local rearrangement of the TMD sampled at 200 ns. The second model (*MD-open-symm*) was obtained from the *MD-open* structure by overlapping all subunits and computing an average, see Chapter 3 for all details. This average subunit was then superimposed to the individual subunits in the original structure to obtain a symmetric model. Before BD, these models were energy minimized by 5000 steps of conjugated gradient and line search algorithm in NAMD 2.12. Trajectory manipulation and structural averaging were carried out using the software Wordom (Seeber et al. 2007; Seeber et al. 2011). To prepare for BD simulations, the protocol by (K. I. Lee et al. 2012) was followed; see details on <http://www.charmm-gui.org/>. In brief, the membrane thickness was set to 30 Å. A 5 Å-thick ion buffer region was placed at the top and the bottom of the box, 20 Å away from the protein in the direction. Dielectric constants of 2 and 80 were used to model the protein/membrane and the water regions, respectively. Symmetrical 145 mM NaCl solution was applied to mimic the experimental setup of Bor-

mann et al. 1993. The bulk diffusion constants for chloride and sodium ions were set to  $0.203$  and  $0.133 \text{ \AA}^2 \text{ ps}^{-1}$ , respectively. Before running the simulations, grid-based calculations of the electrostatic potential generated by the protein charges and the transmembrane potential, the reaction field arising from the dielectric hetero-junction between the solvent, the protein and the lipids, and the core-repulsive steric potential from the ion-inaccessible region were computed using the PB and PNP equation solver (PB/PNP) (K. I. Lee et al. 2012). For each protein structure, three  $1\text{-}\mu\text{s}$  simulations in the presence of membrane potentials were carried out for a total of simulation per structure with randomized initial positions and velocities for the ions. Estimates of the anionic and cationic currents per simulation were obtained by counting the number of anions or cations permeating the pore per nanosecond. Mean currents per voltage  $\pm$  standard error over triplicate simulations are given in displayed in the figures. By fitting the total ionic (anionic + cationic) current as a function of the membrane potential, an ion-conductance per structure was estimated from the slope of the linear interpolation of the I-V curve. Since strong rectification was observed at large membrane voltages, the conductance was measured by linear regression in the  $[-150 : +150]$  mV range. Channel selectivity, i.e., the probability of chloride versus sodium permeation, was calculated from the current ratio (i.e., anionic over cationic) in the same voltage range. The numerical results correspond to the average ratios over triplicate simulations  $\pm$  the standard error.

### Results

The physiological significance of the three open-channel structures of GlyR $\alpha$ 1, i.e., *wide-open*, *semi-open*, and *MD-open*, was challenged by comparing the conductance measured in computational electrophysiology versus single-channel, outside-out patch clamp experiments (Bormann et al. 1993). For this purpose, structure-dependent I-V-curves were calculated using Grand-Canonical Monte-Carlo BD simulations (Im et al. 2000) with symmetrical 145 mM concentration of NaCl and membrane potentials ranging from  $-250$  mV to  $250$  mV. This simulation approach explores the movement of ions in a transmembrane channel without treating all the water, the membrane, and the protein degrees of freedom explicitly, which allows for microsecond sampling in a few days of calculation on a single CPU. By collecting statistics over hundreds of permeation events, the BD simulations provided converged estimates of both channel conductance and ion selectivity for the three open-channel structures.

Surprisingly, both cryo-EM structures were non-permeable to ions within the whole range of voltage, see Figure F.1 (left). Ions were unable to pass through the ECD even if its diameter is larger than what is required for chloride permeation (Nightingale 1959). Interestingly, this result is in excellent agreement with the results obtained in all-atom MD, see Chapter 4. Similarly to our MD simulations (Chapter 3 and 4), the ECD removal permits to recover the permeability to chloride at positive membrane voltages, see Figure F.1 (right).

Without knowing about the existence of ECD lateral portals, we *fixed* the odd behavior of the cryo-EM structures removing the original ECD and by replacing it by an MD-relaxed ECD. The following analysis referring to *wide-open* and *semi-open* will be about the MD-corrected structures.

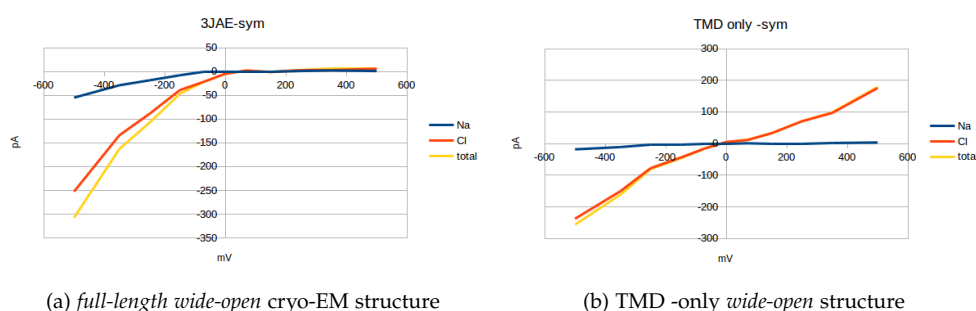


Figure F.1 – I-V-curves produced by BD during  $1\ \mu\text{s}$  per voltages. Tested membrane potentials are:  $-500, -350, -250, -150, -100 - 70 - 30, 0, 30, 70, 100, 150, 250, 350, 300\ \text{mV}$ . Under positive voltages the *full-length* GlyR cryo-EM structures are impermeable to chloride.

The results are showed in Figure F.2. In the voltage range of  $-150 : 150\ \text{mV}$ , the simulations provide conductance values of  $208 \pm 14\ \text{pS}$  for the *wide-open*,  $96 \pm 6\ \text{pS}$  for the *semi-open*, and  $88 \pm 6\ \text{pS}$  for the *MD-open* structures. Strikingly, the simulation results for both the *semi-open* ( $96\ \text{pS}$ ) and the *MD-open* ( $88\ \text{pS}$ ) structures are in quantitative agreement with the experiments ( $86\ \text{pS}$ ) for homomeric GlyR $\alpha 1$  (Bormann et al. 1993), whereas the *wide-open* conductance ( $208\ \text{pS}$ ) is twice as large. Based on these results, we conclude that the *wide-open* structure is not representative of the physiologically active state. Also, the results of the *semi-open* versus the *wide-open* structures provide evidence that the organization of the proline residues at the position  $-2'$  is critical for ion-conductance in the active state, in agreement with previous mutagenesis studies (D. J. S. Lee et al. 2003). The analysis of other snapshots extracted from the MD trajectory after pore re-opening provides consistent conductance results in the range of  $80 - 90\ \text{pS}$ , which supports the significance of the *MD-open* state.

Permeation selectivity measured from BD simulations show that the three investigated structures manifest a clear preference for chloride over sodium translocation in quantitative agreement with experiments (Keramidas et al. 2002). Perhaps surprisingly, these data indicate that the *wide-open* structure is also strongly selective for chloride, which indicates that selectivity is only weakly correlated with the pore shape and dimensions.

### Discussion

Of note, we obtained the results from the BD before the ones produced by all-atom MD in presence of an electric field (Chapters 3 and 4). For that reason, our understanding of the phenomena controlling chloride permeation in GlyR was limited at that time. However, BD simulations allowed us to strikingly discriminate between the two cryo-EM structures. The *wide-open* structure being two times more conductive than experiments, but the *semi-open* and *MD-open* structures were able to reproduce the physiological currents.

These results are different from what we later obtained by all-atom MD and were at the origin of our doubts concerning the domain of applicability of BD simulations. Indeed, in BD simulations, the *semi-open* structure is permeable at physiological conditions, which is not the case in all-atom MD, see Chapter 3. Moreover, both the *semi-open* and *MD-open*

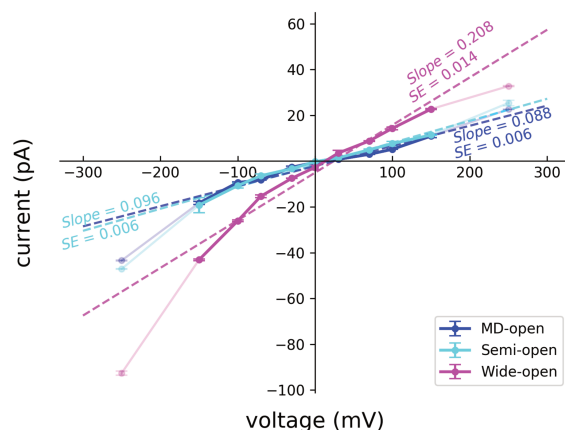


Figure F.2 – Calculated I-V-curves for the three open structures of GlyR $\alpha$ 1. Structure-dependent I-V-curves were obtained by measuring average ionic currents from 11 BD runs of 1  $\mu$ s with membrane voltages ranging from  $-250 : 250$  mV. The uncertainty on the ionic current was estimated from the standard error of the mean in triplicate experiments. Ion conductance was determined from the slope of the linear best-fit in the physiological voltage range of  $-150 : 150$  mV.

structures display in BD a solid conductance of  $\sim 90$  pS, which is again, in contradiction to the results obtained in MD. These results are particularly important since we showed that the difference in conductance between *semi-open* and *MD-open* in MD can be explained by the larger dehydration of the constriction point in the *semi-open* pore, in comparison to *MD-open*. This observation suggests that the BD simulations were not able to discriminate between the symmetric and asymmetric organizations of the gate observed in *semi-open* and *MD-open*, respectively. More importantly, BD simulations failed at detecting the partial dehydration of the gate in *semi-open*, which is possibly responsible for the impermeability to chloride.

Altogether these results suggest that in anionic pLGICs, where the pore radius at the constriction point is so narrow and where only apolar residues line the pore, BD simulations might fail to capture the proper conductive behavior of the channel. It is not the case in cationic pLGICs (Song and Corry 2010), where BD was successfully applied to channels of similar size. However, in cationic channels, the constriction point is lined by charged residues which are responsible for the selectivity, by assisting the permeation of the cations (Sauguet et al. 2013b). Charged residues are participating to the *hydration* of the permeating cations (Sauguet et al. 2013b), lowering the role of water in the permeation mechanism.

Overall, it seems possible to apply BD simulations in narrow pores such as the ones in pLGICs if charged residues assist the permeation, but in anionic, it is not the case, and the permeation is solely enabled by the presence of a sufficient number of water molecules. For that reason, we would exclude anionic pLGICs from the domain of applicability of BD simulations.

# Exploration de la transmission synaptique et de la régulation des récepteurs ionotropes par simulations de dynamique moléculaire et électrophysiologie numérique

## Résumé

Au sein du système nerveux central, les signaux entre les neurones sont principalement transmis au travers des synapses chimiques. La transduction du signal y a lieu grâce à la liaison des neurotransmetteurs aux récepteurs membranaires, ce qui induit l'ouverture de canaux ioniques. Le Récepteur de la Glycine (RGly) est un récepteur ionotrope impliqué dans de nombreux troubles neurologiques tels que l'addiction, la douleur chronique, l'autisme, ou encore l'hyperekplexie. Du fait de son rôle dans plusieurs pathologies, il est important de développer des nouveaux traitements ciblant ce récepteur. Pour cette raison, nous avons utilisé des simulations de Dynamiques Moléculaire (DM) et d'électrophysiologie numérique afin d'évaluer les propriétés fonctionnelles des structures du RGly disponibles. Dans cette thèse, nous avons montré qu'aucune des structures obtenues expérimentalement ne satisfait les propriétés fonctionnelles de l'état actif du récepteur. Grâce aux simulations de DM, nous avons caractérisé une nouvelle conformation du RGly, qui est compatible avec l'état actif du récepteur. De plus, nous avons souligné le rôle majeur des portails latéraux pour la perméation des ions. Finalement, nous avons proposé un protocole original, nommé *pharmacologie dépendante de l'état*, pour identifier de nouvelles petites molécules modulatrices de protéines allostériques.

Dynamique moléculaire ; Récepteur ionotrope ; électrophysiologie numérique ; Récepteur de la Glycine ; Transmission synaptique ; pLGIC ; allostérie

## Résumé en anglais

In the central nervous system, signals within neurons are mostly transmitted through chemical synapses. At the level of the synapse, signal transduction arises from the binding of neurotransmitters to membrane receptors in order to open ion channels. The Glycine Receptor (GlyR) is an ionotropic receptor which is involved in several neurological disorders such as addiction, chronic pain, autism, or hyperekplexia. Because of its implication in many human diseases, it is of particular interest to design novel drugs targeting this receptor. With this goal in mind, we used Molecular Dynamics (MD) simulations and computational electrophysiology to probe the functional properties of available GlyR structures. In this thesis, we showed that none of the experimental structures display the physiological behavior of the conductive state. Using MD simulations, we captured a novel conformation of the GlyR compatible with a conductive state and demonstrated the importance of lateral portals for ionic permeation. Lastly, we proposed an original protocol, named *state-based pharmacology*, to discover modulators of allosteric proteins.

Molecular Dynamics; ionotropic receptor; computational electrophysiology; Glycine receptor; synaptic transmission; pLGIC; allostery